eman ta zabal zazu

Universidad del País Vasco

Euskal Herriko Unibertsitatea

DEVELOPMENT OF MAIZE STARCH-BASED NANOCOMPOSITE FILMS AND HYDROGELS INCORPORATING POLYSACCHARIDE AND GRAPHENE DERIVED NANOENTITIES

KIZKITZA GONZALEZ MUNDUATE

July 2019

Kizkitza González Munduate
Faculty of Engineering, Gipuzkoa
Donostia/San Sebastian, July 2019

Development of maize starch-based nanocomposites films and hydrogels incorporating polysaccharide and graphene derived nanoentities

PhD dissertation presented by

KIZKITZA GONZALEZ MUNDUATE

Supervised by

Dr. NAGORE GABILONDO LOPEZ and Dr. ARANTXA ECEIZA MENDIGUREN

Donostia/San Sebastian, July 2019

ACKNOWLEDGMENT

Lehenik eta behin, tesi honen zuzendari izan diren Nagore Gabilondo eta Arantxa Eceiza eskertu nahi ditut, lan hau burutzeko aukera eman izanagatik eta urte hauetan eskeini didazuten etengabeko laguntzagatik.

Bestalde, Euskal Herriko Unibertsitatea (UPV/EHU) eskertu nahi dut, lan hau aurrera eraman ahal izateko emandako diru laguntzagatik (Doktoratu Aurreko Ikertzaileak Prestatzeko beka, PIF-G-003-2015). Eskerrak eman ere Euskal Herriko Unibertsitateko Ikerkuntzarako Zerbitzu Orokorrari (SGIker) emandako laguntza teknikoa eta gizatiarragatik. Bereziki, makroportaera-mesoegitura-nanoteknologia zerbitzuko Loli Martin doktoreari, denbora honetan emandako aholku guztiengatik.

Mila esker Luc Avérous doktoreari, bere ikerkuntza taldean (BioTeam/ICPEES-ECPM, UMR CNRS 7515, Université de Strasbourg) eta hiru hilabeteko egonaldian elkarlanean lan egiteko aukera eman izanagatik. Era berean, POLYMAT institutuko (Polimeroen Zientzia eta Teknologia saila, Kimika Fakultatea, UPV/EHU) Alba González eta Lourdes Irusta doktoreei filmen iragazkortasun karakterizazioa burutzeko emandako laguntzagatik eta Ana Alonso Varona doktoreari (Zelula Biologia eta Histologia saila, Medikuntza eta Erizaintza Fakultatea, UPV/EHU) biobateragarritasun saiakuntzetarako eskeinitako laguntzagatik.

Ingeniaritza Kimikoa eta Ingurumenaren Ingeniaritza saileko 'Materialak + Teknologiak' ikerkuntza taldeko kideei ere eskerrik asko zuen laguntzagatik. Baina bereziki eskerrak eman behar dizkizuet zuei, laborategiko lagunei, urte hauetan elkarrekin igarotako mila abenturengatik.

Azkenik, eskerrik beroenak nere familia eta lagunentzat. Etxekoengatik jaso dudan babesa eta maitasuna ezinbestekoa izan da tesi hau aurrera eraman eta amaitu ahal izateko. Nere bizitzaren euskarria zarete.

Kizkitza González Munduate

SUMMARY

This thesis research was focused on the development and characterisation of starch-based materials. Two types of materials with different applications were prepared: plasticised starch films and nanocomposite films as alternative of packaging materials and starch cross-linked hydrogel nanocomposites for biomedical applications.

Firstly, plasticised maize starch films were prepared by solvent casting using glycerol, D-isosorbide and 1,3-propanediol as plasticisers in order to analyse the effect of the plasticiser on the final properties and the retrogradation phenomenon. Then, nanocomposite films were developed by the incorporation of polysaccharide nanocrystals, i.e. waxy maize starch nanocrystals and cellulose nanocrystals. The influence of adding different waxy maize starch nanocrystals contents as well as the effect of adding together waxy maize starch and cellulose nanocrystals was evaluated. In addition, the viability to produce plasticised starch films by extrusion/compression methodology was analysed. Furthermore, plasticised starch nanocomposite films were prepared by the addition of carbonaceous nanoparticles. The influence of adding different graphene and graphene oxide contents into the plasticised starch matrix was analysed. Besides, graphene oxide was reduced with ascorbic acid in order to improve the electrical conductivity of the films.

Regarding the synthesis of hydrogel nanocomposites, on one hand, furan-modified starch was cross-linked by Diels-Alder reaction using a tetramaleimide as cross-linker and reinforced with cellulose nanocrystals. Different nanocrystal contents were added in order to study the influence on the rheological behaviour, swelling capacity and morphology, as well as on the drug release kinetics and the cell viability. Finally, Diels-Alder hydrogel nanocomposites were prepared between furan-modified starch cross-linked by bismaleimide. The effect of using different furan to maleimide weight ratios on the behaviour of hydrogels was analysed. In addition, conductive and antimicrobial hydrogel nanocomposites were designed adding graphene and using Salvia extracts as stabilisers.

TABLE OF CONTENTS

CHAPTER 1:

INTRODUCTION

1. INTRODUCTION

1.1. MOTIVATION

Science, always linked to technology, works intensely looking for solutions to the new challenges that our society is facing every day. The society, in constant evolution, needs to give answer to the handicaps found in sectors such as medicine, environment, transport, energy or food. In this sense, the development of novel materials with specific properties that will improve our wellbeing while contributing to progress and ensuring a more sustainable future is essential.

In this line of investigation, nowadays, multidisciplinary researchers are focused on the development of biopolymer-based (IUPAC definition of biopolymer: polymers formed by living organisms, from biomass) new materials with competitive properties for a wide range of applications. In this context, polysaccharides are the perfect candidate to be "green" alternative materials due to their accessibility and physicochemical properties. Among them, starch is outlined as precursor of environmentally friendly and bio-based materials due to its availability from many species, versatility to be modified both physically and chemically, biodegradability and low cost [1]. However, starch shows some important drawbacks, such as its high hydrophilicity and its poor mechanical behaviour [2]. In addition, the recrystallization and retrogradation phenomena affect the evolution of the properties with the time. Therefore, several strategies such as polymeric blending, use of different plasticisers, development of nanocomposites, chemical modification and cross-linking have been proposed in the literature as methods to improve the physicochemical behaviour of starch-based materials [2–5].

Thus, in this work, we focused in two challenges: the development of "green" alternatives for packaging and the synthesis of hydrogels to be applied as biomaterials.

In order to reduce environmental concerns of using commodity plastics derived from petroleum sources, researchers are focused in the design of biodegradable, compostable and/or recyclable bioplastics that could reduce the use of raw materials from fossil sources and could decrease the emission of greenhouse gases at the end of their useful life. Thus starch, in particular in form of plasticised starch (PLS) and thermoplastic starch (TPS), have been revealed as an appropriate candidate to be employed as substitute of synthetic polymers traditionally used for packaging.

On the other hand, hydrogels derived from biopolymers can overcome the limitations that some other biomaterials show (foreign body response, mechanic failure, electrical response) [6], since they are able to retain large amount of water and biological fluids, present high biocompatibility and functional versatility [7]. Starch, in addition to its specific physicochemical and biological behaviour, presents primary and secondary hydroxyl groups that allows the incorporation of functional groups [8]. Thus, starch emerged as an appropriate polysaccharide for the formation of hydrogels to be applied in biomedicine [9].

1.2. STATE OF ART

1.2.1. Starch

Starch is a hydrophilic and semi-crystalline natural biopolymer of renewable origin and biodegradable character produced by many green plants as a source of energy [10–15]. It is one of the most abundant biopolymers in the world [16], since it can be found in roots, tubers, seeds, stem, leaves and fruits of several agricultural crops [15,17–19].

Historically, starch besides being an essential carbohydrate in the human diet [19], has been used as adhesive of Egyptian papyrus (4000 BC), in Chinese papers (312 AD) or as stiffener in the textile industry (16th century) [20]. However, over the last centuries the production and applications

of starch have increased. According to the European Starch Industry Association (Starch Europe) [20], in 2017, 24 million tons of agricultural raw materials were processed into 11 million tons of starch and 5 million tons of co-products (Figure 1.1). The principal processed crops were potato (30%), maize (34%) and wheat (36%). That year, the European market consumed a total of 9.4 million tons of starch (without considering the starch bi-products around 5 million tons), including modified starches (19%), native starches (27%) and starch sweeteners (54%). The starch market is divided in three main sectors: animal feed (2%), non-food (40%, principally corrugating and papers) and food applications (58%, mainly confectionary and drinks) (Figure 1.1).

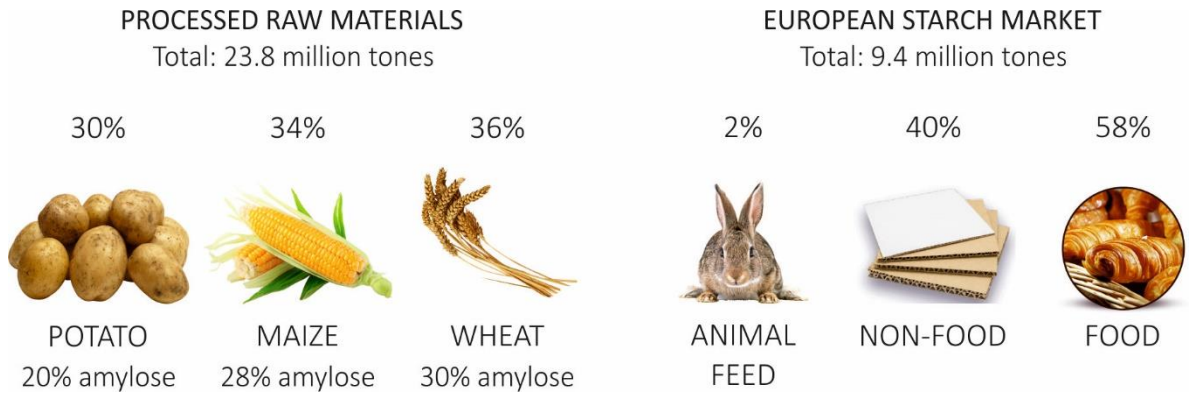

Figure 1.1 – Agriculture crops processed in Europe and applications of the starch market [20].

Starch is mainly composed of a mixture of two glycosidic macromolecules, i.e. amylose and amylopectin [11,16,21]. Amylose is a linear polysaccharide made up of (1-4)α-d-glycopyranose units, whereas amylopectin is a highly branched macromolecule composed of both α(1-4) and α(1-6) glycopyranosyl linkages [3,16,22] and it is the main responsible of the crystalline character [17,23–25] (Figure 1.2). In addition to amylose and amylopectin, starch granules contain small amounts of proteins (0.1 – 0.7%), lipids (<1.5%, fatty acids and lysophospholipids) and phosphorous (found in phospholipids and as phosphate monoesters) [15].

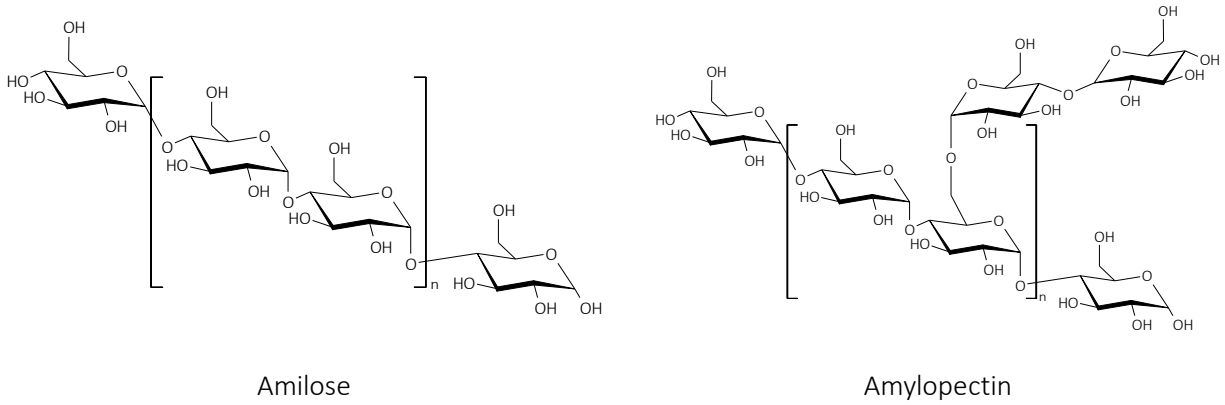

Figure 1.2 – Chemical structure of amylose and amylopectin.

Starch is synthesised in form of granules in plastids (organelles of eukaryote cells), namely in chloroplasts or amyloplasts [15]. In the case of maize starch, as well as other cereals, starch is stored in the plastids at seed endosperm [26,27] (as shown in Figure 1.3). The size (diameter varying from 1 to 100 μm) and morphology (spheres, ellipsoids, polygon, platelets or irregular tubules) of the resulting granules, as well as the amylose/amylopectin ratio and crystallinity depends on the botanical origin [15,28–30].

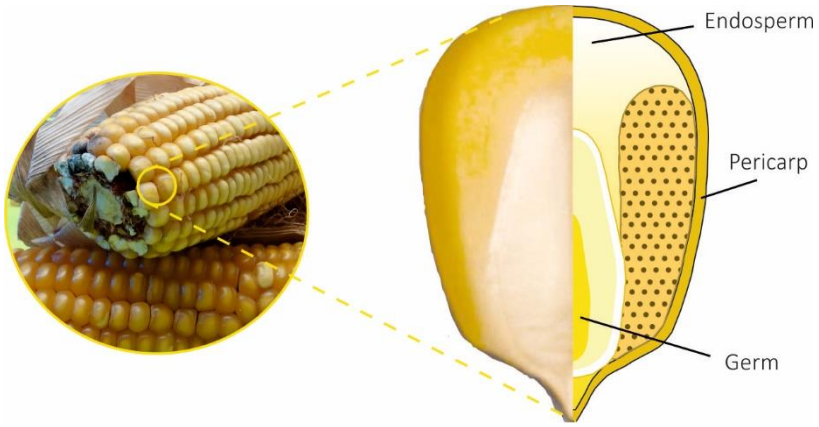

Figure 1.3 – Scheme of maize grain.

Figure 1.4 describes the structure of the starch granules and illustrates the different organisation levels: granule, blocklet structure, lamellae structure, amylopectin cluster, amylopectin double helix and crystal structures.

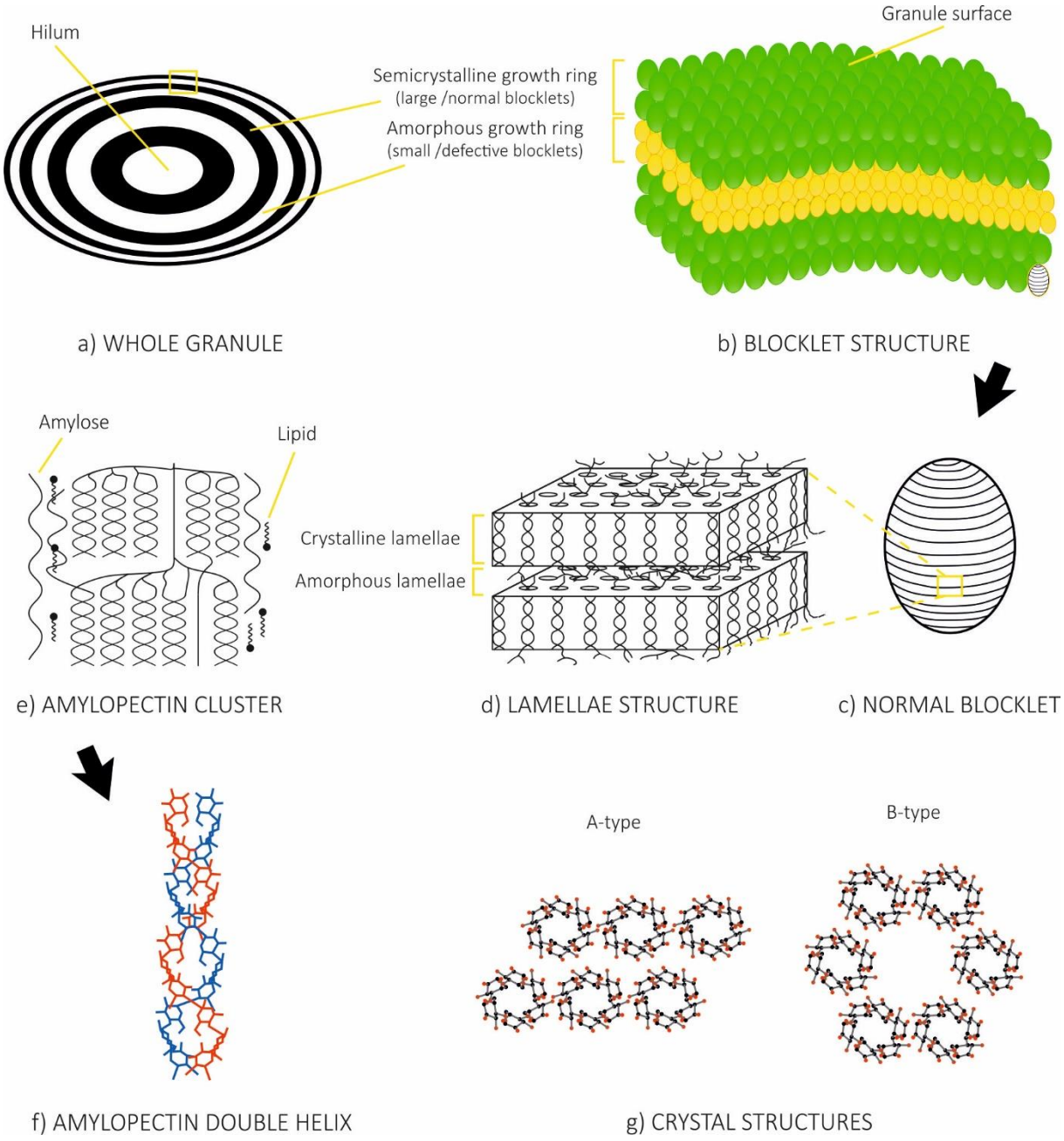

Figure 1.4 – Model of different levels of structural organisation of the starch granule. a) Section of the whole granule showing the radial organisation of alternating semi-crystalline (black) and amorphous (white) growth rings extending from the hilum. b) The blocklet structure where blocklet size is bigger in the semi-crystalline growth rings (green blocklets) than in the amorphous growth rings (yellow blocklets). c) Normal blocklet that presents several crystalline and amorphous lamellae. d) Lamellae structure presenting the organisation of amylopectin chains on it. e) Amylopectin cluster: amylose and lipid arrangement in the organisation of amylopectin chains. f) Amylopectin double helix structure. g) Top view of the organisation of amylopectin double helix leading to different crystalline structures, named A- and B-type polymorphism.

The synthesis and growth of starch granules starts from the hilum and is arranged in form of alternant amorphous (named elsewhere as semi-crystalline or soft shells [23,31,32]) and semi-crystalline growth rings (also named crystalline or hard shells [23,31,32]) around it [31] (Figure 1.4a). The growth rings are thicker near the hilum and thinner in the granule surface due to the increasing surface area that is added to the constant growth rate [23,31]. However, they are considered to present an average thickness of 100 – 400 nm [31]. The surface of the granule is sometimes, especially in many cereals, connected with the interior of the granule by channels containing proteins and phospholipids [31].

At a higher level of structure, in 1997 Gallant et al. [23] proposed the blocklet concept, describing a new level of structural organisation in the starch granule (Figure 1.4b). Gallant et al. [23] stated that both amorphous and semi-crystalline growth rings are composed by spherical protrusions called blocklets. Besides, they defined that the amorphous rings are formed by small blocklets, whereas the semi-crystalline rings are made up of bigger ones.

A decade later, Tang et al., [32] differentiated defective and normal blocklets, the first constitutes the amorphous rings, while the latter form the semi-crystalline rings (Figure 1.4c). The defective blocklets that constitutes the amorphous rings, are formed due to the presence of lower branching molecules (amylose and other intermediate materials) that hindered the crystallization. On the contrary, the semi-crystalline rings are made up of normal blocklets that are formed by the clusters of amylopectin molecules.

Despite all this knowledge, the internal structure of blocklets has not still been completely defined, since the method to isolate the blocklets from the granules has not been established yet [31,32]. However, nowadays, it is well accepted that the blocklets are a semi-crystalline ultrastructure containing several amorphous (3 - 4 nm thickness) and crystalline lamellae (5 - 6 nm thickness) [23,32] (Figure 1.4d). The structure of amorphous lamellae is scarcely described. It is suggested to be

formed by amylopectin branching regions [23]. In contrast, the crystalline lamellae consist in ordered double helixes of amylopectin side chain clusters [23] (Figure 1.4e) that consist of two polyglycosyl chains [31] (Figure 1.4f).

The double helices of amylopectin crystallize leading to different allomorphisms [15] (Figure 1.4g). The crystallinity of native starch granules has been widely studied by X-ray diffraction (XRD), and it has been determined to be around 15 - 45% [23,25,33]. Due to different packing of the amylopectin double helices, starch crystallinity can be classified in different polymorphism, i.e., A-, B- and C-type crystalline patterns [15,23]. The A- (cereals) and B-type (tubers) are the most common polymorphisms, whereas the C-type (legumes) is a combination of both [1,24]. The A-type organisation exhibits a monoclinic unit cell where the double helices are stacked together and the water molecules fill the space between them [1,24,25]. In contrast, in the B-type pattern the double helices remain separated and water is accumulated inside the central cavity [1,25]. The described structure of the starch granules is illustrated in the Figure 1.4.

As mentioned earlier, in order to overcome the disadvantages of starch derived products, mainly its hydrophilic character, the weak mechanical behaviour and the instability of its properties due to retrogradation, the following solutions routes are elsewhere suggested: polymeric blending, use of different plasticisers and development of nanocomposites, chemical modification and cross-linking [2–5]. In the mentioned situations, the above described crystalline structure of the starch is normally destroyed by dissolution or by the so-called gelatinisation process in order to obtain flexible, highly reactive or more stable materials depending on the case.

1.2.2. Gelatinisation of starch

The thermal processing of starch-based polymers may include several chemical and physical reactions, namely water diffusion, granule expansion, gelatinisation, decomposition, melting and crystallization [34]. Among them, the irreversible process known as gelatinisation is of deal

importance since it is the basis of the processing of most starch-based materials to obtain biodegradable plastics [34,35].

Actually, starch in the native form is not processable as a real thermoplastic polymer [1,28,36,37], since the melting temperature is higher than the decomposition temperature [34,38]. Therefore, it is necessary to use plasticisers, heat and/or shear forces to induce the gelatinisation process [38] and obtain a material that can be processed. Thus, when starch is mixed with an appropriate plasticiser in presence of water and heated to an appropriated temperature, the starch chains reach enough chain mobility for being gelatinised [39]. Consequently, the starch granules are swelled and disrupted and the native crystalline domains are partially or completely destroyed and the birefringence is lost [40,41] due to the disappearance of the double helices and the lamellar long range crystalline structure [39]. This complex process results in the so-called Plasticised Starch (PLS) [42] which seems suitable as substitute synthetic polymers in packaging applications. Besides, the material known as Thermoplastic Starch (TPS) is obtained when a mechanical energy is also applied during the gelatinisation, usually by extrusion technique. In this case, the gelatinisation of starch is facilitated by mechanical shear stress [39] which would increase the mechanical disruption of molecular bonds leading to the loss of crystallinity [34,43].

1.2.2.1. Plasticisers

When starch is gelatinised using only water and temperature, brittle materials with null applicability in the packaging field are obtained. However, when an appropriate plasticiser is added into the gelatinisation media, the mechanical and thermal properties of the obtained materials are improved [44], since the addition of plasticisers result in increased flexibility and better processability [45]. Indeed, the use of convenient plasticisers facilitates the disruption of starch granules and the destruction of the crystalline domains. During the gelatinisation the inter- and intramolecular hydrogen bonds in starch are substituted by starch/plastisizer intermolecular forces leading to the

increase of the free volume and the mobility of the chains, as well as the decrease of the glass transition temperature (T_g) [45–47].

Thus, the selection of a suitable plasticiser is crucial since the disruption of the starch granules and the final behaviour of the material will be highly dependent on the chemical nature and content of the plasticiser [12,47,48]. The compatibility with the matrix, the desired physicochemical properties and the cost are factors that must be also taken into account [49].

The gelatinisation is normally performed with low molecular weight plasticisers that facilitate the disruption of the starch granules. Due to its low cost, nontoxic behaviour, and high boiling point the most widely used plasticiser in starch-based materials is glycerol, with three hydroxyl groups in its structure [36,50–52]. However, other water-soluble additives such as polyols (xylitol, sorbitol, ethylene glycol) [40,41,46,53], citric acid [53,54], fatty acids [46,53,54], urea [41,53], or formamide [45,53] have also been investigated as plasticisers.

In the present research work, considering the importance of the molecular weight [49] as well as the available hydroxyl groups [48], D-isosorbide and 1,3-propanediol were hereby studied as plasticisers comparing their effectiveness and suitability with the most used glycerol (Figure 1.5). D-isosorbide (1,4:3,6-dianhydro-D-sorbitol), is a secondary cyclic alcohol composed by two adjacent tetrahydrofuran rings with two hydroxyl groups in the positions 2 and 5. It could be obtained from cellulose or starch, by a multistep reaction including depolymerization of the polysaccharide into glucose units, hydrogenation to sorbitol, and two-step dehydration [55]. 1,3-propanediol, is obtained directly from the fermentation of corn sugar. Not only it is used in cosmetic, food, pharmaceutical and textile applications, but also as a precursor in the synthesis of polymers such as polyurethanes, polyether and polyesters or heterocyclic compounds [56–58]. Both compounds are expected to be able to disrupt the crystalline structure of starch granules and reduce the inter- and intramolecular starch-starch interactions leading to the reduction of T_g.

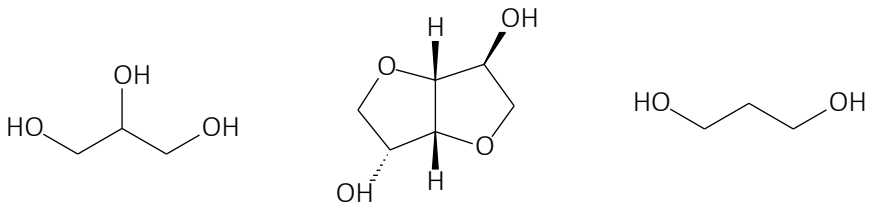

Figure 1.5 – Chemical structures of employed plastisizers.

1.2.2.2. Retrogradation

The final properties of starch-based materials not only depend on the gelatinisation process and the chosen plasticiser type and content. In fact, plasticised starch is susceptible to *retrogradation* during storage, which involves a reorganisation of both amylose and amylopectin macromolecules regenerating a new crystalline structure [40]. As a consequence of this recrystallization, the mechanical properties of the starch-based materials change, usually by increasing the Young's modulus [42], which is the major drawback of starch-based films [59]. In a similar way to gelatinisation, the retrogradation degree and its subsequent effects seem to be strongly dependent on the nature of the plasticiser and the T_g [41]. It is therefore important to keep in mind that although some plasticisers may lead to more flexible materials and even facilitate the gelatinisation process, the stability of the final properties of starch-based films could be compromised. Therefore, when looking for an appropriate plasticiser, not only the desired properties must be taken into account, but also if the plasticiser favours or prevents the retrogradation should be considered.

1.2.2.3. Manufacture techniques

Biopolymer based competitive films prepared using the traditional technologies, i.e. solvent casting, extrusion, compression, injection and blowing are necessary, choosing the most appropriate method depending on the final application. The solvent casting technique, which consists on pouring a suspension into a mould and drying it by evaporating the solvent [60], is the most widely

process used for the development of small sized films in research areas or lab scale productions [61,62] since it requires inexpensive equipment and limited space [63]. However, from an industrial point of view other techniques, such as extrusion or thermomoulding are more feasible [60,61] due to its low cost, avoided drying times and scale-up and continuous production [60,62]. In addition, the extrusion process stands out against solvent casting technique due to its excellent mixing capacity and operational flexibility [64]. However, it should be considered that the final properties of extruded materials would be influenced by the operation conditions (temperature profile or screw speed) [63].

1.2.3. Nanocomposites

Nanocomposites have already been identified as useful materials since the addition of nanofillers such as polysaccharide nanocrystals, nanoparticles or nanoclays to the biopolymeric matrix resulted in the significant improvement of the mechanical, thermal and barrier properties. In a similar way, in our case, the incorporation of different nanofillers into the starch-based matrixes could lead to the enhancement of several relevant properties of both film and hydrogel. However, the effectiveness of the reinforcement would depend on the formation of an active nanofiller/matrix interphase as a result of the good affinity between them and the correct dispersion of the nanoreinforcement.

1.2.3.1. Polysaccharide nanocrystals

Disordered amorphous domains of several polysaccharides as cellulose, starch or chitin can be removed, normally by acid hydrolysis under controlled conditions, leaving the crystalline regions intact [65–67]. Thus, the crystalline regions are then extracted and isolated in the form of nanosized and highly crystalline particles [67]. The characteristics of the nanocrystals, such as the crystallinity degree, dimensions or even geometry are affected by the reaction conditions, as well as by the type of the polysaccharide [66].

Thereby, nanocrystals extracted from different sources have a variety of geometrical structures and crystallinity degrees [68], and thus, they are supposed to have their own properties and applicability as reinforcing agent. Indeed, cellulose nanocrystals (CNC) or chitin nanocrystals (ChCN) presented a rod-like or fibrillar morphology [65,67,69,70], a high aspect ratio and a crystallinity degree up to 88% and 93% for CNC and ChCN, respectively [67,70], so they would be preferred for the improvement of the mechanical properties. In contrast, waxy maize starch nanocrystals (WSNC) isolated from the so-called waxy corn, are platelet-like [36,67,68] with a crystallinity degree close to 50% [67] and, therefore, their effect is expected to be more noticeable on barrier properties [67,71].

Large amount of work has been published mainly with CNC and, in a less extent, with chitin or starch nanocrystals in combination with different biopolymers [14,36,68,72,73]. However, little work has been reported using different polysaccharide nanocrystals simultaneously [68]. In this work polysaccharide nanocrystals, i.e. WSNC and CNC, were chosen as nanofillers for the development of both PLS and TPS nanocomposite films and CNC nanocrystals for the synthesis of Diels-Alder (DA) nanocomposite hydrogels.

1.2.3.2. Carbonaceous nanoparticles

Along with the mentioned nanocrystals, the incorporation of carbon-based nanoparticles, such as carbon black, carbon nanotubes and graphene (G) and its derivatives, has been widely used in order to improve the mechanical, electrical and magnetic properties of polymers [74]. Specially G and its derivatives are gaining attention and thus, they have been used in combination with different biopolymers to develop films, foams or hydrogels obtaining conductive materials with improved mechanical properties [75–79].

G is the allotropic form of carbon where a single layer of sp^2 bonded carbon atoms are packed in a two dimensional honeycomb lattice [80–82] and it can be obtained by chemical vapour

deposition of hydrocarbons, micromechanical cleavage or exfoliation of graphite, among other techniques [83,84]. G presents unique optical, mechanical and electrical properties as well as large specific surface area [85–87]. In addition, G is pointing out as a promising material to be use in biomedical applications due to its antimicrobial character [88]. Indeed, Hegab et al. [89] reported that the antimicrobial capacity of G containing materials was caused by the chemical and physical interactions between G nanoflakes and the bacteria cell membranes. The antimicrobial mechanism seems to be caused by the charge transfer and bacterial migration, as well as by the extraction of phospholipids from the membranes due to the insertion of G into the cells [88].

Unfortunately, G presents poor dispersibility in polar solvents and water [80,85,90] what could be a serious drawback for its applicability in biomedicine. Therefore, the oxidized form of G, i.e. the graphene oxide (GO) [91], is commonly preferred as nanofiller in numerous cases.

Indeed, in the last years GO and reduced graphene oxide (rGO) have gained attention as nanofillers to improve the mechanical and electrical properties of several materials [86,92,93]. GO, is obtained from graphite by strong chemical treatments in presence of mineral acids or oxidizing agents [93,94]. Three are the main methods used for the oxidation of G: 1) the Brodie's methods, 2) the Staudenmaier's method and 3) the Hummers' method and its derivatives [93,95,96]. In this work the Hummers' method with slight differences was employed [97], which involves the use of potassium permanganate and sulfuric acid.

The obtained GO nanoflakes present the G skeleton while it contains oxygen containing functional groups (i.e. hydroxyl, epoxide, carbonyl and/or carboxyl groups) in the basal plane and the flake edges [91,98]. These functionalities make GO more hydrophilic [98], facilitating its dispersion in polar solvents and water, as well as the formation of strong filler/matrix hydrogen bonding interactions [90,91] and thus, leading to a better dispersion of the nanofiller [80]. In the case of starch-based materials reinforced with GO, strong hydrogen bonding could be expected between

the hydroxyl groups of starch and the mentioned functional groups of GO [86,90]. However, GO presents the disadvantage of being electrically non-conductor due to both the chemical reactive groups and the presence of defects on its structure [99].

When GO is chemically reduced, the carbon arranged in the hexagonal lattice is almost removed and the sp^2 hybridized structure partially restored, thus the resulting rGO presents electrical conductivity [86,100,101]. The properties of rGO, such as the electrical conductivity, are influenced by both the degree of reduction and the capacity to restore the hybridized structure [99]. In fact, the GO is not usually completely reduced, and, consequently, the residual functional oxygen groups that remains in the surface of rGO allow the formation of polymer/rGO interactions [86]. Figure 1.6 shows the structure of graphite and the preparation of G, GO and rGO. The reduction reaction could be carried out using hydrazine, sodium hydrosulphite, sodium borohydrate, glucose or hydroquinone as reducing agents, among others [87,99,102]. In the last years, vitamin C (ascorbic acid) has been proposed as eco-friendly effective reducing agent for the GO [102].

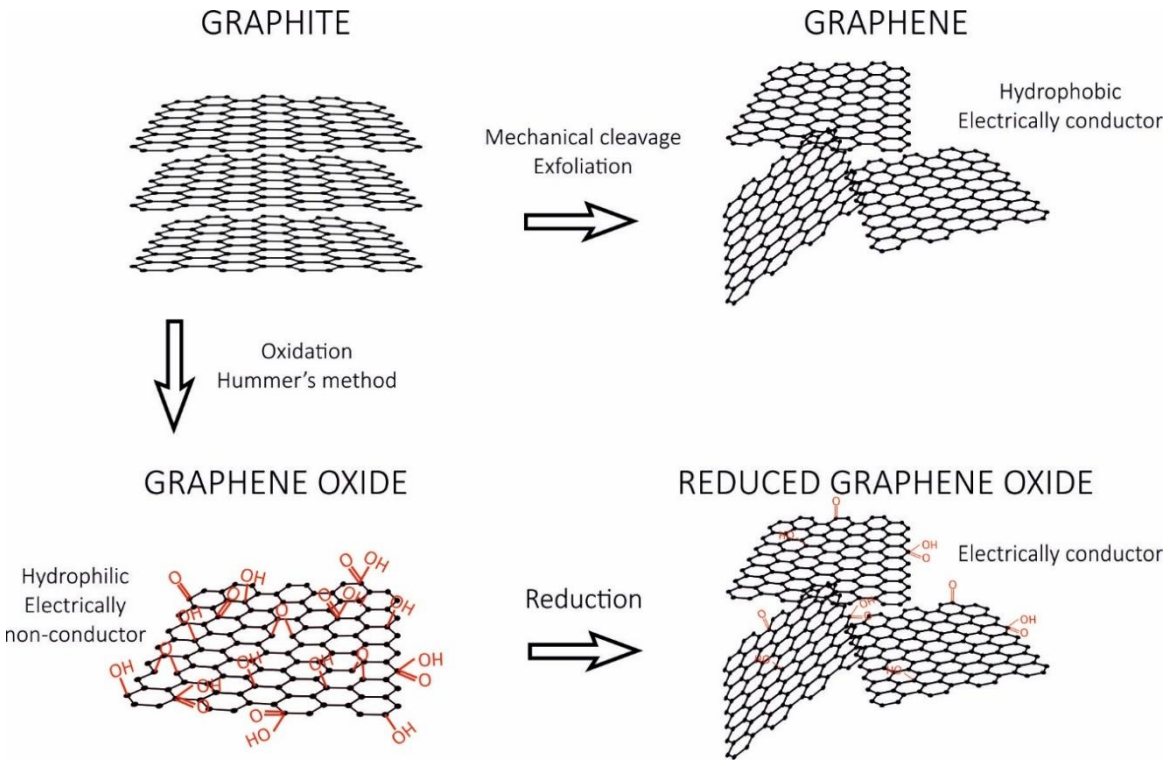

Figure 1.6 – Model of G, GO and rGO from graphite.

However, in addition to the oxidation and subsequent reduction of G as strategy for its incorporation in aqueous systems, other approaches have been also proposed in the literature using different types of surfactants. Among them, those containing phenolic moieties have been reported to be highly "graphene-philic" due to the formation of π-π interactions with G and, hence, increasing the stability of the dispersion [103]. In this context, natural plant extracts could be used as dispersion stabilisers looking for the required water dispersibility as they content high concentration of polyphenolic compounds. Indeed, it was demonstrated that *Salvia officinalis L.* can act as surfactant due to the presence of specific groups on its chemical structure [104]. In addition, Salvia, as well as other medicinal plants, show antimicrobial or anti-inflammatory activity [105], relevant properties in biomedical applications.

1.2.4. Hydrogels

Hydrogels are three-dimensional (3D) hydrophilic polymeric networks which are able to swell and retain large amount of water or biological fluids, maintaining their specific 3D structure in aqueous media [9,106,107]. Among them, the so-called "smart hydrogels" display an extra benefit to the material showing, for example, stimuli response to external factors such as temperature, pH, and/or electric field [108]. For example, hydrogels designed for drug delivery applications are able to release the drug under certain external stimuli in a selected site and in a controlled and non-invasive way [109].

Hydrogels could be classified as physical and chemical hydrogels, depending on the nature of the cross-linking points between polymeric chains. Physical hydrogels form their 3D network through non-covalent interactions between chains [8], i.e. Van der Walls forces [110]. On the contrary, chemical hydrogels are commonly obtained by covalent bonding, normally through the reaction of the polymer with a low molar mass cross-linker [8,107].

1.2.4.1. 'Click' Diels-Alder cross-linking reaction

The 'click' chemistry is revealed as an appropriate strategy for the formation of hydrogels that are designed based on the environmental awareness and biocompatibility and biodegradability requirements. Among them, the DA reaction is receiving increased attention due to its high selectivity, versatility and yielding [111]. The DA reaction was first described in 1928 by Otto Diels and Kurt Alder. In appreciation of their research work, in 1950, they were awarded by the novel prize in chemistry [112]. Since then, it has become one of the most useful tools for the synthesis in the organic chemistry field [112].

The DA reaction is defined as the thermoreversible cycloaddition between a diene and a dienophile [109,113], which proceed in mild temperatures, aqueous environment, free of catalysts or initiators and without undesirable side reactions [113,114]. The DA 'click' coupling reaction is often carried out using furans as dienes and maleimides as dienophiles (Figure 1.7). Therefore, 'click' hydrogels require the polymer to be properly functionalised with specific chemical groups [8].

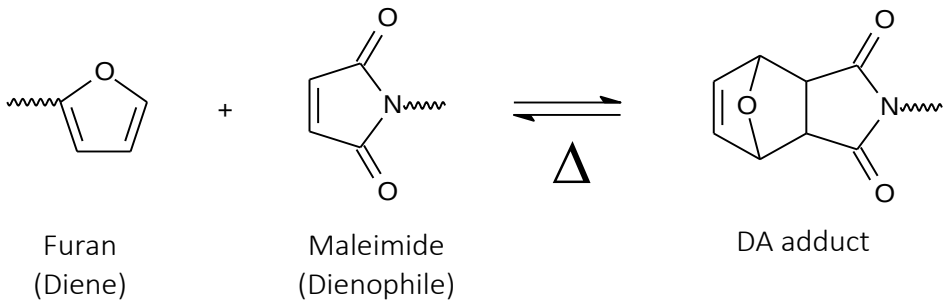

Figure 1.7 – Scheme of DA reaction between furan and maleimide groups.

In this sense, the use of biopolymers is gaining attention due to their biodegradability, biocompatibility, hydrophilicity, and because they show interesting functional groups ready for modification and/or cross-linking [8,30,110].

Starch possesses both primary and secondary hydroxyl groups suitable for modification in order to add specific functionalities [8]. Hesse et al. [115] and Liebert et al. [116] reported the modification of different polysaccharides based on furan-2-carboxylic acid esters, among which stands out the reaction with starch. However, although furan modification of starch was performed, few works have been reported focusing on the DA reaction from the furan-functionalised starch [117] and, as far as our knowledge, none referring to hydrogels. Native starch shows poor water solubility due to the above explained specific 3D crystalline organisation but, its hydrophilic character results in the ability to retain large amount of water upon heating [118]. Thus, with specific physicochemical and biological behaviours, starch seems to be an excellent candidate for the formation of hydrogels with applications in different areas such as biomedicine [9].

1.2.4.2. Diels-Alder hydrogels for biomedical applications

The use of hydrogels covers a wide range of applications including agriculture, water purification, biotechnology, food additives, electrical conductive hydrogels and biosensors, cosmetic or biomedicine [30,107,110]. Nevertheless, nowadays, the biomedical uses of hydrogels (biological scaffolds, bone regeneration, diagnostic or drug and gene delivery) are gaining increasing attention [110,119–121].

It is well known that biomedicine requires biomaterials with enhanced biocompatibility, antimicrobial properties and non-toxicity [122]. Besides, they should also present high biological stability and good resistance to chemical substances in the body, as well as improved mechanical properties [119]. In addition, the cost is also an important issue that must be taken into consideration for future regulation of the applications [9].

The synthesis of covalent bonded hydrogels is commonly performed by conventional chemical reactions leading to tailor-made hydrogels. However, the compatibility of the resulting materials could be compromised due to the use of toxic reagents [109]. Besides, the employment of

some of these reactions involves the use of strong reaction conditions, the appearance of side reactions and low coupling efficiency [8,107,123]. These inconveniences restrict the application areas of the developed materials [8]. In this sense, the 'click' chemistry, and specially the DA reaction, is an interesting strategy for the development of hydrogels for biomedical applications [112,122] since the reaction could be performed in aqueous media, without catalysts and under mild reaction conditions [109,119]. Besides, the resulting hydrogels present a stable network structure [119] and mechanical and rheological properties similar of those of human tissues [120,122,124].

In the last years, several biopolymers have been investigated for the formation of hydrogels, such as proteins (collagen, gelatine) or polysaccharides (alginate, agarose, chitosan) [110] also using 'click' chemistry reactions. Yu et al. [125], reported the preparation of hydrogels based on gelatine suitable for cartilage tissue engineering by DA reaction. On the other hand, Guaresti et al. [126,127] proposed different strategies to obtain hydrogels from chitosan by using the DA reaction with promising results for applications on drug delivery systems.

In this work we focused specifically on the design of starch-based hydrogels that may be used in biomedical applications such as delivery system for a sustained release of drug or as conductive coating of some devices for neurologic diseases, as example. On one hand, the drug delivery systems should present the capacity to deliver and release an active drug with minimum side-effects, optimal response and prolonged efficacy [30]. The drug is intended to act directly in the damaged area without affecting other tissues and organs [30]. The drug loaded in the hydrogel and the subsequent release and efficiency is going to be strongly influenced by the polymeric material, the final microstructure and porosity, the cross-linking density and the affinity with the swollen media [30,112].

On the other hand, regarding the neurologic applications, the electrodes that traditionally have been used were prepared using platinum, gold or platinum/iridium [6]. However nowadays, new

smaller devices with improved mechanical, electrical and biological properties are required. Moreover, due to the necessity to overcome some limitations of the mentioned traditional metallic electrodes (low charge injection, mechanical mismatch or foreign body response) employed for neuronal interfaces [6], several coating materials are being investigated such as conductive polymers or hydrogels, bioactive coatings and tissue engineered neural interfaces. Among these strategies, conductive hydrogels, obtained by the incorporation of conductive carbonaceous particles such as carbon nanotubes or G [85], present the ability to conduct electricity under certain conditions while maintaining their dimensional stability, and find applicability in relevant research fields such as biomedicine, bioengineering and controlled drug delivery [108].

1.3. GENERAL OBJECTIVES

The main objective of this thesis was the development and characterisation of competitive starch-based materials. On one hand, starch-based films and nanocomposite films were developed as alternative for current packaging materials. Besides, starch cross-linked hydrogel nanocomposites were designed by incorporating polysaccharide nanocrystals and graphene, with the purpose to be useful as controlled drug delivery systems or in the neurological field. To achieve the mentioned objective, it was necessary to overcome the drawbacks of starch (high hydrophilicity, poor mechanical behaviour and retrogradation). For that purpose, we focused in the use of plasticisers and development of nanocomposites, as well as the chemical modification and cross-linking. Thus, the specific objectives of this research were:

- Preparation of PLS and TPS films using glycerol, D-isosorbide and 1,3-propanediol as plasticisers. The influence of the plasticiser on the final properties of the material was evaluated. In addition, we sought to study the effect of retrogradation on PLS materials.

- Design of PLS nanocomposites reinforced with the combination of polysaccharide nanocrystals. Firstly, the influence of adding different WSNC contents into the PLS matrix

was investigated. Then, the effect of adding together nanocrystals of similar chemical nature but different geometry, i.e. WSNC and CNC was studied.

- Corroborate the feasibility of preparing TPS films and nanocomposite films by extrusion/compression. The extrusion/compression processing was proposed instead of solvent casting method in order to obtain TPS films with a large-scale production and improved properties.

- Preparation of PLS nanocomposites reinforced with carbonaceous nanoparticles. On one hand, the influence of adding different G and GO contents into the matrix plasticised with glycerol was analysed. Besides, the effect of reducing the GO by reaction with ascorbic acid was studied.

- Synthesis of DA hydrogel nanocomposites between furan-modified starch (S-FI) and a tetrafunctional maleimide (TTMI) reinforced with CNC. Different CNC contents were added in order to study their influence on the rheological behaviour, swelling capacity and morphology. In addition, the drug release profile and cell viability of the final nanocomposite hydrogels was also evaluated.

- Synthesis of DA hydrogel nanocomposites between S-FI and a bismaleimide (BMI) reinforced with G using Salvia extracts as dispersion stabilisers. The effect of using different furan to maleimide weight ratios on the behaviour of hydrogels was analysed. In addition, conductive and antimicrobial properties of the hydrogels were evaluated.

1.4. REFERENCES

[1] M. N. Belgacem, A. Gandini, Starch: Major sources, properties and applications as thermoplastic materials, in: Monomers, Polym. Compos. from Renew. Resour., 2008: pp. 321–342. dx.doi.org/10.1016/B978-0-08-045316-3.00015-6.

[2] F. Xie, E. Pollet, P.J. Halley, L. Avérous, Starch-based nano-biocomposites, Prog. Polym. Sci.

38 (2013) 1590–1628. doi:10.1016/j.progpolymsci.2013.05.002.

[3] N. Masina, Y.E. Choonara, P. Kumar, L.C. du Toit, M. Govender, S. Indermun, V. Pillay, A review of the chemical modification techniques of starch, Carbohydr. Polym. 157 (2017) 1226–1236. doi:10.1016/j.carbpol.2016.09.094.

[4] J. Waterschoot, S. V. Gomand, E. Fierens, J. A. Delcour, Starch blends and their physicochemical properties, Starch - Stärke. 67 (2015) 1–13. doi:10.1002/star.201300214

[5] M. Kaseem, K. Hamad, F. Deri, Thermoplastic starch blends: A review of recent works, Polym. Sci. Ser. A. 54 (2012) 165–176. doi:10.1134/S0965545X1202006X.

[6] U.A. Aregueta-Robles, A.J. Woolley, L.A. Poole-Warren, N.H. Lovell, R.A. Green, Organic electrode coatings for next-generation neural interfaces, Front. Neuroeng. 7 (2014) 1–18. doi:10.3389/fneng.2014.00015.

[7] H.S. Song, O.S. Kwon, J.H. Kim, J. Conde, N. Artzi, 3D hydrogel scaffold doped with 2D graphene materials for biosensors and bioelectronics, Biosens. Bioelectron. 89 (2017) 187–200. doi:10.1016/j.bios.2016.03.045.

[8] C. Xiao, Current advances of chemical and physical starch-based hydrogels, Starch - Stärke. 65 (2013) 82–88. doi:10.1002/star.201200113.

[9] Y. Li, Y. Tan, K. Xu, C. Lu, P. Wang, A biodegradable starch hydrogel synthesized via thiol-ene click chemistry, Polym. Degrad. Stab. 137 (2017) 75–82. doi:10.1016/j.polymdegradstab.2016.07.015.

[10] A. Dufresne, Crystalline starch based nanoparticles, COCIS 19 (2014) 397–408. doi:10.1016/j.cocis.2014.06.001.

[11] K. Zhang, K. Zhang, F. Cheng, Y. Lin, M. Zhou, P. Zhu, Aging properties and hydrophilicity of maize starch plasticized by hyperbranched poly(citrate glyceride), J. Appl. Polym. Sci. 136 (2019) 1–8. doi:10.1002/app.46899.

[12] P. Rychter, M. Kot, K. Bajer, D. Rogacz, A. Šišková, J. Kapušniak, Utilization of starch films plasticized with urea as fertilizer for improvement of plant growth, Carbohydr. Polym. 137 (2016) 127–138. doi:10.1016/j.carbpol.2015.10.051.

[13] A. Giuri, S. Colella, A. Listorti, A. Rizzo, C. Esposito Corcione, Biodegradable extruded thermoplastic maize starch for outdoor applications, J. Therm. Anal. Calorim. 7 (2018). doi:10.1007/s10973-018-7404-7.

[14] B. Montero, M. Rico, S. Rodríguez-Llamazares, L. Barral, R. Bouza, Effect of nanocellulose as a filler on biodegradable thermoplastic starch films from tuber, cereal and legume, Carbohydr. Polym. 157 (2017) 1094–1104. doi:10.1016/j.carbpol.2016.10.073.

[15] S. Pérez, E. Bertoft, The molecular structures of starch components and their contribution to the architecture of starch granules: A comprehensive review, Starch - Stärke. 62 (2010) 389–420. doi:10.1002/star.201000013.

[16] V.K. Shivaraju, S. Vallayil Appukuttan, S. Kumar, The influence of bound water on the FTIR characteristics of starch and starch nanocrystals obtained from selected natural sources, Starch - Stärke. 1700026 (2018) 1–9. doi:10.1002/star.201700026.

[17] D. Le Corre, A. Dufresne, Starch Nanoparticles: A review, (2010) 1139–1153. doi:10.1021/bm901428y.

[18] T.N. Prabhu, K. Prashantha, A review on present status and future challenges of starch based polymer films and their composites in food packaging applications, (2018). doi:10.1002/pc.24236.

[19] P.J. Halley, Starch Polymers : From the Field to Industrial Products, (2014) 3–10. doi:10.1016/B978-0-444-53730-0.00018-X.

[20] www.starch.eu.

[21] A. Gandini, T.M. Lacerda, A.J.F. Carvalho, E. Trovatti, Progress of polymers from renewable resources: furans, vegetable oils, and polysaccharides, Chem. Rev. 116 (2016) 1637–1669. doi:10.1021/acs.chemrev.5b00264.

[22] J. Ren, K.M. Dang, E. Pollet, L. Avérous, Preparation and characterization of thermoplastic potato starch/halloysite nano-biocomposites: Effect of plasticizer nature and nanoclay content, Polymers (Basel). 10 (2018). doi:10.3390/polym10080808.

[23] D.J. Gallant, B. Bouchet, P.W. Baldwin, Evidence for a new level of granule organisation, Carbohydr. Polym. 32 (1997) 177–191. doi: 10.1016/S0144-8617(97)00008-8.

[24] A. Imberty, A. Buléon, V. Tran, S. Péerez, Recent Advances in Knowledge of Starch Structure, Starch - Stärke. 43 (1991) 375–384. doi:10.1002/star.19910431002.

[25] A. Imberty, H. Chanzy, S. Perez, The double-helical nature of the crystalline Part of A-starch, (1988) 365–378.

[26] M.G. James, K. Denyer, A.M. Myers, Starch synthesis in the cereal endosperm, Curr. Opin. Plant Biol. 6 (2003) 215–222. doi:10.1016/S1369-5266(03)00042-6.

[27] J.S. Jeon, N. Ryoo, T.R. Hahn, H. Walia, Y. Nakamura, Starch biosynthesis in cereal endosperm, Plant Physiol. Biochem. 48 (2010) 383–392. doi:10.1016/j.plaphy.2010.03.006.

[28] N.L. García, L. Ribba, A. Dufresne, M. Aranguren, S. Goyanes, Effect of glycerol on the morphology of nanocomposites made from thermoplastic starch and starch nanocrystals, Carbohydr. Polym. 84 (2011) 203–210. doi:10.1016/j.carbpol.2010.11.024.

[29] B. Khan, M. Bilal, K. Niazi, G. Samin, Z. Jahan, Thermoplastic starch: a possible biodegradable food packaging material - A review, (2017). doi:10.1111/jfpe.12447.

[30] H. Ismail, M. Irani, Z. Ahmad, Starch-based hydrogels: Present status and applications, Int. J. Polym. Mater. Polym. Biomater. 62 (2013) 411–420. doi:10.1080/00914037.2012.719141.

[31] E. Bertoft, Understanding starch structure: Recent progress, Agronomy. 7 (2017) 56. doi:10.3390/agronomy7030056.

[32] H. Tang, T. Mitsunaga, Y. Kawamura, Molecular arrangement in blocklets and starch granule architecture, Carbohydr. Polym. 63 (2006) 555–560. doi:10.1016/j.carbpol.2005.10.016.

[33] J.-L. Jane, J.F. Robyt, H. Zobel, S. Leas, T. Kasemsuwan, Anthology of starch granule morphology by scanning electron microscopy, Starch - Stärke. 46 (2006) 121–129.

doi:10.1002/star.19940460402.

[34] H. Liu, F. Xie, L. Yu, L. Chen, L. Li, Thermal processing of starch-based polymers, Prog. Polym. Sci. 34 (2009) 1348–1368. doi:10.1016/j.progpolymsci.2009.07.001.

[35] H. Liu, L. Yu, F. Xie, L. Chen, Gelatinization of cornstarch with different amylose/amylopectin content, Carbohydr. Polym. 65 (2006) 357–363. doi:10.1016/j.carbpol.2006.01.026.

[36] H. Angellier, S. Molina-Boisseau, P. Dole, A. Dufresne, Thermoplastic starch - Waxy maize starch nanocrystals nanocomposites, Biomacromolecules. 7 (2006) 531–539. doi:10.1021/bm050797s.

[37] J. Viguié, S. Molina-boisseau, A. Dufresne, Processing and characterization of waxy maize starch films plasticized by sorbitol and reinforced with starch nanocrystals, Macromol. Biosci. 7 (2007) 1206–1216. doi:10.1002/mabi.200700136.

[38] S.C. Lara, F. Salcedo, Gelatinization and retrogradation phenomena in starch/montmorillonite nanocomposites plasticized with different glycerol/water ratios, Carbohydr. Polym. 151 (2016) 206–212. doi:10.1016/j.carbpol.2016.05.065.

[39] A. Taghizadeh, B.D. Favis, Effect of high molecular weight plasticizers on the gelatinization of starch under static and shear conditions, Carbohydr. Polym. 92 (2013) 1799–1808. doi:10.1016/j.carbpol.2012.11.018.

[40] D. Battegazzore, S. Bocchini, G. Nicola, E. Martini, A. Frache, Isosorbide, a green plasticizer for thermoplastic starch that does not retrogradate, Carbohydr. Polym. 119 (2015) 78–84. doi:10.1016/j.carbpol.2014.11.030.

[41] H. Schmitt, A. Guidez, K. Prashantha, J. Soulestin, M.F. Lacrampe, P. Krawczak, Studies on the effect of storage time and plasticizers on the structural variations in thermoplastic starch, Carbohydr. Polym. 115 (2015) 364–372. doi:10.1016/j.carbpol.2014.09.004.

[42] L. Averous, E. Pollet, Nanobiocomposites Based on Plasticized Starch, 2014. doi:10.1016/B978-0-444-53730-0.00028-2.

[43] L.-F. Wen, P. Rodis, B.P. Wasserman, Starch fragmentation and protein insolubilization during twin-screw extrusion of corn meal, Cereal Chem. 67 (1990) 268–275.

[44] P.A. Sreekumar, M.A. Al-harthi, Effect of glycerol on thermal and mechanical properties of polyvinyl alcohol/Starch blends, J. Appl. Polym. Sci. 123 (2012) 135–142. doi:10.1002/app.34465.

[45] X. Tang, S. Alavi, Recent advances in starch, polyvinyl alcohol based polymer blends, nanocomposites and their biodegradability, Carbohydr. Polym. 85 (2011) 7–16. doi:10.1016/j.carbpol.2011.01.030.

[46] T. Mekonnen, P. Mussone, H. Khalil, D. Bressler, Progress in bio-based plastics and plasticizing modifications, J. Mater. Chem. A. 1 (2013) 13379–13398. doi:10.1039/c3ta12555f.

[47] M.L. Sanyang, S.M. Sapuan, M. Jawaid, M.R. Ishak, J. Sahari, Effect of plasticizer type and concentration on physical properties of biodegradable films based on sugar palm (arenga

pinnata) starch for food packaging, J. Food Sci. Technol. 53 (2016) 326–336. doi:10.1007/s13197-015-2009-7.

[48] A.L. Da Róz, A.J.F. Carvalho, A. Gandini, A.A.S. Curvelo, The effect of plasticizers on thermoplastic starch compositions obtained by melt processing, Carbohydr. Polym. 63 (2006) 417–424. doi:10.1016/j.carbpol.2005.09.017.

[49] M.G.A. Vieira, M.A. da Silva, L.O. dos Santos, M.M. Beppu, Natural-based plasticizers and biopolymer films: A review, Eur. Polym. J. 47 (2011) 254–263. doi:10.1016/j.eurpolymj.2010.12.011.

[50] M.A. Bertuzzi, E.F. Castro Vidaurre, M. Armada, J.C. Gottifredi, Water vapor permeability of edible starch based films, J. Food Eng. 80 (2007) 972–978. doi:10.1016/j.jfoodeng.2006.07.016.

[51] N.L. García, L. Ribba, A. Dufresne, M.I. Aranguren, S. Goyanes, Physico-mechanical properties of biodegradable starch nanocomposites physico-mechanical properties of biodegradable starch nanocomposites, Macromol. Mater. Eng. 294 (2009) 169–177. doi:10.1002/mame.200800271.

[52] Q. Yan, H. Hou, P. Guo, H. Dong, Effects of extrusion and glycerol content on properties of oxidized and acetylated corn starch-based films, Carbohydr. Polym. 87 (2012) 707–712. doi:10.1016/j.carbpol.2011.08.048.

[53] M.B.K. Niazi, M. Zijlstra, A.A. Broekhuis, Influence of plasticizer with different functional groups on thermoplastic starch, J. Appl. Polym. Sci. (2015). doi:10.1002/app.42012.

[54] A.M. Nafchi, M. Moradpour, M. Saeidi, A.K. Alias, Thermoplastic starches: Properties, challenges, and prospects, Starch - Stärke. 65 (2013) 61–72. doi:10.1002/star.201200201.

[55] M. Rose, R. Palkovits, Isosorbide as a renewable platform chemical for versatile applications — Quo Vadis ?, ChemSusChem. 5 (2012) 167–176. doi:10.1002/cssc.201100580.

[56] N. Vivek, A. Pandey, P. Binod, Biological valorization of pure and crude glycerol into 1,3-propanediol using a novel isolate Lactobacillus brevis N1E9.3.3, Bioresour. Technol. 213 (2016) 222–230. doi:10.1016/j.biortech.2016.02.020.

[57] C.S. Lee, M.K. Aroua, W.M.A.W. Daud, P. Cognet, Y. Pérès-Lucchese, P. Fabre, O. Reynes, L. Latapie, A review : Conversion of bioglycerol into 1 , 3-propanediol via biological and chemical method, Renew. Sustain. Energy Rev. 42 (2015) 963–972. doi:10.1016/j.rser.2014.10.033.

[58] M.B.K. Niazi, A.A. Broekhuis, Production of amorphous starch powders by solution spray Drying, J. Appl. Polym. Sci. 126 (2012) 143–153. doi:10.1002/app.36551.

[59] A. Jiménez, M.J. Fabra, P. Talens, A. Chiralt, Effect of re-crystallization on tensile, optical and water vapour barrier properties of corn starch films containing fatty acids, Food Hydrocoll. 26 (2012) 302–310. doi:10.1016/j.foodhyd.2011.06.009.

[60] J.O. De Moraes, A.S. Scheibe, A. Sereno, J.B. Laurindo, Scale-up of the production of cassava starch based films using tape-casting, J. Food Eng. 119 (2013) 800–808. doi:10.1016/j.jfoodeng.2013.07.009.

[61] C.P.B. Melo, M.V.E. Grossmann, F. Yamashita, E.Y. Youssef, L.H. Dall'Antônia, S. Mali, Effect of manufacturing process and xanthan gum addition on the properties of cassava starch films, J. Polym. Environ. 19 (2011) 739–749. doi:10.1007/s10924-011-0325-1.

[62] M.C. Galdeano, M.V.E. Grossmann, S. Mali, L.A. Bello-Perez, M.A. Garcia, P.B. Zamudio-Flores, Effects of production process and plasticizers on stability of films and sheets of oat starch, Mater. Sci. Eng. C. 29 (2009) 492–498. doi:10.1016/j.msec.2008.08.031.

[63] O.O. Yepes, L. Di Giogio, S. Goyanes, A. Mauri, L. Famá, Influence of process (extrusion/thermo-compression, casting) and lentil protein content on physicochemical properties of starch films, Carbohydr. Polym. 14 (2018) 291–305. doi:10.1016/j.carbpol.2018.12.030.

[64] P. González-Seligra, L. Guz, O. Ochoa-Yepes, S. Goyanes, L. Famá, Influence of extrusion process conditions on starch film morphology, LWT - Food Sci. Technol. 84 (2017) 520–528. doi:10.1016/j.lwt.2017.06.027.

[65] Y. Habibi, L.A. Lucia, O.J. Rojas, Cellulose Nanocrystals: Chemistry, Self-Assembly, and Applications, 110 (2010) 3479–3500. doi:10.1021/cr900339w.

[66] N. Lin, J. Huang, P.R. Chang, D.P. Anderson, J. Yu, Preparation, modification, and application of starch nanocrystals in nanomaterials: A review, J. Nanomater. 2011 (2011). doi:10.1155/2011/573687.

[67] N. Lin, J. Huang, A. Dufresne, Preparation, properties and applications of polysaccharide nanocrystals in advanced functional nanomaterials: a review, Nanoscale. 4 (2012) 3274–3294. doi:10.1039/c2nr30260h.

[68] Y. Wang, H. Tian, L. Zhang, Role of starch nanocrystals and cellulose whiskers in synergistic reinforcement of waterborne polyurethane, Carbohydr. Polym. 80 (2010) 665–671. doi:10.1016/j.carbpol.2009.10.043.

[69] A. Saralegi, L. Rueda, L. Martin, A. Arbelaiz, A. Eceiza, M.A. Corcuera, From elastomeric to rigid polyurethane/cellulose nanocrystal bionanocomposites, Compos. Sci. Technol. 88 (2013) 39–47. doi:10.1016/j.compscitech.2013.08.025.

[70] T. Calvo-Correas, P. Garrido, A. Alonso-Varona, T. Palomares, M.A. Corcuera, A. Eceiza, Biocompatible thermoresponsive polyurethane bionanocomposites with chitin nanocrystals, J. Appl. Polym. Sci. 136 (2019) 1–12. doi:10.1002/app.47430.

[71] D. Lecorre, J. Bras, A. Dufresne, Influence of native starch's properties on starch nanocrystals thermal properties, Carbohydr. Polym. 87 (2012) 658–666. doi:10.1016/j.carbpol.2011.08.042.

[72] A.P.M. Silva, A.V. Oliveira, S.M.A. Pontes, A.L.S. Pereira, M. de sá M. Souza Filho, M.F. Rosa, H.M.C. Azeredo, Mango kernel starch films as affected by starch nanocrystals and cellulose nanocrystals, Carbohydr. Polym. 211 (2019) 209–216. doi:10.1016/j.carbpol.2019.02.013.

[73] A.M. Salaberria, R.H. Diaz, J. Labidi, S.C.M. Fernandes, Role of chitin nanocrystals and nanofibers on physical, mechanical and functional properties in thermoplastic starch films, Food Hydrocoll. 46 (2015) 93–102. doi:10.1016/j.foodhyd.2014.12.016.

[74] R. Arrigo, V. Marona, L. Magagnin, G. Zerillo, M. Sansotera, E. Morici, N.T. Dintcheva, W. Navarrini, High performance composites containing perfluoropolyethers-functionalized carbon-based nanoparticles: Rheological behavior and wettability, Compos. Part B Eng. 95 (2016) 29–39. doi:10.1016/j.compositesb.2016.03.095.

[75] B. Gao, J. Mei, Y. Ma, G. Yuan, L. Ren, Environmental-friendly assembly of functional graphene hydrogels with excellent antibacterial properties, Chemistry Select. 2 (2017) 7474–7482. doi:10.1002/slct.201701419.

[76] H.N. Lim, N.M. Huang, C.H. Loo, Facile preparation of graphene-based chitosan films: Enhanced thermal, mechanical and antibacterial properties, J. Non. Cryst. Solids. 358 (2012) 525–530. doi:10.1016/j.jnoncrysol.2011.11.007.

[77] A. Riaz, A. Usman, Z. Hussain, Synthesis of 4, 4'-stilbene dicarboxylic acid and aniline modified graphene oxide and its electrochemical performance for supercapacitors, Int. J. Electrochem. Sci. 11 (2016) 1099–1110.

[78] L. Ugarte, S. Gómez-Fernández, A. Tercjak, A. Martínez-Amesti, M.A. Corcuera, A. Eceiza, Strain sensitive conductive polyurethane foam/graphene nanocomposites prepared by impregnation method, Eur. Polym. J. 90 (2017) 323–333. doi:10.1016/j.eurpolymj.2017.03.035.

[79] S. Wang, J. Wang, W. Zhang, J. Ji, Y. Li, G. Zhang, F. Zhang, X. Fan, Ethylenediamine modified graphene and its chemically responsive supramolecular hydrogels, Ind. Eng. Chem. Res. 53 (2014) 13205–13209. doi:10.1021/ie501448p.

[80] C.D. Grande, J. Mangadlao, J. Fan, A. De Leon, J. Delgado-Ospina, J.G. Rojas, D.F. Rodrigues, R. Advincula, Chitosan cross-linked graphene oxide nanocomposite films with antimicrobial activity for application in food industry, Macromol. Symp. 374 (2017) 1–8. doi:10.1002/masy.201600114.

[81] H. Ji, H. Sun, X. Qu, Antibacterial applications of graphene-based nanomaterials: Recent achievements and challenges, Adv. Drug Deliv. Rev. 105 (2016) 176–189. doi:10.1016/j.addr.2016.04.009.

[82] P. Zheng, T. Ma, X. Ma, Fabrication and properties of starch-grafted graphene nanosheet/ plasticized-starch composites, Ind. Eng. Chem. Res. 52 (2013) 14201–14207. doi:10.1021/ie402220d.

[83] F.T. Johra, J.W. Lee, W.G. Jung, Facile and safe graphene preparation on solution based platform, J. Ind. Eng. Chem. 20 (2014) 2883–2887. doi:10.1016/j.jiec.2013.11.022.

[84] P.-P. Zuo, H.-F. Feng, Z.-Z. Xu, L.-F. Zhang, Y.-L. Zhang, W. Xia and W.-Q. Zhang, Fabrication of biocompatible and mechanically reinforced graphene oxide-chitosan nanocomposite films, Chem. Cent. J. 7 (2013) 1–11. doi: 10.1186/1752-153X-7-39.

[85] S. Ganguly, D. Ray, P. Das, P.P. Maity, S. Mondal, V.K. Aswal, S. Dhara, N.C. Das, Mechanically robust dual responsive water dispersible-graphene based conductive elastomeric hydrogel for tunable pulsatile drug release, Ultrason. Sonochem. 42 (2018) 212–227. doi:10.1016/j.ultsonch.2017.11.028.

[86] T. Ma, P.R. Chang, P. Zheng, X. Ma, The composites based on plasticized starch and

graphene oxide/reduced graphene oxide, Carbohydr. Polym. 94 (2013) 63–70. doi:10.1016/j.carbpol.2013.01.007.

[87] H. Bai, Q. Zhang, T. Zhou, Q. Fu, H. Deng, C. Tang, F. Chen, The preparation of high performance and conductive poly (vinyl alcohol)/graphene nanocomposite via reducing graphite oxide with sodium hydrosulfite, Compos. Sci. Technol. 71 (2011) 1266–1270. doi:10.1016/j.compscitech.2011.04.016.

[88] L. Pang, C. Dai, L. Bi, Z. Guo, J. Fan, Biosafety and antibacterial ability of graphene and graphene oxide in vitro and in vivo, (2017). doi:10.1186/s11671-017-2317-0.

[89] H.M. Hegab, A. Elmekawy, L. Zou, D. Mulcahy, C.P. Saint, M. Ginic-markovic, The controversial antibacterial activity of graphene-based materials, Carbon N. Y. 105 (2016) 362–376. doi:10.1016/j.carbon.2016.04.046.

[90] R. Li, C. Liu, J. Ma, Studies on the properties of graphene oxide-reinforced starch biocomposites, Carbohydr. Polym. 84 (2011) 631–637. doi:10.1016/j.carbpol.2010.12.041.

[91] A. Usman, Z. Hussain, A. Riaz, A.N. Khan, Enhanced mechanical, thermal and antimicrobial properties of poly(vinyl alcohol)/graphene oxide/starch/silver nanocomposites films, Carbohydr. Polym. 153 (2016) 592–599. doi:10.1016/j.carbpol.2016.08.026.

[92] Y. Feng, X. Zhang, Y. Shen, K. Yoshino, W. Feng, A mechanically strong, flexible and conductive film based on bacterial cellulose/graphene nanocomposite, Carbohydr. Polym. 87 (2012) 644–649. doi:10.1016/j.carbpol.2011.08.039.

[93] J.R. Potts, D.R. Dreyer, C.W. Bielawski, R.S. Ruoff, Graphene-based polymer nanocomposites, Polymer (Guildf). 52 (2011) 5–25. doi:10.1016/j.polymer.2010.11.042.

[94] E.C. Romani, S. Nardecchia, C. Vilani, S. Qi, H. Dong, F.L. Freire, Synthesis and characterization of polyurethane/reduced graphene oxide composite deposited on steel, J. Coatings Technol. Res. 15 (2018) 1371–1377. doi:10.1007/s11998-018-0088-x.

[95] W. Gao, The chemistry of graphene oxide, Graphene Oxide Reduct. Recipes, Spectrosc. Appl. (2015) 61–95. doi:10.1007/978-3-319-15500-5_3.

[96] T.B. Rouf, J.L. Kokini, Biodegradable biopolymer–graphene nanocomposites, J. Mater. Sci. 51 (2016) 9915–9945. doi:10.1007/s10853-016-0238-4.

[97] J.Ri.E.O. William S. Hummers, Preparation of graphitic oxide, J. Am. Chem. Soc. 80 (1958) 1339–1339.

[98] J. Guerrero-Contreras, F. Caballero-Briones, Graphene oxide powders with different oxidation degree, prepared by synthesis variations of the Hummers method, Mater. Chem. Phys. 153 (2015) 209–220. doi:10.1016/j.matchemphys.2015.01.005.

[99] M.F. Zainuddin, N.H. Nik Raikhan, N.H. Othman, W.F.H. Abdullah, Synthesis of reduced Graphene Oxide (rGO) using different treatments of Graphene Oxide (GO), IOP Conf. Ser. Mater. Sci. Eng. 358 (2018). doi:10.1088/1757-899X/358/1/012046.

[100] I. Kanayama, H. Miyaji, H. Takita, E. Nishida, M. Tsuji, B. Fugetsu, L. Sun, K. Inoue, A. Ibara, T. Akasaka, T. Sugaya, M. Kawanami, Comparative study of bioactivity of collagen scaffolds coated with graphene oxide and reduced graphene oxide, Int. J. Nanomedicine. 9

(2014) 3363–3373. doi:10.2147/IJN.S62342.

[101] L. Nguyen Dang, J. Seppälä, Electrically conductive nanocellulose/graphene composites exhibiting improved mechanical properties in high-moisture condition, Cellulose. 22 (2015) 1799–1812. doi:10.1007/s10570-015-0622-2.

[102] L. Guardia, J.I. Paredes, P. Solı, J.M.D. Tasco, Vitamin C is an ideal substitute for hydrazine in the reduction of graphene oxide suspensions 114, (2010) 6426–6432.

[103] A. Mohamed, T. Ardyani, S. Abu Bakar, M. Sagisaka, Y. Umetsu, J.J. Hamon, B.A. Rahim, S.R. Esa, H.P.S. Abdul Khalil, M.H. Mamat, S. King, J. Eastoe, Rational design of aromatic surfactants for graphene/natural rubber latex nanocomposites with enhanced electrical conductivity, J. Colloid Inter. Sci. 516 (2018) 34–47. doi:10.1016/j.jcis.2018.01.041.

[104] A. Santamaria-Echart, I. Fernandes, F. Barreiro, A. Retegi, A. Arbelaiz, M.A. Corcuera, A. Eceiza, Development of waterborne polyurethane-ureas added with plant extracts: Study of different incorporation routes and their influence on particle size, thermal, mechanical and antibacterial properties, Prog. Org. Coatings. 117 (2018) 76–90. doi:10.1016/j.porgcoat.2018.01.006.

[105] N. Martins, L. Barros, C. Santos-Buelga, M. Henriques, S. Silva, I.C.F.R. Ferreira, Evaluation of bioactive properties and phenolic compounds in different extracts prepared from Salvia officinalis L., Food Chem. 170 (2014) 378–385. doi:10.1016/j.foodchem.2014.08.096.

[106] E.S. Dragan, Design and applications of interpenetrating polymer network hydrogels, Chem. Eng. J. 243 (2014) 572–590.

[107] F. Ullah, M. Bisyrul Hafi Othman, F. Javed, A. Zulkifli, H. Akil, Classification, processing and application of hydrogels : A review, Mater. Sci. Eng. C. 57 (2015) 414–433. doi:10.1016/j.msec.2015.07.053.

[108] X. Liang, B. Qu, J. Li, H. Xiao, B. He, L. Qian, Preparation of cellulose-based conductive hydrogels with ionic liquid, React. Funct. Polym. 86 (2015) 1–6. doi:10.1016/j.reactfunctpolym.2014.11.002.

[109] C. García-Astrain, L. Avérous, Synthesis and evaluation of functional alginate hydrogels based on click chemistry for drug delivery applications, Carbohydr. Polym. 190 (2018) 271–280. doi:10.1016/j.carbpol.2018.02.086.

[110] E.M. Ahmed, Hydrogel: Preparation, characterization, and applications, J. Adv. Res. 6 (2015) 105–121. doi:10.1016/j.jare.2013.07.006.

[111] K.S. Anseth, H.-A. Klok, Click chemistry in biomaterials, nanomedicine, and drug delivery, biomacromolecules. 17 (2016) 1–3. doi:10.1021/acs.biomac.5b01660.

[112] M. Gregoritza, F.P. Brandl, The Diels-Alder reaction: A powerful tool for the design of drug delivery systems and biomaterials, Eur. J. Pharm. Biopharm. 97 (2015) 438–453. doi:10.1016/j.ejpb.2015.06.007.

[113] A. Gandini, Progress in Polymer Science The furan / maleimide Diels – Alder reaction : A versatile click – unclick tool in macromolecular synthesis, Prog. Polym. Sci. 38 (2013) 1–29. doi:10.1016/j.progpolymsci.2012.04.002.

[114] C. García-astrain, R. Hernández, O. Guaresti, L. Fruk, C. Mijangos, A. Eceiza, N. Gabilondo, Click Crosslinked Chitosan / Gold Nanocomposite Hydrogels, Macromol. JOurnals. 301 (2016) 1295–1300.

[115] S. Hesse, T. Liebert, T. Heinze, Studies on the film formation of polysaccharide based furan-2-carboxylic acid esters, Macromol. Symp. 232 (2006) 57–67. doi:10.1002/masy.200551407.

[116] T.F. Liebert, T. Heinze, Tailored cellulose esters: Synthesis and structure determination, Biomacromolecules. 6 (2005) 333–340. doi:10.1021/bm049532o.

[117] T.S. Nossa, N.M. Belgacem, A. Gandini, A.J.F. Carvalho, Thermoreversible crosslinked thermoplastic starch, Polym. Int. 64 (2015) 1366–1372. doi:10.1002/pi.4925.

[118] N. Abhari, A. Madadlou, A. Dini, O. H. Naveh, Textural and cargo release attributes of trisodium citrate cross-linked starch hydrogel, Food Chem. 214 (2017) 16–24. doi:10.1016/j.foodchem.2016.07.042.

[119] S. Li, J. Yi, X. Yu, H. Shi, J. Zhu, L. Wang, Preparation and characterization of acid resistant double cross-linked hydrogel for potential biomedical applications, ACS Biomater. Sci. Eng. 4 (2018) 872–883. doi:10.1021/acsbiomaterials.7b00818.

[120] X. Bai, S. Lü, Z. Cao, B. Ni, X. Wang, P. Ning, D. Ma, H. Wei, M. Liu, Dual crosslinked chondroitin sulfate injectable hydrogel formed via continuous Diels-Alder (DA) click chemistry for bone repair, Carbohydr. Polym. 166 (2017) 123–130. doi:10.1016/j.carbpol.2017.02.062.

[121] M. Montiel-Herrera, A. Gandini, F.M. Goycoolea, N.E. Jacobsen, J. Lizardi-Mendoza, M. Recillas-Mota, W.M. Argüelles-Monal, N-(furfural) chitosan hydrogels based on Diels-Alder cycloadditions and application as microspheres for controlled drug release, Carbohydr. Polym. 128 (2015) 220–227. doi:10.1016/j.carbpol.2015.03.052.

[122] G. Wang, J. Zhu, X. Chen, H. Dong, Q. Li, L. Zeng, X. Cao, Alginate based antimicrobial hydrogels formed by integrating Diels-Alder "click chemistry" and the thiol-ene reaction, RSC Adv. 8 (2018) 11036–11042. doi:10.1039/c8ra00668g.

[123] M. Fan, Y. Ma, Z. Zhang, J. Mao, H. Tan, X. Hu, Biodegradable hyaluronic acid hydrogels to control release of dexamethasone through aqueous Diels-Alder chemistry for adipose tissue engineering, Mater. Sci. Eng. C. 56 (2015) 311–317. doi:10.1016/j.msec.2015.04.004.

[124] C. García-Astrain, I. Ahmed, D. Kendziora, O. Guaresti, A. Eceiza, L. Fruk, M.A. Corcuera, N. Gabilondo, P. Yang, I.K. Kwon, J.M. Greneche, Effect of maleimide-functionalized gold nanoparticles on hybrid biohydrogels properties, RSC Adv. 5 (2015) 50268–50277. doi:10.1039/C5RA06806A.

[125] F. Yu, X. Cao, L. Zeng, Q. Zhang, X. Chen, An interpenetrating HA/G/CS biomimic hydrogel via Diels-Alder click chemistry for cartilage tissue engineering, Carbohydr. Polym. 97 (2013) 188–195. doi:10.1016/j.carbpol.2013.04.046.

[126] O. Guaresti, C. García-Astrain, R.H. Aguirresarobe, A. Eceiza, N. Gabilondo, Synthesis of stimuli–responsive chitosan–based hydrogels by Diels–Alder cross–linking `click´ reaction as potential carriers for drug administration, Carbohydr. Polym. 183 (2018) 278–286. doi:10.1016/j.carbpol.2017.12.034.

[127] O. Guaresti, C. García–Astrain, T. Palomares, A. Alonso–Varona, A. Eceiza, N. Gabilondo, Synthesis and characterization of a biocompatible chitosan–based hydrogel cross–linked via 'click' chemistry for controlled drug release, Int. J. Biol. Macromol. 102 (2017) 1–9. doi:10.1016/j.ijbiomac.2017.04.003.

CHAPTER 2:

MATERIALS AND CHARACTERISATION TECHNIQUES

2. MATERIALS AND CHARACTERISATION TECHNIQUES

In this chapter the materials used in the development of all starch-based materials are described. In addition, the techniques, procedures and conditions employed for the physicochemical, thermal, morphological and rheological characterisation of films and hydrogels were also detailed. Moreover, the procedures employed for swelling and drug delivery studies, as well as protocol employed for the in vitro cell viability evaluation are also presented.

2.1. CHEMICALS AND REACTANTS

Normal maize starch containing 73% amylopectin and 27% amylose (from Sigma-Aldrich) was employed to obtain both PLS and TPS films as well as hydrogels. Glycerol (provided by Panreac, 99%), D-isosorbide (from Sigma-Aldrich), and 1,3-propanediol (from Quimidroga S.A.) were employed as plasticisers.

Waxy maize starch (~99% amylopectin) and microcyrstalline cellulose (both provided by Sigma-Aldrich) were used to obtain starch and cellulose nanocrystals, subsequently. For the hydrolysis, sulfuric acid (from Panreac, 96%) was employed. Graphite flakes provided by Sigma-Aldrich were used to obtain graphene (G) and graphene oxide (GO). Besides, for the obtainment of G and GO and the reduction of GO the following reactants were also employed: N-methyl pyrrolidone (from Sigma-Aldrich, NMP, 97%), sodium nitrate, sulfuric acid (96%), potassium permanganate, hydrogen peroxide (30% purity), hydrochloric acid (37%) and ascorbic acid provided by Panreac. For obtaining the plant extracts used as emulsifier of G, *Salvia officinalis L.* was employed as dry material purchased in an herbalist.

For the chemical modification and cross-linking of starch, furfuryl isocyanate (97%), Jeffamine® ED 900 (O,O'-bis (2-aminopropyl) polypropylene glycol-b-polyethylene glycol-b-

polypropylene glycol, number-average molar mass = 900 g mol^{-1}), sodium acetate trihydrate (≥99.0%) and 4arm-PEG10K-Maleimide (number-average molar mass = 10000 g mol^{-1}) were purchased from Sigma-Aldrich. Dimethyl sulfoxide (DMSO, for analysis), maleic anhydride, trimethylamine (99.5%), acetic anhydride (98%) and acetone (for analysis) were provided by Panreac. Chloroform (99.8%) was purchased from Lab Scan Analytical Sciences.

All reagents and solvents were employed as received. Distilled water was used in all cases as solvent.

For the characterisation techniques, deuterium oxide (D_2O) for NMR (deuteration degree min. 99.96%) was purchased from Sigma-Aldrich. Ethylene glycol provided by Panreac was used for contact angle measurements. The phosphate buffered saline (PBS) tablets employed for the swelling measurements were purchased from Panreac. For short-term cytotoxicity assays the following reactants were additionally used: L929 mouse fibroblast cells (clon 929 of the NCTC:CCL from American Type Culture Collection, ATCC), minimum essential medium containing Earle salts and L-glutamine 2mM, non-essential aminoacids and sodic pyruvate (from Gibco®), penicillin and streptomycin (provided by Lonza), fetal bovine serum (supplied by Biochor) and DMSO from Sigma-Aldrich.

2.2. CHARACTERISATION METHODS

2.2.1. Physicochemical characterisation

2.2.1.1. Fourier transform infrared spectroscopy

Fourier transform infrared spectroscopy (FTIR) measurements were performed in a Nicolet Nexus spectrophotometer. Measurements were recorded in the range from 4000 cm^{-1} to 650 cm^{-1} in attenuated reflection mode, with a 4 cm^{-1} resolution and 32 scans. The spectra were recorded

with a Specac MKII Golden Gate accessory equipped with a diamond crystal at a nominal incident angle of 45 degrees and ZnSe lens.

2.2.1.2. Nuclear magnetic resonance

Proton nuclear magnetic resonance (^{1}H NMR) measurements were performed with an Avance Bruker equipment equipped with BBO z–gradient probe. Experimental conditions were as follows: frequency of 500 MHz, number of scans 64, spectral window of 5000 Hz and recovery delay of 1 s. D_2O was used as solvent. Moreover, ^{1}H NMR results were also employed to calculate the degree of substitution (DS) of functionalised starch. DS could be defined as the average number of substituted units per glucose monomer [1]. The DS was determined by the integration of the α-anomeric hydrogen signal of the glucose unit.

2.2.1.3. X-ray diffraction

Starch films, obtained by both solvent casting and extrusion/compression techniques, were analysed by X-ray diffraction (XRD) in order to assess the effectiveness of the gelatinization protocols to destroy the native crystalline domains of starch granules and obtain amorphous plasticised materials. All measurements were performed using a Philips Xpert Pro diffractometer operating at 40 kV and 40 mA, in θ - θ configuration secondary monochromator with Cu-Kα radiation (λ = 1.5418 Å) and a PIXcel solid state detector (active length in 2θ = 3.347°). Scattered radiation was detected in the angular range 1 - 40° (2θ).

In addition, the crystallinity of both nanoentities, i.e. polysaccharide nanocrystals and carbonaceous nanoparticles was also analysed by XRD. In the case of polysaccharide nanocrystals, the XRD diffractograms were used to determine the crystallinity percentage of WSNC and CNC. For WSNC an appropriate method is not so widely established, for this reason the crystallinity degree was determined by the ratio of the crystalline area to the total area [2,3]:

$$\text{WSNC, Crystallinity percentage (\%)} = \frac{\text{Area under the peak}}{\text{Total area}} \times 100 \quad \text{(Eq. 2.1)}$$

Crystallinity for CNC was calculated according to the method described in literature [4,5]:

$$\text{CNC, Crystallinity percentage (\%)} = \frac{I_{002} - I_{am}}{I_{002}} \times 100 \quad \text{(Eq. 2.2)}$$

where I_{002} is the peak intensity of the (002) crystallographic plane [4], i.e. the intensity peak around $2\theta = 22.5^{\circ}$ [6] and I_{am} is the intensity scattered by the amorphous part of the sample measured around $2\theta = 18.0^{\circ}$ [4].

2.2.1.4. Ultraviolet-visible spectroscopy

Ultraviolet-visible spectroscopy (UV-vis spectroscopy) was used to follow the DA reactions between the furan-modified starch and the corresponding two different cross-linkers. The kinetics of the reaction was analysed using a Shimadzu UV-3600/3100 instrument equipped with a thermoelectric cell holder, operating at 65 °C in a range of 200 to 400 nm and recording a spectra every 30 min during 24 h.

2.2.1.5. Raman spectroscopy

Raman spectroscopy of G and GO were obtained with a Renishaw InVia microscope (50X) with a laser of 514 nm wavelength (Modu Laser) at 10% potency. Data were collected in the range of 150 - 3500 cm^{-1}. Exposure time and accumulations were set at 20 s and 5, respectively.

2.2.2. Optical properties

2.2.2.1. Ultraviolet-visible spectroscopy

The optical transmittance of films plasticised with glycerol, D-isosorbide and 1,3-propanediol was measured by UV-vis spectroscopy using a Shimadzu UV-3600/3100 instrument, operating at room temperature in a range of 400 to 700 nm.

2.2.2.2. Colourimetry

The colour of carbonaceous nanoparticles containing films was analysed using a X-rite 962 spectrophotometer. The colour of the films was evaluated according to the Hunter's parameters according to the CIELAB scale (L^*, a^*, b^*) and repeating five measurements for each sample. Standard plate ($L^* = 92.82$; $a^* = -1.24$; and $b^* = 0.46$) was used as a standard. The colour parameters vary from L = 0 (black) to L = 100 (white), from –a (greenness) to +a (redness) and from –b (blueness) to +b (yellowness). The colour difference parameter, ΔE, was determined as indicated in Equation 2.3:

$$\Delta E = \sqrt{\left(\Delta L^{*2} + \Delta a^{*2} + \Delta b^{*2}\right)} \quad \text{(Eq. 2.3)}$$

$$\Delta L^* = L^*_{standard} - L^*_{sample} \quad \text{(Eq. 2.4)}$$

$$\Delta a^* = a^*_{standard} - a^*_{sample} \quad \text{(Eq. 2.5)}$$

$$\Delta b^* = b^*_{standard} - b^*_{sample} \quad \text{(Eq. 2.6)}$$

2.2.3. Thermal and thermomechanical characterisation

2.2.3.1. Thermogravimetric analysis

Thermogravimetric analysis (TGA) was performed using a Mettler Toledo TGA-SDTA 851 instrument. The measurements were conducted from 25 to 800 °C, with a heating rate of 10 °C min^{-1} under nitrogen atmosphere. On the other hand, the thermal stability of nanocomposite films reinforced with G and GO was evaluated with a TGA/DSC3+ Mettler Toledo equipment following the same assay conditions.

2.2.3.2. Differential scanning calorimetry

Differential scanning calorimetry (DSC) was performed in a Mettler Toledo DSC3+ equipment. Samples with a weight between 5 - 10 mg were sealed in medium pressure pans and were heated from -75 °C to 250 °C at 20 °C min^{-1} heating rate under nitrogen atmosphere. The temperature and enthalpy of gelatinisation were calculated as the maximum and the area under the thermogram, respectively.

2.2.3.3. Dynamic mechanical analysis

Dynamic mechanical analysis (DMA) of all films was carried out using an Eplexor 100N instrument from Gabo Qualimeter registering the storage modulus (E'), the loss modulus (E") and the tan δ = E"/E' while heating. Measurements were performed at 1 Hz and with a heating rate of 2 °C min^{-1}, working from -100 °C to 0 °C. A constant strain of 0.05% was used in Chapters 3 and 5, whereas a constant strain of 0.5% in Chapter 6. The samples were cut as rectangular strips (25 x 3 x 0.2 mm^3).

2.2.4. Surface properties

2.2.4.1. Dynamic contact angle

Dynamic contact angle measurements were carried out using the Dataphysics OCA equipment with needle-in-drop configuration. The advancing contact angle was measured increasing the drop volume from 3.0 μL to 6.0 μL after each volume increment (0.5 μL at 0.1 μL s^{-1}). The receding contact angle was determined reducing the drop volume down to 3.0 μL. Due to the high hydrophilicity of the films, the measurements could not be carried out using water, and thus, ethylene glycol was used in all cases.

2.2.4.2. Static contact angle

Static contact angle measurements of films reinforced with carbonaceous nanoparticles was performed using a Surface Electro Optics (SEO) Contact Angle Analyzer with a needle-in-drop technique. The contact angle measurements were carried out with a drop volume of 3.0 μL and using ethylene glycol as solvent.

2.2.5. Mechanical characterisation

2.2.5.1. Tensile tests

Tensile tests of starch-based films obtained by solvent casting were performed using a Universal Testing Machine (MTS Insight 10) using a load cell of 250 N at room temperature. Samples were cut into dumbbell shaped specimens with a testing section of 5 mm wide and 15 mm long. Tests were performed at a crosshead rate of 5 mm min^{-1}.

The tensile tests of extruded films as well as nanocomposites reinforced with G and GO were carried out using a Instron 5967 equipment and a load cell of 50 N. Samples dimensions and testing rates were the same that above described.

2.2.6. Barrier properties

2.2.6.1. Water vapour transmission rate

Water vapour transmission rate (WVTR) determination was performed at 25 °C on a gravimetric cell in which a small amount of liquid water was sealed by the sample. The cell was put on a weighting scale with a readability of 10^{-5} g and the weight loss of the cell, solely due to the permeation of the water vapour through the film, was registered by means of a computer connected to the scale. The WVTR can be defined by:

$$WVTR = \frac{m \cdot l}{A(a_{int} - a_{ext})} \quad \text{(Eq. 2.7)}$$

where m is the weight loss of the cell; l is the film thickness; A is the exposed area of film (2.54 cm^2); and a_{ext} is the penetrant activity outside the cell (assumed to be equal to the relative humidity in case of water). In all cases values of 0.3 of relative humidity (one percent) in the outside of the cell was considered.

The water vapour permeability (WVP) values were calculated according to the following Equation 2.8:

$$WVP = \frac{WVTR}{\Delta P} \quad \text{(Eq. 2.8)}$$

where ΔP is the vapour pressure difference.

2.2.6.2. Oxygen transmission rate

Oxygen transmission rate (OTR) measurements of all films were carried out using a MOCON OXTRAN Model 2/21 gas permeability tester in accordance with the ASTM standard D3985. The OTR of the samples was tested at 760 mmHg, relative humidity (RH) of 50% and 23 °C. The oxygen permeability was defined by:

$$OP = \frac{OTR}{\Delta P} \quad \text{(Eq. 2.9)}$$

where ΔP is the vapour pressure difference.

2.2.7. Morphological characterisation

2.2.7.1. Atomic force microscopy

Atomic force microscopy (AFM) measurements of polysaccharide nanocrystals and PLS nanocomposite films were performed in tapping mode using a Veeco Multimode scanning probe microscope equipped with a Nanoscope IIIa Controller. All measurements were recorded using

TESP type silicon tips having a resonance frequency of approximately 340 kHz and a cantilever spring constant about 40 N m^{-1}. The nanocrystals were prepared by spin coating of an ultrasonicated dispersion (0.001 mg NC ml^{-1} distilled water).

AFM images of the cryofractured surfaces of the films were performed in tapping mode using a Bruker Dimension ICON scanning probe microscope equipped with a Nanoscope V Controller. The morphology of the samples was examined using TESP-V2 type silicon tips having a resonance frequency of approximately 320 kHz and a cantilever spring constant about 42 N m^{-1}.

2.2.7.2. Transmission optical microscopy

The gelatinisation process was followed using transmission optical microscopy (TOM) and analysing the change of the crystalline structure and the evolution of the birefringence. The analyses were carried out with a Nicon Eclipse E600 instrument in reflectance under polarised light and with a magnification of ×500.

2.2.7.3. Scanning electron microscopy

Scanning electron microscopy (SEM) images of hydrogels were recorded in order to analyse de porous microstructure of hydrogels. Samples were freeze-dried after swollen in distilled water and gold coated prior to the measurements. VEGA3 LM, TESCAN equipment with an operation voltage of 5 kV was used for the bismaleimide containing neat hydrogels, while JEOL JSM–6400 microscope with an operating at an accelerated voltage of 20 kV was employed for the nanocomposite hydrogels.

2.2.7.4. Transmission electron microscopy

Transmission electron microscopy (TEM) was used to analyse the morphology of G and GO. Images were recorded on a FEI Titan Cubed G2 60-300 microscope, equipped with a Schottky X-FEG field emission electron gun, monochromator and CEOS GmbH spherical aberration (Cs)

corrector on the image side. The microscope was operated at 80 kV to minimize the knock-on damage to the graphene. The third-order spherical aberration (Cs) was tuned to -10 μm. Images were obtained for an underfocus of -8 nm and were recorded on a CCD camera (2kx2k, Gatan UltraScan 1000), using exposition times of 1s per image.

Samples were prepared by ultrasonication in distilled water using a concentration of 0.005 mg ml^{-1} for 1 h (with on/off periods of 4 s and 2 s). Then, a drop of the sonicated suspension was placed in a TEM copper grid (300 Mesh) covered by a holey carbon film followed by drying under vacuum.

2.2.8. Rheological measurements

The rheological study of the hydrogels was performed (the measurements were repeated three times, n = 3) using a Scientific Advanced Rheometric Expansion System (ARES) using plate-plate geometry (25 mm diameter). Frequency sweep measurements were performed at 37 °C from 0.1 to 500 rad s^{-1} at a fixed strain, in the linear viscoelastic region, previously assessed by stress sweep experiments. Measurements were performed at the human body temperature (37 °C) to analyse the applicability of hydrogels in biomedical fields.

2.2.9. Swelling capacity

The swelling capacity of hydrogels (n = 3) was determined by gravimetric method. Freeze-dried hydrogels were incubated at 37 °C until equilibrium using simulated intestinal fluid, PBS at pH = 7.4. At selected time intervals, the swollen hydrogels were taken out and the excess of water was removed with a filter paper and the sample weighed. The swelling ratio (SR) was determined by Equation 2.10:

$$SR\ (\%) = \frac{W_s - W_t}{W_t} \times 100 \qquad \text{(Eq. 2.10)}$$

where W_s is the weight of the swollen sample and W_t is the weight of the final dried sample. The equilibrium swelling was considered to be achieved when the weight of the hydrogels no longer increased.

2.2.10. Hydrolytic degradation

The degradation of hydrogels was also measured gravimetrically incubating the samples in PBS for one week and calculated from equation 2.11:

$$\text{Degradation (\%)} = \frac{W_t}{W_d} \times 100 \qquad \text{(Eq. 2.11)}$$

where W_t is the weight of the final dried sample and W_d is the initial weight of the freeze-dried sample.

2.2.11. Specific characterisation

2.2.11.1. Drug delivery

For drug delivery measurements chloramphenicol (ClPh) was selected as the model drug for in vitro release studies in a simulated intestinal medium (PBS). Freeze-dried hydrogels were loaded with a drug solution (0.5 mg ClPh mL^{-1} distilled water) at 25 °C for 3 h (stated based on the equilibrium swelling times from the swelling studies). After the immersion time, samples were dried at room temperature until constant weight. For the release studies, the dried loaded hydrogel samples were introduced in a metallic perforated bag and stirred in 80 mL of PBS solution (pH=7.4) at 37 °C. At selected time intervals, an aliquot of 1 mL of the solution was taken and analysed by UV–vis spectroscopy. After that, the aliquot was returned to the beaker. The amount of released ClPh was determined by comparing the absorbance signal at 275 nm (maximum absorbance wavelength of ClPh) with a standard calibration curve.

The cumulative drug release (CR) at each time interval was calculated using Equation 2.12.

$$CR\ (\%) = \frac{m_t}{m_0} \times 100 \qquad \text{(Eq. 2.12)}$$

where m_t is the cumulative mass of ClPh released at time t and m_0 is the total amount of ClPh loaded.

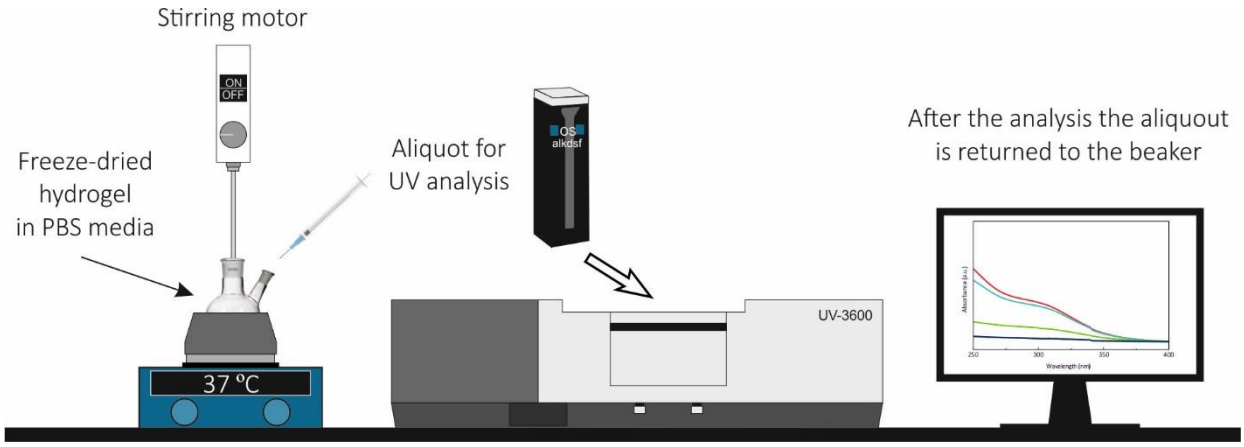

Figure 2.1 – Scheme of drug delivery measurements.

2.2.11.2. Antibacterial tests

Antimicrobial activity of G containing nanocomposite hydrogels against *Escherichia coli* CECT 405 (*E. coli*, gram positive) and *Staphylococcus aureus* CECT 239 (*S. aureus*, gram negative) bacteria was analysed following the disc-plate antibiogram test. The hydrogel was placed in the inoculated agar of a petri dish containing the microorganism to be tested. The samples were then incubated at 37 °C for 24 and 48 h.

2.2.11.3. Short-term cytotoxicity assays

The *in vitro* cell viability and proliferation in CNC containing hydrogels was analysed by short-term cytotoxicity assays. Measurements were carried out using L929 mouse fibroblasts cells and following ISO 10993 standard. Briefly, sterilised samples were incubated separately in complete cell culture medium (Dulbeccoís modified Eagleís medium) and 10% fecal calf serum and supplemented

with antibiotics (100 U mL^{-1} penicillin and 100 g mL^{-1} of streptomycin) at 37 °C for 24 h to obtain the extracted culture medium. In addition, L929 mouse fibroblast were seeded and allowed to grow in 96-well microplates at a density of 4 x 10^3 cells/well in the presence of standard culture medium for 2 h before the experiments. In the cytotoxicity test, cultures were treated for 24 and 48 h with the extracted media. As controls, standard culture media (negative control) and 10% DMSO (positive control) were used.

The metabolic activity of viable cells was determined using the colourimetric MTT assay, in which 3–(4,5–dimethyltriazol–2–yl)−2,5 diphenyltetra–sodium bromide is reduced to formazan in the mitochondria of living cells. The cell number per well was proportional to the amount of formazan crystals and was determined by measuring the absorbance at 540 nm using a microplate reader. Viability (%) was calculated as follows:

$$\text{Viability (\%)} = \frac{[\text{A}]_{\text{test}}}{[\text{A}]_{\text{control}}} \times 100 \qquad \text{(Eq. 2.13)}$$

where $[A]_{test}$ is the absorbance of the sample cells and $[A]_{control}$ is the absorbance of the negative control cells. All assays were conducted in triplicate and mean values and their standard deviations were calculated.

2.2.12. Electrical conductivity

The electrical response of G and GO containing film and hydrogel nanocomposites were analysed by a Keithley 4200-SCS equipment for semiconductor analysis using a two points measurements technique. The measurements were performed working at 0 - 5 V linear scans, with 0.01 V step and a compliance of 0.1. In the case of hydrogels wet samples were studied.

2.3. REFERENCES

[1] M.J. Tizzotti, M.C. Sweedman, D. Tang, C. Schaefer, R.G. Gilbert, New 1H NMR procedure for the characterization of native and modified food-grade starches, J. Agric. Food Chem. 59

(2011) 6913–6919. doi:10.1021/jf201209z.

[2] M.J. Jivan, A. Madadlou, M. Yarmand, An attempt to cast light into starch nanocrystals preparation and cross-linking, Food Chem. 141 (2013) 1661–1666. doi:10.1016/j.foodchem.2013.04.071.

[3] M.F. Rosa, E.S. Medeiros, J.A. Malmonge, K.S. Gregorski, D.F. Wood, L.H.C. Mattoso, G. Glenn, W.J. Orts, S.H. Imam, Cellulose nanowhiskers from coconut husk fibers: Effect of preparation conditions on their thermal and morphological behavior, Carbohydr. Polym. 81 (2010) 83–92. doi:10.1016/j.carbpol.2010.01.059.

[4] H. Kargarzadeh, I. Ahmad, I. Abdullah, A. Dufresne, S.Y. Zainudin, R.M. Sheltami, Effects of hydrolysis conditions on the morphology, crystallinity, and thermal stability of cellulose nanocrystals extracted from kenaf bast fibers, Cellulose. 19 (2012) 855–866. doi:10.1007/s10570-012-9684-6.

[5] L. Segal, J.J. Creely, A.E. Martin, C.M. Conrad, An empirical method for estimating the degree of crystallinity of native cellulose using the X-ray diffractometer, Text. Res. J. 29 (1959) 786–794. doi:10.1177/004051755902901003.

[6] N. Lin, J. Huang, P.R. Chang, L. Feng, J. Yu, Effect of polysaccharide nanocrystals on structure, properties, and drug release kinetics of alginate-based microspheres, Colloids Surfaces B Biointerfaces. 85 (2011) 270–279. doi:10.1016/j.colsurfb.2011.02.039.

CHAPTER 3:

MAIZE STARCH-BASED FILMS

3. MAIZE STARCH-BASED FILMS

3.1. OBJECTIVE

The aim of this chapter was to study the suitability of glycerol, D-isosorbide and 1,3-propanediol to be used as plasticisers for starch-based films. As it is well known, glycerol has been commonly used as plasticiser in a wide range of materials. Thus, it was hypothesised that in our case, the use of glycerol would also reduce the brittleness and would improve the mechanical behaviour of the material. In addition, the use of other plasticisers from renewable sources, such as D-isosorbide and 1,3-propanediol, was proposed as novel "green" alternatives.

The production of starch-based flexible films is often performed by solvent casting technique at the laboratory scale. However, from an industrial and commercial point of view the thermomechanical processing gives the opportunity to obtain a scale-up production. Thus, the viability and effect of preparing plasticised starch flexible films by both solvent casting (PLS) and extrusion/compression (TPS) methods was evaluated. In addition, due to the tendency of ageing of plasticised starch materials because of retrogradation, the evolution of the properties of the films was also analysed.

All the resulting films were characterised in terms of optical properties, thermal stability, surface, mechanical and barrier properties, and morphology. The retrogradation phenomenon was also studied in the case of films prepared by solvent casting.

3.2. OBTAINMENT OF MAIZE STARCH-BASED FILMS

3.2.1. Preparation of plasticised starch films by solvent casting (PLS)

PLS films were prepared by solvent casting following the method described by Angellier et al., [1] with slight modifications. 3.58 g of normal maize starch were mixed with 35 mL of distilled H_2O

and 1.93 g of the selected plasticiser (glycerol, D-isosorbide or 1,3-propanediol) and the mixture was heated to 90 °C and maintained with continuous magnetic stirring until the viscosity increased (near 20 min). A plasticiser content of 35 wt.% was employed, relative to the starch plus plasticiser mixture weight. After that, the viscous gel was homogenised in a dispersing system for 3 min at 15,000 rpm (POLYTRON® PT 2500 E). The homogenised solution was casted into petri dishes and dried in an oven at 55 °C for 2 h. The manufacturing process for PLS films prepared by solvent casting is illustrated in Figure 3.1.

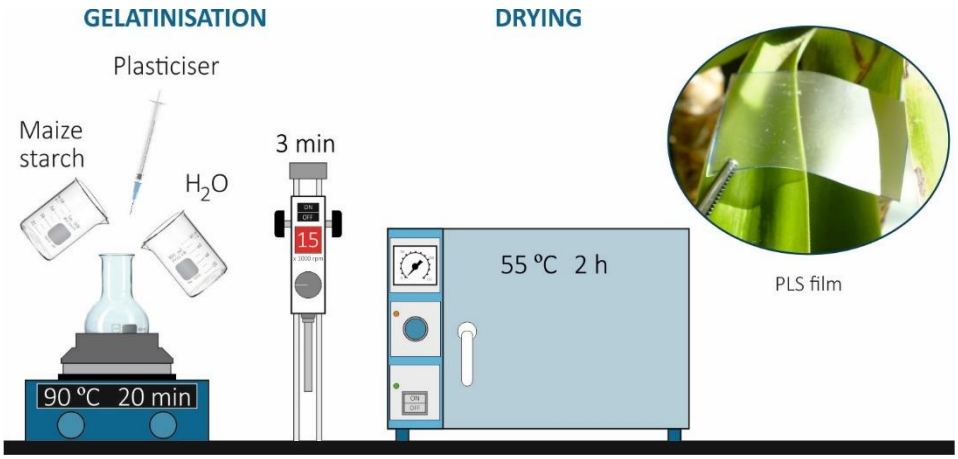

Figure 3.1 – Manufacturing process for PLS films prepared by solvent casting.

Samples were named CSg35, CSi35, and CSpd35 when plasticised with glycerol, D-isosorbide, and 1,3-propanediol, respectively (Table 3.1).

Resulting films were stored at 43% RH for two weeks before the first characterisation fixed by using K_2CO_3 saturated solution. For retrogradation study, the characterisation was repeated after four weeks from gelatinisation (named as aged).

3.2.2. Preparation of thermoplastic starch films by extrusion/compression (TPS)

The obtainment of TPS films by extrusion/compression was carried out following a 4-step methodology: gelatinization, freeze-drying, extrusion and compression. The first step consisted on a

preliminary gelatinization process in the same way as carried out for the solvent casting procedure, i.e. heating a mixture of normal maize starch (3.59 g), distilled water (35 ml) and the desired plasticiser (1.93 g) at 90 °C during 20 min. Then, the gel was homogenised using a POLYTRON® PT 2500 E system. In the same way as for PLS samples, a plasticiser content of 35 wt.% was used for all extruded samples, relative to the starch plus plasticiser mixture weight.

After that, the homogenised gel was freeze-dried. Then, the freeze-dried material was extruded using a HAAKE MiniLab extruder at 120 °C and 50 rpm. Finally, the material was compressed using a Specac's Atlas Series Manual Hydraulic Press with a temperature controller cell working at 1) 120 °C for 5 min and 2) 120 °C and 2.5 t for 5 min. The films were also stored at RH = 43% for two weeks before characterisation. The manufacturing process for TPS obtained by extrusion/compression process is illustrated in Figure 3.2.

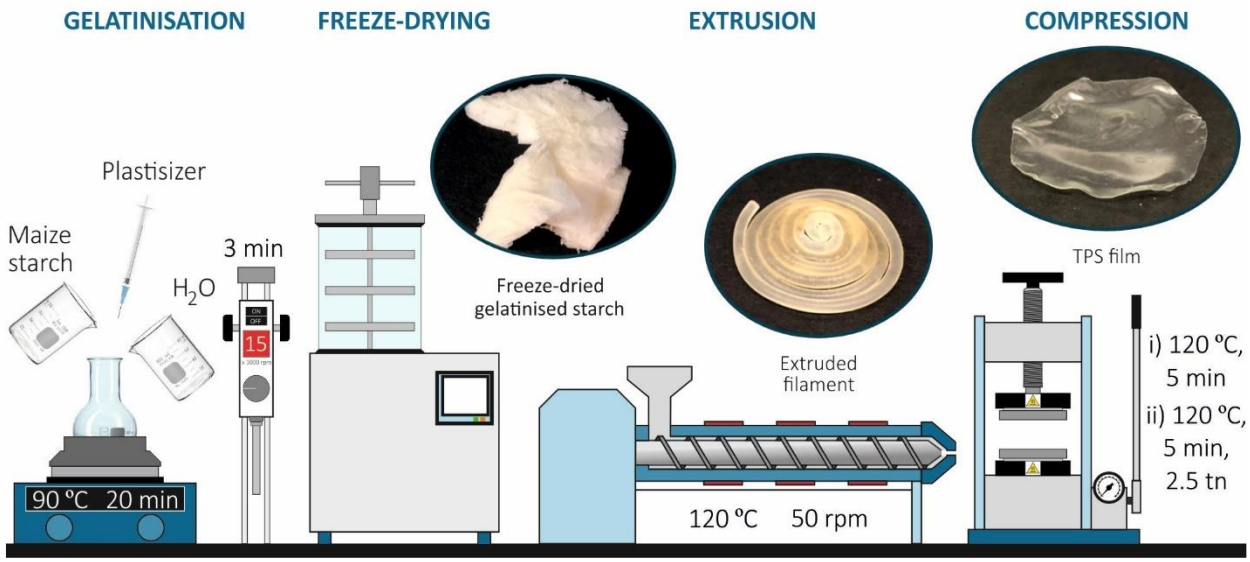

Figure 3.2 – Manufacturing process for TPS films prepared by extrusion/compression.

Extruded TPS films gelatinized with glycerol, D-isosorbide and 1,3-propanediol were named as ESg35, ESi35, and ESpd35, subsequently (Table 3.1).

Table 3.1 – Description of obtained PLS and TPS films.

Sample	Technique	Plasticiser	Storage time	Starch (g)	Plast. (g)	H_2O (ml)
CSg35	Solvent casting	glycerol	2 weeks			
CSi35	Solvent casting	D-isosorbide	2 weeks			
CSpd35	Solvent casting	1,3-propanediol	2 weeks			
ESg35	Extrusion/compression	glycerol	2 weeks			
ESi35	Extrusion/compression	D-isosorbide	2 weeks	3.58	1.93	35.0
ESpd35	Extrusion/compression	1,3-propanediol	2 weeks			
CSg35-aged	Solvent casting	glycerol	4 weeks			
CSi35-aged	Solvent casting	D-isosorbide	4 weeks			
CSpd35-aged	Solvent casting	1,3-propanediol	4 weeks			

3.3. STUDY OF THE GELATINISATION PROCESS

The gelatinisation temperature (T) and gelatinization enthalpy (ΔH) were analysed by DSC, whereas the evolution of the birefringence was evaluated by TOM.

3.3.1. Differential scanning calorimetry

The thermal behaviour and gelatinisation phenomenon of starch can be evaluated by DSC [2]. As defined elsewhere the gelatinization is an endothermic first order transition [3,4]. Therefore, the DSC thermograms give us information about the temperature at which the crystalline domains of starch granules are irreversibly melt, i.e. the gelatinisation temperature [2]. Besides, the gelatinisation enthalpy is related with the amount of crystal order and could be determined by the area under the endothermic peak [2,5,6]. The gelatinisation enthalpy is influenced by the starch source, water content and amylose/amylopectin ratio, plasticiser as well as the measurements conditions [2,7].

In this sense, the gelatinization process with the three plasticisers was evaluated by conducting dynamic heating measurements of the initial starch/water/plasticiser [5]. The obtained DSC

thermograms are shown in Figure 3.3 and the calculated gelatinization temperatures and enthalpies are gathered in Table 3.2.

As shown in the thermograms the gelatinisation was detected as an endothermic first order transition, generally accepted to be ascribed to the gelatinisation of the amylopectin, and usually denoted as G [3,4]. The T_G and ΔH_G were thus calculated as the maximum and the area under the curve of the endothermic peak, respectively. As it could be observed, the gelatinisation temperature was found to be almost the same for all systems. Indeed, all samples presented the T_G close to 72 °C, detecting only a slight decrease for Spd35. In contrast, remarkable differences were observed regarding the ΔH_G values. Both Sg35 and Spd35 samples presented a ΔH_G of 1.12 and 1.33 J g^{-1}, respectively, whereas for Si35 the value was 0.43 J g^{-1}. These results are in concordance with those obtained by Yingfeng et al. [6,7] who stated that the use of different plasticisers lead to different ΔH_G values, while T_G remains almost constant. They concluded that differences on ΔH_G may be associated with the molecular weight of each plasticiser and the capacity to penetrate into the starch structure and the ability to form H-bonds with starch, leading to an increase of ΔH_G for plasticisers with higher molecular weight. However, in our case the opposite effect was observed since the Si35 sample presented the highest molecular weight and the lowest ΔH_G value. It has to be taken into account that the gelatinisation consists in a multistep phenomenon involving the fragmentation of starch granules, the loss of crystallinity and the partial depolymerisation of starch [3]. Thus, gelatinisation is a complex thermal mechanism that sometimes leads to non-consistent and controversial results [2]. Therefore, in our case, we considered that the plasticiser plays an important role in the gelatinisation mechanism. Thus, the similar ΔH_G values detected for glycerol and 1,3-propanediol systems, being molecules of similar chemical structure, could indicate similar gelatinization mechanisms and, at the same time, denotes different gelatinisation mechanism for the D-isosorbide with lower ΔH_G values.

It should be mentioned that all samples presented a small second endothermic peak close to 86 °C denoted as M1 being in all cases around 0.10 J g^{-1} the associated enthalpy value. This second endothermic peak was attributed to the non-equilibrium melting of crystallites [4]. Liu et al. [2] systematically studied the gelatinization process of maize starch/water systems by DSC and concluded that the number of endotherms and the enthalpy of gelatinisation depend on the amylose/amylopectin ratio and the moisture and lipid contents. However, the reported DSC results are not always consistent and are sometimes controversial, due to the complexity of the thermal behaviours of starches. Nevertheless, in order to ensure that all the crystalline domains of the native starch granules were destroyed 90 °C was chosen for the gelatinization in all cases.

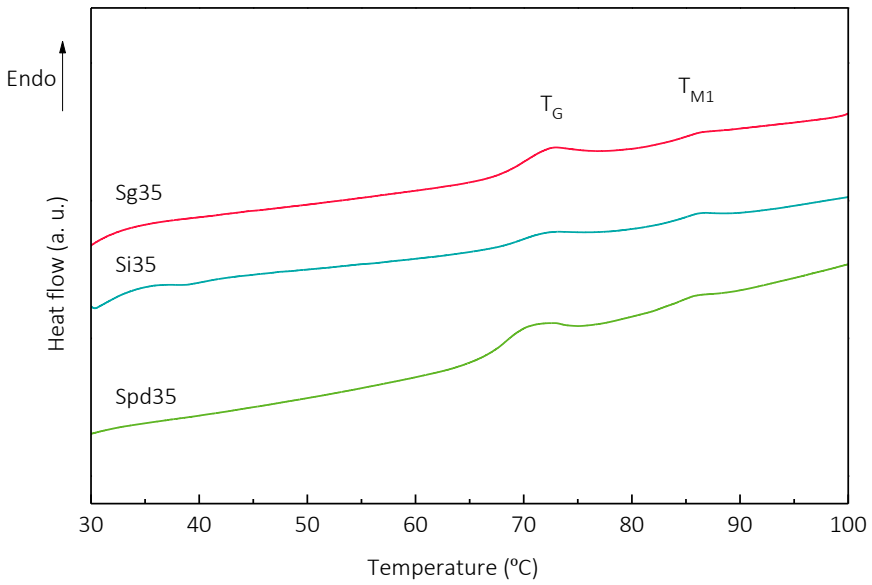

Figure 3.3 – DSC thermograms of gelatinisation using different plasticisers.

Table 3.2 – Gelatinisation temperatures and enthalpy values of gelatinisation using different plasticisers.

	G		M1	
Sample	**T_G (°C)**	**ΔH_G (J g^{-1})**	**T_{M1} (°C)**	**ΔH_{M1} (J g^{-1})**
Sg35	72.5	1.12	86.5	0.10
Si35	72.3	0.43	86.3	0.12
Spd35	70.5	1.33	85.8	0.10

3.3.2. Transmission optical microscopy

When starch is analysed under polarised light, Maltese crosses are commonly observed due to the semi-crystalline character of starch granules which is associated with the birefringence [8–10]. Thus, the evolution of the gelatinisation process was followed by means of TOM, recording images under polarised light at selected time intervals. Collected sequence of images for the Sg35 sample is presented in Figure 3.4.

As it could be observed, the disruption of starch granules was clearly observable as far as the Maltese crosses amount decreased until disappearing at the end of the process. Thereby, once the gelatinisation was completed the crystalline domains of starch granules were undetectable. Therefore, it could be concluded that the gelatinization occurred successfully following the proposed processing conditions.

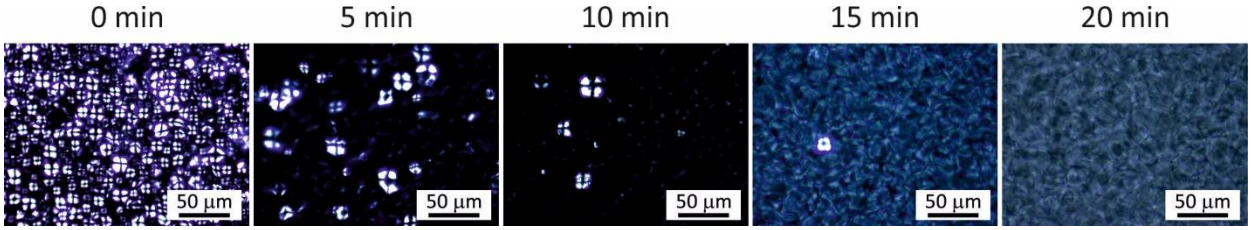

Figure 3.4 – Polarised light images of gelatinization of Sg35 at selected time intervals.

3.4. EFFECT OF THE PLASTICISER ON THE PROPERTIES OF PLS FILMS

Once demonstrated that glycerol, D-isosorbide and 1,3-propanediol met the objective and thus, could be used as plasticisers in starch-based materials, PLS films using the three plasticisers were prepared and characterised. In this section, the results of PLS films obtained by solvent casting are discussed.

3.4.1. X-ray diffraction

The effectiveness of the gelatinization process using glycerol, D-isosorbide and 1,3-propanediol was deduced from XRD patterns (Figure 3.5). As defined by other authors [11,12] the crystalline structure of native maize starch, similar to other cereals, is classified as A-type polymorphism, which exhibits several diffraction reflection peaks located at 2θ = 10.1° and 2θ = 11.5°, an intense peak centred at 2θ = 15.2°, a double peak at 2θ = 17.3°/18.1° and a peak at 2θ = 23.2°. As mentioned in Chapter 1, during the gelatinization of starch, the existing crystalline structure is destroyed due to the diffusion of water into the granules and the solubilisation of the amylose leading to the disruption of the granule. As it could be observed, CSg35, CSi35 and CSpd35 plasticised starch materials showed considerably reduced crystalline area in their diffractograms with low intensity residual peaks located around 2θ = 20.0°, indicating that the three gelatinized materials were obtained successfully. Slight differences were obtained for each plasticiser in accordance with previous studies [13]. In our case, the intensity of the residual peak at around 20° was higher for the CSpd35 sample, which could indicate differences in the final crystalline arrangement and suggesting that less plasticisation degree was obtained when 1,3-propanediol was used.

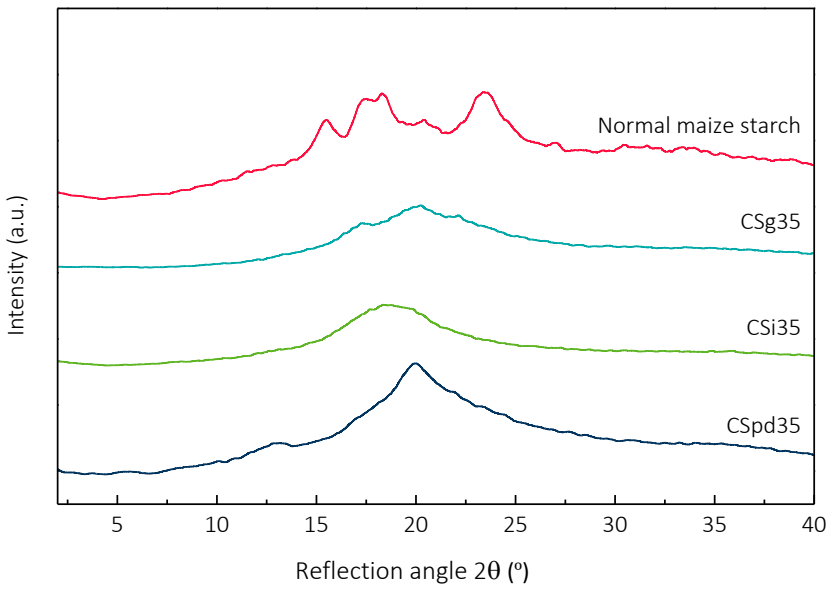

Figure 3.5 – XRD patterns of normal maize starch and PLS films.

3.4.2. Optical properties

From an industrial and commercial point of view, the measurement of the transmittance values is essential to evaluate the potentiality of the films as packaging materials. As reported by Castillo et al. [14], materials with low transmittance values could be interesting as they would improve the shelf life of packaged products preventing them from the oxidative degradation. Nevertheless, films with high light transmittance values could be valuable when the packaged foodstuffs is needed to be sanitized by UV light to reduce their antimicrobial charge [14]. Thus, the optical properties of the films obtained by solvent casting were evaluated by UV-vis spectroscopy measuring the transmittance value in the visible spectrum range (400 - 700 nm). Obtained results are shown in Figure 3.6.

As it could be noticed, the optical properties of the obtained PLS films were strongly influenced by the type of plasticiser. Films plasticised with glycerol and D-isosorbide presented higher transmittance and thus, higher transparency compared with those containing 1,3-propanediol. As it can be observed, when glycerol and D-isosorbide were used similar transmittance values (18.2% for CSg35 and 16.8% for CSi35 at 600 nm) were obtained in the visible scan range whereas for CSpd35 the transmittance value decreased to 9.2%.

These relatively low values of transmittance presented by all films could be related to the high plasticiser content employed for the gelatinisation (35 wt.% in all cases). Notwithstanding, similar results were obtained by Tomé et al. [15], i.e., transmittance values of 20% for gelatinised starch, even with lower glycerol content. As explained by Bertuzzi et al. [16], films opacity increases upon the addition of certain amount of plasticiser. On the other hand, the lower transmittance value obtained for the sample plasticised with 1,3-propanediol may indicate poorer compatibility between starch and 1,3-propanediol. Besides, as concluded from the XRD results in Section 3.4.1, different

crystalline arrangements found for CSpd35 samples could also be related to a less effectiveness during the gelatinisation process for this plasticiser.

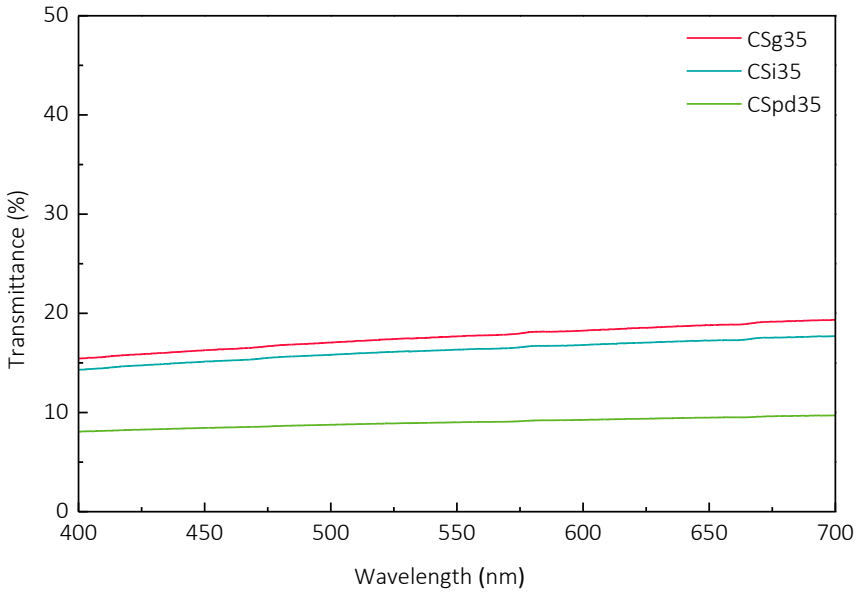

Figure 3.6 – UV-vis transmittance measurements of PLS films.

3.4.3. Surface properties

Static or dynamic contact angle assays are relevant techniques when referring to the study of the hydrophobicity of the materials. In this case, dynamic contact angle measurements (advancing and receding) with needle-in drop technique were performed in order to analyse the effect of the plasticiser on the wettability of PLS films. In all cases, ethylene glycol was used instead of water due to the impossibility of measuring the angle due to the high hydrophilicity of the films. The results are presented in Figure 3.7.

The results indicate that the advancing contact angle value (θ_a) was higher than receding contact angle value (θ_r) that working with polar liquids are associated to the interactions with the dispersive and polar groups on the surface, respectively [17]. The influence of the chemical structure of the plasticiser on surface properties of PLS was clearly appreciated. As it could be observed, CSi35 films presented the highest contact angle values, revealing the lowest wettability of the

material and, hence, the lower surface energy value. Lower contact angle values were observed for both CSg35 and CSpd35 samples. Both glycerol and 1,3-propanediol plasticised films showed similar contact angle values, although the measurements were sometimes erratic for the latter. Different interactions between the liquid and the surface are responsible of the contact angle hysteresis, i.e. the number of polar and dispersive interactions between the liquid and the surface, the surface roughness or the chemical heterogeneity [17]. It is generally assumed that the advancing contact angle is similar to the static angle when using polar liquids and higher than the dynamic receding angle. From the obtained results, homogeneous large polar surface in case of glycerol could be concluded with both advancing and receding low angle values, whereas significant contribution of dispersive groups was observed in the case of D-isosorbide plasticised PLS films attending to the higher value of the advancing angle as well as large hysteresis observed.

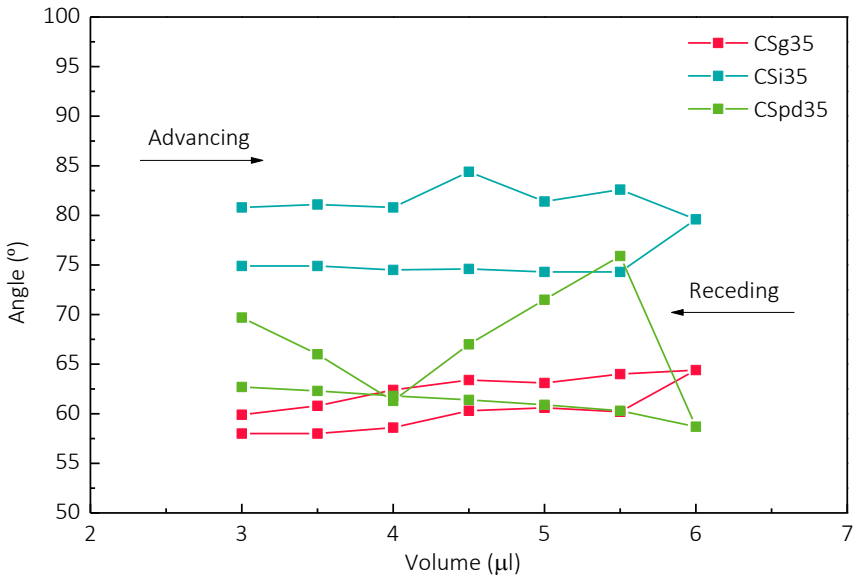

Figure 3.7 – Advancing and receding contact angle measurements of PLS films.

3.4.4. Dynamic mechanical analysis

In order to evaluate the viscoelastic behaviour and determine the temperature of the main relaxations for each film, DMA measurements were performed. The evolution of the normalised

storage modulus (E'/E'$_g$) (where E'$_g$ corresponds to the experimental storage modulus at -100 °C) and tan δ with temperature are presented in Figure 3.8.

All samples showed two-step modulus drop related to the temperature of the tan δ peak, which are commonly associated with the relaxation temperatures of the plasticiser-rich phase ($T_{\alpha 1}$) and the starch-rich phase ($T_{\alpha 2}$) [8,18,19]. As it could be observed, the relaxation temperatures associated with the plasticiser-rich domains were highly dependent on the type of plasticiser. Temperatures of -70 °C, -63 °C and -30 °C were measured for the maximum of tan δ for CSpd35, CSg35 and CSi35 samples, subsequently. However, it is worth noting that the two main relaxations were largely separated in case of 1,3-propanediol, closer one to each other in case of glycerol and almost overlapped in case of D-isosorbide. Those findings would be indicating that the mentioned biphasic organisation of the plasticised starch was not at the same scale in all cases, going from clearly separated phases for the CSpd35 to almost monophasic organisation for the CSi35. Those results are in agreement with the lower transmittance values measured for the CSpd35 film.

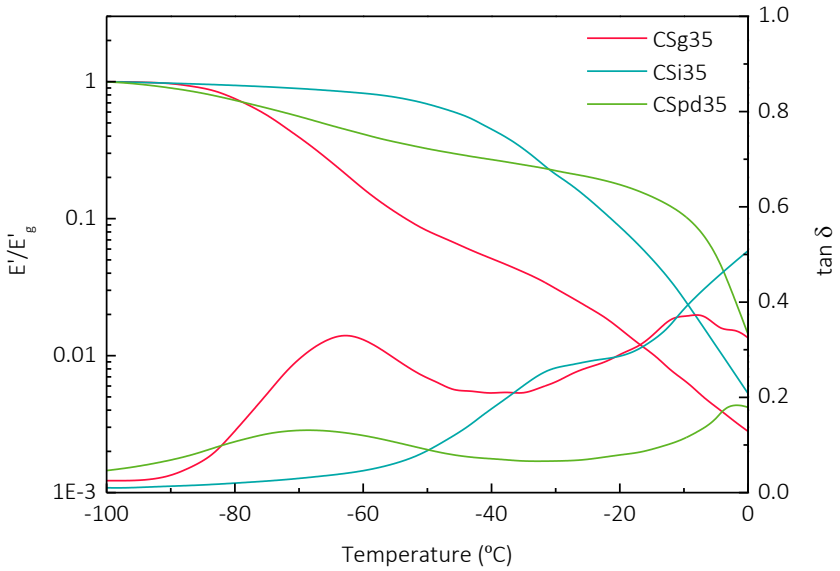

Figure 3.8 – Evolution of E'/E'$_g$ and tan δ with temperature of PLS films.

3.4.5. Mechanical properties

Tensile tests were carried out to assess the mechanical behaviour of PLS films. The obtained results are collected in Figure 3.9. As it has been demonstrated in literature, when solely temperature and water are used to obtain gelatinised starch, the final material is too brittle. As reported in literature [16,20,21], the addition of plasticisers improves the flexibility and the processability of starch-based materials due to their capability to reduce the intermolecular hydrogen bonds between starch chains and increase the free volume, while enhancing the mobility of the polymeric chains. The new starch/plasticiser intermolecular forces formed after the gelatinisation decrease the final T_g value obtaining a processable material [22].

As expected, the tensile properties of the obtained films were highly dependent on the employed plasticiser. It is worth noting that decisive variables in terms of mechanical performance such as the relative humidity and the storage time [23,24] were the same in all cases and thus, molecular weight, chemical structure or hydrophobicity of the plasticiser would be determinant in the obtained results. As it can be observed, clear initial differences were found when comparing glycerol and 1,3-propanediol with D-isosorbide, with a higher Young's modulus value for the latter. The higher molecular weight and the cyclic chemical structure of D-isosorbide seem to be the responsible of the higher stiffness measured for CSi35. Furthermore, the films plasticised with D-isosorbide presented the highest strength values, followed by those with glycerol, while those containing 1,3-propanediol showed the weakest behaviour. In addition, it was observed from Figure 3.9 that the use of D-isosorbide results in remarkable high strain at break values that, along with the increased strength and Young modulus, resulted in exceptional toughness improvement for CSi35.

The results confirmed the previously argued good affinity between the starch and the D-isosorbide since the mechanical response could be attributed to the effective interfacial hydrogen bonding interactions [21].

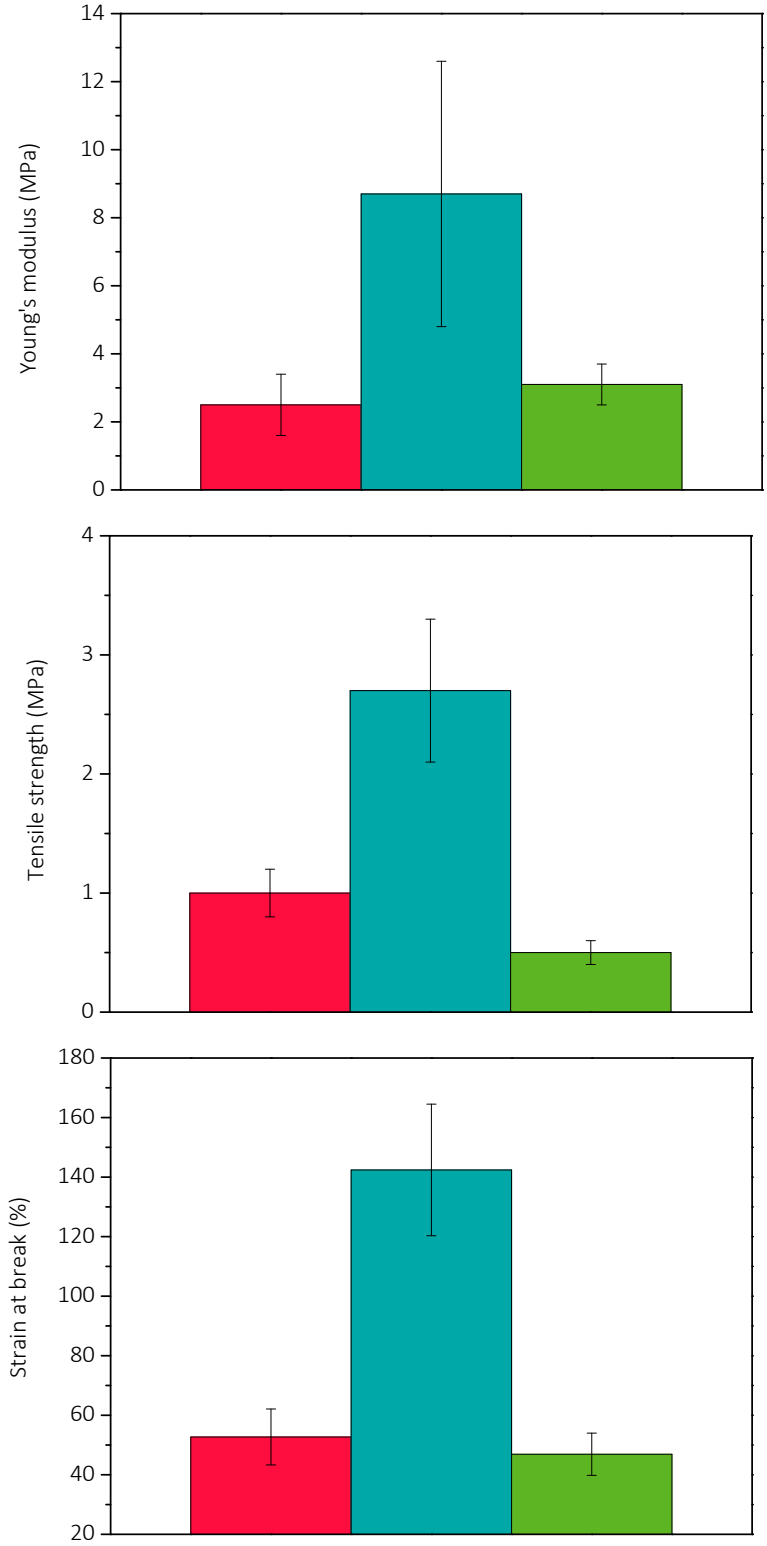

Figure 3.9 – Mechanical properties of ■ CSg35, ■ CSi35 and ■ CSpd35.

3.4.6. Barrier properties

The gas and water vapour transport through the films was measured in order to analyse the influence of the plasticiser in the barrier properties. It is well known that polysaccharide based films have good barrier properties to gases (O_2, CO_2), whereas they present poorer behaviour against water vapour [16,20]. Water vapour and oxygen permeability (WVP and OP) values were calculated according to Equations 2.8 and 2.9.

WVP and OP results are collected in Table 3.3. Focusing firstly on WVP, high permeability values were obtained for all samples with little differences between them. The transport of the vapour molecules across the film is known to be governed by both diffusion and solubility phenomena [25], related to the ability of water molecules to penetrate through the film and to the degree of polymer/water interaction, respectively. The use of plasticisers in polymers increases the free volume fraction between the chains of the macromolecule, thereby increasing the diffusion coefficient. Moreover, the good affinity and H-bonding interactions between the starch and the plasticiser with water lead to increased solubility coefficient [16,21,25,26]. Moreover, factors such as polarity and structural features of polymeric side chains, hydrogen bonding characteristics, molecular weight and polydispersity, degree of branching or cross-linking, processing methodology and degree of crystallinity would affect the solubility and diffusivity coefficients and thus the permeability of the material [27]. The similarity of the values obtained for the WVP in all samples indicates that probably, in the case of PLS films, the high solubility of water is governing the whole transport process, not being dependent on the quality of the interactions between the starch and the plasticiser.

On the contrary, significant differences were observed in terms of the OP values. It should be noted the low OP value obtained for films plasticised with D-isosorbide. According to the mentioned free volume increasing effect of plasticisation, the results seemed to indicate that it was

lower for the D-isosorbide containing films. In this case, the permeability decrease could be indicating that the path for the diffusion of the oxygen small molecules was harder, thus concluding higher interaction degree between the starch and the plasticiser. This conclusion is in agreement with the observed main relaxation transitions in the DMA indicating that D-isosorbide presented the greater compatibility with starch. On the contrary regarding to samples plasticised with 1,3-propanediol, significantly higher OP values were observed what could be associated with a previously observed worse compatibility between the starch and the plasticiser.

Table 3.3 – Barrier properties of PLS films.

Sample	WVP (kg m m^{-2} s^{-1} Pa^{-1}) x 10^{13}	OP (cm^3 mm m^{-2} day^{-1} atm^{-1})
CSg35	6.8 ± 0.6	3.7 ± 0.1
CSi35	6.0 ± 0.6	0.5 ± 0.0
CSpd35	8.5 ± 0.6	10.9 ± 0.1

3.4.7. Thermogravimetric analysis

TGA was performed in order to study the influence of different plasticisers on the thermal stability of the PLS films. The thermal degradations behaviour of raw plasticiser and resulting films as well as the water content of the films are shown in Figures 3.10 and 3.11 and Table 3.4, respectively.

For comparison purposes, TGA of plasticisers was firstly performed. As shown in Figure 3.10 the thermal decompositions of 1,3-propanediol, glycerol and D-isosorbide showed a single degradation step at around 160, 230, and 242 °C, respectively.

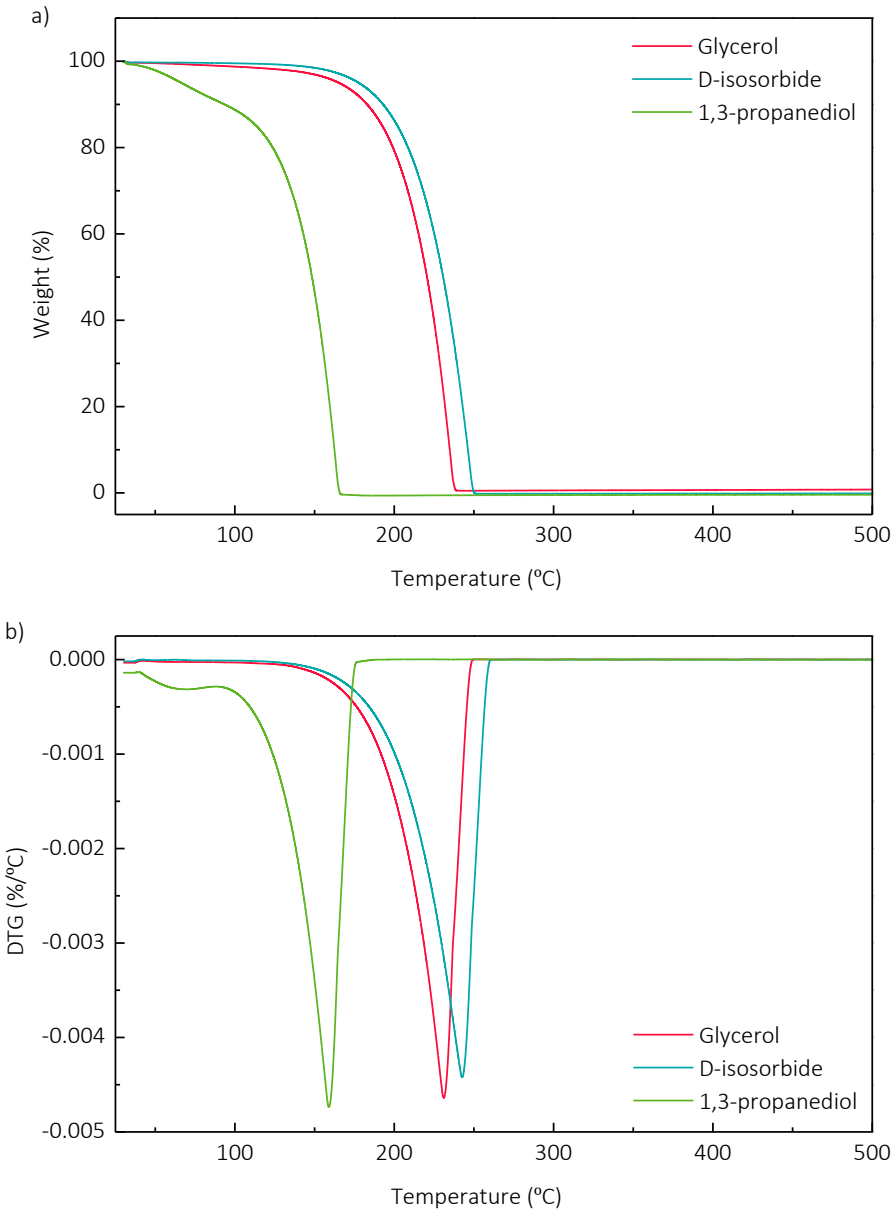

Figure 3.10 – a) TG and b) DTG curves of raw plasticisers.

Regarding the PLS films, results showed that thermal degradation of starch-based films was influenced by the used plasticiser, especially during the first degradation steps. The degradation pattern of glycerol-plasticised starch films under nitrogen atmosphere has been widely studied and it is generally accepted to involve three main mass-loss steps [8,28], i.e., 1) the loss of the humidity (25 - 100 ˚C), 2) the decomposition of the glycerol-rich phase (100 - 200 ˚C) and 3) the oxidation of the partially decomposed starch (around 340 ˚C). In our case, glycerol plasticised samples presented the

above mentioned three steps pattern, whereas D-isosorbide and 1,3-propanediol containing films presented some relevant differences. On the one hand, for CSpd35 sample, below 200 °C the mass loss occurred gradually in a broad range that may include the two steps at lower temperatures where the degradation appeared practically overlapped and the onset of the main degradation step was slightly shifted to higher temperatures. On the other hand, the degradation of CSi35 film proceeded in two main steps. The first one near 100 °C and, after that, the decomposition presented a unique step, which covered the range between 170 °C and 370 °C. It is worth noting that even if the plasticiser content was the same, in this case, the film maintained the thermal stability almost until the main degradation step, close to 300 °C. The results obtained are in agreement with the scarce literature reported for D-isosorbide/starch blends, obtained by extrusion [29].

Rico et al. [30] investigated the effect of different polyols as plasticisers for starch and concluded that the thermal stability of PLS increased with the molecular weight of the plasticiser and it is also well known that the thermal stability of starch based materials would be affected by the humidity content [31] that comes determined by starch/plasticiser interaction degree. The moisture contents calculated from the TG curves in the PLS are presented in Table 3.4. These results showed that D-isosorbide sample presented the lower moisture content value. Avérous and Pollet [19] stated that depending on the nature and content of the plasticiser different interactions would take place in the systems. When the starch/plasticiser interactions are strong, the plasticiser occupies specific sorption sites and the water content decrease. Thus, the higher water content of samples plasticised with 1,3-propanediol could be related to a poor interaction between the polysaccharide chains and the plasticiser [19]. For 1,3-propanediol and glycerol containing samples, the second degradation step matched with the vaporization temperature of the pure plasticisers, 160 ºC and 230 ºC, respectively. On the contrary, the samples plasticised with D-isosorbide presented better stability until higher temperatures, being not appreciable in this case any degradation steps corresponding to plasticiser rich domain. Those results could be indicating larger homogeneity of the samples

plasticised with D-isosorbide in comparison with the glycerol and the 1,3-propanediol. These results corroborated the conclusions obtained by UV-vis spectroscopy, DMA measurements and OP values.

Finally, no differences were observed in terms of the residue percentage due to the plasticiser nature, which was close to 10% in all cases.

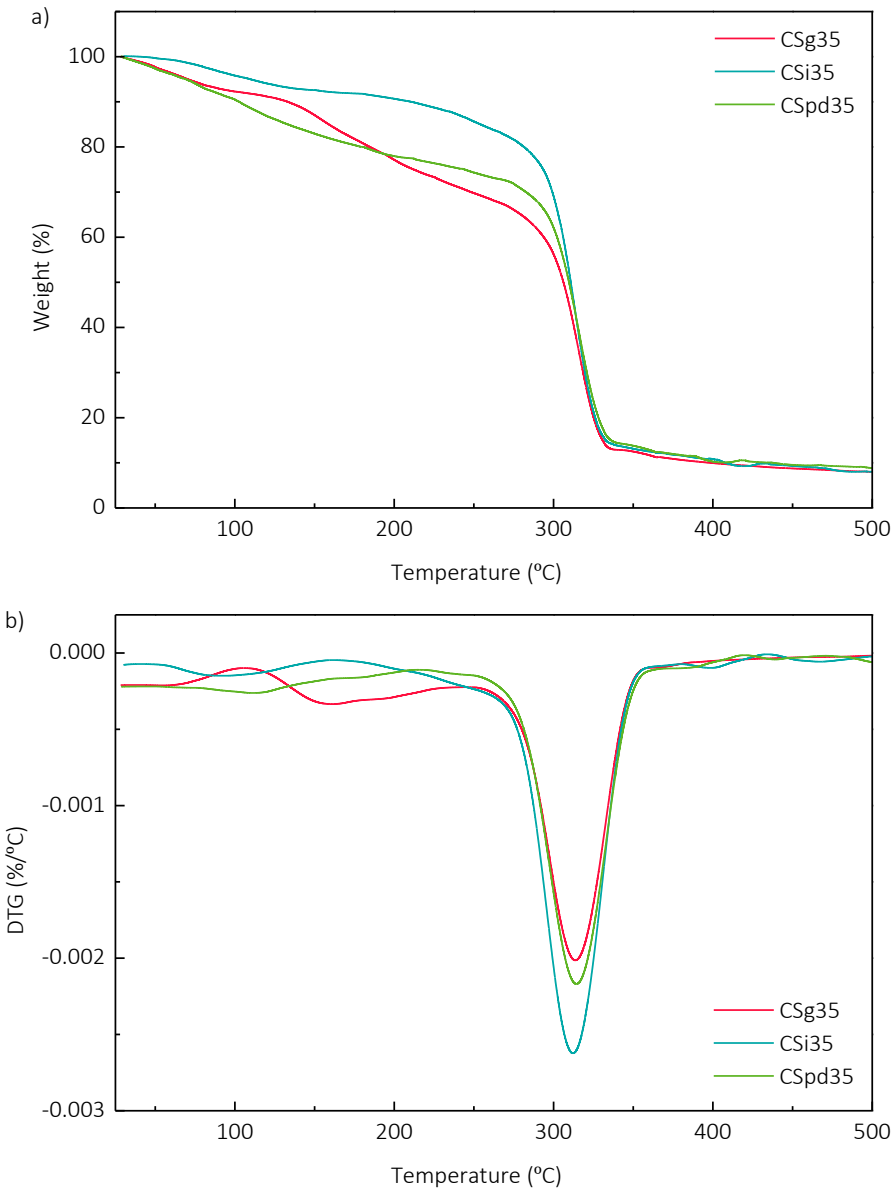

Figure 3.11 – a) TG and b) DTG curves of PLS films.

Table 3.4 – Moisture content of PLS films.

Sample	Moisture content (%)
CSg35	7.68
CSi35	4.71
CSpd35	10.23

3.4.8. Morphological characterisation

The morphological characteristics of all samples and the influence of the plasticiser on the topography of the samples were investigated by AFM. Obtained images are presented in Figure 3.12.

It could be observed that AFM images of all samples presented a two-phase microstructure clearly distinguishable by their different roughness. Unfortunately, few works have been reported in literature related to phase distribution and morphological features of starch-based materials by AFM [32–35]. Among them, Thiré et al. [34] used the AFM to follow the gelatinization process of maize starch suspensions with glycerol. They also observed the mentioned two different regions or domains and, as shown in Figure 3.12 (a - c) (whole surface, 25 μm × 25 μm), smoother regions surrounded by rougher domains appeared. As it could be noted in some of the images of the whole surface, the shape of the surrounding rougher area was almost perfectly polyhedral, which could be attributable to the original shape of the starch granules before their disruption [34]. Rindlav-Westling and Gatenholm [36] investigated amylose and amylopectin films by AFM and concluded that the rougher zones presented in the starch films were attributable to amylose, due to its semi-crystalline nature, whereas the smoother regions were mainly amylopectin domains. The images obtained deeper into each region (Figure 3.12 (a - c), smooth and rough regions, 3 μm × 3 μm) showed the detailed features of the aforementioned domains: in the three cases smooth regions showed two different zones, that appeared darker and lighter in the AFM phase images caused by their lower and higher rigidity, respectively. Those rigidity differences were not distinguishable in the rougher areas.

Regarding the roughness of the films, those plasticised with 1,3-propanediol presented the highest values (R_q = 356 nm against R_q = 281 nm and R_q = 205 nm for the CSg35 and CSi35 samples, respectively). As it can be observed in Figure 3.12 (c) (rough region), 1,3-propanediol samples presented more fibrillary appearance in the rough domain that could contribute to the whole roughness measurement.

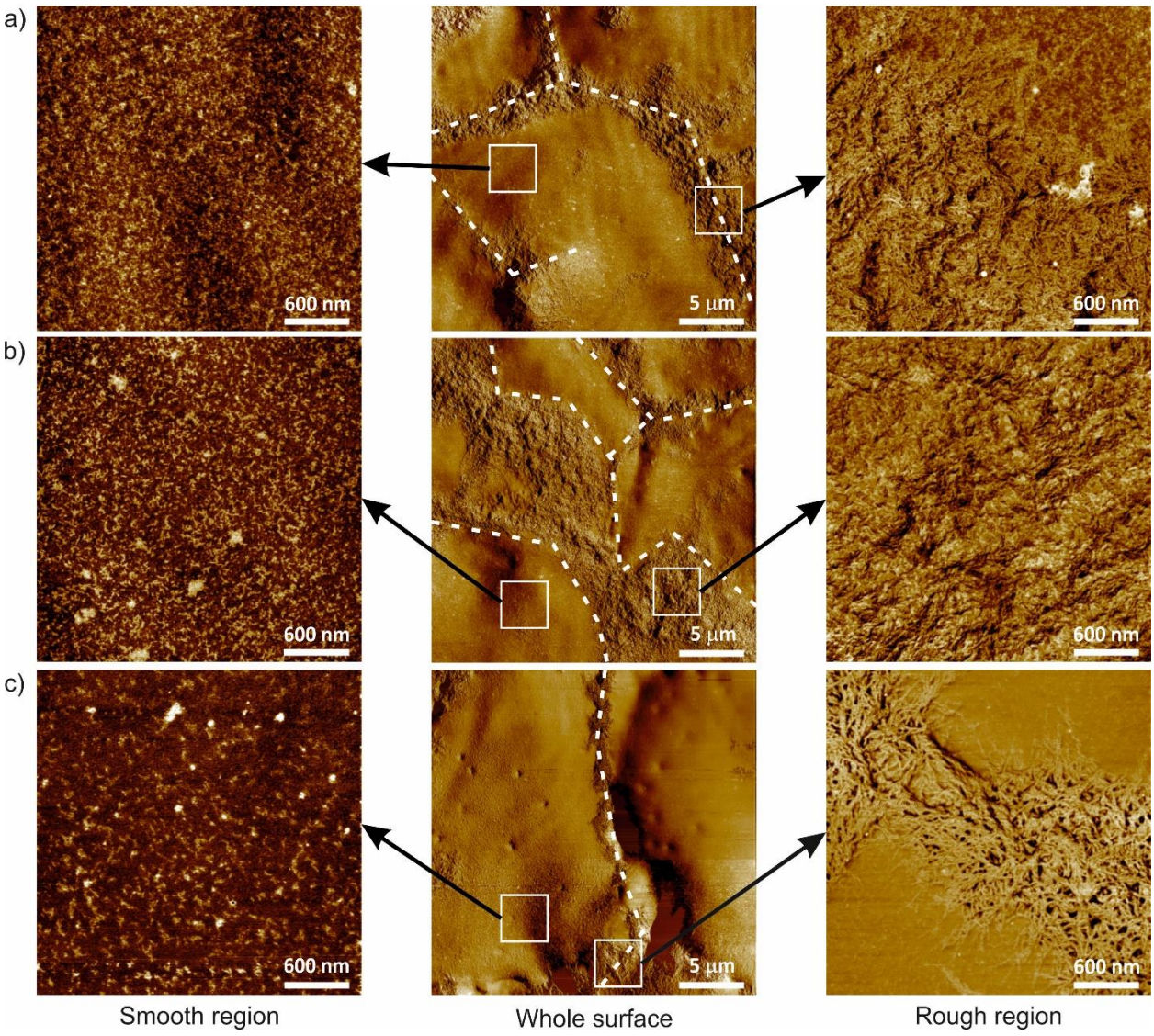

Figure 3.12 – AFM height images of a) CSg35, b) CSi35 and c) CSpd35 films.

3.5. EFFECT OF THE PLASTICISER ON THE PROPERTIES OF TPS FILMS

Considering an industrial point of view, extrusion and compression techniques were selected as appropriate manufacturing methods. TPS films were prepared adding glycerol, D-isosorbide and 1,3-propanediol in order to obtain materials with promising properties and scale-up productions. The influence of the nature of the plasticiser and the manufacturing technique on the physico-chemical, thermal, mechanical and barrier properties of the resulting materials was evaluated.

3.5.1. X-ray diffraction

The effectiveness of the plasticisation was analysed by XRD diffraction. The obtained XRD patterns are shown in Figure 3.13.

As it could be observed, the initial A-type crystalline structure was destroyed due to the thermomechanical energy applied to the starch/water/plasticiser mixture during the process. ESg35, ESi35 and ESpd35 starch materials showed considerably reduced crystalline area in their diffractograms with low intensity residual peaks centred at $2\theta = 19^{\circ}$, $2\theta = 18^{\circ}$ and $2\theta = 21^{\circ}$, respectively, indicating that the three materials were obtained successfully.

The peak located at $2\theta = 19^{\circ}$ that appeared in glycerol containing samples and that is usually accompanied by another one at $2\theta = 13.3^{\circ}$, is normally attributed to Vh-type crystalline structure, commonly resulted as a consequence of the shear stress during the thermomechanical processing [29]. However, in the case of ESi35, the peak was located at $2\theta = 18^{\circ}$, which is related to the Eh-type crystalline structure, and it is formed generally when starch is processed at higher shear stress than that necessary to form Vh-type. This finding was also observed by other authors [29] and could indicate the great ability of D-isosorbide to plasticize starch even at low processing temperatures.

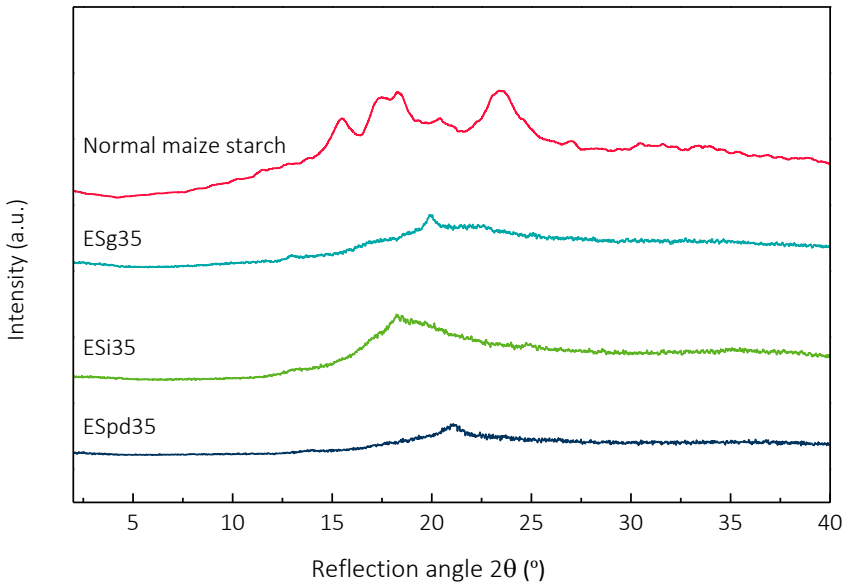

Figure 3.13 – XRD patterns of normal maize starch and TPS films.

3.5.2. Optical properties

The transparency of extruded TPS samples was studied by UV-vis spectroscopy. Results are shown in Figure 3.14. As it could be observed, remarkable differences were observed on the transmittance value between the three TPS indicating the notable influence of the plasticiser. As commonly occur, the transmittance value increased in all cases as the wavelength increases [37]. However, films plasticised with D-isosorbide showed much higher transmittance values (65.0%) compared with those plasticised with glycerol and 1,3-propanediol (36.5% and 35.8%, respectively).

Besides, it is worth noting that the transmittance values showed by melt processed samples were in all cases higher than those obtained for PLS films (Section 3.4.2) i.e. 18.2% for CSg35, 16.8% for CSi35 and 9.2% for CSpd35. Moreover, although the transparency of the films would be influenced by the thickness [38], the mentioned differences noticed in this study could not be attributable to this factor since the thickness of films obtained by solvent casting were close to those processed by extrusion/compression. Therefore, it could be concluded that the shear stress to which the material is subjected during the extrusion process, resulted in significant improvement in terms

of starch/plasticiser compatibility due to the thermomechanical processing step, leading to enhanced transparency properties.

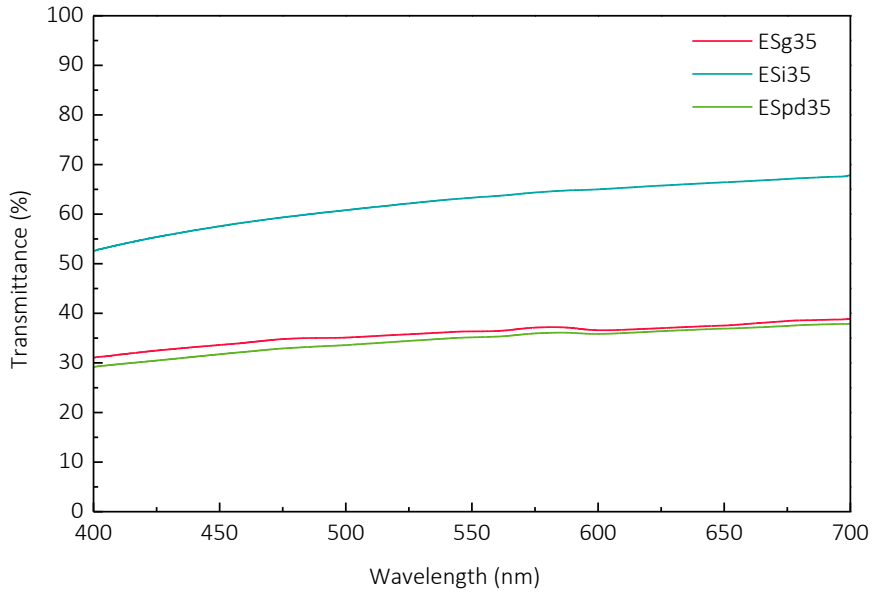

Figure 3.14 – UV-vis transmittance measurements of TPS films.

3.5.3. Dynamic mechanical analysis

DMA analysis was performed to evaluate the main relaxation temperatures of TPS films plasticised with glycerol, D-isosorbide and 1,3-propanediol. The evolution of the normalised storage modulus (E'/E'_g) and tan δ with temperature is presented in Figure 3.15.

As could be observed, samples plasticised with glycerol and 1,3-propanediol showed the two-step modulus drop related to the relaxation of the plasticiser-rich phase ($T_{\alpha 1}$) and the starch-rich phase ($T_{\alpha 2}$) almost at the same temperatures than that for the PLS films [18,39,40]. On the contrary, the TPS films obtained with D-isosorbide presented a different viscoelastic pattern, with a single broad modulus drop at significantly higher temperatures. The results would indicate that higher degree of miscibility had been achieved in case of the ESi35 by comparing with its PLS counterpart, CSi35, where even though the two main transitions were overlapped, they were distinguishable. The

evidence of a single-phase homogeneous material explained the significantly increase of the transmittance values obtained for the TPS in comparison with the same PLS sample.

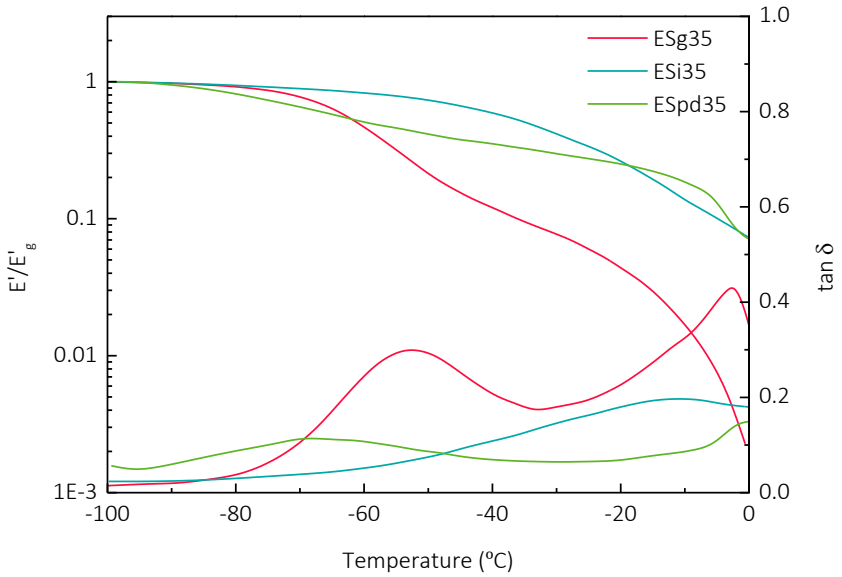

Figure 3.15 – Evolution of E'/E'$_g$ and tan δ with temperature of TPS films.

3.5.4. Thermogravimetric analysis

The thermal degradation of extruded TPS films was evaluated by TGA. Figure 3.16 shows the TG and DTG curves obtained for ESg35, ESi35 and ESpd35 films.

As it could be observed, the thermal degradation of extruded starch-based films was influenced by the nature of the plasticiser. The results showed the same patterns as PLS films. It is worth noting the reduced moisture content of ESi35. Comparing CSpd35 and ESpd35, in the case of ESpd35 sample, a lower weight loss is observed in the second degradation step related to the plasticiser. This fact could suggest that during the extrusion and compression steps the plasticiser was lost, since at high temperatures the 1,3-propanediol could be evaporated or degraded (see Figure 3.10).

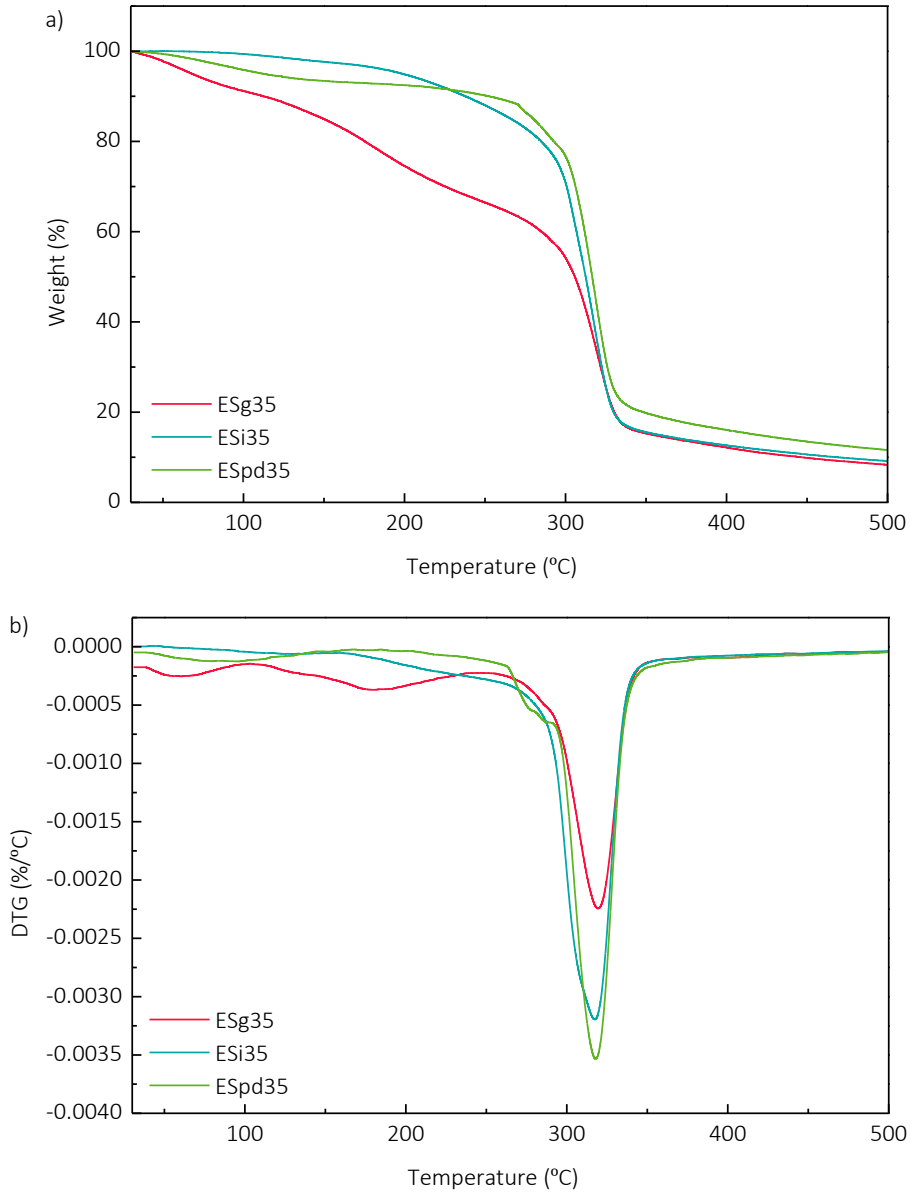

Figure 3.16 – a) TG and b) DTG curves of TPS films.

3.5.5. Mechanical properties

The influence of the plasticiser on the mechanical behaviour of the extruded films was evaluated by tensile test measurements. The results of all samples are collected in Figure 3.17. The stress-strain values of PLS films (Section 3.4.5) are also represented for comparative purposes.

As in the case of PLS films, the overall mechanical behaviour of the material was strongly affected by the plasticiser type and significant differences were observed, mainly in the case of using

1,3-propanediol. Indeed, the Epd35 film showed the highest Young's modulus and tensile strength values, while presented extremely low strain at break value typical of brittle materials. These results suggest that no effective plasticisation was achieved in TPS films plasticised with 1,3-propanediol, which could be attributed to the evaporation or degradation of 1,3-propanediol during the extrusion or compression steps. On the contrary, the films containing glycerol and D-isosorbide showed better overall mechanical performance. Comparing both samples tougher and stiffer mechanical behaviour was observed for the latter. In fact, the Young's modulus of ESi35 was found to be close to 5 times higher than that for ESg35 with considerably higher values of elongation at break. From the results it could be concluded that D-isosorbide led to the most effective plasticisation, whereas non expected poor behaviour was obtained with 1,3-propanediol.

By comparing the obtained TPS films with those prepared by solvent casting, it could be noticed that the thermomechanical processing led to stiffer materials with higher tensile strength values and less elongation at break capacity. Attending to the results observed for 1,3-propanediol, it could be concluded that the mechanical behaviour is strongly influenced by the films preparation conditions, since the extrusion and compression temperatures of TPS is too close to the evaporation or degradation temperatures of 1,3-propanediol. Thus, 1,3-propanediol was not an effective plasticiser for TPS, while could be suitable for PLS films. These results agreed with TGA conclusions, corroborating that the evaporation or degradation of 1,3-propanediol during the extrusion and compression processes resulted in a less plasticisation effect leading to a poor mechanical behaviour.

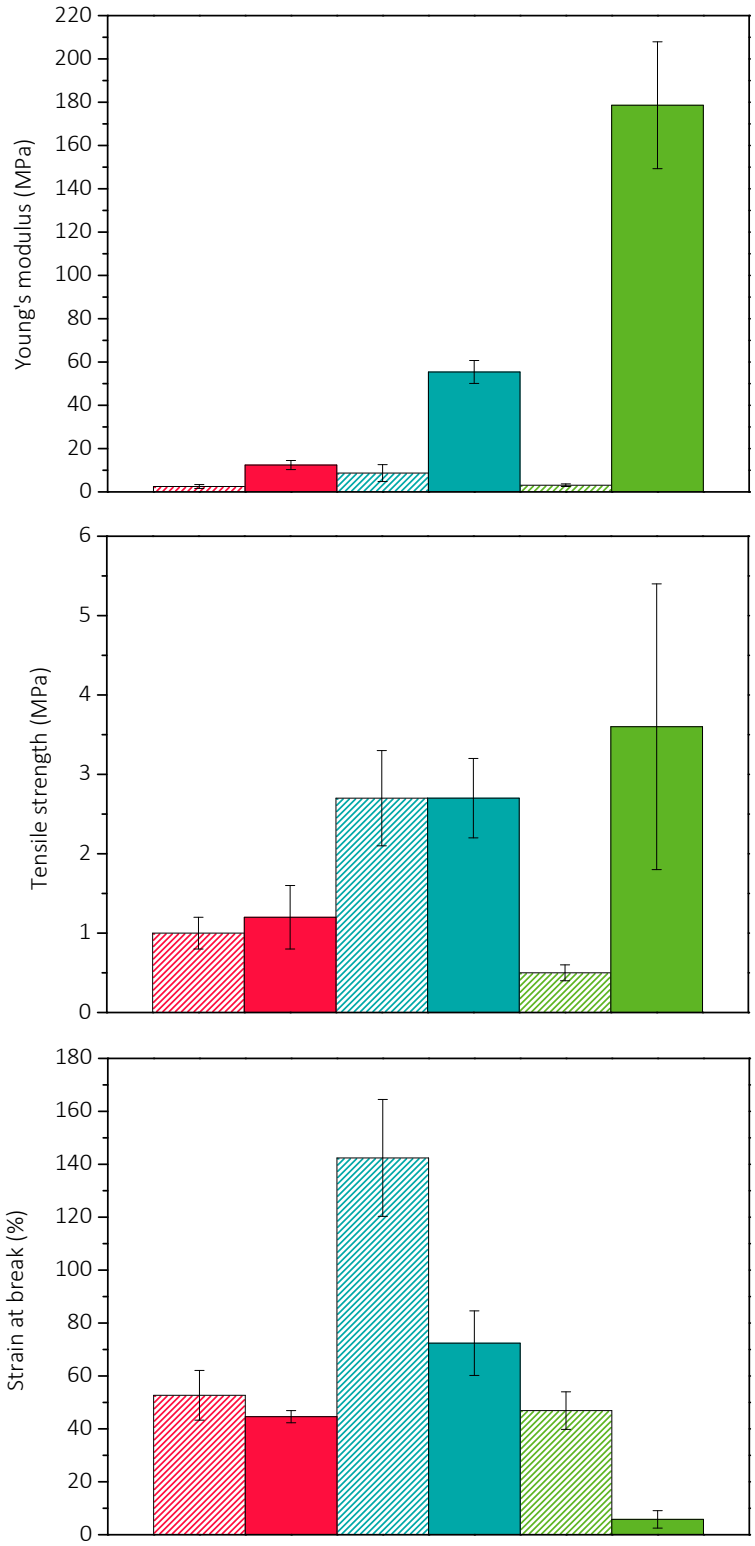

Figure 3.17 – Mechanical properties of films plasticised with ■ glycerol, ■ D-isosorbide and ■ 1,3-propanediol obtained by solvent casting (striped pattern) and extrusion/compression (filled pattern).

3.5.6. Barrier properties

The barrier properties of the different starch-based extruded materials were also investigated gravimetrically by evaluating the oxygen and water vapour transport through the films. The results are summarised in Table 3.5. ESpd35 sample resulted extremely brittle and, unfortunately, the characterisation of the barrier properties was not possible in that case.

The results presented for casted films (Section 3.4.6) demonstrated that the WVP was mainly governed by the high ability of water molecules to interact and penetrate through the film because of the strong starch/water affinity, and thus was independent on the quality of starch/plasticiser interactions. It has also taken into account that the plasticiser content is also a critical factor in barrier properties [41]. The results obtained for the TPS were similar to those obtained by solvent casting for the same plasticisation compositions showing no relevant differences regarding the WVP with different plasticisers. WVP values of (8.3 ± 1.5) x 10^{-13} and (10.9 ± 3.7) x 10^{-13} kg m m^{-2} s^{-1} Pa^{-1} were measured for ESg35 and ESi35, respectively. On the contrary, the OP was again found to be strongly influenced by the plasticiser used, and near twenty times lower OP value was obtained for ESi35 comparing to that for glycerol plasticised one. OP values of 10.9 ± 3.5 and 0.6 ± 0.3 cm^3 mm m^{-2} day^{-1} atm^{-1} were measured for ESg35 and ESi35, respectively. The improvement of the OP was explained by the reduced amount of free volume introduced during the plasticisation with D-isosorbide, resulting from the strong interactions between the plasticiser molecules and the polymeric chains and, at the same time, the reduced mobility of the cyclic chemical structure of the plasticiser.

3.6. EFFECT OF RETROGRADATION ON THE PROPERTIES OF PLS FILMS

The retrogradation involves the reorganisation and recrystallization of amylose and amylopectin chains immediately after the gelatinization and during the storage time, affecting the mechanical behaviour of starch-based films and, therefore, compromising the applicability of the

material [37,42]. Considering the importance of retrogradation in the evolution of the properties of starch-based materials, the characterisation of the films was repeated after certain storage time in order to evaluate the effect of the plasticiser type on the retrogradation degree. Thus, the PLS films obtained by solvent casting (Section 3.2.1) were allowed to age for four weeks since gelatinization.

3.6.1. Optical properties

In order to analyse the evolution of the optical properties, UV-vis tests of all samples were repeated over aged samples (2 weeks after the characterisation of fresh films). The results are shown in Figure 3.18. The transmittance values of aged films were found to be the same of those measured with non-aged samples. The obtained results are agreed with that reported by Jiménez et al. [43], where it was concluded that retrogradation process did not affect the optical properties of the starch films.

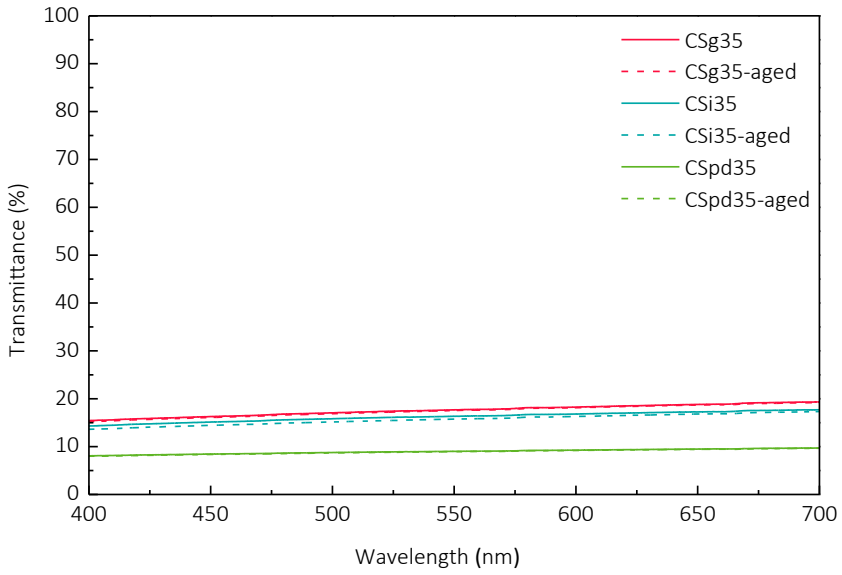

Figure 3.18 – UV-vis transmittance measurements of PLS (continuous lines) and aged films (dotted lines).

3.6.2. Surface properties

The influence of the retrogradation in the surface properties was analysed in terms of the evolution of the dynamic contact angle (Figure 3.19). As noticed, significant differences were observed due to the retrogradation of the films. Indeed, the contact angle values of samples

plasticised with glycerol and 1,3-propanediol increased significantly after storage time, mainly in CSg35-aged films. On the contrary, contact angle values for CSi35 decreased after retrogradation. The retrogradation of the PLS is usually assumed to be consequence of the alignment of the amylose chains and the partial recrystallization of amylopectin and, according to our results, it seemed to affect significantly the surface energy of the films. Therefore, remarkable influence could be noticed for the glycerol and 1,3-propanediol containing samples, whereas the use of D-isosorbide as plasticiser seemed to reduce the impact of this phenomenon. Avérous and Pollet [19] reported that the retrogradation of starch-based materials is strongly influenced by the T_g, since lower values indicate higher mobility of the polymeric chains and, hence, facilitates the reorganisation [19].

As it was demonstrated by DMA measurements in Section 3.4.4, the relaxation temperatures associated with the plasticiser-rich domains ($T_{\alpha 1}$) were highly dependent on the type of plasticiser. Relaxation temperatures of -70 °C, -63 °C, and -30 °C were measured for the maximum of tan δ for CSpd35, CSg35, and CSi35 samples, subsequently. At room temperature, retrogradation involves the rearrangement of the polysaccharide chains [19]. Thus, the mobility of the starch chains located in the plasticiser rich domains was higher in samples plasticised with 1,3-propanediol and glycerol compared with CSi35 sample. Therefore, the retrogradation may occur in a greater extent leading to significant variations of the contact angle measurements for CSpd35 and CSg35 materials. However, plasticiser migration effects have to be considered during the storage time of the films [44]. As it could be appreciated in the Figure 3.19, the increase in the contact angle of the CSg35-aged films was considerable and, at the same time, the hysteresis between the advancing and receding angles increased. Attending to the results, the evolution of the molecules at the surface was evident in this case revealing the presence of highly dispersive interactions after retrogradation. On the contrary, the use of D-isosorbide as plasticiser for PLS led to higher stability of the surface properties of the films that maintained almost at the same value.

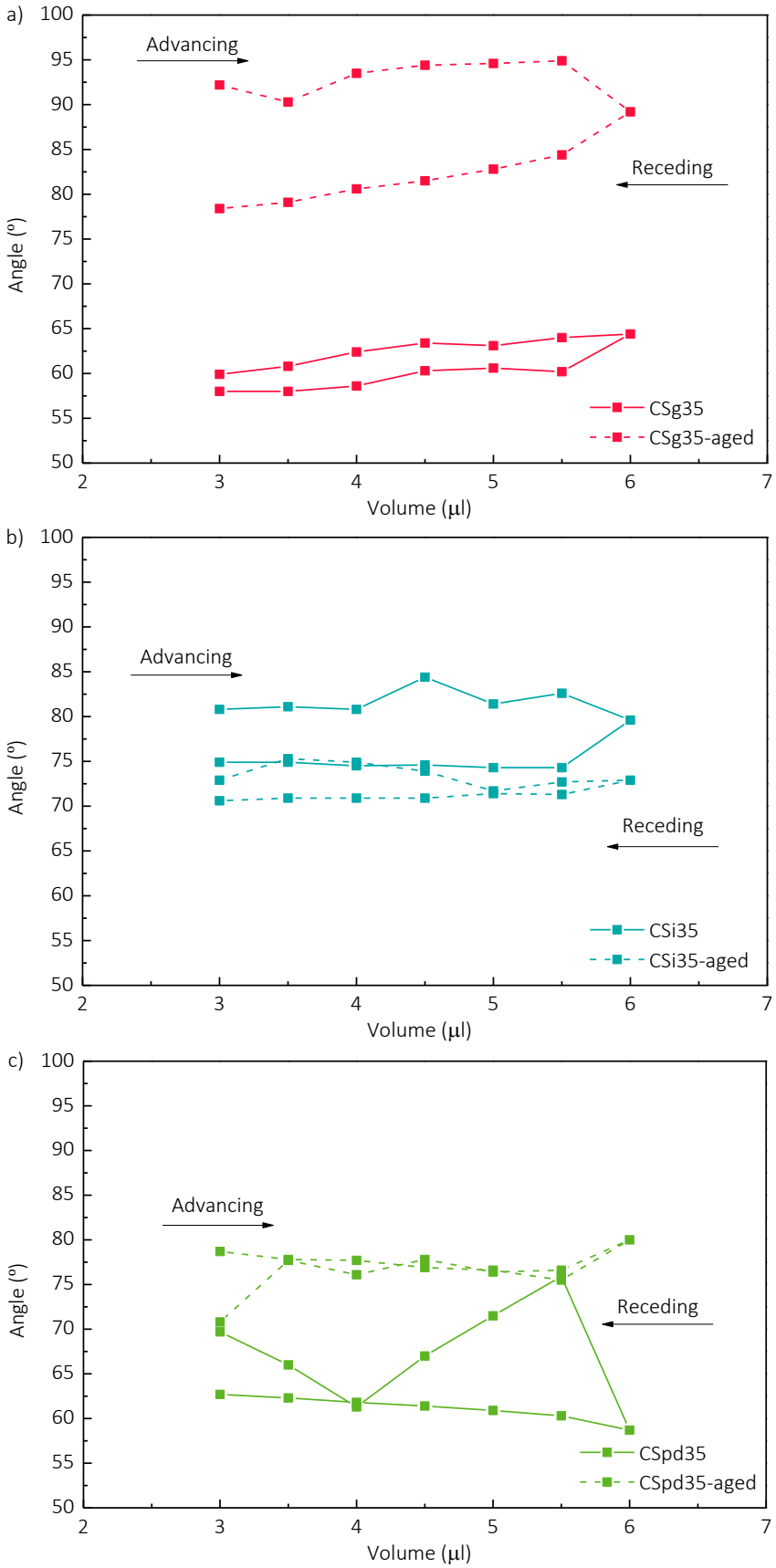

Figure 3.19 – Advancing and receding contact angle measurements of PLS films (continuous lines) and after aged (dotted lines).

3.6.3. Mechanical properties

The strengthening due to retrogradation was assessed repeating the tensile tests (Figure 3.20).

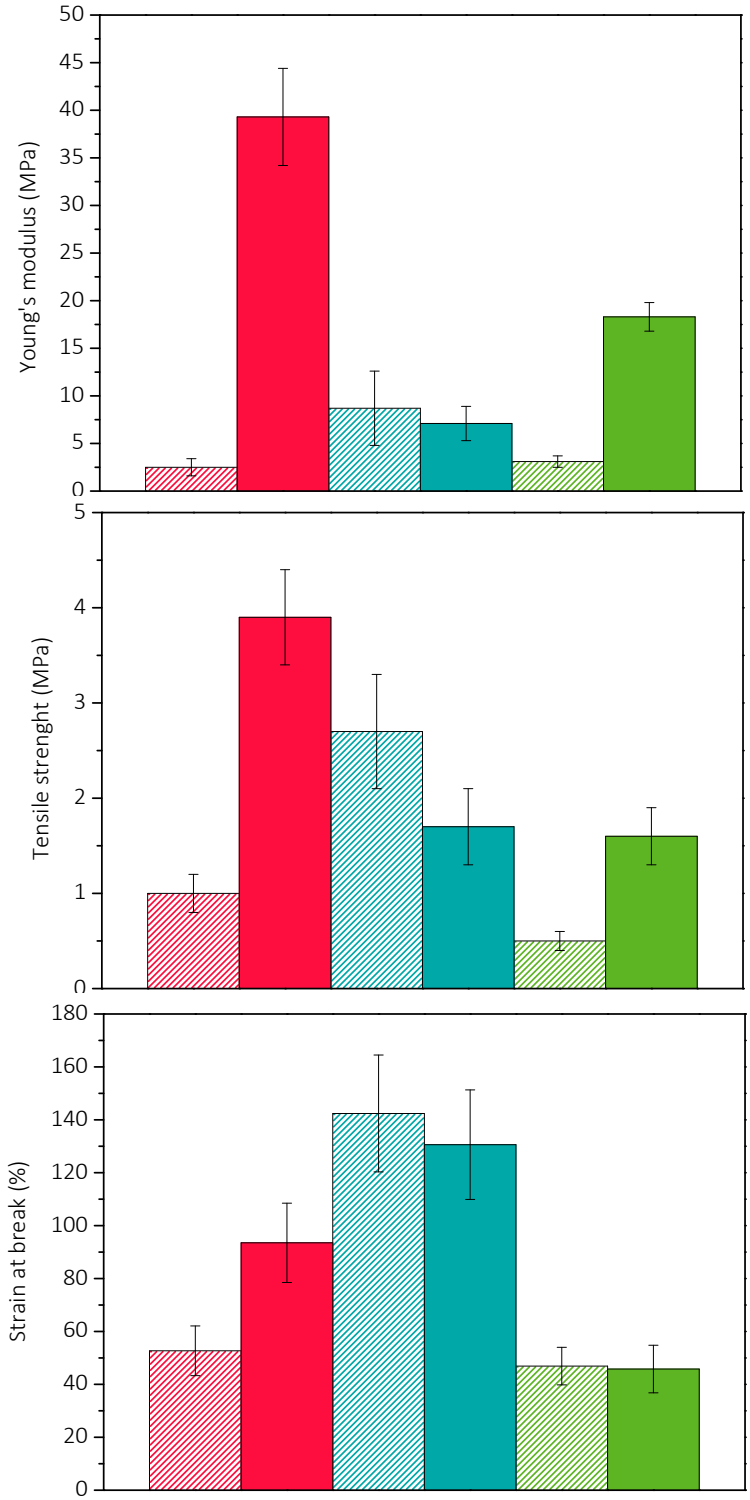

Figure 3.20 – Mechanical properties of PLS (striped pattern) and aged films (filled pattern) plasticised with ■ glycerol, ■ D-isosorbide and ■ 1,3-propanediol.

As it could be observed, significant increase in both the Young's modulus and tensile strength values were detected for CSg35-aged and CSpd35-aged samples, whereas CSi35-aged films did not show such variations on their mechanical properties. According to published literature [8,23,26], one of the major effects of the retrogradation of gelatinized starch is referred to be the strengthening of the material along with the increase in the Young's modulus value due to the reorientation and recrystallization that restricts the chain's mobility [23,30]. However, this general behaviour was not detected in the D-isosorbide plasticised films. These findings are in concordance with DMA results reported by Battegazzore et al. [29] for extruded starch plasticised with D-isosorbide. The stability of the mechanical properties along with the contact angle measurements also confirmed the lower degree of retrogradation in CSi35 samples.

3.6.4. Barrier properties

The effect of retrogradation on the barrier properties was evaluated by performing again the water vapour and oxygen transport measurements after the selected storage time. Results are shown in Table 3.6. As it was noticed, both WVP and OP were not influenced by the retrogradation phenomenon. As concluded in Section 3.4.6, the WVP was governed by starch/water interactions since the OP was dependent on the type of plasticiser. Although slight differences were observed, it seemed that the permeability values remained almost constant after the storage time.

Table 3.5 – Barrier properties of PLS films and after storage.

Sample	WVP (kg m m^{-2} s^{-1} Pa^{-1}) x 10^{13}	OP (cm^3 mm m^{-2} day^{-1} atm^{-1})
CSg35	6.8 ± 0.6	3.7 ± 0.1
CSg35-aged	6.4 ± 0.7	3.1 ± 0.3
CSi35	6.0 ± 0.6	0.5 ± 0.0
CSi35-aged	6.6 ± 1.1	0.3 ± 0.0
CSpd35	8.5 ± 0.6	10.9 ± 0.1
CSpd35-aged	7.1 ± 0.3	11.1 ± 0.6

3.6.5. Morphological characterisation

AFM images of aged samples were recorded in order to evaluate the evolution of the morphology due to the retrogradation of starch. Figure 3.21 shows images of CSg35-aged, CSi35-aged, and CSpd35-aged samples (3 μm × 3 μm). After the storage time, the two different regions above discussed were also observed, but more homogeneous general appearance and uniform roughness was appreciated. Those changes in the surface of the films might be related to the phase-reorganisation because of the retrogradation. As mentioned above, the alignment of the amylose is likely to occur almost immediately after casting and drying processes, but the recrystallization of the amylopectin needed longer storage times. Indeed, those smoother zones that were attributable to the amylopectin-rich domains presented enhanced roughness after the two weeks of storage. It is worth noting that phase images of the aged samples did not show lighter and darker zones as the non-aged samples did. This could be attributable to the retrogradation phenomenon, but it should be also considered that a certain degree of migration of the plasticiser to the surface could interfere in the indispensable good interaction between the tip and the surface, which could lead to resolution limitations.

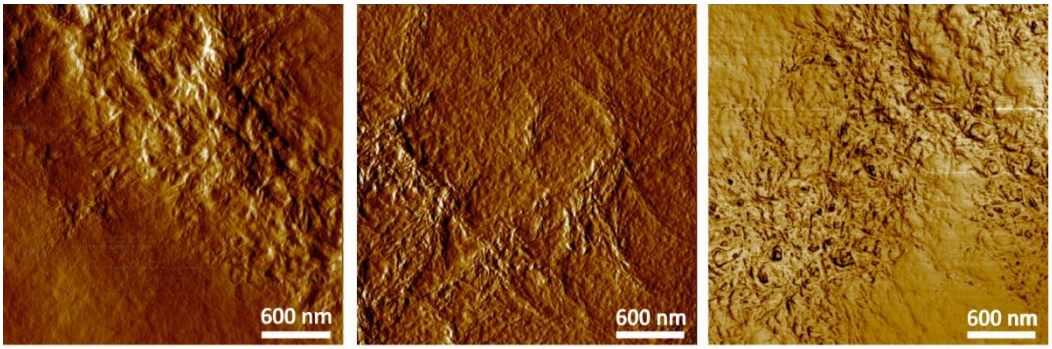

Figure 3.21 – AFM phase images of aged PLS films.

3.7. CONCLUSIONS

Starch-based films plasticised with glycerol, D-isosorbide and 1,3-propanediol were successfully prepared in order to study the suitability of the three plasticisers to be used as plasticisers for starch-based films following both solvent casting and extrusion/compression methods. Firstly, the capacity of all plasticisers to destroy the crystalline domains of the native starch granules was analysed by DSC and TOM.

After that, PLS films were satisfactorily prepared by solvent casting and it was confirmed that the use of different plasticisers resulted in significant differences. CSi35 sample presented significantly higher transmittance values, as well as higher Young's modulus, elongation at break and tensile strength and much lower OP value. Regarding the surface morphology, similar results were obtained in all cases, where a two-phase microstructure, related to the amylose and amylopectin rich domains was determined by AFM.

After that, the viability of extrusion/compression technique was demonstrated. Besides, the effect of the plasticiser and manufacturing technique was analysed. As demonstrated, the good D-isosorbide/starch affinity resulted in excellent optical, mechanical and barrier properties whereas 1,3-propanediol containing films were extremely brittle due to the loss of the plasticisers during the processing. Finally, the variation on the final properties of PLS due to retrogradation was studied, concluding that those films plasticised with D-isosorbide were less affected by retrogradation and showed a remarkable higher general stability. Thus, the use of D-isosorbide enhanced the reliability of the material.

3.8. REFERENCES

[1] H. Angellier, S. Molina-Boisseau, P. Dole, A. Dufresne, Thermoplastic starch - Waxy maize starch nanocrystals nanocomposites, Biomacromolecules. 7 (2006) 531–539. doi:10.1021/bm050797s.

[2] H. Liu, L. Yu, F. Xie, L. Chen, Gelatinization of corn starch with different amylose/amylopectin content, Carbohydr. Polym. 65 (2006) 357–363. doi:10.1016/j.carbpol.2006.01.026.

[3] A. Taghizadeh, B.D. Favis, Effect of high molecular weight plasticizers on the gelatinization of starch under static and shear conditions, Carbohydr. Polym. 92 (2013) 1799–1808. doi:10.1016/j.carbpol.2012.11.018.

[4] H. Liu, F. Xie, L. Yu, L. Chen, L. Li, Thermal processing of starch-based polymers, Prog. Polym. Sci. 34 (2009) 1348–1368. doi:10.1016/j.progpolymsci.2009.07.001.

[5] R.P. Cuevas, V.D. Daygon, H.M. Corpuz, L. Nora, R.F. Reinke, D.L.E. Waters, M.A. Fitzgerald, Melting the secrets of gelatinisation temperature in rice, Funct. Plant Biol. 37 (2010) 439–447. doi:10.1071/FP09258.

[6] Y. Zuo, J. Gu, H. Tan, Y. Zhang, Thermoplastic starch prepared with different plasticizers: Relation between degree of plasticization and properties, J. Wuhan Univ. Technol. Mater. Sci. Ed. 30 (2015) 423–428. doi:10.1007/s11595-015-1164-z.

[7] Z. Yingfeng, G. Jiyou, T. Haiyan, Z. Yanhua, Comparative study of plasticizing effect of corn starch using formamide and urea, Proc. 2012 Int. Conf. Biobase Mater. Sci. Eng. BMSE 2012. (2012) 4–7. doi:10.1109/BMSE.2012.6466167.

[8] N.L. García, L. Ribba, A. Dufresne, M.I. Aranguren, S. Goyanes, Physico-mechanical properties of biodegradable starch nanocomposites physico-mechanical properties of biodegradable starch nanocomposites, Macromol. Mater. Eng. 294 (2009) 169–177. doi:10.1002/mame.200800271.

[9] S. Pérez, E. Bertoft, The molecular structures of starch components and their contribution to the architecture of starch granules: A comprehensive review, Starch - Stärke. 62 (2010) 389–420. doi:10.1002/star.201000013.

[10] J.-L. Jane, J.F. Robyt, H. Zobel, S. Leas, T. Kasemsuwan, Anthology of starch granule morphology by scanning electron microscopy, Starch - Stärke. 46 (2006) 121–129. doi:10.1002/star.19940460402.

[11] Y.V. García-Tejeda, Y. Salinas-Moreno, F. Martínez-Bustos, Preparation and characterization of octenyl succinylated normal and waxy starches of maize as encapsulating agents for anthocyanins by spray-drying, Food Bioprod. Process. 94 (2015) 717–726. doi:10.1016/j.fbp.2014.10.003.

[12] W. Li, X. Tian, P. Wang, A.S.M. Saleh, Q. Luo, J. Zheng, S. Ouyang, G. Zhang, Recrystallization characteristics of high hydrostatic pressure gelatinized normal and waxy corn starch, Int. J. Biol. Macromol. 83 (2016) 171–177. doi:10.1016/j.ijbiomac.2015.11.057.

[13] S. Sharma, N. Dhiman, D. Pathak, R. Kumar, Effect of nano-size fumed silica on ionic conductivity of PVdF-HFP-based plasticized nano-composite polymer electrolytes, Ionics (Kiel). 22 (2016) 1865–1872. doi:10.1007/s11581-016-1721-2.

[14] L. Castillo, O. López, C. López, N. Zaritzky, M.A. García, S. Barbosa, M. Villar, Thermoplastic starch films reinforced with talc nanoparticles, Carbohydr. Polym. 95 (2013) 664–674. doi:10.1016/j.carbpol.2013.03.026.

[15] L.C. Tomé, S.C.M. Fernandes, D.S. Perez, P. Sadocco, A.J.D. Silvestre, C.P. Neto, I.M. Marrucho, C.S.R. Freire, The role of nanocellulose fibers, starch and chitosan on multipolysaccharide based films, Cellulose. 20 (2013) 1807–1818. doi:10.1007/s10570-013-9959-6.

[16] M.A. Bertuzzi, M. Armada, J.C. Gottifredi, Physicochemical characterization of starch based films, J. Food Eng. 82 (2007) 17–25. doi:10.1016/j.jfoodeng.2006.12.016.

[17] D. Polster, H. Graaf, Advancing and receding angles – Dynamic contact angle measurements on mixed alkyl monolayers, Appl. Surf. Sci. 265 (2013) 88–93. doi:10.1016/j.apsusc.2012.10.128.

[18] J.M. Lagarón, A. López-Rubio, M. José Fabra, Bio-based packaging, J. Appl. Polym. Sci. 133 (2016). doi:10.1002/app.42971.

[19] L. Averous, E. Pollet, Nanobiocomposites Based on Plasticized Starch, 2014. doi:10.1016/B978-0-444-53730-0.00028-2.

[20] X. Tang, S. Alavi, Recent advances in starch, polyvinyl alcohol based polymer blends, nanocomposites and their biodegradability, Carbohydr. Polym. 85 (2011) 7–16. doi:10.1016/j.carbpol.2011.01.030.

[21] A.P. Mathew, A. Dufresne, Plasticized waxy maize starch: Effect of polyols and relative humidity on material properties, Biomacromolecules. 3 (2002) 1101–1108.

[22] T. Mekonnen, P. Mussone, H. Khalil, D. Bressler, Progress in bio-based plastics and plasticizing modifications, J. Mater. Chem. A. 1 (2013) 13379–13398. doi:10.1039/c3ta12555f.

[23] J. Viguié, S. Molina-Boisseau, A. Dufresne, Processing and characterization of waxy maize starch films plasticized by sorbitol and reinforced with starch nanocrystals, Macromol. Biosci. 7 (2007) 1206–1216. doi:10.1002/mabi.200700136.

[24] A. Jiménez, M.J. Fabra, P. Talens, A. Chiralt, Effect of re-crystallization on tensile, optical and water vapour barrier properties of corn starch films containing fatty acids, Food Hydrocoll. 26 (2012) 302–310. doi:10.1016/j.foodhyd.2011.06.009.

[25] R.P. Herrera Brandelero, F. Yamashita, M.V. Eiras Grossmann, The effect of surfactant Tween 80 on the hydrophilicity, water vapor permeation, and the mechanical properties of cassava starch and poly(butylene adipate-co-terephthalate) (PBAT) blend films, Carbohydr. Polym. 82 (2010) 1102–1109. doi:10.1016/j.carbpol.2010.06.034.

[26] A. Cano, A. Jiménez, M. Cháfer, C. Gónzalez, A. Chiralt, Effect of amylose:amylopectin ratio and rice bran addition on starch films properties, Carbohydr. Polym. 111 (2014) 543–555. doi:10.1016/j.carbpol.2014.04.075.

[27] T. V. Duncan, Applications of nanotechnology in food packaging and food safety: Barrier materials, antimicrobials and sensors, J. Colloid Interface Sci. 363 (2011) 1–24. doi:10.1016/j.jcis.2011.07.017.

[28] N.L. García, L. Ribba, A. Dufresne, M. Aranguren, S. Goyanes, Effect of glycerol on the morphology of nanocomposites made from thermoplastic starch and starch nanocrystals, Carbohydr. Polym. 84 (2011) 203–210. doi:10.1016/j.carbpol.2010.11.024.

[29] D. Battegazzore, S. Bocchini, G. Nicola, E. Martini, A. Frache, Isosorbide, a green plasticizer for thermoplastic starch that does not retrogradate, Carbohydr. Polym. 119 (2015) 78–84. doi:10.1016/j.carbpol.2014.11.030.

[30] M. Rico, S. Rodríguez-Llamazares, L. Barral, R. Bouza, B. Montero, Processing and characterization of polyols plasticized-starch reinforced with microcrystalline cellulose, Carbohydr. Polym. 149 (2016) 83–93. doi:10.1016/j.carbpol.2016.04.087.

[31] D. Lecorre, J. Bras, A. Dufresne, Influence of native starch's properties on starch nanocrystals thermal properties, Carbohydr. Polym. 87 (2012) 658–666. doi:10.1016/j.carbpol.2011.08.042.

[32] D.C. Bastos, A.E.F. Santos, M.L.V.J. da Silva, R.A. Simao, Hydrophobic corn starch thermoplastic films produced by plasma treatment, Ultramicroscopy. 109 (2009) 1089–1093. doi:10.1016/j.ultramic.2009.03.031.

[33] R.A. Simão, R.M.S.M. Thiré, P.R. Coutinho, P.J.G. Araújo, C.A. Achete, C.T. Andrade, Application of glow discharge butadiene coatings on plasticized cornstarch substrates, Thin Solid Films. 515 (2006) 1714–1720. doi:10.1016/j.tsf.2006.06.013.

[34] R.M.S.M. Thiré, R.A. Simao, C.T. Andrade, High resolution imaging of the microstructure of maize starch films, Carbohydr. Polym. 54 (2003) 149–158. doi:10.1016/S0144-8617(03)00167-X.

[35] W. Ning, Z. Xingxiang, L. Haihui, H. Benqiao, 1-Allyl-3-methylimidazolium chloride plasticized-corn starch as solid biopolymer electrolytes, Carbohydr. Polym. 76 (2009) 482–484. doi:10.1016/j.carbpol.2008.11.005.

[36] A. Rindlav-Westling, P. Gatenholm, Surface composition and morphology of starch, amylose, and amylopectin Films, Biomacromolecules. 4 (2003) 166–172.

[37] K.M. Dang, R. Yoksan, Development of thermoplastic starch blown film by incorporating plasticized chitosan, Carbohydr. Polym. 115 (2015) 575–581. doi:10.1016/j.carbpol.2014.09.005.

[38] J. González-Gutiérrez, P. Partal, M. García-Morales, C. Gallegos, Effect of processing on the viscoelastic, tensile and optical properties of albumen/starch-based bioplastics, Carbohydr. Polym. 84 (2011) 308–315. doi:10.1016/j.carbpol.2010.11.040.

[39] W.H. Ferreira, C.T. Andrade, Characterization of glycerol-plasticized starch and graphene oxide extruded hybrids, Ind. Crops Prod. 77 (2015) 684–690. doi:10.1016/j.indcrop.2015.09.051.

[40] N.L. Garcia, L. Ribba, A. Dufresne, M.I. Aranguren, S. Goyanes, Physico-mechanical properties of biodegradable starch nanocomposites, Macromol. Mater. Eng. 294 (2009) 169–177. doi:10.1002/mame.200800271.

[41] M.A. Bertuzzi, E.F. Castro Vidaurre, M. Armada, J.C. Gottifredi, Water vapor permeability of edible starch based films, J. Food Eng. 80 (2007) 972–978. doi:10.1016/j.jfoodeng.2006.07.016.

[42] S.C. Lara, F. Salcedo, Gelatinization and retrogradation phenomena in starch/montmorillonite nanocomposites plasticized with different glycerol/water ratios,

Carbohydr. Polym. 151 (2016) 206–212. doi:10.1016/j.carbpol.2016.05.065.

[43] A. Jiménez, M.J. Fabra, P. Talens, A. Chiralt, Effect of sodium caseinate on properties and ageing behaviour of corn starch based films, Food Hydrocoll. 29 (2012) 265–271. doi:10.1016/j.foodhyd.2012.03.014.

[44] J. Zhu, X. Li, C. Huang, L. Chen, L. Li, Structural changes and triacetin migration of starch acetate film contacting with distilled water as food simulant, Carbohydr. Polym. 104 (2014) 1–7. doi:10.1016/j.carbpol.2013.12.087.

CHAPTER 4:

NANOENTITIES

4. NANOENTITIES

4.1. OBJECTIVE

The objective of the present chapter is the description of the obtainment and characterisation of the two types of nanoentities used in this research, i.e. the two types of polysaccharide nanocrystals (NC) and the graphene (G) or graphene oxide (G).

Regarding the polysaccharide nanocrystals, waxy maize starch nanocrystals (WSNC) and cellulose nanocrystals (CNC) were employed. The NCs were isolated by acid hydrolysis obtaining the crystalline domains of waxy maize starch and microcrystalline cellulose. The crystallinity of both NCs was investigated by XRD and their morphological features and nanoscale dimensions were characterised by AFM.

In addition, G and GO were prepared. G was exfoliated from graphite, whereas GO was obtained from the oxidation reaction of graphite. The crystalline structure of both nanoflakes was studied by XRD. The chemical structure was corroborated by Raman spectroscopy and the morphology and size distribution of both G and GO nanoflakes was analysed by TEM.

The obtained polysaccharide NCs and G or GO nanoflakes were further used as nanoreinforcements in film nanocomposites and also in starch-based nanocomposite hydrogels.

4.2. OBTAINMENT OF POLYSACCHARIDE NANOCRYSTALS

The amorphous domains of both waxy maize starch (~99% amylopectin) and microcrystalline cellulose were degraded and dissolved by performing controlled acidic hydrolysis in order to obtain nanosized highly crystalline polysaccharide nanoparticles, i.e. WSNC and CNC.

4.2.1. Isolation of waxy maize starch nanocrystals (WSNC)

The preparation of WSNC was carried out by acidic hydrolysis according to the method described elsewhere [1,2]. 36.7 g of waxy maize starch were mixed with 250 mL of sulfuric acid aqueous solution (3.16 M) maintaining the reaction for 5 days at 40 °C under continuous magnetic stirring. The reaction was stopped with distilled water and the suspension was then washed and centrifuged with distilled water until complete neutralisation. The obtained WSNC were stored at 4 °C after adding some drops of chloroform and freeze-dried.

4.2.2. Isolation of cellulose nanocrystals (CNC)

The extraction of the crystalline parts of microcrystalline cellulose (MCC) was also performed by acidic hydrolysis following the procedure employed by Saralegi et al. [3] and Santamaria-Echart et al. [4]. 5 g of MCC were treated with sulfuric acid 64 wt.% aqueous solution. The reaction was carried out during 30 min at 45 °C with continuous stirring. The suspension was diluted with distilled water to stop the reaction. After that, the acidity was firstly reduced by centrifugation (twice, 4500 rpm, 20 min) and the precipitate was then neutralised by dialysis (4 - 5 days). Finally, the suspension was ultrasonicated for 15 min and freeze-dried.

4.3. CHARACTERISATION OF POLYSACCHARIDE NANOCRYTALS

As explained above the crystalline domains of waxy maize starch and microcrystalline cellulose were isolated by acid hydrolysis in order to obtain polysaccharide nanoscale nanofillers, i. e. WSNC and CNC. The crystalline structure as well as the crystallinity degree of the NCs was determined by XRD, whereas the morphology and the nanoscale dimensions were corroborated by AFM.

4.3.1. X-ray diffraction

XRD measurements were carried out in order to observe the crystalline polymorphism of polysaccharide NCs. Results are shown in Figure 4.1. Native starch, depending on its origin,

presents three different crystalline arrangements namely A-type, B-type and C-type polymorphism, which differ due to different packaging organisation of the double helices [5,6]. XRD pattern of WSNC showed the typical A-type polymorphism [7] already described in Chapter 3. The XRD pattern of CNC exhibited strong peaks at 2θ = 14.5°, 2θ = 16.8°, 2θ = 22.7° and a small peak at 2θ = 34.5° associated to the typical cellulose I crystalline structure [8].

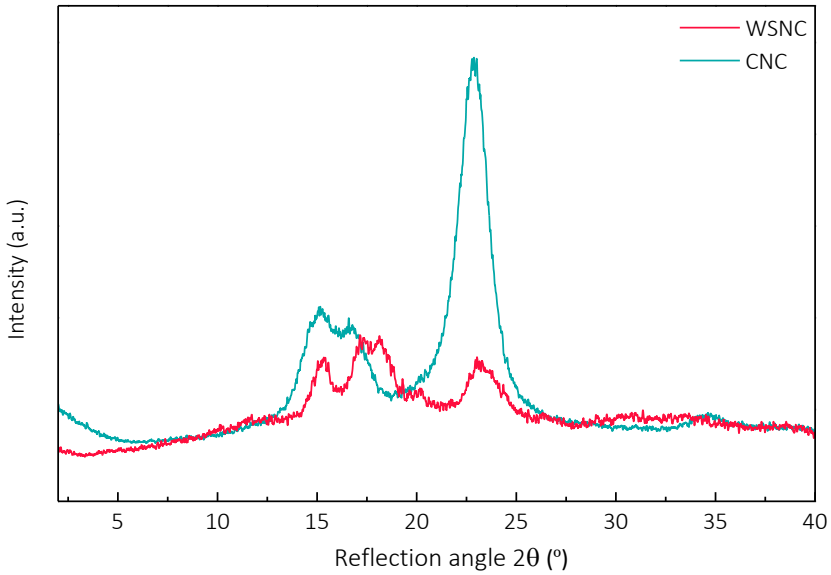

Figure 4.1 – XRD patterns for WSNC and CNC.

As explained by Lin et al. [9], the crystallinity degree of polysaccharide NCs should be 100%. However, disorder or amorphous domains cannot be completely removed by hydrolysis, leading to a lower crystallinity degree. Following the method described elsewhere [10,11], a crystallinity percentage of 22.8% for WSNC was calculated (Equation 2.1, Section 2.2.1.3). Besides, according to the method reported previously [12] a crystallinity percentage of 83.6% was calculated for CNC (Equation 2.2, Section 2.2.1.3). Other authors [9,13] determined similar values for CNC obtained from MCC (54–88%) [9], but higher crystallinity degree percentages for WSNC (38–48%) [13]. Differences could be related to the different extraction protocol employed, along with the method used for calculating crystallinity degrees [10,11]. However, even if the crystallinity percentage of the

WSNC could be affected slightly by the calculation method, the results for CNC were, as expected, significantly higher.

4.3.2. Thermogravimetric analysis

TGA measurements were performed to study the thermal behaviour of both WSNC and CNC. The obtained TG and DTG curves are shown in Figure 4.2.

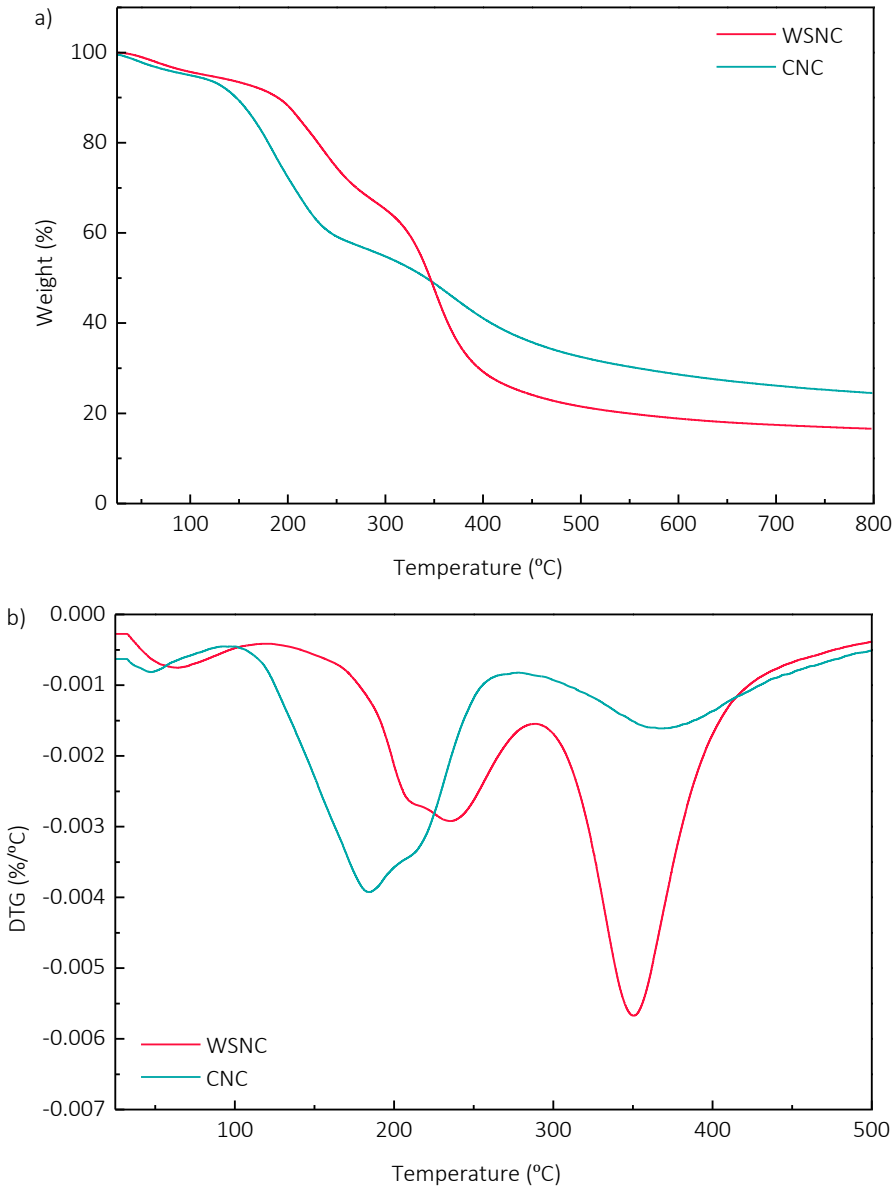

Figure 4.2 – a) TG and b) DTG curves of WSNC and CNC.

The degradation process of both NCs, i.e. WSNC and CNC, involves two steps. As explained by Wang et al. [14] CNC obtained by hydrolysis with sulfuric acid presented three degradation steps. The first step is associated with the evaporation of absorbed water (below 120 °C). Then, the second is related to the remove of these sulphate groups from the surface of the CNCs (around 180 °C), whereas the latter is associated to the degradation of cellulose (near 370 °C). In our case, slight differences were observed which may be due the different botanical origin of cellulose and reaction conditions. On the other hand, the WSNC also obtained by sulfuric acid hydrolysis followed the same thermal degradation pattern described by Wang et al. [14], presenting the above mentioned three step degradation pattern, where the removal of the sulphate groups and the degradation of starch occurred at 225 °C and 350 °C, respectively.

4.3.3. Atomic force microscopy

Morphological features and the dimensions at the nanoscale of the NCs were studied by AFM. Obtained phase and height images, as well as an example of the cross-sectional height profile of CNC (indicated with a blue line) are shown in Figure 4.3.

Width and length values of WSNC, as well as cellulose length values, were measured from AFM height images. Assuming the cylindrical shape of CNC [3] average diameter values were obtained by the evaluation of a hundred CNC from the AFM height profiles. The AFM height profiles were also used to determine the thickness and corroborate the length of WSNC measured from AFM height images. For WSNC, since they trend to agglomerate, less single NCs were possible to measure. Dimensions in the nanoscale of both WSNC and CNC were confirmed. WSNC were found to be platelet-like, with 28.2 ± 7.4 nm in width and 35.0 ± 7.9 nm in length. Besides, the thickness was found to be around 6.0 nm. CNC presented the typical fibril-like geometry with 9.1 ± 2.6 nm in diameter and 150.6 ± 29.1 nm in length. These results agreed with those obtained in

literature [1,3,4,15]. Attending to AFM and XRD results, it was concluded that the employed hydrolysis methods were satisfactory.

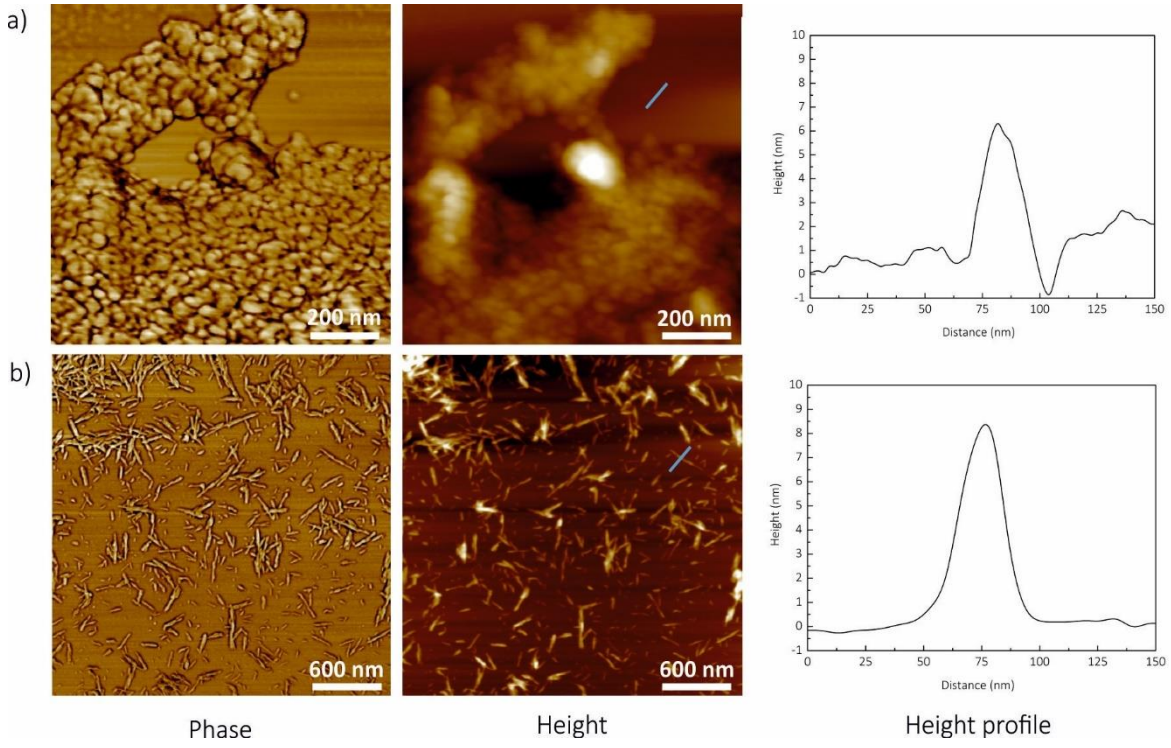

Figure 4.3 – Phase and height AFM images of isolated a) WSNC and b) CNC (including the height profiles).

4.4. OBTAINMENT OF GRAPHENE AND GRAPHENE OXIDE

G and GO were both obtained by exfoliation from graphite by ultrasound assisted and oxidation methods, respectively. Besides, GO was reduced assisted by ascorbic acid.

4.4.1. Preparation of graphene nanoflakes

The exfoliation of G was performed as described by Ugarte et al. [16]. 20 g of graphite were sonicated in 1.5 L of N-methyl pyrrolidone (NMP) for 100 h. The obtained dispersion was centrifuged at 4000 rpm for 45 min and the supernatant was filtered (Polyamide filters, Sartorius, pore size 0.2 μm), washed with acetone and dried for 48 h at room temperature.

4.4.2. Preparation of graphene oxide nanoflakes

The GO nanosflakes were obtained following the Hummers' method [17] with slight differences. 1 g of graphite was mixed and stirred with 0.5 g of $NaNO_3$ and 23 ml of sulfuric acid (96% purity) during 30 min at 0 °C. After that, 3 g of $KMnO_4$ were added and the resulting dispersion was maintained in continuous magnetic stirring during 2 h at 0 °C. Then, the mixture was heated for 30 min at 35 °C. Next, 46 mL of distilled water were added drop by drop, heated at 98 °C and maintained during 30 min. Finally, 10 mL of H_2O_2 (30% purity) were added at room temperature and when the formation of bubbles in the mixture ended, 150 mL of distilled water were added. The supernatant of the mixture was discarded, and the resulting sediment was washed by centrifugation with a 5% HCl aqueous solution (4500 rpm, 20 min, 5 times) and distilled water (4500 rpm, 20 min, until pH = 7). The sediment was filtered (Polyamide filters, Sartorius, pore size 0.2 μm) and dried in an oven for 48 h at 50 °C. Figure 4.4 shows images of the obtained G and GO.

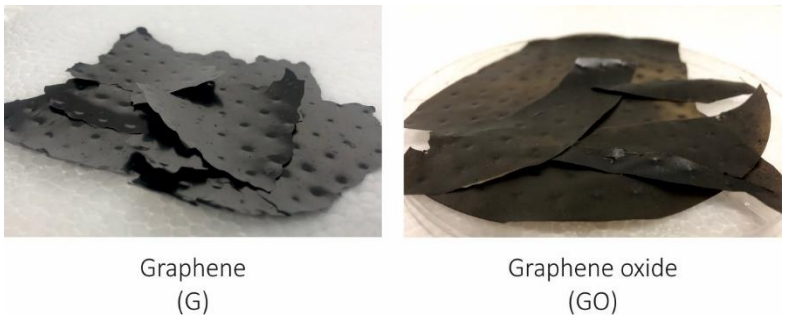

Figure 4.4 – Images of isolated G and GO.

4.4.3. Reduction of graphene oxide

The reduced graphene oxide (rGO) was obtained using ascorbic acid as reduction agent. Thus, GO was submerged in a solution of 30 g of ascorbic acid L^{-1} of distilled water at 95 °C for 2 h. After that, in order to remove the excess of ascorbic acid, the rGO was washed several times with distilled water and dried at room temperature for 24 h.

4.5. CHARACTERISATION OF GRAPHENE AND GRAPHENE OXIDE

G and GO nanoflakes were both obtained from graphite, by ultrasound assisted exfoliation procedure and by the Hummers' method, respectively. The chemical structure and the crystallite size of both nanoparticles was corroborated by Raman spectroscopy, and the crystallinity by XRD. Besides, the morphology was studied by TEM.

4.5.1. Raman spectroscopy

Raman spectroscopy was performed in order to analyse the structure of graphite and its derivatives G, GO and rGO. Obtained Raman spectra are presented in Figure 4.5.

All samples showed the typical pattern of carbon materials [16,18]. In the case of graphite, the disorder-induced *D* band that requires a defect (such as vacancies, grain boundaries and amorphous carbon spaces) to be activated and is related to the nanoflake edges appeared at 1364 cm^{-1} [16,19,20]. This band appeared weakly due to perfect benzene structure of graphite [21]. The first order *G* band associated to the in-plane sp^2 C-C stretching mode is located around 1580 cm^{-1}. Besides, the second order *2D* band that corresponds to the zone boundary phonons and is highly sensitive to stacking [16,20] is centred at 2711 cm^{-1}.

Regarding the pattern of G, the increase of the intensity of the *D* band, the appearance of the *D'* shoulder and the new *D+G* band at 2939 cm^{-1} demonstrated that the exfoliation of graphite occurred satisfactorily [22]. The *D+G* band was also observed for GO and rGO. Besides, for GO the *G* band shifted to higher values due to the new oxygen functional groups on the structure and the formation of sp^3 carbon atoms, whereas the *D* band broadened due to the creation of defects, vacancies and distortions after the oxidation and reduction [23].

The intensity ratio of *D* and *G* bands, I_D/I_G, is inversely related with the size of the defect-free sp^2 cluster region [16,22], and thus, reflected the quality and the disorder degree of the material

[19,24]. An I_D/I_G of 0.54 was obtained for G, whereas the value increased up to 0.87 and 1.26 for the GO and rGO, respectively, indicating that the exfoliation of graphite by ultrasound assisted procedure led to nanoflakes with fewer defects. On the other and, the intensity ratio of *2D* and *G* bands, I_{2D}/I_G, is associated with the number of layers of carbon materials, obtaining typical values of ~1.6, ~0.8, ~0.30 and ~0.07 for single-, double-, triple-, and multi-layer materials, respectively [18,25]. In our case, the I_{2D}/I_G values of 0.53 and 0.41 were calculated for G and GO, respectively, indicating that both nanoentities were obtained as few-layered materials.

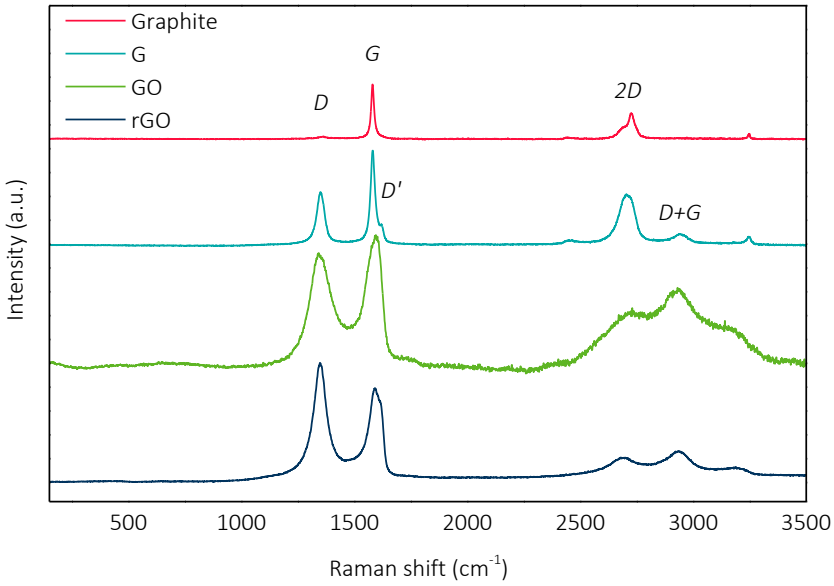

Figure 4.5 – Raman spectra of graphite, G, GO and rGO.

4.5.2. X-ray diffraction

XRD measurements were performed to analyse the crystalline structure of the obtained carbon materials. Figure 4.6 shows the diffractograms of G, GO and rGO as well as, for a better understanding of the results, the diffractograms of graphite. The obtained XRD results were used to calculate the interlayer distance following the Bragg's law (Equation 4.1) [26].

$$n\,\lambda = 2\,d\,\sin\theta \qquad \text{(Eq. 4.1)}$$

where n is a whole number (in our case 1), λ is the incident radiation wavelength (0.154 nm), d is the shortest distance between successive identical planes in the crystal which is associated to the interlayer separation and θ is the angle of incidence of the primary rays on the plane.

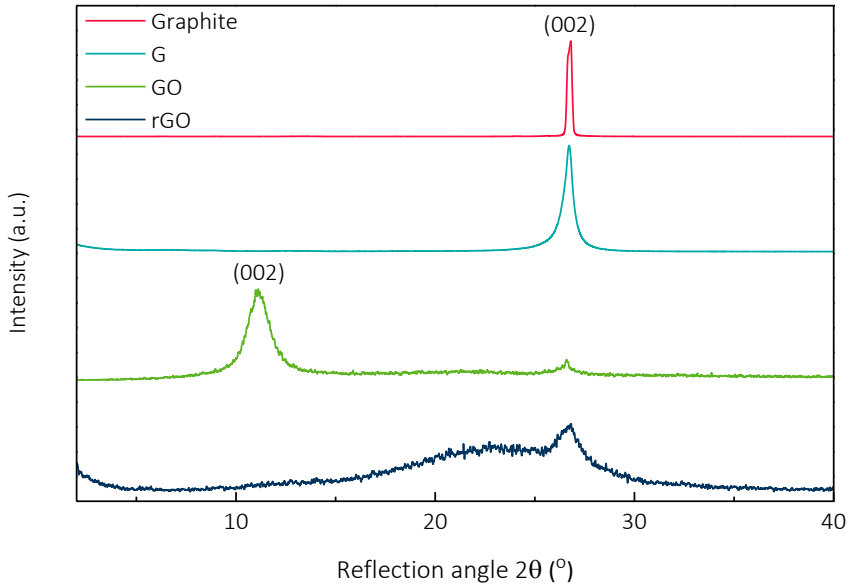

Figure 4.6 – XRD patterns of graphite, G, GO and rGO.

The XRD spectra of G presented a unique peak at $2\theta = 26.8^{\circ}$ related to the (002) plane of the hexagonal structure of pure graphite with an interlayer separation of 3.32 Å which is very close to graphite ($2\theta = 26.7^{\circ}$; 3.33 Å) and also to the reported in the literature [27–29]. In the case of GO, in addition to the small peak at $2\theta = 26.6^{\circ}$ a new signal located at $2\theta = 11.2^{\circ}$ was observed associated to the (002) plane of GO with an interlayer separation of 7.89 Å [30]. This increase of the interlayer separation was related with the intercalation of water molecules and the presence of oxygen containing functional groups between GO layers. In addition, in the case of GO, the presence of the peak of pure graphite (also appeared in G), indicates that some GO nanoflakes still maintained the graphitic structure. After the reduction of GO, rGO did not show the characteristic peak of GO and showed a peak at $2\theta = 26.8^{\circ}$ with an interlayer separation of 3.32 Å, suggesting the existence of π - π stacking between G nanoflakes due to the removal of oxygenated functional groups. Moreover,

when GO is reduced by external factors like heat treatment or reducing agents, the peak position of GO nanoflakes shift toward higher scattering angles, according to the degree of reduction [31]. Thus, the peak around $2\theta = 22.5^{\circ}$ belongs to the partially reduced GO.

4.5.3. Thermogravimetric analysis

The thermal stability of graphite, G, GO and rGO was determined by TGA analysis. Figure 4.7 shows the TG and DTG curves of all samples.

As it was expected, graphite presented an almost negligible degradation step along the studied temperature range [32]. In a similar way, G since it is also made of only sp^2 bonds [33], possesses a very low mass loss, which could be associated to existing defects and residual solvents [34].

In contrast, the degradation of GO involves larger mass loss in two main degradation steps: 1) removal of water molecules at the GO surface (25 - 150°C), 2) pyrolysis of oxygen containing functional groups (175 - 320°C) generating carbon monoxide, carbon dioxide and water [35–37]. Above 320 °C, the weight remains almost constant [35]. TG analysis revealed a weight loss of 14% related to the water and a weight loss of 33% associated with the oxygen containing groups. According to the conclusions obtained by Ma et al. [38], rGO presented a similar behaviour compared with GO but showing a lower weight loss. A weight loss of 20% associated with the oxygen containing groups determined for rGO. These results would indicate that oxygen groups were not totally removed, and the G structure would be partially restored.

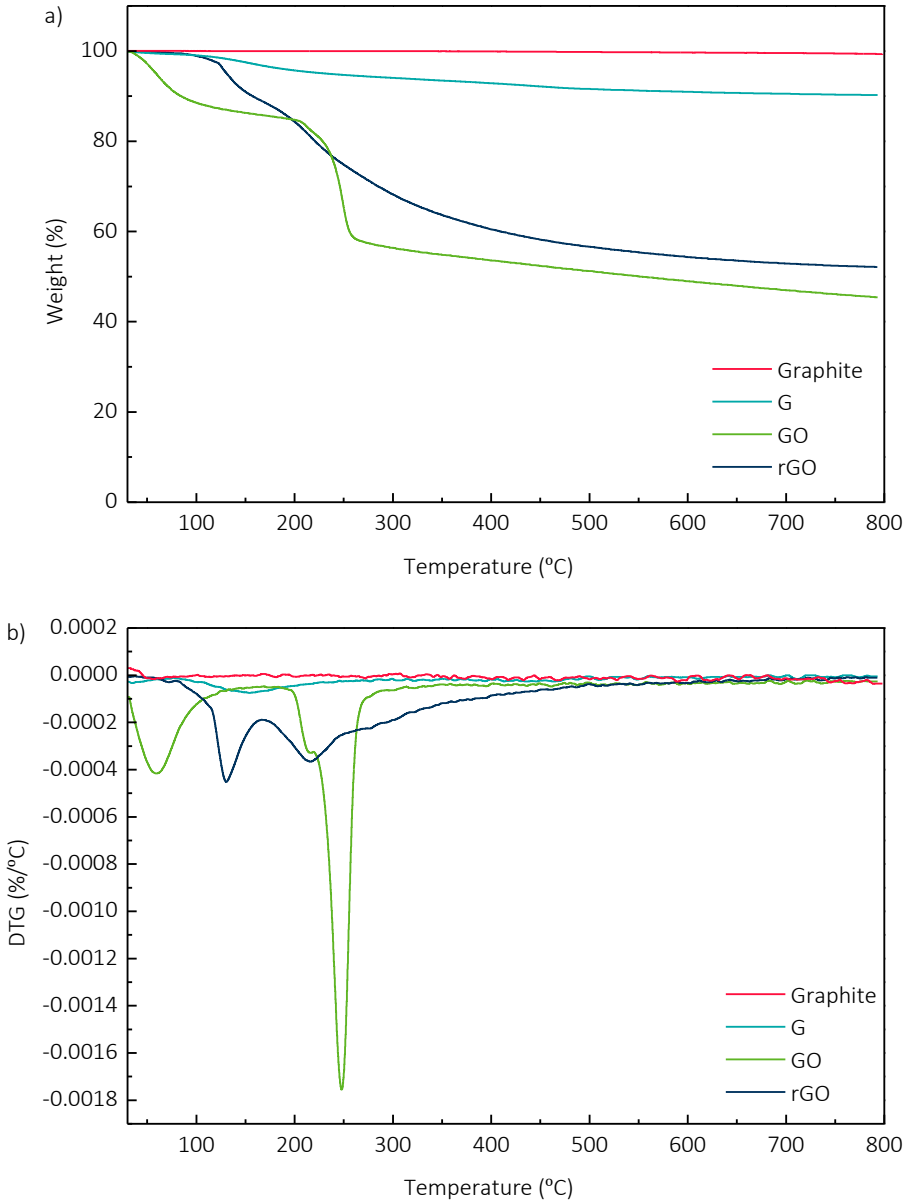

Figure 4.7 – a) TG and b) DTG curves of graphite, G, GO and rGO.

4.5.4. Transmission electron microscopy

The morphology of G and GO was characterised by TEM. For the preparation of the samples they were sonicated in distilled water (0.5 wt.%) for 1 h. In the case of G, Salvia extracts were used in order to improve the stability of the dispersion in water. One drop of the resulting suspension was placed in a copper grid covered by holey carbon film. Finally, it was dried under vacuum. Figure 4.8 shows the recorded TEM images of both carbonaceous nanoparticles.

By comparing the TEM phase images of G and GO (Figure 4.8, left column), it could be concluded that the latter showed a more homogeneous morphology. It should be taken into account that G TEM images were obtained in water using Salvia as emulsifier which could be affecting the arrangement of G nanoflakes. On the other hand, comparing the high resolution TEM images (Figure 4.8, right column) of both samples, in the case of GO highly oriented domains could be observed, whereas they were not so appreciable for G. Thus, it could be suggested that Salvia is also interfering in the orientation of G.

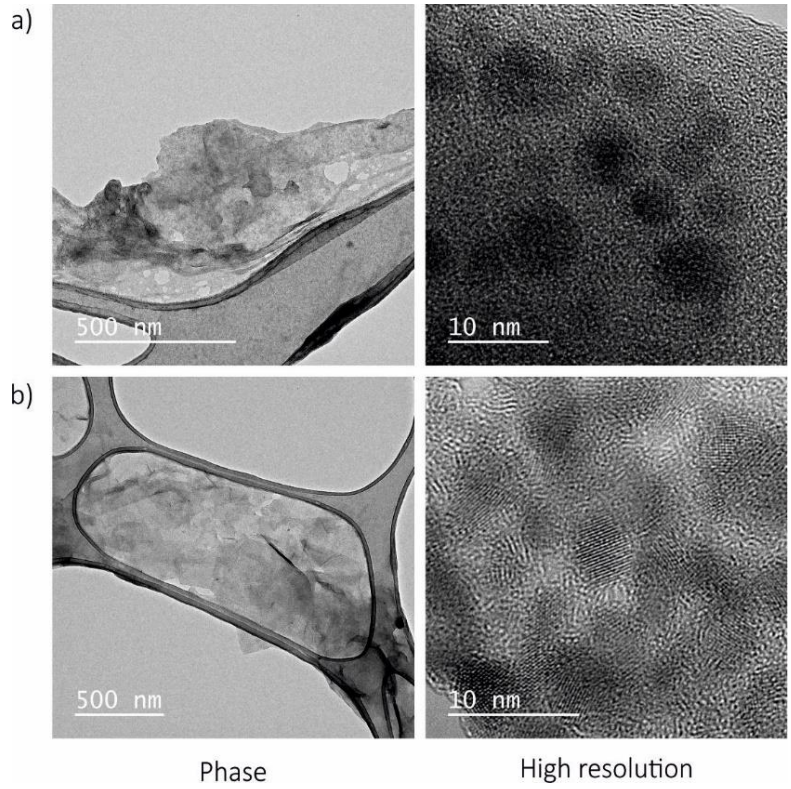

Figure 4.8 – TEM phase and high resolution images of a) G and b) GO.

4.6. CONCLUSIONS

WSNC and CNC were successfully isolated by acid hydrolysis. According to XRD results it was concluded that both NCs showed the expected polymorphisms. Besides, it was found that the crystalline degree of CNC was significantly higher as expected. As the AFM images showed, obtained WSNC presented the predicted platelet-like shape whereas the CNC possessed rod like

geometry. Therefore, AFM and XRD results demonstrated that the acid hydrolysis protocols used in each case were satisfactory, and thus, the NCs were appropriate to be employed as nanoreinforcements in starch-based nanocomposites.

Carbonaceous nanoparticles were also successfully obtained from graphite. The structure of all nanoparticles was confirmed by Raman spectroscopy and XRD and the morphology by TEM. It was observed that GO presented higher interlayer separation. In contrast, it was noticed that the morphology of G nanoflakes was affected by Salvia extracts.

4.7. REFERENCES

[1] H. Angellier, L. Choisnard, S. Molina-Boisseau, P. Ozil, A. Dufresne, Optimization of the preparation of aqueous suspensions of waxy maize starch nanocrystals using a response surface methodology, Biomacromolecules. 5 (2004) 1545–51. doi:10.1021/bm049914u.

[2] N.L. García, L. Ribba, A. Dufresne, M. Aranguren, S. Goyanes, Effect of glycerol on the morphology of nanocomposites made from thermoplastic starch and starch nanocrystals, Carbohydr. Polym. 84 (2011) 203–210. doi:10.1016/j.carbpol.2010.11.024.

[3] A. Saralegi, L. Rueda, L. Martin, A. Arbelaiz, A. Eceiza, M.A. Corcuera, From elastomeric to rigid polyurethane/cellulose nanocrystal bionanocomposites, Compos. Sci. Technol. 88 (2013) 39–47. doi:10.1016/j.compscitech.2013.08.025.

[4] A. Santamaria-Echart, L. Ugarte, C. García-Astrain, A. Arbelaiz, M.A. Corcuera, A. Eceiza, Cellulose nanocrystals reinforced environmentally-friendly waterborne polyurethane nanocomposites, Carbohydr. Polym. 151 (2016) 1203–1209. doi:10.1016/j.carbpol.2016.06.069.

[5] D. Le Corre, A. Dufresne, Starch Nanoparticles: A review starch nanoparticles: A review, (2010) 1139–1153. doi:10.1021/bm901428y.

[6] A. Dufresne, Crystalline starch based nanoparticles, Curr. Opin. Colloid Interface Sci. 19 (2014) 397–408. doi:10.1016/j.cocis.2014.06.001.

[7] B.B. Sanchez de la Concha, E. Agama-Acevedo, M.C. Nuñez-Santiago, L.A. Bello-Perez, H.S. Garcia, J. Alvarez-Ramirez, Acid hydrolysis of waxy starches with different granule size for nanocrystal production, J. Cereal Sci. 79 (2018) 193–200. doi:10.1016/j.jcs.2017.10.018.

[8] M.C. Li, Q. Wu, K. Song, S. Lee, Y. Qing, Y. Wu, Cellulose Nanoparticles: Structure-Morphology-Rheology Relationships, ACS Sustain. Chem. Eng. 3 (2015) 821–832. doi:10.1021/acssuschemeng.5b00144.

[9] N. Lin, J. Huang, A. Dufresne, Preparation, properties and applications of polysaccharide nanocrystals in advanced functional nanomaterials: a review, Nanoscale. 4 (2012) 3274–3294.

doi:10.1039/c2nr30260h.

[10] M.J. Jivan, A. Madadlou, M. Yarmand, An attempt to cast light into starch nanocrystals preparation and cross-linking, Food Chem. 141 (2013) 1661–1666. doi:10.1016/j.foodchem.2013.04.071.

[11] M.F. Rosa, E.S. Medeiros, J.A. Malmonge, K.S. Gregorski, D.F. Wood, L.H.C. Mattoso, G. Glenn, W.J. Orts, S.H. Imam, Cellulose nanowhiskers from coconut husk fibers: Effect of preparation conditions on their thermal and morphological behavior, Carbohydr. Polym. 81 (2010) 83–92. doi:10.1016/j.carbpol.2010.01.059.

[12] H. Kargarzadeh, I. Ahmad, I. Abdullah, A. Dufresne, S.Y. Zainudin, R.M. Sheltami, Effects of hydrolysis conditions on the morphology, crystallinity, and thermal stability of cellulose nanocrystals extracted from kenaf bast fibers, Cellulose. 19 (2012) 855–866. doi:10.1007/s10570-012-9684-6.

[13] A. Bul??on, P. Colonna, V. Planchot, S. Ball, Starch granules: Structure and biosynthesis, Int. J. Biol. Macromol. 23 (1998) 85–112. doi:10.1016/S0141-8130(98)00040-3.

[14] N. Wang, E. Ding, R. Cheng, Thermal degradation behaviors of spherical cellulose nanocrystals with sulfate groups, Polymer (Guildf). 48 (2007) 3486–3493. doi:10.1016/j.polymer.2007.03.062.

[15] Y. Wang, H. Tian, L. Zhang, Role of starch nanocrystals and cellulose whiskers in synergistic reinforcement of waterborne polyurethane, Carbohydr. Polym. 80 (2010) 665–671. doi:10.1016/j.carbpol.2009.10.043.

[16] L. Ugarte, S. Gómez-Fernández, A. Tercjak, A. Martínez-Amesti, M.A. Corcuera, A. Eceiza, Strain sensitive conductive polyurethane foam/graphene nanocomposites prepared by impregnation method, Eur. Polym. J. 90 (2017) 323–333. doi:10.1016/j.eurpolymj.2017.03.035.

[17] J.Ri.E.O. William S. Hummers, Preparation of graphitic oxide, J. Am. Chem. Soc. 80 (1958) 1339–1339.

[18] H. Luo, J. Dong, F. Yao, Z. Yang, W. Li, J. Wang, X. Xu, J. Hu, Y. Wan, Layer-by-Layer Assembled Bacterial Cellulose/Graphene Oxide Hydrogels with Extremely Enhanced Mechanical Properties, Nano-Micro Lett. 10 (2018) 1–10. doi:10.1007/s40820-018-0195-3.

[19] F.T. Johra, J.W. Lee, W.G. Jung, Facile and safe graphene preparation on solution based platform, J. Ind. Eng. Chem. 20 (2014) 2883–2887. doi:10.1016/j.jiec.2013.11.022.

[20] R. Beams, L. Gustavo Cançado, L. Novotny, Raman characterization of defects and dopants in graphene, J. Phys. Condens. Matter. 27 (2015). doi:10.1088/0953-8984/27/8/083002.

[21] H. Li, L. Song, H. Liu, J. Li, A. Yang, C. Sun, R. Li, Y. Fu, C. Yu, Antimony-doped tin oxide embedding graphene-based aerogel for infrared barriering, Ceram. Int. 45 (2019) 7894–7905. doi:10.1016/j.ceramint.2019.01.100.

[22] A.G. and K.E.G. Dickson Joseph, Nisha Tyagi, A direct route towards preparing pH-sensitive graphene nanosheets with anti-cancer activity, RSC Adv. 4 (2014) 4085–4093. doi:10.1039/c3ra45984e.

[23] A. You, M.A.Y. Be, I. In, White light Z-scan measurements of ultrafast optical nonlinearity in reduced graphene oxide nanosheets in the 400 – 700 nm region, 051104 (2015). doi:10.1063/1.4928124.

[24] M.Z. Ansari, R. Johari, W.A. Siddiqi, Novel and green synthesis of chemically reduced graphene sheets using Phyllanthus emblica (Indian Gooseberry) and its photovoltaic activity, Mater. Res. Express. 6 (2019). doi:10.1088/2053-1591/ab0439.

[25] O. Akhavan, Bacteriorhodopsin as a superior substitute for hydrazine in chemical reduction of single-layer graphene oxide sheets, Carbon N. Y. 81 (2015) 158–166. doi:10.1016/j.carbon.2014.09.044.

[26] W.L. Bragg, The Dawn of X-ray Crystallography, Proc. Camb. Philol. Soc. 12 (1913) 43–57.

[27] J. Fan, Z. Shi, J. Wang, J. Yin, Glycidyl methacrylate-modified gum arabic mediated graphene exfoliation and its use for enhancing mechanical performance of hydrogel, Polymer (Guildf). 54 (2013) 3921–3930. doi:10.1016/j.polymer.2013.05.057.

[28] J. Cao, Y. Zhu, X. Yang, Y. Chen, Y. Li, H. Xiao, W. Hou, J. Liu, The promising photo anode of graphene/zinc titanium mixed metal oxides for the CdS quantum dot-sensitized solar cell, Sol. Energy Mater. Sol. Cells. 157 (2016) 814–819. doi:10.1016/j.solmat.2016.08.003.

[29] E. Mahmoudi, L.Y. Ng, M.M. Ba-Abbad, A.W. Mohammad, Novel nanohybrid polysulfone membrane embedded with silver nanoparticles on graphene oxide nanoplates, Chem. Eng. J. 277 (2015) 1–10. doi:10.1016/j.cej.2015.04.107.

[30] J. Guerrero-Contreras, F. Caballero-Briones, Graphene oxide powders with different oxidation degree, prepared by synthesis variations of the Hummers method, Mater. Chem. Phys. 153 (2015) 209–220. doi:10.1016/j.matchemphys.2015.01.005.

[31] M. Lee, S.K. Balasingam, H.Y. Jeong, W.G. Hong, H.B.R. Lee, B.H. Kim, Y. Jun, One-step hydrothermal synthesis of Graphene decorated V2O5 nanobelts for enhanced electrochemical energy storage, Sci. Rep. 5 (2015) 1–8. doi:10.1038/srep08151.

[32] V. Loryuenyong, K. Totepvimarn, P. Eimburanapravat, W. Boonchompoo, A. Buasri, Preparation and characterization of reduced graphene oxide sheets via water-based exfoliation and reduction methods, Adv. Mater. Sci. Eng. 2013 (2013) 1–5. doi:10.1155/2013/923403.

[33] A. Graziano, S. Jaffer, M. Sain, B. Processing, Graphene oxide modification for enhancing high density polyethylene properties: A comparison between solvent reaction and melt mixing, J Polym Eng 39 (2019) 1–16. doi:10.1515/polyeng-2018-0106

[34] X. Zhang, W.R. Browne, B.L. Feringa, Preparation of dispersible graphene through organic functionalization of graphene using a zwitterion intermediate cycloaddition approach, RSC Adv. 2 (2012) 12173–12176. doi:10.1039/c2ra22440b.

[35] S. Gupta, V. Subramanian, Encapsulating Bi2Ti2O7 (BTO) with reduced graphene oxide (RGO): An effective strategy to enhance photocatalytic and photoelectrocatalytic activity of BTO, ACS Appl. Mater. Interfaces. 6 (2014) 18597–18608. doi:10.1021/am503396r.

[36] T. Wu, X. Wang, H. Qiu, J. Gao, W. Wang, Y. Liu, Graphene oxide reduced and modified by

soft nanoparticles and its catalysis of the Knoevenagel condensation, J. Mater. Chem. 22 (2012) 4772–4779. doi:10.1039/c2jm15311d.

[37] S. Jin, Q. Gao, X. Zeng, R. Zhang, K. Liu, X. Shao, M. Jin, Effects of reduction methods on the structure and thermal conductivity of free-standing reduced graphene oxide films, Diam. Relat. Mater. 58 (2015) 54–61. doi:10.1016/j.diamond.2015.06.005.

[38] T. Ma, P.R. Chang, P. Zheng, X. Ma, The composites based on plasticized starch and graphene oxide/reduced graphene oxide, Carbohydr. Polym. 94 (2013) 63–70. doi:10.1016/j.carbpol.2013.01.007.

CHAPTER 5:

NANOCOMPOSITE FILMS BASED ON STARCH AND POLYSACCHARIDE NANOCRYSTALS

5. NANOCOMPOSITE FILMS BASED ON STARCH AND POLYSACCHARIDE NANOCRYSTALS

5.1. OBJECTIVE

As a general conclusion of Chapter 3, films plasticised with 1,3-propanediol could be discarded as they showed poor starch/plasticiser compatibility leading to phase separation, higher opacity, brittle material and higher permeability values. Moreover, in the case of TPS films, at high processing temperatures the loss of 1,3-propanediol occurred, resulting in a more brittle material. On the contrary, the use of D-isosorbide led to optimized transparency and mechanical and barrier properties. Glycerol plasticised films showed better starch/plasticiser compatibility in comparison with 1,3-propanediol films, but worst mechanical and barrier properties than films plasticised with D-isosorbide. Therefore, in order to increase the competitiveness of glycerol plasticised films, we considered that the incorporation of polysaccharide NCs into glycerol plasticised PLS and TPS matrixes could lead to the improvement of the behaviour of the material, especially the one related to the mechanical and the barrier properties.

Thus, the main objective of the present chapter was the development of nanocomposite films by adding polysaccharide NCs. The effect of different contents of WSNC on a normal maize starch matrix plasticised with glycerol was analysed. In addition, the influence of using together NCs with similar chemical structure but different geometries, i.e. WSNC and CNC, was also studied.

Moreover, films were obtained by both solvent casting and extrusion/compression techniques, obtaining PLS and TPS nanocomposites, subsequently. As concluded in Chapter 3, the films obtained by extrusion/compression method showed improved mechanical and barrier properties than those obtained by solvent casting. However, nanocomposites were also prepared by solvent casting since we considered that a better dispersion of the nanofiller could be achieved by

this technique which could lead to enhanced mechanical and barrier behaviour. Thus, in order to corroborate these hypotheses, the effect of using different processing techniques in the properties of starch-based films was also evaluated. All the resulting nanocomposites were characterised in terms of thermal stability, mechanical and barrier properties and morphology.

5.2. OBTAINMENT OF STARCH/POLYSACCHARIDE NANOCRYSTALS NANOCOMPOSITE FILMS

5.2.1. Preparation of nanocomposite films based on PLS and polysaccharide nanocrystals by solvent casting

The nanocomposites were obtained following the method described in Section 3.2.1. A mixture of 3.58 g of normal maize starch, 1.93 g of glycerol and 35 g of distilled water was heated to 90 °C with continuous stirring for the gelatinization during 20 minutes. After that, the desired amount of NCs was added, after their previous dispersion in distilled water by ultrasonication. In order to avoid the gelatinization of the WSNC, the mixture was cooled down below 50 °C before adding the NCs. Thereafter, the viscous gel was homogenised in a dispersing system for 3 min at 15,000 rpm (POLYTRON® PT 2500 E). After that, the material was spread into glass petri and dried in an oven at 55 °C for 2 h. The samples were named as CSg35 plus the NCs content, followed by the WSNC and/or CNC proportion (CSg35 + wt.% (WSNC/CNC)).

The glycerol content was set on of 35 wt.% for all samples, i.e. relative to the starch plus plasticiser mixture weight. The nanofiller content was relative to the starch plus glycerol weight and WSNC or CNC contents were relative to the total NCs weight. All the samples were stored at 43% RH for two weeks before all characterisation tests.

5.2.2. Preparation of nanocomposite films based on TPS and polysaccharide nanocrystals by extrusion/compression

The preparation of the TPS nanocomposites was carried out in a similar way that the employed in Section 3.2.2, following the 4-step methodology: gelatinization, freeze-drying, extrusion and compression. Once the gelatinization was completed as described for solvent casting process, the desired amount of NCs was added to obtain the nanocomposites, homogenised and finally freeze-dried. Thereafter, the freeze-dried material was extruded and compressed following the same processing methodology presented in Chapter 3, i.e. extrusion at 120 °C/50 rpm and subsequent compression moulding working at 1) 120 °C/0 t/5 min and 2) 120 °C/2.5 t/5 min. The samples were named as ESg35 plus the NCs content, followed by the WSNC and/or CNC proportion (ESg35 + wt.% (WSNC/CNC)).

Similarly as for casted films, a glycerol content of 35 wt.% was used for all samples, i.e. relative to the starch plus plasticiser mixture weight. In addition, the nanofiller content was relative to the starch plus glycerol weight and WSNC or CNC contents were relative to the total NCs weight. All the samples were stored for two weeks at 43% RH before characterisation.

5.3. EFFECT OF *WAXY* MAIZE STARCH NANOCRYSTALS CONTENT ON THE PROPERTIES OF PLS FILMS

In order to improve the overall behaviour of PLS films plasticised with glycerol WSNCs were incorporated. Thus, the influence of adding different contents of WSNC (1, 2.5 and 5 wt.%) on the final properties of the nanocomposites was analysed.

5.3.1. Dynamic mechanical analysis

The viscoelastic behaviour of the bionanocomposites was studied by DMA. Figure 5.1 presents the evolution of E'/E'_g and tan δ with temperature of films obtained by solvent casting. In

agreement with results obtained in Section 3.4.4, two-step modulus drops simultaneously to the tan δ peak temperatures near −60 °C ($T_{\alpha 1}$) and −20 °C ($T_{\alpha 2}$) were observed. As explained, it is generally assumed that they corresponded to the main relaxation temperatures of glycerol-rich and starch-rich phases, respectively [1]. As it can be noted, the addition of WSNC resulted in a significant shift of $T_{\alpha 1}$ and $T_{\alpha 2}$ to higher temperatures which indicated strong interactions between the NCs and starch affecting the mobility of both phases. Indeed, it could be appreciated that as WSNC content increased, the peaks shifted up to temperatures close to −50 °C and, and at the same time, a marked decrease of the intensity of the tan δ was evidenced as less glycerol molecules relaxed. In addition, the mentioned effect in the both transitions was especially noticeable for 2.5 wt.% and 5 wt.% samples, where a remarkable increase of the E'/E'_g was also observed revealing that a good dispersion of the NCs was achieved.

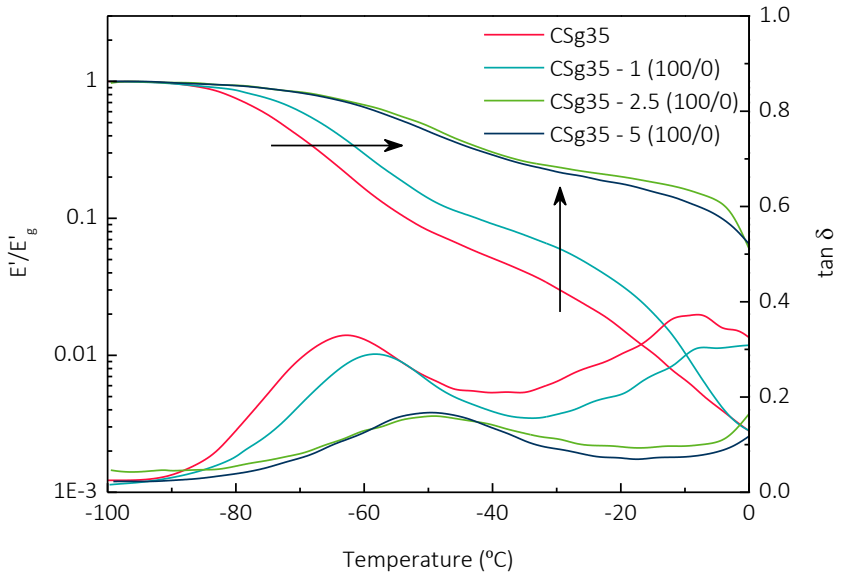

Figure 5.1 – Evolution of E'/E'_g and tan δ with temperature of obtained PLS nanocomposite films reinforced with WSNC.

5.3.2. Mechanical properties

The mechanical properties of bionanocomposites reinforced with different contents of WSNC were determined by means of tensile tests. Obtained results are collected in Figure 5.2.

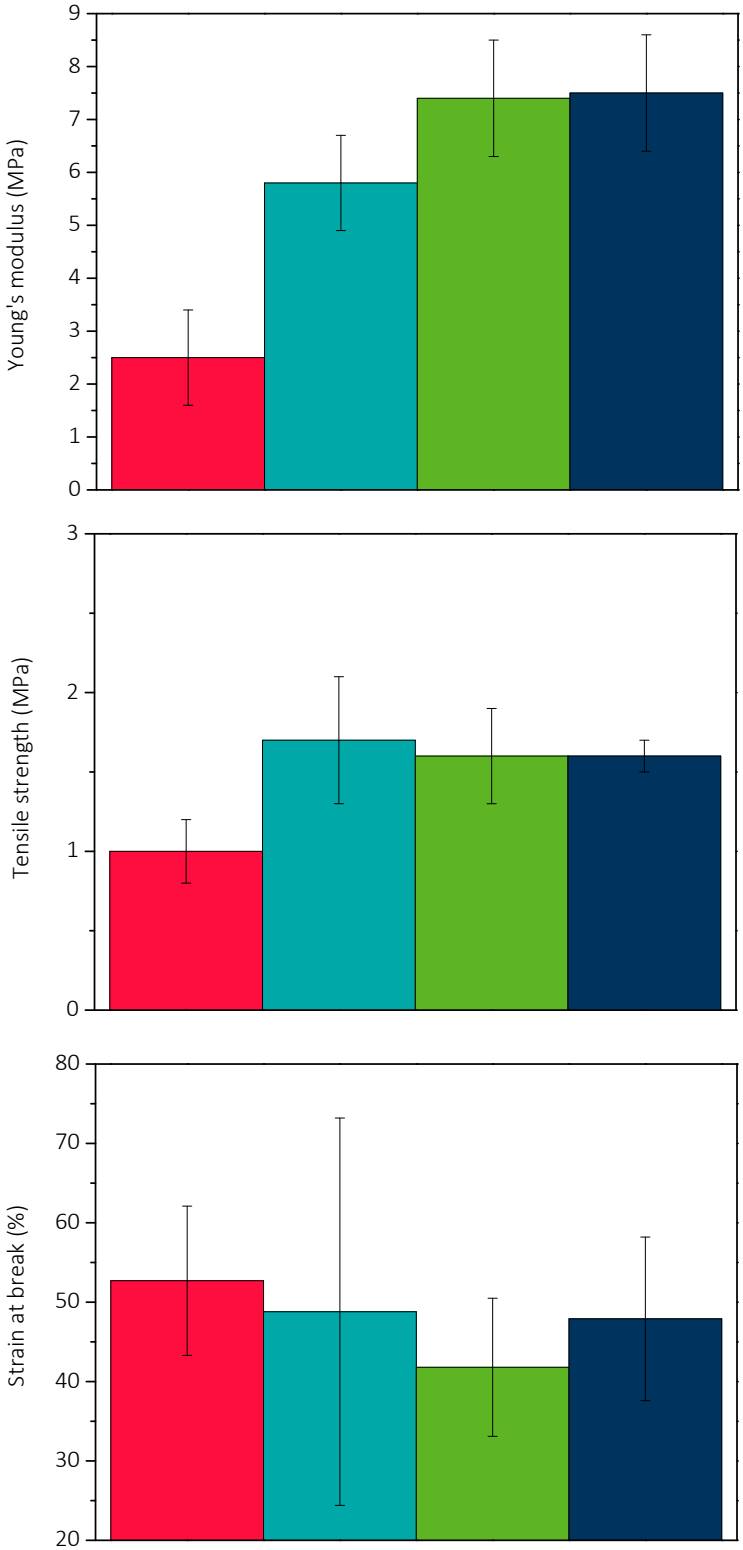

Figure 5.2 – Mechanical properties of ■ CSg35, ■ CSg35 - 1 (100/0), ■ CSg35 - 2.5 (100/0) and ■ CSg35 - 1 (100/0).

The addition of WSNC resulted in a significant improvement of the mechanical properties of the PLS matrix plasticised with glycerol. Indeed, the Young's modulus increased from 2.5 MPa for the unfilled PLS to 7.5 MPa for the bionanocomposites with 2.5 and 5 wt.% of WSNC and the tensile strength was improved in a 70%. Moreover, with both 2.5 and 5 wt.% of WSNC similar elongation at break values were measured. Due to the identical chemical nature of the matrix and the nanofiller, a good affinity between both components was observed as expected, allowing strong PLS/WSNC hydrogen bonding at the interface and the subsequent favourable reinforcing effect as also observed by DMA.

5.3.3. Barrier properties

The barrier properties of PLS based nanocomposites reinforced with polysaccharide NCs were analysed by WVP and OP measurements. Obtained results are collected in Table 5.1. The interest in the development of nanocomposites responds to the hypothesis that nanometric particles incorporated into the polymeric matrix would generate a tortuous path against vapour or gas and, consequently, the diffusive component of the permeability would decrease. However, besides the diffusion, barrier properties of polymers depend on the solubility coefficient which is associated with the polymer/plasticiser/NC/gas interactions [2–5]. Platelet-like WSNC are supposed to have good attributes in the improvement of barrier properties but, according to WVP, due to their hydrophilic nature, low crystallinity and possible agglomeration, opposite conclusions have been reported for their nanocomposites [6].

In our particular investigation, whereas WVP values were not reduced by the addition of WSNC, OP was significantly decreased for 2.5 and 5 wt.% of WSNC contents. Bertuzzi et al. [7] and Forssell et al. [8] correlated these results with sorbed water-starch interactions that are closely related with water transport phenomenon for high amylose maize starch, waxy maize starch and potato amylose films obtained by solvent casting. These interactions would not be generated with oxygen

molecules, and that could be why OP values were reduced. As it could be noted, whereas CSg35 and CSg35 - 1 (100/0) presented similar permeability to O_2, it was reduced to 1.0 ± 0.2 cm^3 mm m^{-2} day^{-1} atm^{-1} for 5 wt.% of WSNC content, suggesting that the presence of a minimum concentration was necessary to create an effective tortuous pathway. This significant barrier improvement for higher WSNC contents suggests that those were effectively dispersed in the PLS matrix and points out the good efficient interface adhesion between the NCs and the matrix. Thus, permeability results were in good agreement with results obtained from both DMA and tensile measurements.

Table 5.1 – Barrier properties of obtained PLS nanocomposite films reinforced with WSNC.

Sample	WVP (kg m m^{-2} s^{-1} Pa^{-1}) x 10^{13}	OP (cm^3 mm m^{-2} day^{-1} atm^{-1})
Sg35	6.8 ± 0.6	3.7 ± 0.1
CSg35 - 1.0 (100/0)	7.1 ± 0.4	2.9 ± 0.2
CSg35 - 2.5 (100/0)	5.1 ± 0.7	1.6 ± 0.5
CSg35 - 5.0 (100/0)	5.9 ± 0.3	1.0 ± 0.2

5.3.4. Thermogravimetric analysis

TGA measurements were carried out to assess the thermal decomposition of nanocomposites. TG and DTG curves are shown in Figure 5.3. As observed for PLS films in Section 3.4.7, the thermal decomposition process for as-prepared nanocomposites proceeds in three main steps [1,9]. The first step (25 – 100 °C) related to the loss of sorbed humidity, the second one (100 – 200 °C) associated to the decomposition of the glycerol-rich phase and the last one due to the oxidation of the partially decomposed starch (around 340 °C).

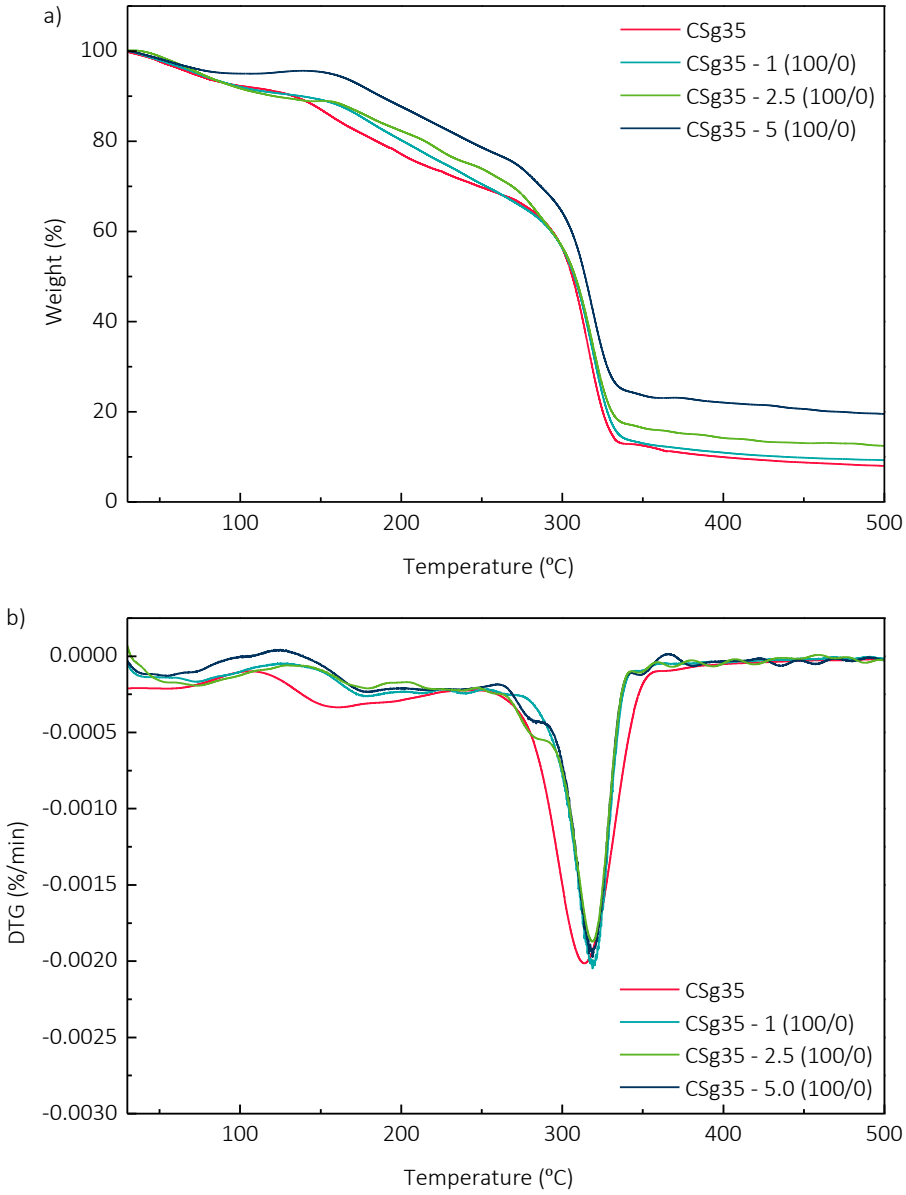

Figure 5.3 – a) TG and b) DTG curves of obtained PLS nanocomposite films reinforced with WSNC.

As observed, the thermal behaviour of the starch-based materials was influenced by the addition of WSNC. The thermal properties of polysaccharide NC are governed by their origin, the reaction conditions and the type of the surface modification [10]. Besides, it has been widely reported by other authors [11–13], that when polysaccharides are subjected to hydrolysis with sulfuric acid, sulphate groups are grafted to the surface of the resulting NC, leading to the decrease of their thermal stability. However, in our case the opposite effect was observed. Indeed, comparing

the thermal stability of the nanocomposites with that of the unfilled matrix, it was noticed that it was enhanced in all cases, which may be due to a good affinity between starch chains and NC in agreement with DMA results. It was appreciated that just the addition of a 1 wt.% of WSNC leaded to an improvement of the thermal stability. Focusing on the DTG curves the displacement of the main degradation temperature was noticeable and the appearance of a small shoulder was also appreciable. As mentioned in Chapter 4, the sulphate groups incorporated in the surface of WSNC after the hydrolysis could catalyse the main degradations step, which could be the reason for the apparition of the new shoulder that increased increasing the WSNC content.

It was concluded that the addition of polysaccharides increased the thermal stability compared with that of the unfilled matrix. At the same time, the final char percentage increased with the nanoreinforcement content which could be also related to the sulphate groups in the surface of the NCs.

5.4. COMBINATION OF POLYSACCHARIDE NANOCRYSTALS ON THE PROPERTIES OF PLS FILMS

The influence of the type of the NCs was analysed when WSNC and CNC were combined together in PLS matrix. 1 wt.% composition was chosen in order to better analysing any synergistic effect resulting from the simultaneous action of both NCs. This assumption lays on the fact that the platelet shape of WSNC would enhance barrier properties improvement [14], whereas rod-like high crystalline CNC would contribute in a higher extent to the mechanical reinforcement as they present higher crystallinity and aspect ratio. In this section nanocomposites were obtained by solvent casting technique.

5.4.1. Dynamic mechanical analysis

The influence of using together WSNC and CNC in the viscoelastic behaviour of nanocomposites was studied by DMA. Results are shown in Figure 5.4.

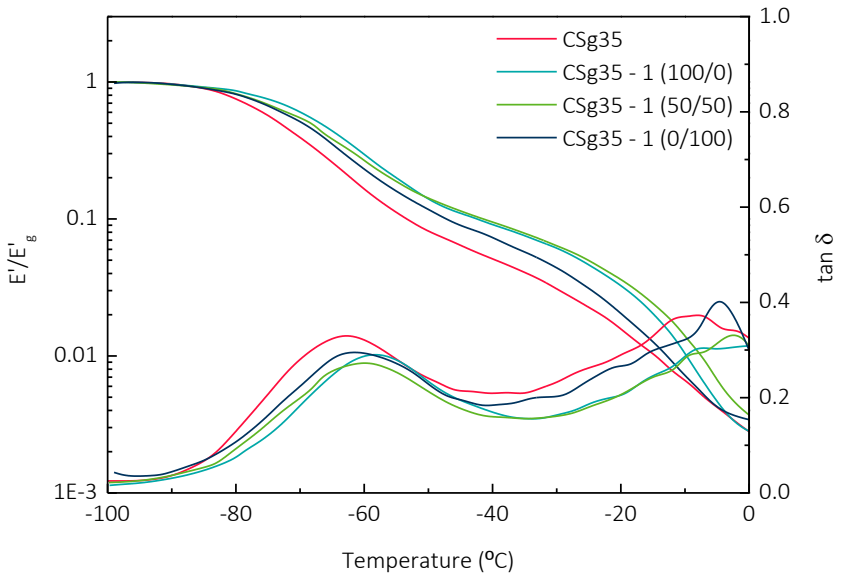

Figure 5.4 – Evolution of E'/E'$_g$ and tan δ with temperature of obtained PLS nanocomposite films reinforced combining WSNC and CNC.

Nanocomposites reinforced with WSNC and CNC showed the same viscoelastic pattern in comparison with films reinforced only with WSNC (Section 5.3.1). Indeed, almost identical DMA curves were obtained with the characteristic two-step modulus drop related to the two different phases. The addition of polysaccharide NCs resulted in higher relaxation temperature values of both phases whatever the NCs origin was. This effect could be ascribed to the fact that both WSNC and CNC interacted strongly with starch. However, higher shift was observed for nanocomposites containing WSNC. Regarding the E'/E'$_g$, higher values were also obtained for nanocomposite containing WSNC. These results confirmed the interaction of NCs with starch domains and the formation of an effective reinforcing network, especially with WSNC.

5.4.2. Mechanical properties

Mechanical behaviour of nanocomposites was evaluated by means of tensile tests. The obtained results are shown in Figure 5.5.

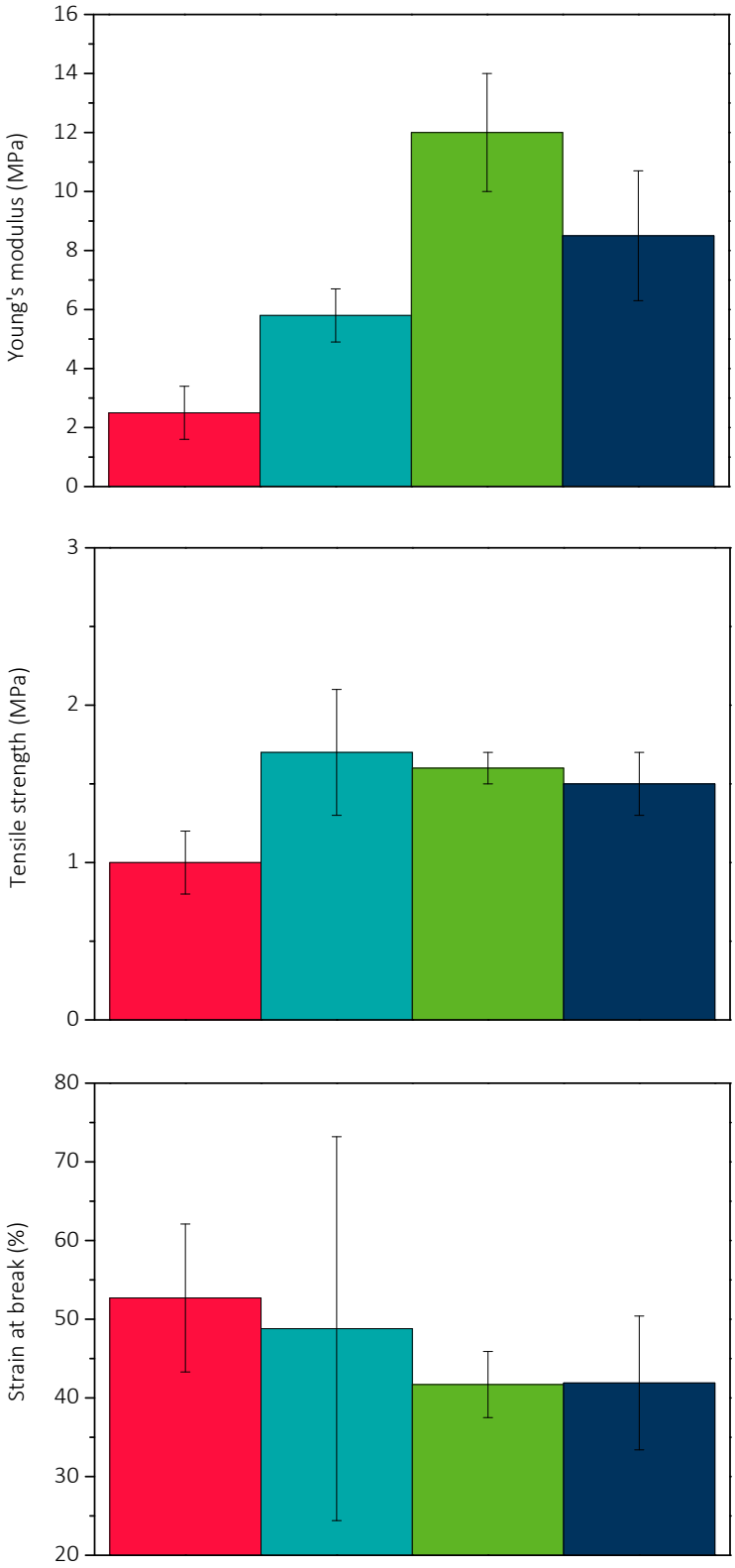

Figure 5.5 – Mechanical properties of ■ CSg35, ■ CSg35 - 1 (100/0), ■ CSg35 - 1 (50/50) and ■ CSg35 - 1 (0/100).

Some remarkable changes were detected when WSNC or CNC were added into the matrix. Firstly, higher values of Young's modulus were obtained for CNC filled nanocomposites at the same weight content. This finding agrees with the fact that higher stiffness was likely to be achieved by using higher crystallinity and aspect ratio rod-like NCs [15,16]. The opposite effect was detected for strain at break, as it was reduced in a larger extent. It is worth noting that the Young's modulus was considerably improved up to 12.0 MPa for the CSg35 - 1 (50/50) system, i.e. the one where WSNC and CNC were combined. Wang et al. [16] obtained similar results using waterborne polyurethane as matrix and nanoreinforced with starch and cellulose nanocrystals simultaneously. As they explained, the combination of both nanometric reinforcements would lead to a much jammed hydrogen bonding network between nanofiller and the matrix also in agreement with DMA results.

5.4.3. Barrier properties

The barrier properties of PLS nanocomposites reinforced with WSNC and/or CNC were analysed by WVP and OP measurements. Table 5.2 summarised the results of WVP and OP obtained for the nanocomposites containing WSNC and/or CNC. It is accepted that large nanoparticle aspect ratios are required to reduce the gas permeability by an appreciable degree [14]. However, attending to our results, it could be concluded that the incorporation of CNC to the nanocomposite did not improve the barrier properties. A comparable tendency was obtained by García et al. [9] for nanocomposites prepared based on a waxy maize starch matrix gelatinized with a similar glycerol content and reinforced with WSNC. On one hand, WVP seemed to be again governed by the strong chemical affinity of the material with water gaseous molecules. On the other hand, the higher aspect ratio and crystallinity of CNC did not reduce the OP values with only slight decrease for CSg35-1 (0/100), revealing that in the studied polysaccharide-based films, barrier properties improvement was more correlated to the nanofiller content than to the geometrical shape of the NC. Although the WVP and OP tend to decrease due to the addition of NC, the obtained

results are similar for all nanocomposite and may be due to the employed high plasticiser content, which as explained in Section 3.5.6 is a decisive factor in barrier properties.

Table 5.2 – Barrier properties of obtained PLS nanocomposite films reinforced combining WSNC and CNC.

Sample	WVP (kg m m^{-2} s^{-1} Pa^{-1}) x10^{13}	OP (cm^3 mm m^{-2} day^{-1} atm^{-1})
CSg35	6.8 ± 0.6	3.7 ± 0.1
CSg35 - 1 (100/0)	7.1 ± 0.4	2.9 ± 0.2
CSg35 - 1 (50/50)	6.1 ± 0.2	2.8 ± 0.2
CSg35 - 1 (0/100)	6.5 ± 0.3	2.5 ± 0.1

5.4.4. Atomic force microscopy

AFM was used for the morphological characterisation of the cryofractured surfaces of the nanocomposite samples (Figure 5.6).

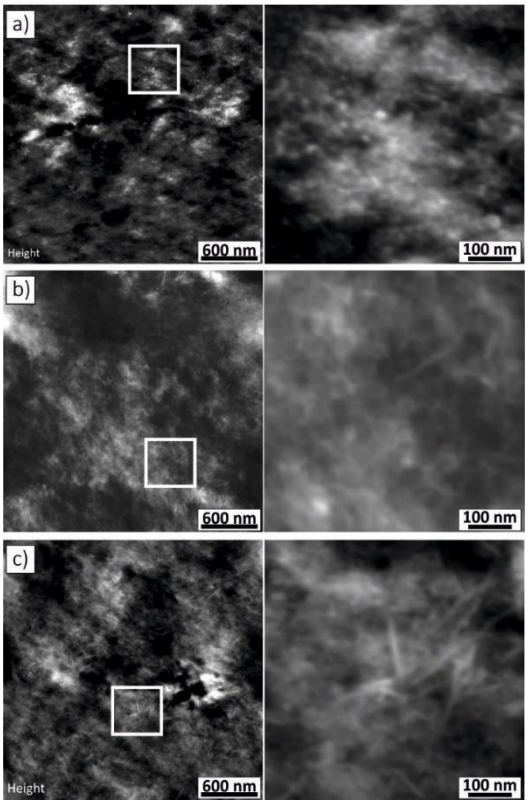

Figure 5.6 – AFM height images of CSg35 - 1 (100/0), CSg35 - 1 (50/50) and CSg35 - 1 (0/100). The white square indicates the magnified area shown in the right image.

In case of the CSg35-1 (100/0) sample, WSNC were observed as ill-defined nanoparticles due to their extremely reduced dimensions. However, focusing on the amplified image it was possible to observe the nanofillers individually and it could be concluded that NCs were correctly dispersed, in good agreement with the conclusions extracted previously.

5.5. EFFECT OF *WAXY* MAIZE STARCH NANOCRYSTALS CONTENT ON THE PROPERTIES OF TPS FILMS

Extruded starch-based nanocomposites were developed using glycerol and adding different amounts of WSNC (1, 2.5 and 5 wt.%). The nanocomposites were characterised evaluating the effect of WSNC content in the thermal stability, mechanical and barrier properties and morphology.

5.5.1. Dynamic mechanical analysis

The viscoelastic behaviour of TPS nanocomposites was analysed by DMA. In order to analyse the effect of the processing method both matrixes were represented together (Figure 5.7).

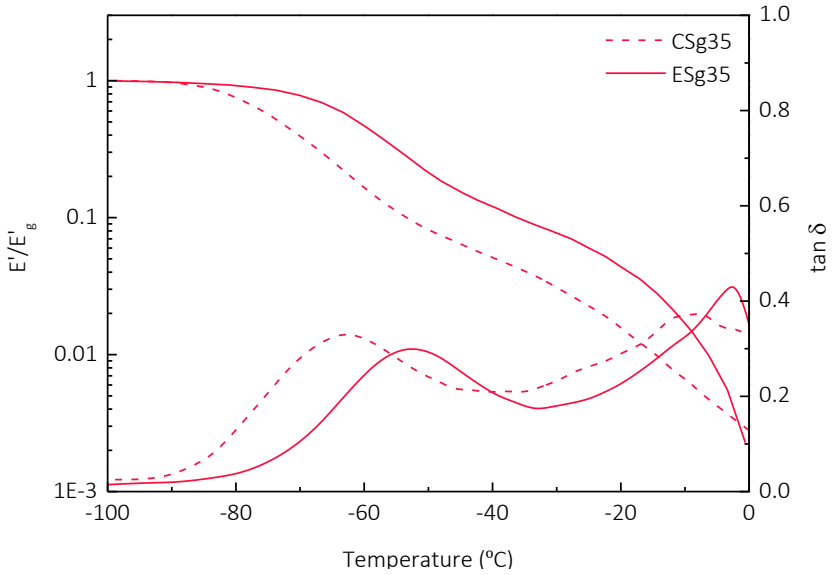

Figure 5.7 – Evolution of E'/E'$_g$ and tan δ with temperature of obtained CSg35 and ESg35 films.

It was observed that when the film is prepared by extrusion/compression technique, relaxation temperatures of both phases shifted to higher values, mainly the one correlated to the glycerol-rich phase. This could be as a result of the shear forces and the high processing temperatures employed during the extrusion and compression steps leading to strong interactions.

DMA results of the TPS reinforced with WSNC are shown in Figure 5.8. The most remarkable finding was the shift of the onset of $T_{\alpha 2}$ to higher values, especially in the case of 5 wt.% content indicating the proper integration of WSNC in the matrix and effective PLS/WSNC interactions. Indeed, it could be suggested that the WSNC were affecting preferably the mobility of the starch-rich phase, revealing enough hydrogen bonding interactions between the WSNC and amylose/amylopectin chains. However, it is worth noting that the intensity of the maximum of tan δ of glycerol-rich phase decreased with increasing amount the of WSNC, specially upon the addition of 5 wt.% content, indicating a decrease of the relaxed glycerol molecules during the transition. Although the reported literature with WSNC is scarce, the behaviour of the two main relaxations of the glycerol plasticised TPS is in agreement with that reported by Angellier et al. [17].

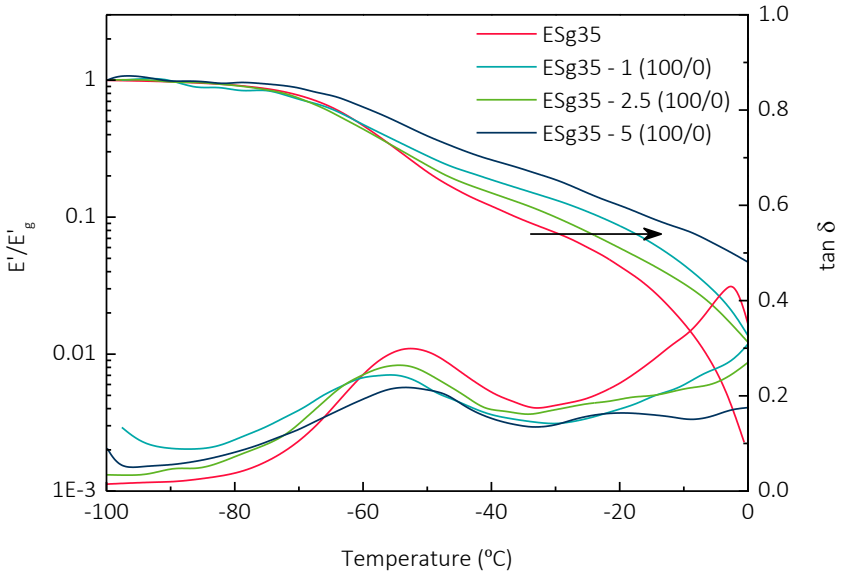

Figure 5.8 – Evolution of E'/E'$_g$ and tan δ with temperature of obtained TPS nanocomposite films reinforced with WSNC.

5.5.2. Mechanical properties

The reinforcing effect of WSNC into the TPS was evaluated by tensile test tests (Figure 5.9).

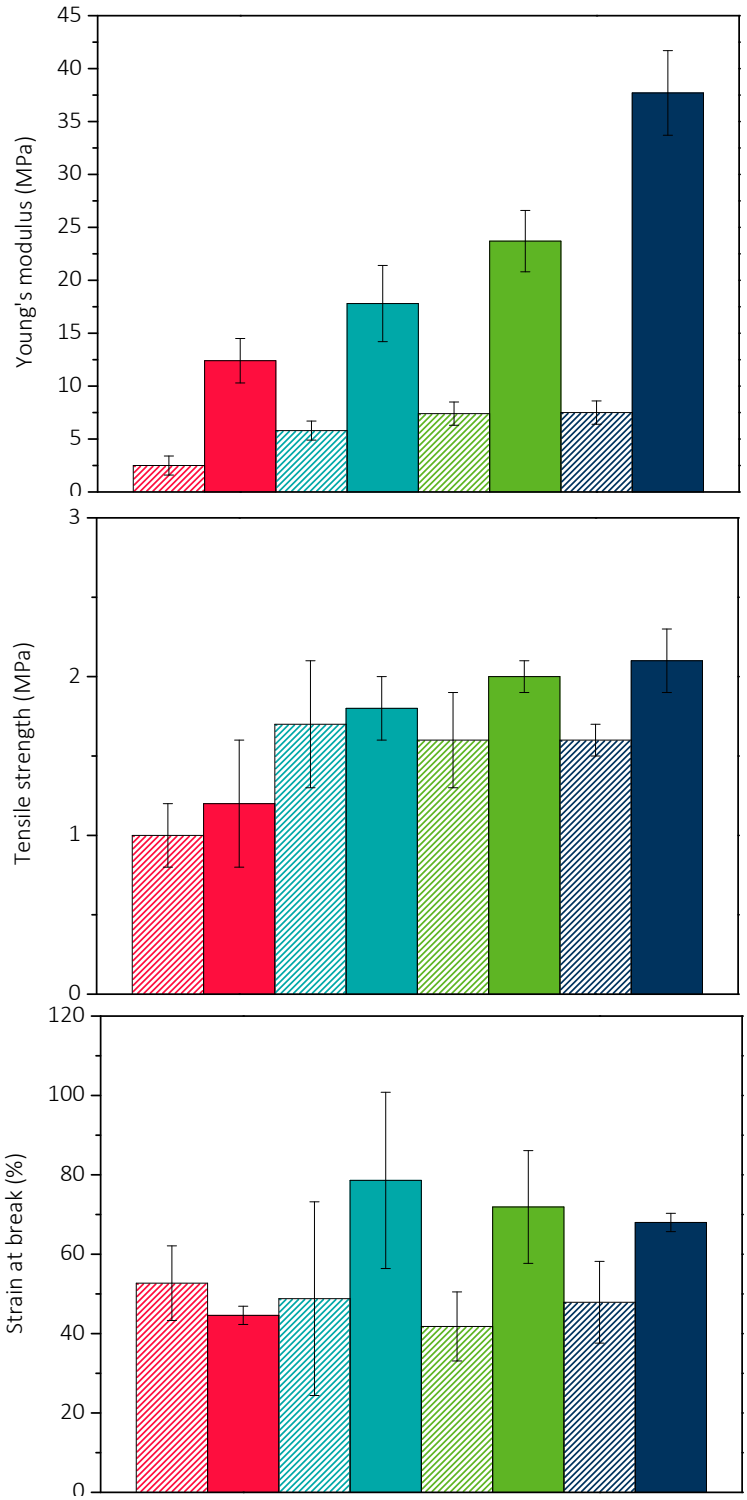

Figure 5.9 – Mechanical properties of obtained nanocomposite films reinforced with ■ 0 wt.% of WSNC, ■ 1 wt.% of WSNC, ■ 2.5 wt.% of WSNC and ■ 5 wt.% of WSNC and obtained by solvent casting (striped pattern) and extrusion/compression (filled pattern).

The Young's modulus of all nanocomposites reinforced with WSNC increased as the nanofiller content increased. In addition, the nanocomposites presented significantly higher elongation at break values comparing to the unfilled TPS. This improvement demonstrated the suitability of extrusion/compression to reach a good integration and a good affinity between the matrix and the nanoreinforcement, expected due to their identical chemical structure, thus revealing strong interfacial interactions that resulted in the effective transmission of mechanical stress. It is worth noting that even though upon the addition of 1 wt.% of WSNC the strain at break value slightly trended to decrease, whereas the tensile strength value continued increasing. Thus, it could be concluded that the presence of WSNC up to the used 5 wt.% provided a significant enhancement of the area under the curves, improving the toughness of the films.

It should be mentioned that comparing the results of films obtained by extrusion/compression with their analogues obtained by solvent casting (presented in Section 5.3.3), considerably higher Young's modulus, tensile strength and strain at break values were obtained for those extruded films, indicating the good integration of the nanoreinforcement.

5.5.3. Barrier properties

The barrier properties of nanocomposites reinforced with WSNC were evaluated by WVTR and OTR measurements. As it was seen for PLS films, the WVP was not strongly influenced by the addition of WSNC. Similar WVP values were obtained for all nanocomposites, around 12.5 x 10^{-13} kg m m^{-2} s^{-1} Pa^{-1}. This fact suggested that WVP was mostly dependent on the strong starch/water interactions. Besides, as explained for solvent casting results, the high plasticiser content used could be also affecting the barrier properties.

Regarding the OP results, it was expected that the increase of WSNC content could led to the decrease of the OP values, due to the capacity of these platelet-like NCs to generate a tortuous path for the O_2 molecules, decreasing the diffusivity, as long as a good dispersion of the nanofiller and

appropriate nanofiller/matrix interface were achieved. In this sense, the OP of the TPS with the highest WSNC content was evaluated. A reduction of around 80% in the OP value was seen for the TPS nanocomposite containing 5 wt.% of WSNC, from (10.9 ± 3.9) to (2.0 ± 0.3) cm^3 mm m^{-2} day^{-1} atm^{-1} for ESg35 and ESg35 – 5 (100/0), respectively. In addition, by comparing the WVP and OP results obtained by the two processing methods, the extruded and compressed films presented higher permeability values.

5.5.4. Thermogravimetric analysis

The thermal stability of TPS nanocomposites was also studied by TGA and the obtained TG and DTG curves are presented in Figure 5.10.

The thermal degradation process of all nanocomposites followed the same pattern than the TPS matrix plasticised with glycerol and PLS nacocomposite films. It is worth noting that the appearance of the shoulder was also observed for extruded samples. In this case, the main transition was not shifted and thus the shoulder was not so appreciable. In addition, no further enhancement was achieved for ESg35 - 2.5 (100/0) and ESg35 - 5.0 (100/0) samples. Thus, it was demonstrated that despite using higher contents than 1 wt.% of WSNC, the thermal stability remained constant.

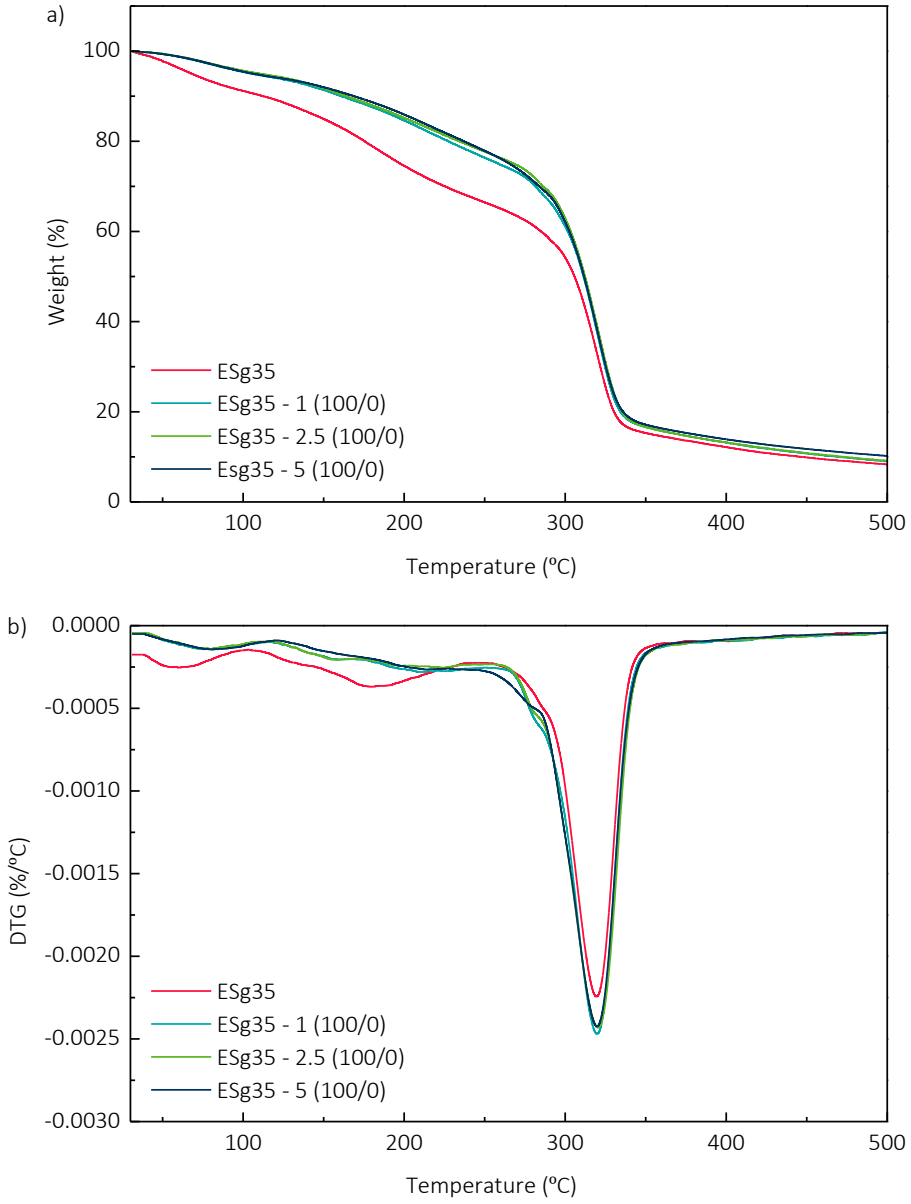

Figure 5.10 – a) TG and b) DTG curves of obtained TPS nanocomposite films reinforced with WSNC.

5.6. COMBINATION OF POLYSACCHARIDE NANOCRYSTALS ON THE PROPERTIES OF TPS FILMS

The effect of 1 wt.% of reinforcement combining WSNC and CNC in different proportions was also evaluated. TPS films were processed following the previous gelatinisation-lyophilisation-extrusion-compression methodology and resulting films were characterised in terms of thermal, mechanical and barrier properties.

5.6.1. Dynamic mechanical analysis

The viscoelastic response of TPS films reinforced by combining both NCs was evaluated by DMA. The obtained E'/E_g and tan δ curves against temperature are presented in Figure 5.11. In a similar way that observed for the viscoelastic properties of TPS reinforced with WSNC (Section 5.5.1), the glycerol chains that relaxed during the first transition decreased as CNC were incorporated, resulting in a slight decrease of the intensity of the maximum of the tan δ. Regarding the effect of NCs type, a shift to higher temperatures of $T_{\alpha 1}$ was observed for nanocomposites reinforced with CNC, which could be attributed to the mobility restrictions imposed by high aspect ratio NCs. Concerning the relaxation of the starch-rich phase, although a shift of the respect to the infilled matrix was observed for $T_{\alpha 2}$, similar values were measured in all samples reinforced with 1 wt.% WSNC/CNC, being not dependent on the type of nanoreinforcement. Regarding E'/E'$_g$, similar values were obtained for nanocomposites, independent on the NCs type, but higher than the unfilled matrix, corroborating the reinforcing effect of NCs.

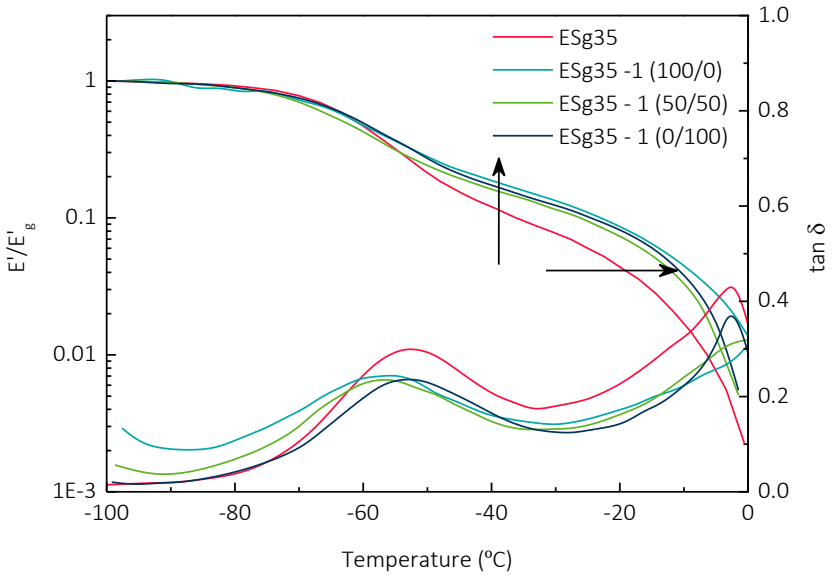

Figure 5.11 – Evolution of E'/E'$_g$ and tan δ with temperature of obtained TPS nanocomposite films reinforced combining WSNC and CNC and obtained by extrusion/compression.

5.6.2. Mechanical properties

The effect of adding both CNC and WSNC in TPS was assesed by tensile tests (Figure 5.12).

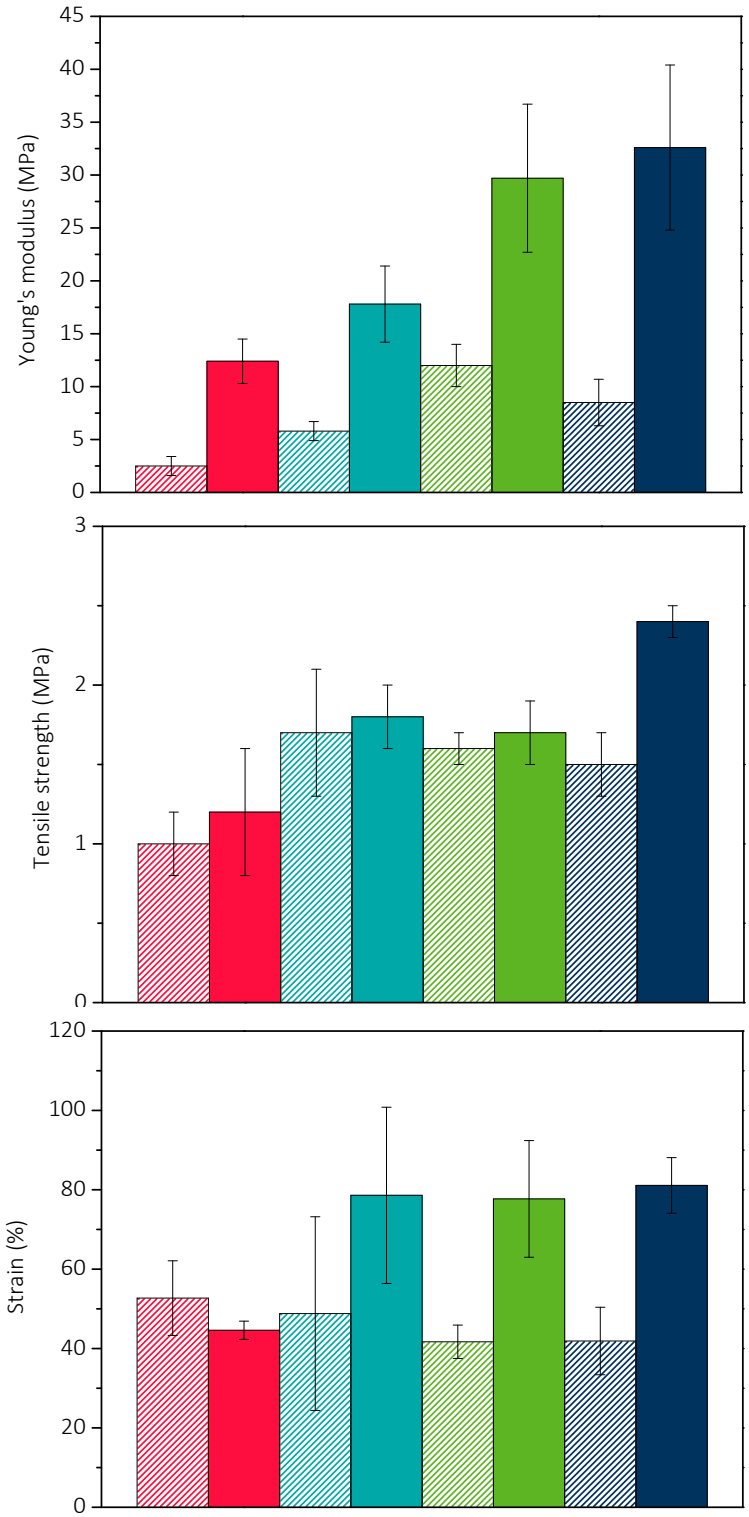

Figure 5.12 – Mechanical properties of obtained nanocomposite films reinforced with ■ 0 wt.% of WSNC, ■ 1 wt.% of NC (0/100), ■ 1 wt.% of NC (50/50) and ■ 1 wt.% of NC (0/100) and obtained by solvent casting (striped pattern) and extrusion/compression (filled pattern).

The incorporation of CNCs into the TPS matrix resulted in higher Young's modulus and maximum strength values. In fact, when CNC were used as nanoreinforcement, the Young's modulus increased from 17.8 ± 3.6 MPa for ESg35 – 1 (100/0) up to 32.6 ± 7.8 MPa for ESg35 – 1 (0/100) and the tensile strength increased from 1.8 ± 0.2 MPa up to 2.4 ± 0.1 MPa. Indeed, as shown in Figure 5.12, the values obtained for the film nanoreinforced with only 1 wt.% of CNC were similar to those obtained when adding 5 wt.% of WSNC. This would be related to the high crystallinity degree of CNC which was demonstrated to be near 80%, significantly higher than that for WSNC (close to 20%) (Section 4.3.1). Besides, the rod-like geometry and the high aspect ratio of CNC facilitated the interactions with the matrix and the effective improvement of the mechanical properties.

5.6.3. Barrier properties

The barrier properties of the prepared TPS nanocomposite containing WSNC and CNC were gravimetrically studied by OTR measurements. As discussed previously, the addition of polysaccharide NCs did not improved the WVP, since it is manly governed by starch/water interactions.

On the contrary, when focusing in the OP properties, it was observed that the permeability value decreased due to the incorporation of CNC into the TPS matrix. OP values of 7.1 ± 0.6 cm^3 mm m^{-2} day^{-1} atm^{-1} was measured for the ESg35 – 1 (0/100) sample. However, as hypothesised, the WSNC showed greater effectiveness in the decrease of the permeability against O_2 molecules due to their platelet-shape morphology. Furthermore, it should be pointed that adding 1 wt.% of WSNC, the OP value decreased up to 4.4 ± 1.0 cm^3 mm m^{-2} day^{-1} atm^{-1}, evidencing the importance of nanoreinforcement morphology. Besides, it should be mentioned that lower OP values were achieved for samples obtained by solvent casting, especially for PLS films containing 1 wt.% of CNC.

5.7. CONCLUSIONS

Starch-based nanocomposite films were successfully obtained by adding WSNC in different amounts and by using together WSNC and CNC as nanoreinforcements. Both solvent casting and extrusion/compression techniques were satisfactorily employed in a feasible way.

Regarding the nanocomposites obtained by solvent casting, it was demonstrated that the addition of NCs increased the thermal stability of all samples. The mechanical properties of the nanocomposites reinforced with WSNC were clearly higher than those of the unfilled matrix. Besides, it was demonstrated that the mechanical properties were also remarkably enhanced with the addition of CNC, due to the reinforcement ability of CNC. Regarding the barrier properties, similar WVP values were obtained for all nanocomposites, suggesting that WVP is more influenced by starch/plasticiser/water interactions than by nanofiller type and content. However, the OP values decreased after the addition of both WSNC and CNC, revealing the strong dependency on the NC morphology. The DMA results showed that the addition of WSNCs resulted in stronger affinity between the matrix and the nanofiller, according to the enhancement achieved for the mechanical properties.

Similarly, when nanocomposites were obtained by extrusion/compression, the mechanical properties were remarkably enhanced due to the addition of NCs, especially with the incorporation for highly crystalline fibrillar CNC even at low contents. The DMA results showed that in the case of extruded and compressed films, the phase that was more affected by the NCs was the starch-rich phase, especially for high WSNC contents. Overall, it could be concluded that the PLS films presented better barrier properties, while the TPS films showed enhanced mechanical behaviour.

5.8. REFERENCES

[1] N.L. Garcia, L. Ribba, A. Dufresne, M.I. Aranguren, S. Goyanes, Physico-Mechanical properties of biodegradable starch nanocomposites, Macromol. Mater. Eng. 294 (2009) 169–

177. doi:10.1002/mame.200800271.

[2] M.A. Bertuzzi, M. Armada, J.C. Gottifredi, Physicochemical characterization of starch based films, J. Food Eng. 82 (2007) 17–25. doi:10.1016/j.jfoodeng.2006.12.016.

[3] A.P. Mathew, A. Dufresne, Plasticized waxy maize starch: Effect of polyols and relative humidity on material properties, Biomacromolecules. 3 (2002) 1101–1108.

[4] A. Cano, A. Jiménez, M. Cháfer, C. Gónzalez, A. Chiralt, Effect of amylose:amylopectin ratio and rice bran addition on starch films properties, Carbohydr. Polym. 111 (2014) 543–555. doi:10.1016/j.carbpol.2014.04.075.

[5] R.P. Herrera Brandelero, F. Yamashita, M.V. Eiras Grossmann, The effect of surfactant Tween 80 on the hydrophilicity, water vapor permeation, and the mechanical properties of cassava starch and poly(butylene adipate-co-terephthalate) (PBAT) blend films, Carbohydr. Polym. 82 (2010) 1102–1109. doi:10.1016/j.carbpol.2010.06.034.

[6] D. Le Corre, A. Dufresne, Starch Nanoparticles : A Review Starch Nanoparticles : A Review, (2010) 1139–1153. doi:10.1021/bm901428y.

[7] M.A. Bertuzzi, E.F. Castro Vidaurre, M. Armada, J.C. Gottifredi, Water vapor permeability of edible starch based films, J. Food Eng. 80 (2007) 972–978. doi:10.1016/j.jfoodeng.2006.07.016.

[8] P. Forssell, R. Lahtinen, M. Lahelin, P. Myllärinen, Oxygen permeability of amylose and amylopectin films, Carbohydr. Polym. 47 (2012) 125–129.

[9] N.L. García, L. Ribba, A. Dufresne, M. Aranguren, S. Goyanes, Effect of glycerol on the morphology of nanocomposites made from thermoplastic starch and starch nanocrystals, Carbohydr. Polym. 84 (2011) 203–210. doi:10.1016/j.carbpol.2010.11.024.

[10] N. Lin, J. Huang, A. Dufresne, Preparation, properties and applications of polysaccharide nanocrystals in advanced functional nanomaterials: a review, Nanoscale. 4 (2012) 3274–3294. doi:10.1039/c2nr30260h.

[11] J. Huang, P.R. Chang, A. Dufresne, Polysaccharide Nanocrystals : Current Status and Prospects, (2015) 1–14.

[12] B. Montero, M. Rico, S. Rodríguez-Llamazares, L. Barral, R. Bouza, Effect of nanocellulose as a filler on biodegradable thermoplastic starch films from tuber, cereal and legume, Carbohydr. Polym. 157 (2017) 1094–1104. doi:10.1016/j.carbpol.2016.10.073.

[13] V.K. Shivaraju, S. Vallayil Appukuttan, S. Kumar, The Influence of Bound Water on the FTIR Characteristics of Starch and Starch Nanocrystals Obtained from Selected Natural Sources, Starch/Staerke. 1700026 (2018) 1–9. doi:10.1002/star.201700026.

[14] T. V. Duncan, Applications of nanotechnology in food packaging and food safety: Barrier materials, antimicrobials and sensors, J. Colloid Interface Sci. 363 (2011) 1–24. doi:10.1016/j.jcis.2011.07.017.

[15] W.P. Flauzino Neto, H.A. Silvério, N.O. Dantas, D. Pasquini, Extraction and characterization of cellulose nanocrystals from agro-industrial residue - Soy hulls, Ind. Crops Prod. 42 (2013) 480–488. doi:10.1016/j.indcrop.2012.06.041.

[16] Y. Wang, H. Tian, L. Zhang, Role of starch nanocrystals and cellulose whiskers in synergistic reinforcement of waterborne polyurethane, Carbohydr. Polym. 80 (2010) 665–671. doi:10.1016/j.carbpol.2009.10.043.

[17] H. Angellier, L. Choisnard, S. Molina-Boisseau, P. Ozil, A. Dufresne, Optimization of the preparation of aqueous suspensions of waxy maize starch nanocrystals using a response surface methodology, Biomacromolecules. 5 (2004) 1545–51. doi:10.1021/bm049914u.

CHAPTER 6:

NANOCOMPOSITE FILMS BASED ON STARCH AND CARBONACEUS NANOPARTICLES

6. NANOCOMPOSITE FILMS BASED ON MAIZE STARCH AND CARBONACEUS NANOPARTICLES

6.1. OBJECTIVE

The aim of this chapter was the development of PLS nanocomposite films plasticised with glycerol and reinforced using carbonaceous nanoparticles, i.e. graphene (G) and graphene oxide (GO). In this case, nanocomposites were prepared by solvent casting procedure. On one hand, the influence of adding different G contents into the PLS matrix was analysed. In order to improve the stability of G nanoflakes in the aqueous gelatinization media, Salvia extracts were added as natural surfactants.

On the other hand, GO was also incorporated as nanofiller to prepare PLS nanocomposites. Thus, the effect of increasing the GO content in the final behaviour of the PLS nanocomposites was evaluated. Besides, the resulting nanocomposites were reduced with ascorbic acid in order to enhance its electrical properties.

All the obtained PLS nanocomposites were characterised in terms of chemical and crystalline structures, optical and surface properties as well as thermal stability and mechanical behaviour. Besides, the electrical conductivity was evaluated.

6.2. OBTAINMENT OF STARCH/CARBONACEUS NANOPARTICLES-BASED FILMS

6.2.1. Obtainment of Salvia extracts

The preparation of Salvia extracts was carried out by infusion method according to the protocol described by Santamaria-Echart et al. [1]. Briefly, 20g of *Salvia officinalis* L. were boiled with 800 ml of distilled water for 5 min. After that, the obtained suspension was filtered and freeze-dried.

6.2.2. Preparation of nanocomposite films based on PLS and carbonaceous nanoparticles

The nanocomposites containing carbonaceous nanoparticles were prepared by solvent casting following the procedure described in Section 3.2.1 with slight modifications. 3.58 g of normal maize starch and 1.93 g of glycerol were mixed with 55 mL of distilled water. Besides, the desired amount of carbonaceous nanoparticles previously dispersed was also incorporated and all the mixture was gelatinized at 90 °C with continuous stirring until viscosity increased (about 30 min). The resulting viscous gel was homogenised using a dispersing system (POLYTRON® PT 2500 E) during 3 min at 15,000 rpm. Finally, the material was spread into glass petri and dried at 45 °C for 3.5 h.

Both G and GO were dispersed by ultrasonication using a concentration of 5 mg of carbonaceous nanoparticle mL^{-1} of distilled water. For the dispersion of G nanoflakes 2.5 mg of Salvia extracts mL^{-1} distilled water were added as stabiliser.

Samples were called as CSg35 plus the carbonaceous nanoparticle content, indicating GE or GO if G and extracts or GO was used (CSg35 - wt.% GE or CSg35 - wt.% GO).

A glycerol content of 35 wt.% was used for all samples, i.e. relative to the starch plus plasticiser mixture weight. The nanofiller and Salvia extract contents were relative to the starch plus glycerol weight. All the samples were stored at 43% RH for two weeks before characterisation.

6.2.3. Reduction of graphene oxide

The reduced graphene oxide (rGO) was obtained using ascorbic acid as reduction agent. Thus, the nanocomposites containing GO (obtained in Section 6.2.2) were submerged in a solution of 30 g of ascorbic acid L^{-1} of distilled H_2O at 95 °C for 2 h. After that, in order to remove the excess of ascorbic acid, the films were washed several times with distilled water. Finally, the films were dried at

room temperature for 24 h. Samples were named as CSg35 plus the rGO content rGO (CSg35 - wt.% rGO).

All the samples were stored at 43% relative humidity (RH) with a K_2CO_3 saturated solution for two weeks before characterisation.

6.3. EFFECT OF GRAPHENE CONTENT ON THE PROPERTIES OF PLS NANOCOMPOSITE FILMS

PLS nanocomposite films were obtained adding G nanoflakes into the starch-based matrix gelatinised with glycerol. In order to improve the poor dispersibility of G in water, natural Salvia extracts were used as dispersion stabiliser since they present high content of polyphenolic groups. It was expected that the final properties of the material would be dependent of the G and extract content. Thus, the nanocomposites were prepared using different G and Salvia extracts contents (1, 2.5 and 5 wt.%).

6.3.1. Fourier transform infrared spectroscopy

FTIR measurements were carried out to analyse the chemical structure of PLS films and obtained nanocomposites reinforced with G nanoflakes. The obtained FTIR spectra of Salvia extracts, PLS films and the resulting nanocomposites are shown in Figure 6.1.

As observed in the spectra, the unfilled PLS matrix showed the stretching band of hydrogen bonded -OH groups at 3280 cm^{-1}, whereas the -OH bending appeared at 1650 cm^{-1} [2,3]. The C-H stretching band related to methylene ($-CH_2$) groups was centred at 2927 cm^{-1} [2,3]. In addition, in the fingerprint region of starch the following peaks were observed: the stretching vibration band of C-O bonds of the C-O-H groups at 1150 cm^{-1} and the stretching vibration bands of C-O in C-O-C groups located at 1077 cm^{-1} and 997 cm^{-1} [4].

Regarding the reinforced nanocomposite films, only slight differences could be observed. As it could be noticed the addition of G and Salvia extracts resulted in the widening and shifting to lower wavenumber value of the band associated with -OH bending. This effect could be related to the contribution of hydrophilic Salvia extracts that showed an intense band related with -OH bending ascribed to moisture. In addition, the small peak that appeared at 1575 cm^{-1} would be related to the double bonds (C=C) of the phenolic groups from Salvia [5] and aromatic structure of G ring [6].

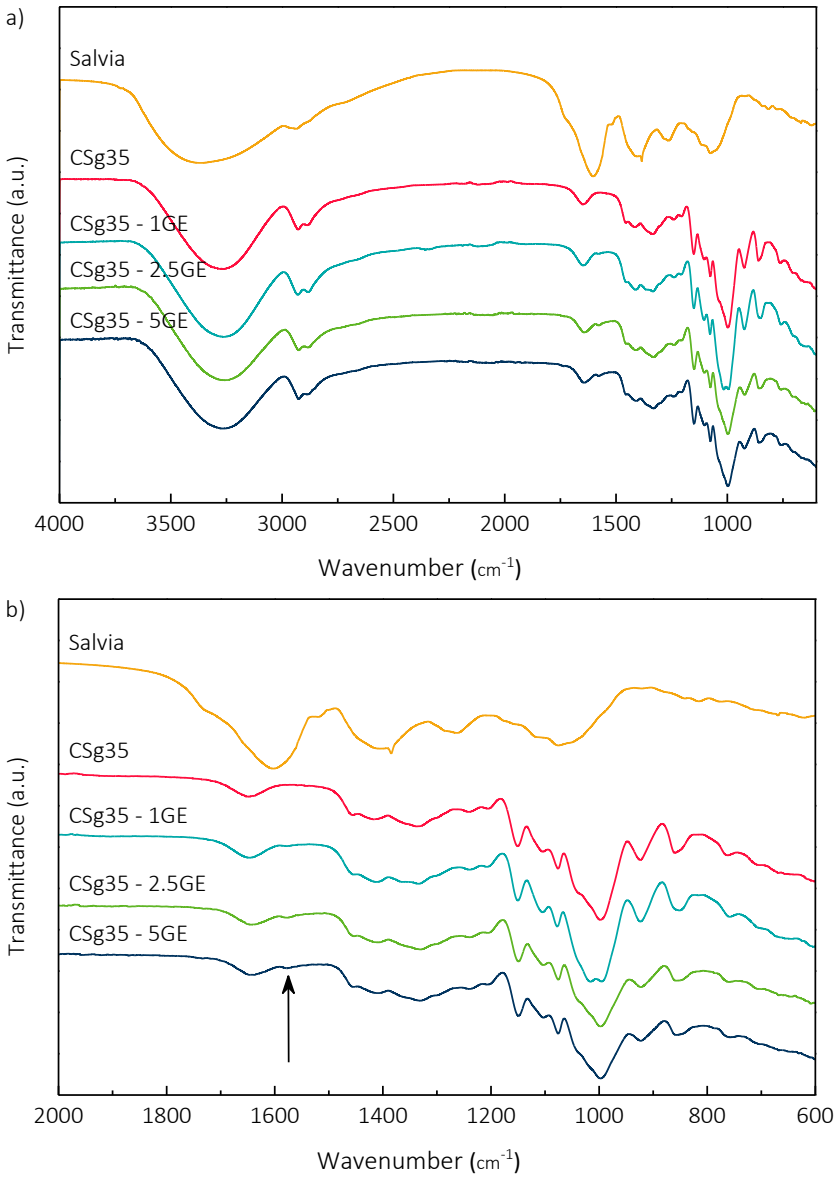

Figure 6.1 - FTIR spectra of Salvia extracts and PLS nanocomposite films reinforced with G in the range of a) 4000 – 600 cm^{-1} and b) a magnification in the range of 2000 – 600 cm^{-1}.

6.3.2. X-ray diffraction

XRD measurements were carried out in order to analyse the crystalline structure of the nanocomposites. Figure 6.2 presents the XRD pattern of unfilled PLS matrix and the nanocomposites obtained with G nanoflakes.

As it could be appreciated, the A-type polymorphism pattern of the native normal maize starch was replaced by a typical broad peak close to $2\theta = 19.8^{\circ}$ in the case of the amorphous PLS matrix. However, in all nanocomposites a new peak associated with G was observed at $2\theta = 26.5^{\circ}$ related to the (002) plane of the hexagonal structure of pure graphite. As expected, the intensity of the mentioned new peak increased as the G content increased, indicating that the crystalline structure of G was not affected by the gelatinisation and drying procedures.

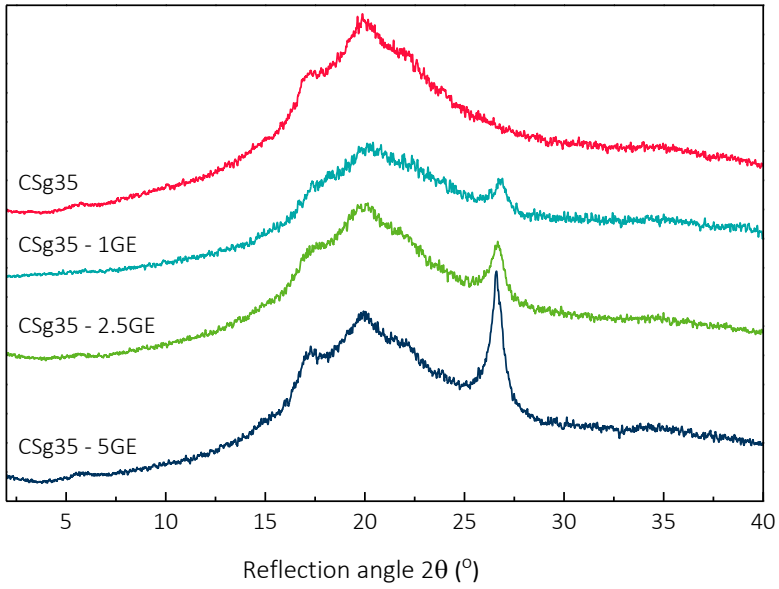

Figure 6.2 – XRD patterns of PLS nanocomposite films reinforced with G.

6.3.3. Optical properties

The optical properties of prepared nanocomposites were analysed in terms of light transmittance and surface colour, which are decisive factor from a commercial point of view in

packaging applications and consumer acceptance [7–9]. The transmittance value of each sample was measured by UV-vis spectroscopy in the visible spectrum range 400 - 700 nm whereas the colour was analysed using a spectrophotometer. Results are shown in Figure 6.3 and Table 6.1.

As demonstrated by the results, the addition of G led to a drastic reduction of the transparency of the material. The unfilled PLS matrix presented 36.9% of transmittance in the visible scan range and just the incorporation of the 1 wt.% of G resulted in the decreased of the transmittance value to 0%, leading to total opaque films. Only the pattern of CSg35 - 1GE is shown because the curves of the other samples were superimposed.

The colour of the films was evaluated according to CIELAB colour parameters (L^*, a^*, b^*). Besides, the colour difference parameter (ΔE) was calculated by Equation 2.3. As it could be observed, the lightness (L^*) decreased remarkably for all nanocomposites compared with that of the unfilled matrix due to the incorporation of dark nanoparticles. In addition, the chromaticity parameters (a^* and b^*) were also affected by the incorporation of G nanoflakes: a^* increased upon the addition of 1 wt.% of G but decreased for higher contents and b^* became more negative with increasing G content. Thus, indicating that increasing the G content, films become specifically more greenness and more blueness, respectively. As expected, all nanocomposites presented significantly higher ΔE values (around $\Delta E \approx 70$) compared with that of the unfilled matrix ($\Delta E = 23.72$), evidencing the colour difference between the matrix and the nanocomposites.

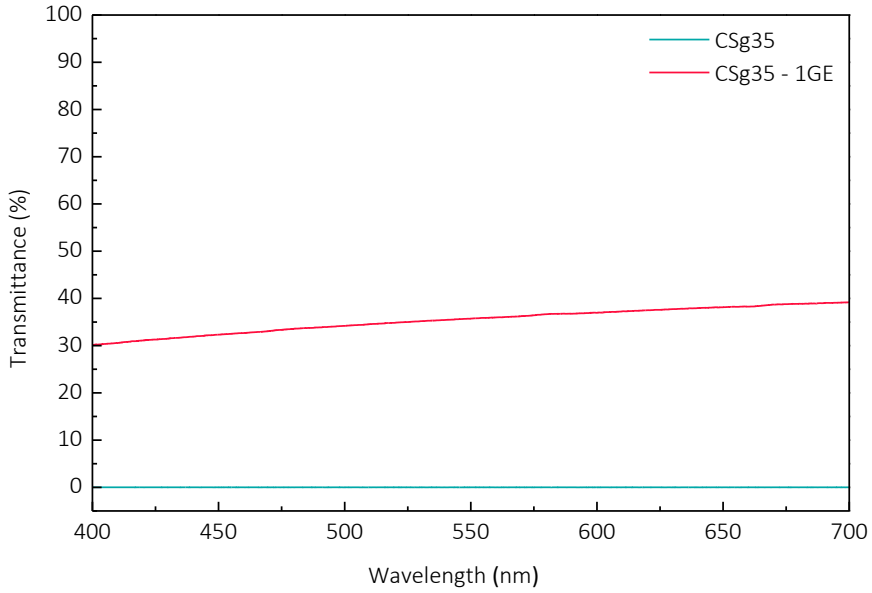

Figure 6.3 – UV-vis transmittance measurements of PLS nanocomposite film reinforced with 1 wt.% of G.

Table 6.1 – Transmittance values and colour parameters of PLS nanocomposite films reinforced with G.

Sample	Transmittance (%)	L^*	a^*	b^*	ΔE
CSg35	36.9	69.24 ± 0.50	-1.40 ± 0.04	3.00 ± 0.04	23.72 ± 0.50
CSg35 - 1GE	0.0	18.17 ± 0.15	-0.06 ± 0.01	-0.53 ± 0.01	74.67 ± 0.15
CSg35 - 2.5GE	0.0	20.60 ± 0.76	-0.30 ± 0.01	-1.32 ± 0.01	72.24 ± 0.76
CSg35 - 5GE	0.0	23.08 ± 0.14	-0.35 ± 0.03	-1.54 ± 0.16	69.77 ± 0.14

6.3.4. Surface properties

Contact angle measurements were carried out in order to characterise the surface properties and the hydrophobicity of the nanocomposite films. Figure 6.4 shows the contact angle measurements of PLS films and G and extracts containing nanocomposites.

As it could be observed in Figure 6.4, the unfilled PLS matrix showed low contact value (24.6°) due to the high hydrophilic character of starch [10]. However, upon the addition of the 1 wt.% of G, the contact angle increased to 37.2°. The incorporation of higher content of G resulted

in a slight decrease of the contact angle values. Although it could be expected that the addition of G could decrease the wettability due to its hydrophobic character (as observed by FTIR), the presence of hydroxyl groups in the Salvia extracts used to disperse and stabilise the hydrophobic G in the starch matrix, contributed to reduce slightly the effect of G.

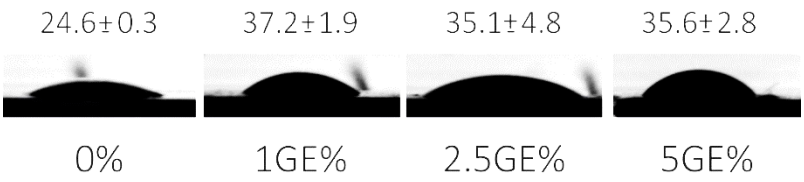

Figure 6.4 – Contact angle measurements of PLS nanocomposite films reinforced with G.

6.3.5. Dynamic mechanical analysis

The viscoelastic behaviour of PLS nanocomposites reinforced with G was studied by DMA analysis. The evolution of E'/E'_g and tan δ with temperature are shown in Figure 6.5.

As it could be observed, all nanocomposites presented the same viscoelastic pattern of the unfilled matrix. In the case of $T_{\alpha 1}$ the relaxation temperature was not influenced by the incorporation of G and Salvia extracts and remains almost constant for high nanofiller contents. It was also observed that $T_{\alpha 2}$ temperature depends on the G and Salvia extracts content. Lower $T_{\alpha 2}$ values were obtained for CSg35 – 1GE, whereas the value increased for CSg35 – 5GE samples. This fact suggested that G and Salvia extracts influenced the relaxation of starch-rich phase, being the plasticising effect of Salvia more remarkable at low G contents. However, as G content increased the reinforcing effect is more important over plasticising effect and thus $T_{\alpha 2}$ tended to higher values. In addition, the incorporation of G nanoflakes and Salvia extracts led to a decrease of E'/E'_g for low contents, but also increased as G content increased behaving as reinforcing agent.

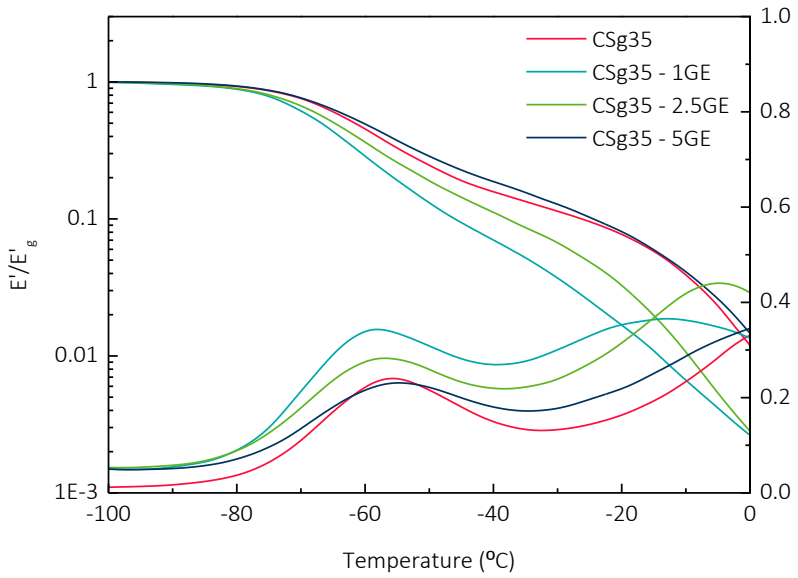

Figure 6.5 – Evolution of E'/E'$_g$ and tan δ with temperature of PLS nanocomposite films reinforced with G.

6.3.6. Tensile tests

The mechanical behaviour of nanocomposites reinforced with G was analysed by means of tensile tests. The obtained results are presented in Figure 6.6.

Results demonstrated that the addition of G nanoflakes resulted in higher Young's modulus that was moderately increased for 1 and 2.5 wt.% of G and increased remarkably for a 5 wt.% of G, achieving a value of 30.6 MPa for the higher G content. Regarding the strength behaviour, similar trend was observed, with a remarkable increase for the sample containing a 5 wt.% of G. In contrast, it should be noted that similar elongation at break values were obtained for all nanocomposites. The elongation decreased upon the addition of 1 wt.% of G but remains constant for higher nanofiller contents. Thus, it was concluded that increasing the G content the stiffness and the strength of the material was progressively improved, while the flexibility was almost not reduced. These results suggested that Salvia is acting as additional plasticiser and G as reinforcing agent and both effects are balanced.

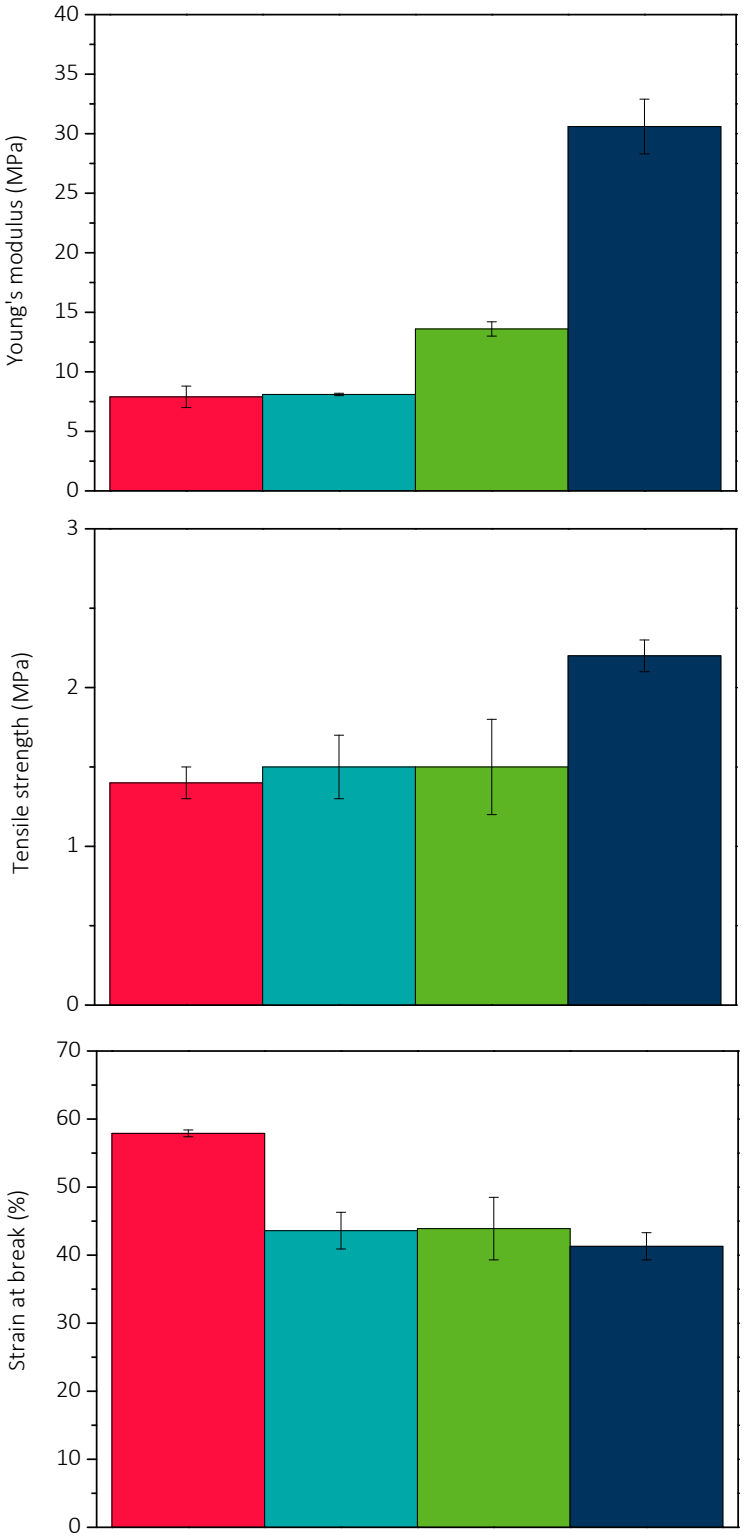

Figure 6.6 – Mechanical properties of ■ CSg35, ■ CSg35 - 1GE, ■ CSg35 - 2.5GE and ■ CSg35 - 5GE.

6.3.7. Electrical properties

It was hypothesised that electrically conductive nanocomposite films could be developed by the incorporation of conductive nanoparticles as G into polymeric matrices. Thus, in order to analyse the electrical response of PLS nanocomposites prepared with G, electrical conductivity measurements by two-probe technique from 0 to 5 V were performed. Results are shown in Figure 6.7.

As it could be observed, the electrical conductivity of the nanocomposites increased while increasing the G content comparing with the non-conductive PLS matrix. However, it should be noted that the obtained electrical conductivity values were not as high as it would be desirable. This little improvement could be related with the presence of Salvia extracts observed by TEM images (Section 4.4.4), that hindered the formation of an effective conductive network in the PLS film.

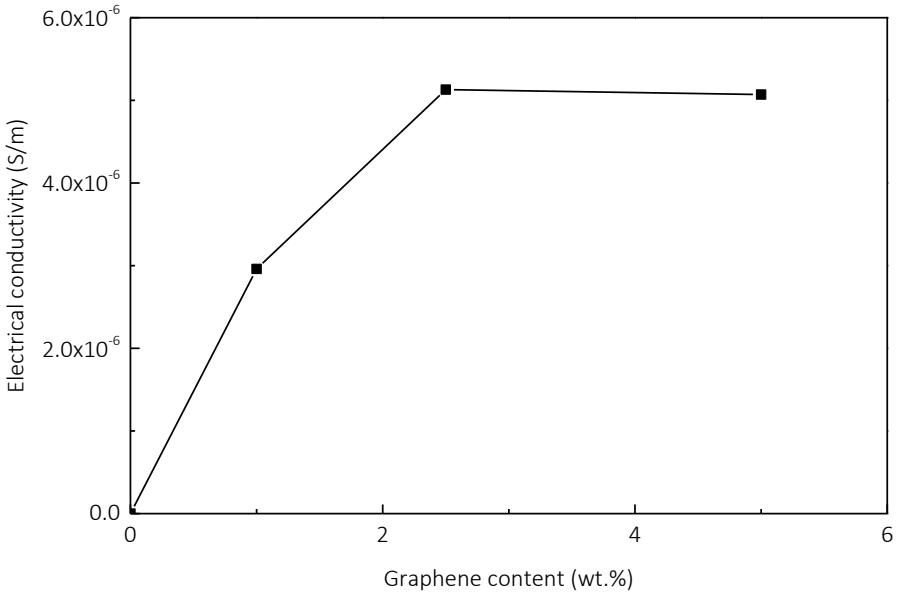

Figure 6.7 – Electrical conductivity against G content curves of PLS nanocomposite films reinforced with G.

6.3.8. Thermogravimetric analysis

TGA measurements were carried out to analyse the thermal decomposition of nanocomposites containing G nanoflakes and Salvia extracts. TG and DTG curves are shown in Figure 6.8.

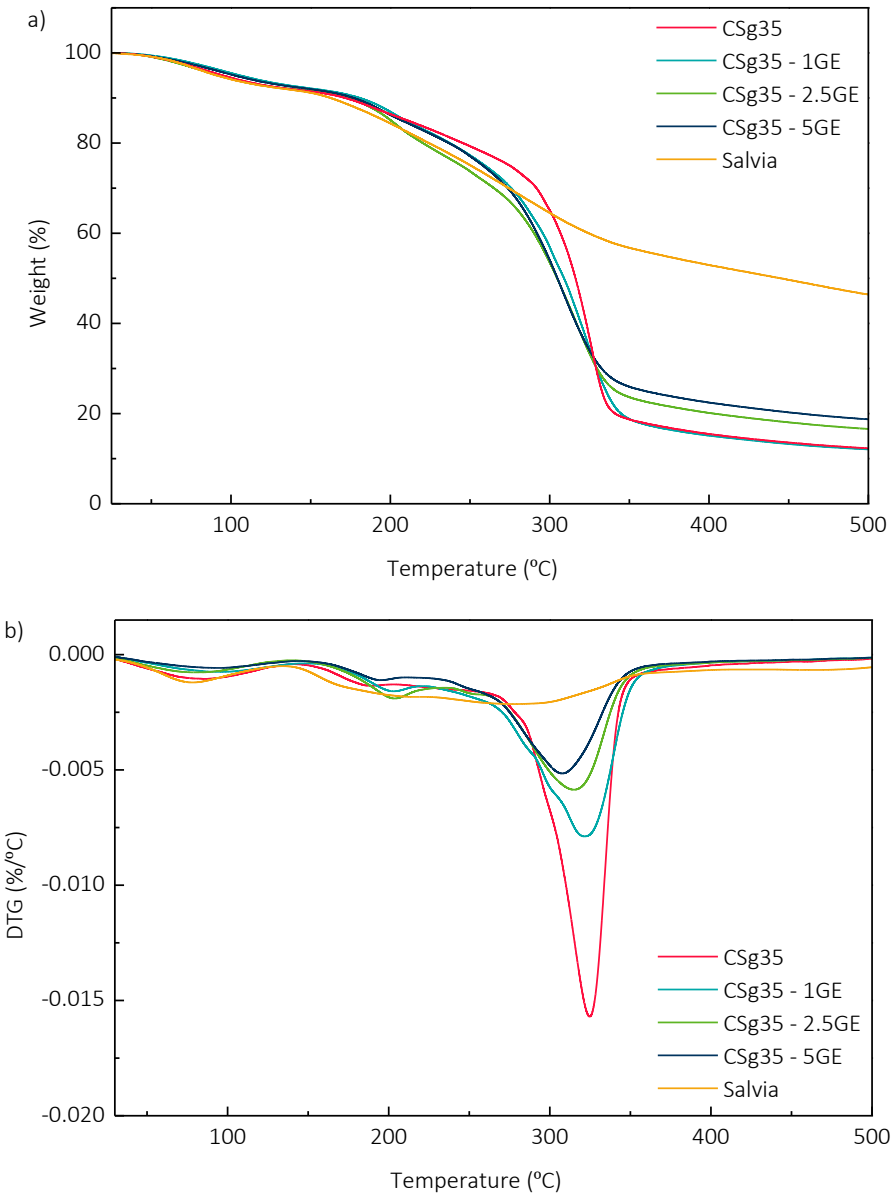

Figure 6.8 – a) TG and b) DTG curves of PLS nanocomposite films reinforced with G.

As observed in the thermograms some remarkable differences were achieved due to the incorporation of G as nanofiller and Salvia extracts as stabilisers. On the one hand, the mass loss

related normally to the degradation of the glycerol-rich phase appeared altered and the contribution of the decomposition of the Salvia extracts was noticeable as their degradation ranges concurred. Besides, a significant decrease of the main degradation temperature from 324 °C (unfilled matrix) to 308 °C (ESg35 – 5GE) was noticed due to the addition of Salvia extracts which showed a lower stability and located in the starch-rich phase. Focusing on the DTG curves the broadening and the decrease of the intensity of this degradation step could be appreciated along with the mentioned reduce in the peak temperature. The same effect was observed for the main degradation step, revealing the influence of the Salvia extracts in the nanocomposite that reduced the overall thermal stability. In addition, it should be also noted that the residue percentage increased while increasing the G and Salvia content.

6.4. EFFECT OF GRAPHENE OXIDE CONTENT ON THE PROPERTIES OF PLS NANOCOMPOSITE FILMS

In this section PLS nanocomposite films were prepared by adding different GO contents (1, 2.5 and 5 wt.%) into the starch-based gelatinised matrix. Compared to G nanoflakes, GO showed much higher dispersibility in water thus facilitating the preparation of homogeneous films. Besides, the introduction of oxidised new functional groups would lead to better compatibility with the matrix since strong nanofiller/matrix interactions could be formed. However, it was expected that the resulting nanocomposites would not present electrical conductivity, as GO in not electrically conductor.

6.4.1. Fourier transform infrared spectroscopy

The differences in the chemical structure of PLS and resulting nanocomposites reinforced with GO were investigated by FTIR measurements. Figure 6.9 presented the obtained FTIR spectra of PLS and nanocomposites films.

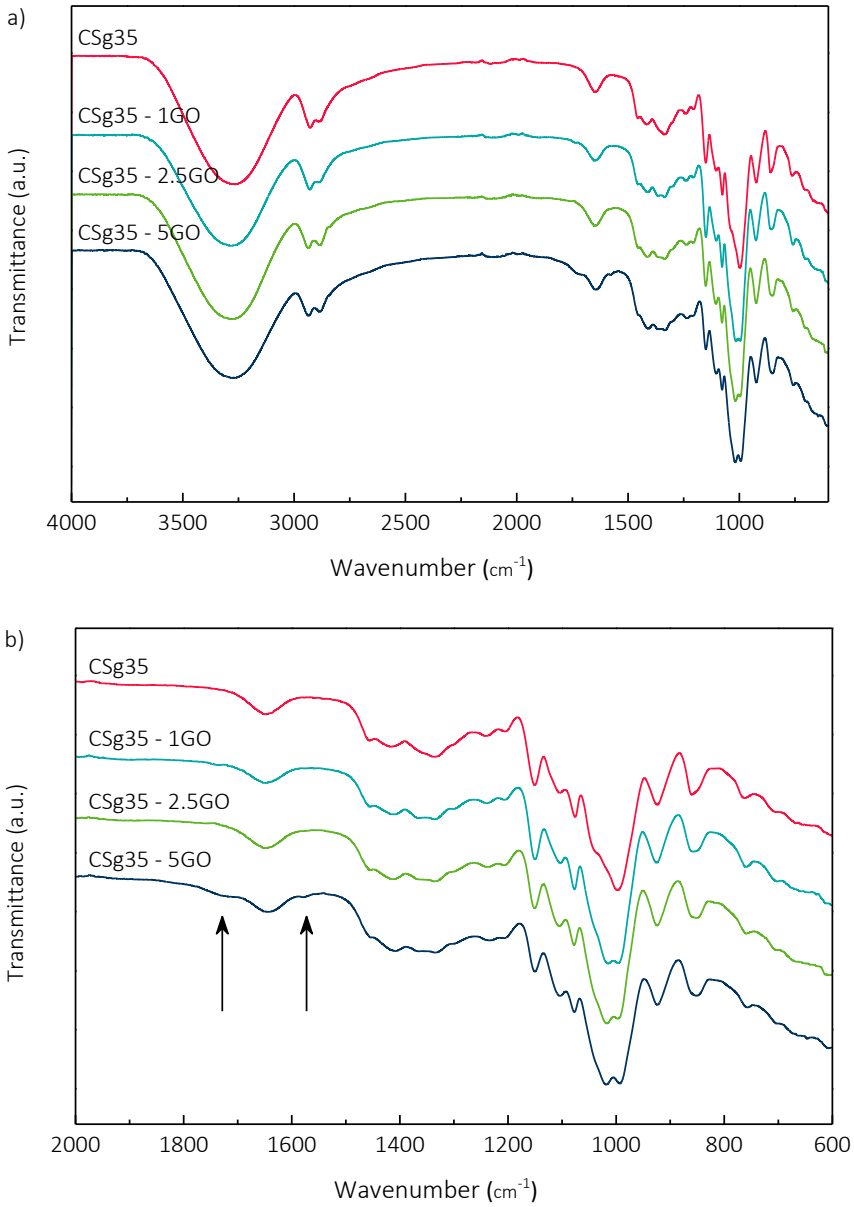

Figure 6.9 – FTIR spectra of PLS nanocomposite films reinforced with GO in the range of a) 4000 – 600 cm^{-1} and b) a magnification in the range of 2000 – 600 cm^{-1}.

In a similar way that occurred for PLS nanocomposites reinforced with G nanoflakes, the FTIR spectra of nanocomposites prepared adding GO showed some differences compared with the PLS unfilled matrix. As stated by other authors, after the incorporation of GO the bands at 1650 cm^{-1}, 1150 cm^{-1} and 1077 cm^{-1} shifted to lower wavenumber values due to the formation of H-bonds between starch chains and GO [2]. In addition, the typical bands associated to the stretching vibrations of the C-O linkages in starch changes notably while increasing the GO content and, thus,

increasing the presence of new C-O linkages introduced with the oxidised nanofiller [11]. Finally, the appearance of a new peak related to GO and located near 1740 cm^{-1}, mainly observable in the 5 wt.% GO containing nanocomposite, is largely attributable to the presence of carbonyl new groups introduced in the oxidised G. Besides, a peak at 1500 cm^{-1} associated with C=C in aromatic structure [6] also observed in nanocomposites containing G.

6.4.2. X-ray diffraction

The crystalline structure of nanocomposites reinforced with GO was analysed by XRD. The resulting XRD patterns are shown in the Figure 6.10. All nanocomposites presented two new peaks associated with the presence of GO namely at $2\theta = 9.6^{\circ}$ and $2\theta = 26.5^{\circ}$ that were more intense as the nanofiller content increased. As described in Section 4.4.2, these signals are related to the (002) plane of GO and to the residual pure graphitic structure, respectively. However, it should be noted that in the case of nanocomposites the signal related to the (002) plane appeared shifted to lower values, i.e. from $2\theta = 11.2^{\circ}$ for the neat GO to $2\theta = 9.6^{\circ}$, indicating that the interlayer separation between GO nanoflakes increased from 7.9 Å for neat GO up to 9.2 Å due to their incorporation into the PLS matrix and revealing effective interactions between starch chains and GO layers.

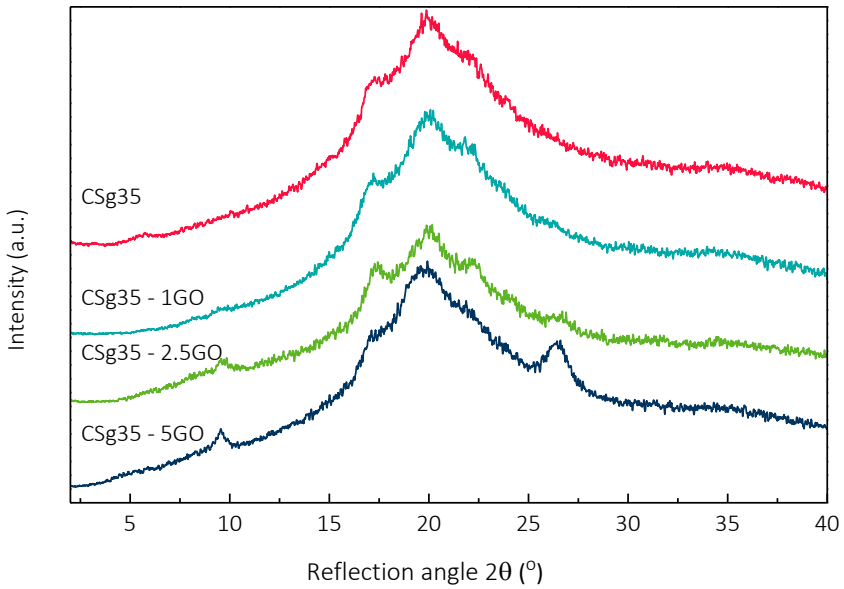

Figure 6.10 – XRD patterns of PLS nanocomposite films reinforced with GO.

6.4.3. Optical properties

UV-vis spectroscopy measurements were performed to analyse the transmittance of the films, whereas the colour of the films was studied using a spectrophotometer. Figure 6.11 and Table 6.2 resumed the obtained transmittance values and colour parameter results.

The transmittance values of PLS nanocomposites was influenced by the GO content as expected. As it could be noticed, the transparency of nanocomposites decreased progressively due to the incorporation of the nanofiller. As shown in Table 6.2, when nanocomposites were prepared adding a 1 wt.% of GO, the transmittance value decreased from 36.9% for the unfilled matrix to 8.7% (ESg35 - 1GO). The incorporation of 2.5 and 5 wt.% of GO led to transmittance values of 1.5% and 0.1%, subsequently. As shown in section 6.3.3., when PLS films were reinforced with G the transmittance decreased to 0% for all reinforcement contents. In contrast, for GO containing nanocomposites the opacity decreased progressively with the reinforcement content, suggesting that better dispersion degree of the nanofiller was achieved for GO. As explained by Mahmoudi et al. [12] the transmittance of G materials is influenced by the number of layers, being higher the absorption of multilayer and stacked GO than that for monolayer GO. Hence, according to the literature these results along with those presented in Section 4.4 would be indicating that in our case the oxidation process led to multilayer GO.

L^*, a^* and b^* as well as ΔE was determined in order to evaluate changes in the surface colour of the nanocomposites. As observed in Table 6.2 the L^* parameter decreased with the GO content because of the dark colour of GO, meaning that the lightness decreased. Besides, the two chromaticity parameters a^* and b^* increased for the lower GO content but decreased while increasing the nanofiller content, indicating that after the addition of GO the films became more redness and yellowness, in opposite to greenness and blueness of G. These results agrees with the brownish and black colour found in literature for GO and G, respectively [13] and also with those

conclusions published previously for chitosan films reinforced with GO [8]. In addition, it should be noted that as expected, higher ΔE values were obtained as the nanofiller contents was increased due to the dark brown colour of GO [14] and in agreement with the colour difference respect to the matrix.

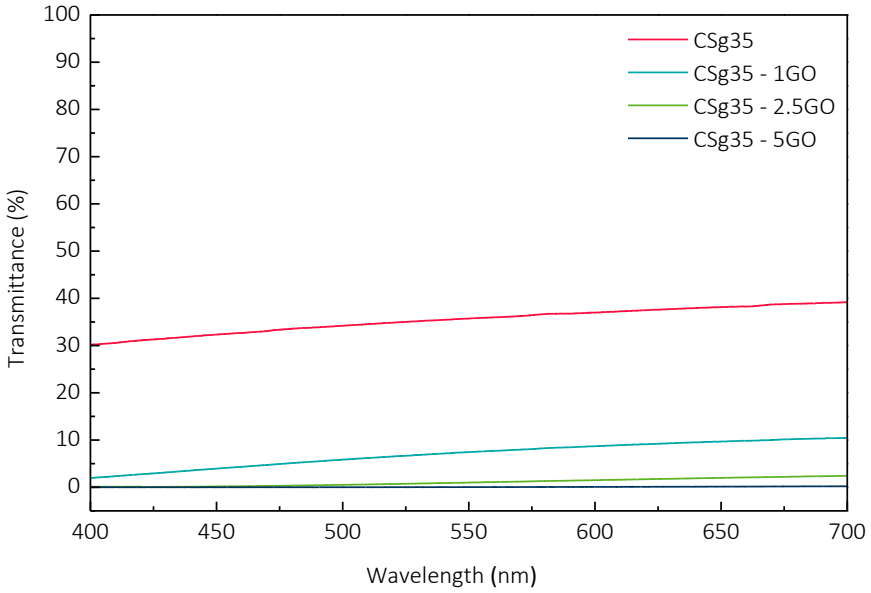

Figure 6.11 – UV-vis transmittance measurements of PLS nanocomposite films reinforced with GO.

Table 6.2 – Transmittance values and colour parameters of PLS nanocomposite films reinforced with GO.

Sample	Transmittance (%)	L^*	a^*	b^*	ΔE
CSg35	36.9	69.24 ± 0.50	-1.40 ± 0.04	3.00 ± 0.04	23.72 ± 0.50
CSg35 - 1GO	8.7	40.74 ± 1.56	4.30 ± 0.33	19.76 ± 0.42	55.82 ± 1.36
CSg35 - 2.5GO	1.5	19.09 ± 0.16	1.62 ± 0.20	7.04 ± 2.00	74.11 ± 0.34
CSg35 - 5GO	0.1	19.88 ± 0.34	0.39 ± 0.04	2.97 ± 0.28	73.01 ± 0.35

6.4.4. Surface properties

The wettability and surface properties of the nanocomposites reinforced with GO were also determined by contact angle analysis using ethylene glycol. The obtained measurements are presented in Figure 6.12.

In contrast with the results obtained for nanocomposites reinforced with G and Salvia extracts, the addition of GO did not affect the hydrophobicity of the films. Indeed, the nanocomposites showed contact angle values ranged from 21.4° to 23.4°, which were very close to that measured for the unfilled matrix. These results are in agreement with those reported by Grande et al. [8] that concluded that the wettability of the nanocomposites did not decrease after the incorporation of the GO.

Figure 6.12 – Contact angle measurements of PLS nanocomposite films reinforced with GO.

6.4.5. Dynamic mechanical analysis

The influence of the GO content in the viscoelastic behaviour of PLS nanocomposite films was analysed by DMA measurements. Figure 6.13 presented the evolution of E'/E'_g and tan δ with temperature.

As noticed in Figure 6.13, $T_{\alpha 1}$ remained constant after the incorporation of GO, however $T_{\alpha 2}$ shifted to higher temperatures for CSg35 – 1GO and CSg35 – 2.5GO and widens for CSg35 – 5GO. It means that GO at 1 and 2.5 wt.% reduced the mobility of starch-rich phase which could be due to effective hydrogen bonding interactions between the oxygen containing functional groups of

GO and starch. Both relaxation magnitudes decreased due to the decrease of glycerol molecules and starch chains relaxed at these transitions.

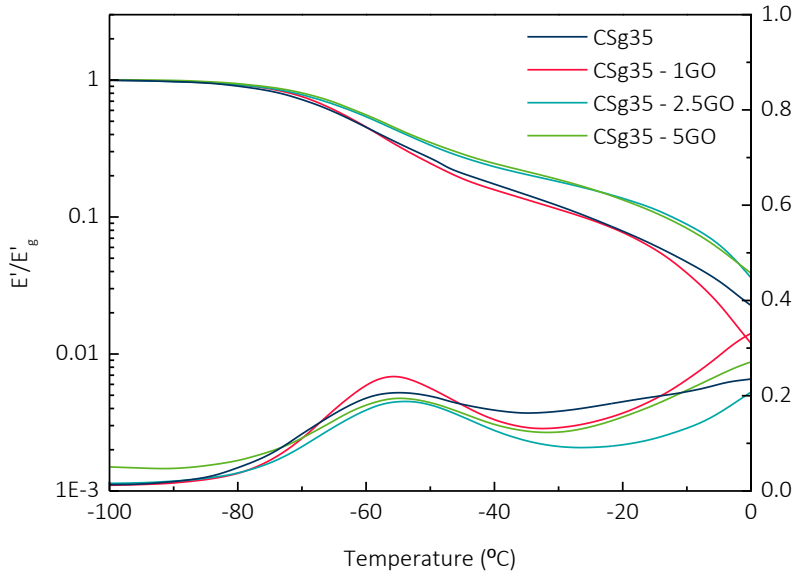

Figure 6.13 – Evolution of E'/E'$_g$ and tan δ with temperature of PLS nanocomposite films reinforced with GO.

6.4.6. Tensile tests

Tensile test measurements were performed to determine the influence of GO content in the mechanical properties of PLS nanocomposites. The obtained results are shown in Figure 6.14.

As it could be observed the nanocomposites reinforced with GO presented higher Young's modulus and tensile strength values, whereas lower elongation at break values were obtained. As stated by Li et al. [2], the incorporation of GO improved the strength and the stiffness of starch-based materials due to the good dispersion of the nanofiller in the matrix and the strong PLS/GO interactions. Comparing with nanocomposites reinforced with G, it should be mentioned that higher tensile values were obtained due to the ability of oxygen containing groups of GO to interact with starch. However, lower elongation at break values were obtained since Salvia extracts could be beavering as plasticisers in nanocomposites with G.

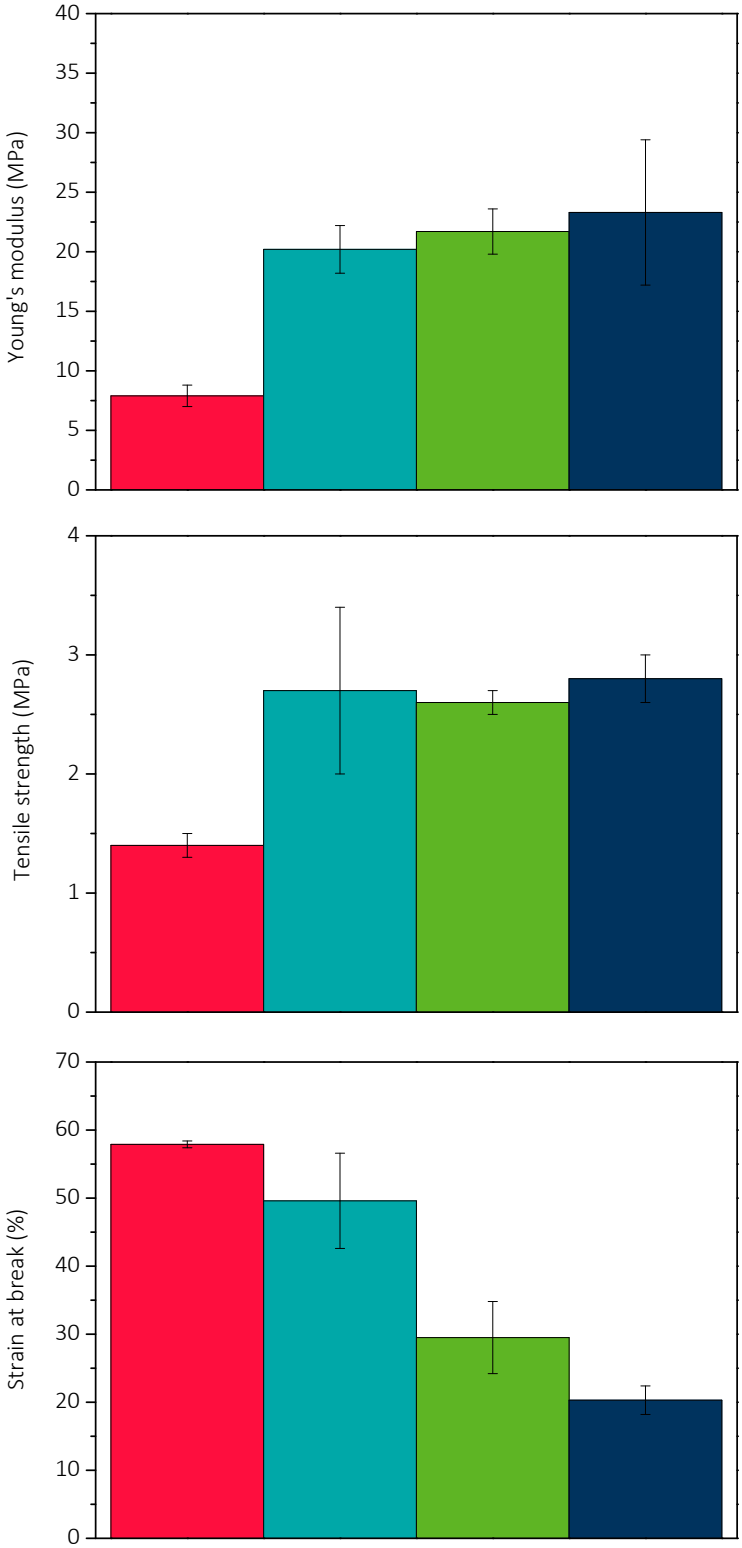

Figure 6.14 – Mechanical properties of ■ CSg35, ■ CSg35 - 1GO, ■ CSg35 - 2.5GO and ■ CSg35 - 5GO.

6.4.7. Electrical properties

Electrical conductivity measurements of GO containing PLS nanocomposites were carried out by two-probe technique in a similar way that presented for G containing ones. Attending to the results, GO reinforced nanocomposites did not show electrical conductivity. As defined by other authors, the non-capacity of GO to be electrically conductor [4,5,15] is because during the oxidation reaction the electronic structure of graphite is disrupted due to the destruction of π-conjugation [4]. Thus, the incorporation of GO could not improve the electrical conductivity of the nanocomposites.

6.4.8. Thermogravimetric analysis

The thermal degradation of nanocomposites reinforced with GO was evaluated by TGA measurements. TG and DTG curves are shown in Figure 6.15.

Only slight differences were observed in the thermal degradation of the nanocomposites comparing with that of the unfilled PLS and discussed above (Section 6.3.8). The main difference was observed in the range of the glycerol-rich phase decomposition where a significant increase of the mass loss was detected. As described by other authors [5], the decomposition and pyrolysis phenomena of the functional groups of GO, which took place around 250 °C (Figure 4.7), provokes the earlier decomposition of starch. Furthermore, the main degradation step slightly shifted from 324 °C to 320 °C and the residue value increased as increasing the GO content.

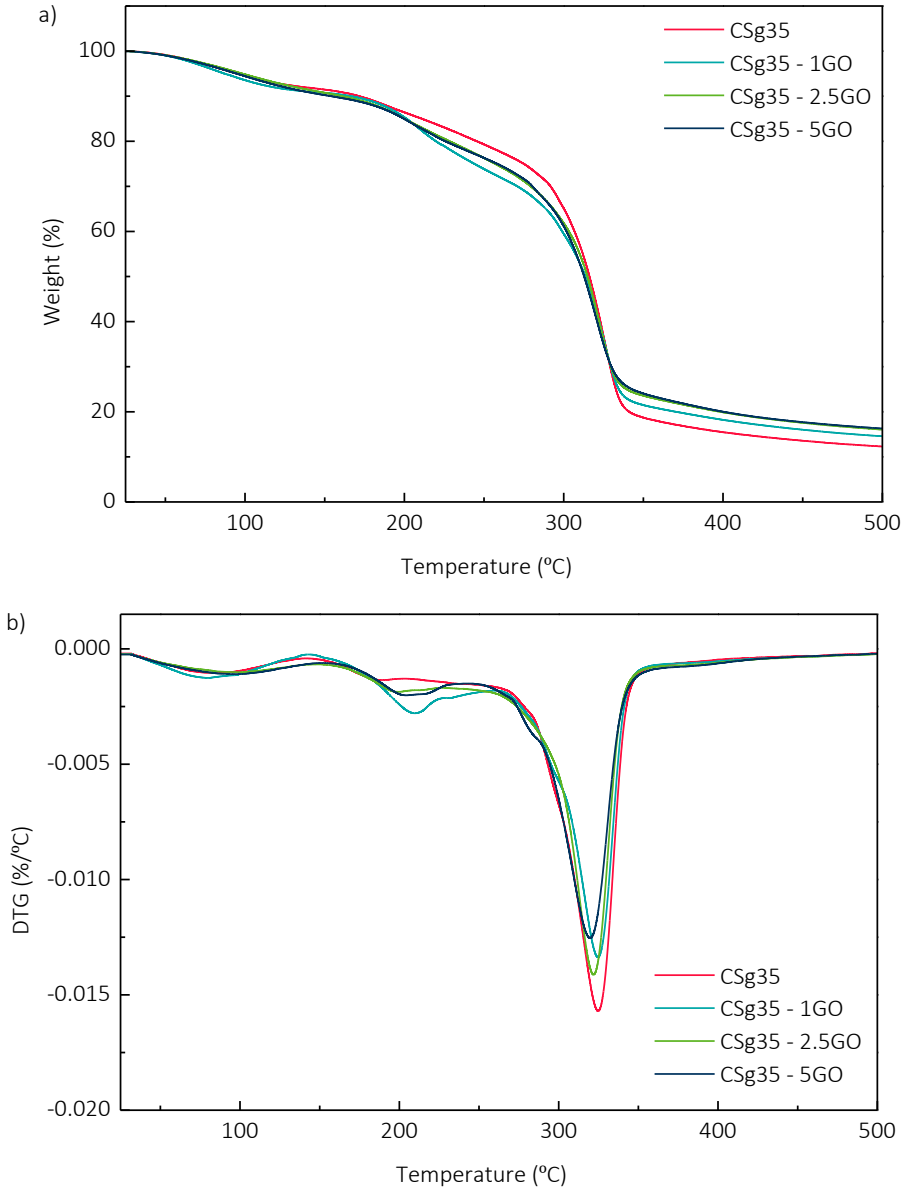

Figure 6.15 – a) TG and b) DTG curves of PLS nanocomposite films reinforced with GO.

6.5. INFLUENCE OF THE REDUCTION OF GRAPHENE OXIDE ON THE PROPERTIES OF PLASTICISED STARCH NANOCOMPOSITE FILMS

As concluded previously (Section 6.4), the addition of GO resulted in interesting optical and mechanical properties that could be attributed to strong nanofiller/matrix interactions and the homogeneous dispersion of GO into the PLS matrix. However, the addition of GO did not contributed to the electrical conductivity of the films. Therefore, the reduction of GO containing

nanocomposites was performed using ascorbic acid as reduction agent. As had been reported in literature [5], the hexagonal lattice could be expected to be restored leading to conductive materials. However, the GO is not usually completely reduced, and the residual hydroxyl, epoxide, carbonyl and carboxyl groups that remains intact could continue contributing by rGO/starch interactions [5].

6.5.1. X-ray diffraction

XRD measurements were carried out to demonstrate the success of the employed method to reduce the GO nanoflakes. The diffractograms of reduced films are presented in Figure 6.16.

As observed for the XRD patterns of reduced nanocomposite the characteristic peak of GO located at $2\theta = 9.6^{\circ}$ disappeared after the reduction, revealing that the oxygen groups were successfully removed [16]. Besides, a broad peak centred around $2\theta = 19.8^{\circ}$ and the peak around $2\theta = 26.5^{\circ}$ associated to the (002) plane of hexagonal structure of pristine graphite [17–19] as it was detected for the GO containing nanocomposites were detected.

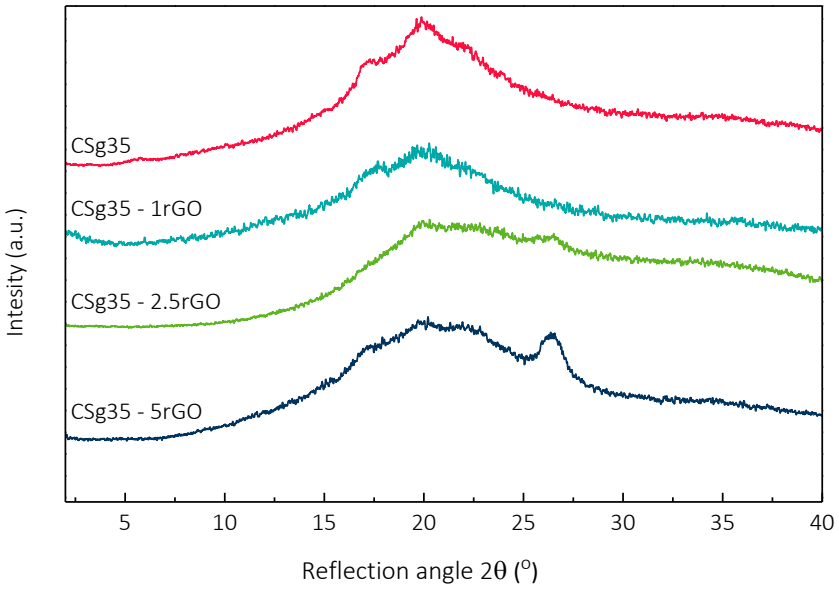

Figure 6.16 – XRD patterns of PLS nanocomposite films reinforced with rGO.

6.5.2. Surface properties

The chemical reduction with ascorbic acid could eliminate the hydroxyl, epoxide, carbonyl groups in the structure of GO and reduce the wettability of the nanocomposites. Thus, in order to analyse the influence of the reduction with ascorbic acid on the surface properties, contact angle measurements were performed. Obtained results are presented in Figure 6.17.

As it could be noted, the wettability of the PLS films decreased after the reduction reaction, obtaining higher contact values for reduced nanocomposite materials. The measured contact angle value was significantly increased from 24.6° for the unfilled matrix to 46.5° for the CSg35 – 5rGO nanocomposites. Similar results were published by Romani et al. [20] for polyurethane composites reinforced with rGO. Therefore, it was concluded that the hydrophobicity of the films was improved since the oxygen groups were satisfactorily removed.

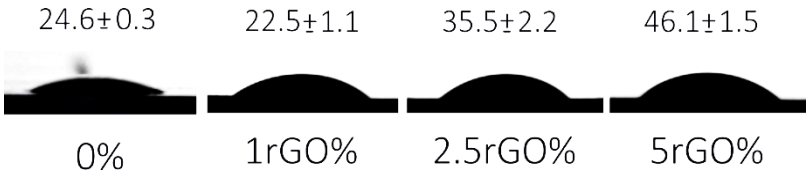

Figure 6.17 – Contact angle measurements of PLS nanocomposite films reinforced with rGO.

The results are in concordance with those conclusions obtained by XRD, demonstrating that during the reduction reaction the oxygen functional groups of GO were almost eliminated and, thus, it was concluded that the employed reaction conditions were successful. Comparing with nanocomposites containing G, higher contact angle values were obtained after the incorporation and reduction of GO, corroborating that Salvia extracts had the opposite effect to G and in addition to stabilise the suspension of G in water, contribute to increase the hydrophilicity of nanocomposites.

6.5.3. Electrical properties

As published elsewhere the reduction of GO restores the sp^2 hybridised structure of the G [5] leading to electrically conductive nanoflakes [16]. Therefore, the influence of the chemical reduction

in the electrical behaviour of PLS nanocomposites was evaluated by two-probe electrical conductivity measurements. Figure 6.18 displayed the electrical conductivity results.

In contrast with GO containing nanocomposites, all reduced films showed electrical conductivity increasing for higher rGO contents. Besides, by comparing the nanocomposites reinforced with rGO with those prepared using G, the higher conductivity values achieved for the former may be due to two reasons: 1) a more uniform initial better dispersion of GO into the matrix and GO/interactions which resulted in the formation of a more effective conductive network once reduced 2) the Salvia used to stabilise G suspension in water and incorporated to the gelatinised starch, could hinder the formation of a conductive network, as previously discussed. These conclusions would be also supported by the mechanical properties of GO containing films. Hence, higher tensile strength values were obtained for GO containing samples indicating good stress transfer from the matrix to the GO and higher elongation at break were obtained for samples reinforced with G suggesting that Salvia acts as plasticiser of starch. Thus, it was concluded that the use of ascorbic acid as reducing agent to restore the electronic structure of GO was suitable.

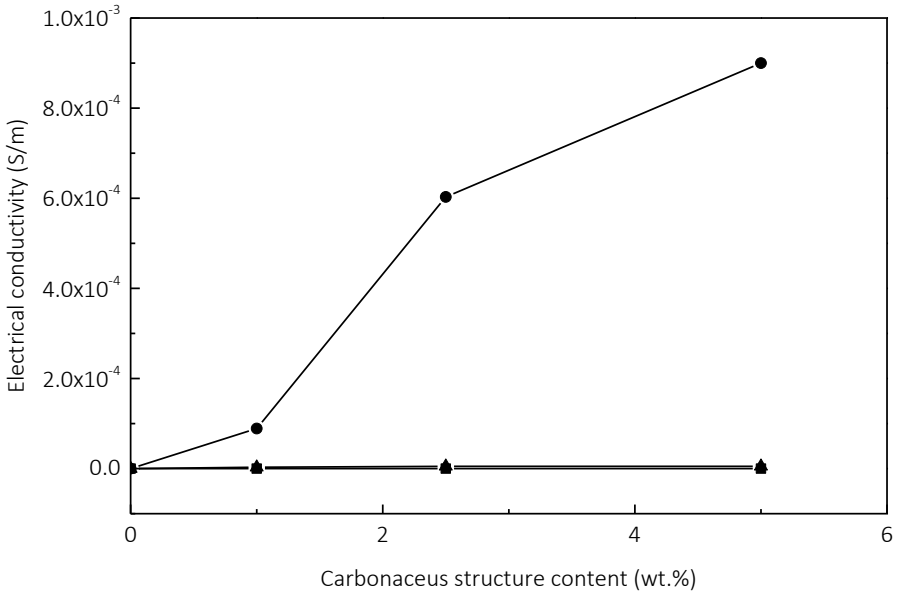

Figure 6.18 – Electrical conductivity against G content curves of PLS nanocomposite films reinforced with G and extracts (▲), GO (■) and rGO (●).

6.5.4. Thermogravimetric analysis

TGA measurements were carried out to study the effect of the reduction treatment in the thermal resistance of PLS/rGO nanocomposites. TG and DTG curves are shown in Figure 6.19.

On the one hand, it was appreciated that the moisture content decreased for all reduced nanocomposites in agreement with contact angle values. On the other hand, as it could be observed the degradations occurred in a wider temperature range. The nanocomposites containing rGO showed a weight loss related to the oxygen functional groups of GO. Usually, the better the interactions between the filler and the matrix was, the higher the thermal stability was. Thereafter, the reduction of GO to rGO, removes previous formed interactions between the filler and the matrix formed during the film formation, thus decreasing dramatically the thermal stability of the nanocomposite compared to nanocomposites prepared from G and Salvia where the assembly of starch chains was not interrupted. It was noticed that the char percentage, that could act as heat barrier, was significantly higher after the reduction reaction. Besides, as expected, the residue was influenced by the rGO content, i.e. the char increased increasing the nanofiller content.

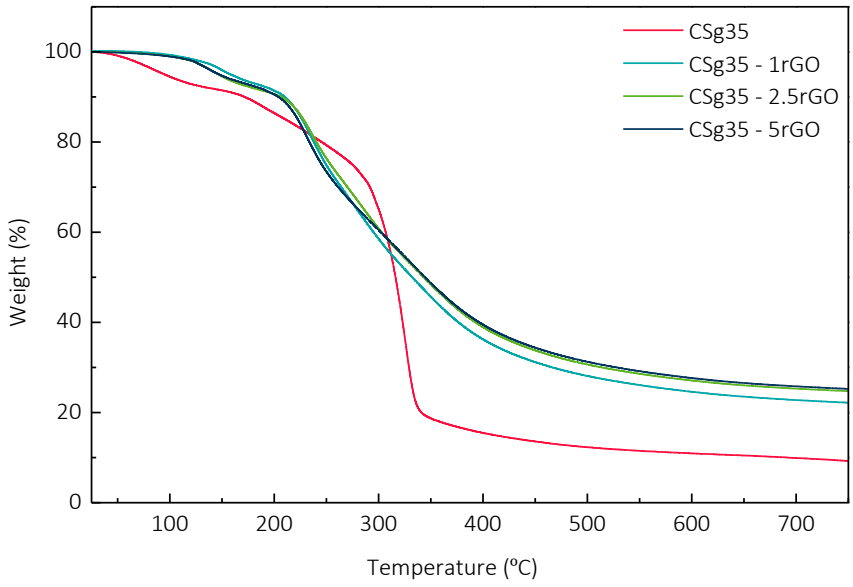

Figure 6.19 – a) TG and b) DTG curves of PLS nanocomposite films reinforced with GO and rGO.

6.6. CONCLUSIONS

PLS nanocomposite films were successfully obtained by the incorporation of carbonaceous nanoparticles, i.e. G and GO. In addition, the nanocomposites prepared with GO were reduced in order to achieved better electrical conductivity properties.

Firstly, G containing nanocomposites were prepared using different nanofiller contents. Salvia extracts were necessary incorporated in order to facilitate the dispersion of G in the aqueous gelatinisation media. The influence of adding different G contents into the matrix was analysed. It was demonstrated that the addition of G nanoflakes slightly increased the hydrophobicity character whatever its content but some plasticising effect of Salvia could be concluded. Besides, the mechanical properties and the electrical conductivity of the nanocomposites were improved compared with the unfilled matrix. In addition, the thermal stability was not significantly modified by the incorporation of G.

On the other hand, in a similar way, PLS nanocomposites were developed adding GO as nanofiller. Regarding the results, it was demonstrated that the strong starch/GO interactions and the good dispersion of GO improved the final behaviour of the films, specially the mechanical properties. Besides, these films were satisfactorily reduced by heating them in presence of ascorbic acid. After the reduction thought the thermal stability was reduced, they were stable up to 200 °C. In addition, the sp^2 hybridised structure of GO was restored obtaining also electrical conductivity properties.

6.7. REFERENCES

[1] A. Santamaria-Echart, I. Fernandes, F. Barreiro, A. Retegi, A. Arbelaiz, M.A. Corcuera, A. Eceiza, Development of waterborne polyurethane-ureas added with plant extracts: Study of different incorporation routes and their influence on particle size, thermal, mechanical and antibacterial properties, Prog. Org. Coatings. 117 (2018) 76–90. doi:10.1016/j.porgcoat.2018.01.006.

[2] R. Li, C. Liu, J. Ma, Studies on the properties of graphene oxide-reinforced starch biocomposites, Carbohydr. Polym. 84 (2011) 631–637. doi:10.1016/j.carbpol.2010.12.041.

[3] J.-L. Li, M. Zhou, G. Cheng, F. Cheng, Y. Lin, P.-X. Zhu, Comparison of mechanical reinforcement effects of cellulose nanofibers and montmorillonite in starch composite, Starch - Stärke. 1800114 (2018) 1–9. doi:10.1002/star.201800114.

[4] T.B. Rouf, J.L. Kokini, Biodegradable biopolymer–graphene nanocomposites, J. Mater. Sci. 51 (2016) 9915–9945. doi:10.1007/s10853-016-0238-4.

[5] T. Ma, P.R. Chang, P. Zheng, X. Ma, The composites based on plasticized starch and graphene oxide/reduced graphene oxide, Carbohydr. Polym. 94 (2013) 63–70. doi:10.1016/j.carbpol.2013.01.007.

[6] J. Li, M. Zhou, G. Cheng, F. Cheng, Y. Lin, P.X. Zhu, Fabrication and characterization of starch-based nanocomposites reinforced with montmorillonite and cellulose nanofibers, Carbohydr. Polym. 210 (2019) 429–436. doi:10.1016/j.carbpol.2019.01.051.

[7] S. Javanbakht, H. Namazi, Solid state photoluminescence thermoplastic starch film containing graphene quantum dots, Carbohydr. Polym. 176 (2017) 220–226. doi:10.1016/j.carbpol.2017.08.080.

[8] C.D. Grande, J. Mangadlao, J. Fan, A. De Leon, J. Delgado-Ospina, J.G. Rojas, D.F. Rodrigues, R. Advincula, Chitosan Cross-Linked Graphene oxide nanocomposite films with antimicrobial activity for application in food industry, Macromol. Symp. 374 (2017) 1–8. doi:10.1002/masy.201600114.

[9] S. Shankar, L. Jaiswal, P.R. Selvakannan, K.S. Ham, J.W. Rhim, Gelatin-based dissolvable antibacterial films reinforced with metallic nanoparticles, RSC Adv. 6 (2016) 67340–67352. doi:10.1039/c6ra10620j.

[10] X. Gong, G. Liu, Y. Li, D.Y.W. Yu, W.Y. Teoh, Functionalized-graphene composites: Fabrication and applications in sustainable energy and environment, Chem. Mater. 28 (2016) 8082–8118. doi:10.1021/acs.chemmater.6b01447.

[11] P. Zheng, T. Ma, X. Ma, Fabrication and properties of starch-grafted graphene nanosheet/ plasticized-starch composites, Ind. Eng. Chem. Res. 52 (2013) 14201–14207. doi:10.1021/ie402220d.

[12] N. Mahmoudi, F. Ostadhossein, A. Simchi, Physicochemical and antibacterial properties of chitosan-polyvinylpyrrolidone films containing self-organized graphene oxide nanolayers, J. Appl. Polym. Sci. 133 (2016) 1–8. doi:10.1002/app.43194.

[13] M.Z. Ansari, R. Johari, W.A. Siddiqi, Novel and green synthesis of chemically reduced graphene sheets using Phyllanthus emblica (Indian Gooseberry) and its photovoltaic activity, Mater. Res. Express. 6 (2019). doi:10.1088/2053-1591/ab0439.

[14] J. Ahmed, M. Mulla, Y.A. Arfat, L.A. Thai T, Mechanical, thermal, structural and barrier properties of crab shell chitosan/graphene oxide composite films, Food Hydrocoll. 71 (2017) 141–148. doi:10.1016/j.foodhyd.2017.05.013.

[15] P.K.S. Mural, M. Sharma, G. Madras, S. Bose, A critical review on in situ reduction of graphene oxide during preparation of conducting polymeric nanocomposites, RSC Adv. 5

(2015) 32078–32087. doi:10.1039/c5ra02877a.

[16] I. Kanayama, H. Miyaji, H. Takita, E. Nishida, M. Tsuji, B. Fugetsu, L. Sun, K. Inoue, A. Ibara, T. Akasaka, T. Sugaya, M. Kawanami, Comparative study of bioactivity of collagen scaffolds coated with graphene oxide and reduced graphene oxide, Int. J. Nanomedicine. 9 (2014) 3363–3373. doi:10.2147/IJN.S62342.

[17] J. Fan, Z. Shi, J. Wang, J. Yin, Glycidyl methacrylate-modified gum arabic mediated graphene exfoliation and its use for enhancing mechanical performance of hydrogel, Polymer (Guildf). 54 (2013) 3921–3930. doi:10.1016/j.polymer.2013.05.057.

[18] J. Cao, Y. Zhu, X. Yang, Y. Chen, Y. Li, H. Xiao, W. Hou, J. Liu, The promising photo anode of graphene/zinc titanium mixed metal oxides for the CdS quantum dot-sensitized solar cell, Sol. Energy Mater. Sol. Cells. 157 (2016) 814–819. doi:10.1016/j.solmat.2016.08.003.

[19] E. Mahmoudi, L.Y. Ng, M.M. Ba-Abbad, A.W. Mohammad, Novel nanohybrid polysulfone membrane embedded with silver nanoparticles on graphene oxide nanoplates, Chem. Eng. J. 277 (2015) 1–10. doi:10.1016/j.cej.2015.04.107.

[20] E.C. Romani, S. Nardecchia, C. Vilani, S. Qi, H. Dong, F.L. Freire, Synthesis and characterization of polyurethane/reduced graphene oxide composite deposited on steel, J. Coatings Technol. Res. 15 (2018) 1371–1377. doi:10.1007/s11998-018-0088-x.

CHAPTER 7:

NANOCOMPOSITE HYDROGELS BASED ON CROSS-LINKED STARCH AND CELLULOSE NANOCRYSTALS

7. NANOCOMPOSITE HYDROGELS BASED ON CROSS-LINKED STARCH AND CELLULOSE NANOCRYSTALS

7.1. OBJECTIVE

The aim of this chapter was the development and characterisation of starch-based hydrogels suitable for be used in the exigent field of biomedicine, mainly in drug delivery systems. With that purpose, firstly, normal maize starch was functionalised with furan moieties by reaction of the gelatinized starch with furfuryl isocyanate. After that, hydrogels and their nanocomposites were obtained by Diels-Alder (DA) reaction between the furan-modified starch derivative and commercial PEG-based tetrafunctional maleimide cross-linker, adding cellulose nanocrystals (CNC) as nanoreinforcement. The influence of the CNCs content in the rheological and swelling properties as well as the morphology of the hydrogels was analysed. Besides, drug delivery measurements and cytotoxicity assays were carried out in order to assess their applicability in the biomedical field.

7.2. OBTAINMENT OF CROSS-LINKED STARCH-BASED HYDROGELS

7.2.1. Synthesis of furanic starch derivative (S-FI)

Furan-modified starch (S-FI) was obtained by the reaction of gelatinized starch with furfuryl isocyanate (FI) considering the method defined by Nossa et al. [1]. Firstly, gelatinized starch was obtained by the gelatinization-casting methodology described previously (Chapters 3,5 and 6) with some modifications. 2 g of normal maize starch were dispersed in 30 mL of distilled water at room temperature. The mixture was heated up to 90 ˚C and gelatinized under continuous magnetic stirring during 40 min. After that, the viscous gel was homogenised in a dispersing system for 3 min at 15,000 rpm (POLYTRON® PT 2500 E). The gel was spread into petri dishes and dried in an oven at 70 ˚C for 5 h.

After that period, 0.45 g of the gelatinised dried starch were dissolved in 6.4 mL of dimethyl sulfoxide (DMSO) and the corresponding amount of furfuryl isocyanate was added in order to use a 1:0.1 gelatinized starch to furfuryl isocyanate molar ratio (S:FI) (based on the molecular weight of anhydroglucose unit 162 g mol^{-1}) [1]. The reaction was allowed to proceed for 2 h at 60 °C with continuous stirring (Scheme 7.1). After that, the product was precipitated and washed with ethanol, and then, it was dissolved in distilled water and purified by dialysis (Spectra Pro 12,000–14,000 MWCO regenerated cellulose dialysis membranes from Spectrum Laboratories, USA) against distilled water for 24 h. The resulting product was obtained once dried at 30 °C for 24 h.

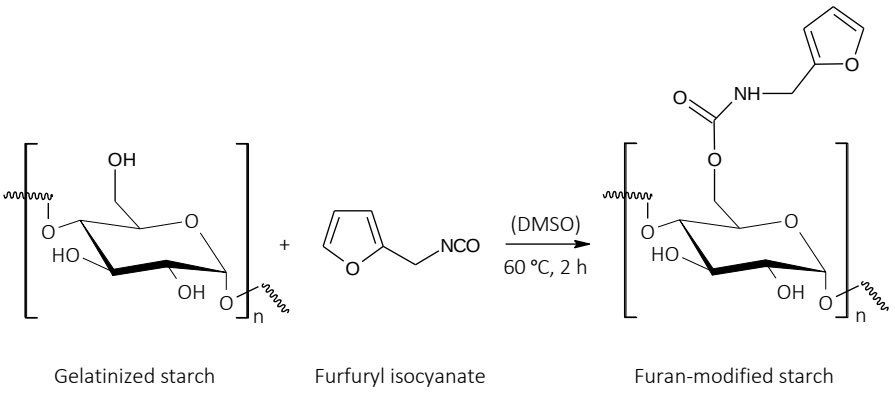

Scheme 7.1 – Synthesis of furan-modified starch.

7.2.2. Hydrogel formation by Diels Alder reaction between S-FI and tetramaleimide (TTMI)

Starch-based hydrogels were obtained by the Diels Alder (DA) reaction between the S-FI derivative and a water-soluble commercial PEG-based tetramaleimide cross-linker (TTMI) (Scheme 7.2). Firstly, 0.128 g of S-FI were dissolved in distilled water (6 wt. %) overnight. Then, 0.064 g of TTMI were added and the mixture was allowed to react at 65 °C for 24 h in a close vial. The furan to maleimide (Fu:Mal) weight ratio of 1:0.5 was used to prepare the hydrogels. The resulting hydrogel was named as HSFI plus de functionality of the cross-linker (in this case, the functionality is 4), therefore as HSFI4.

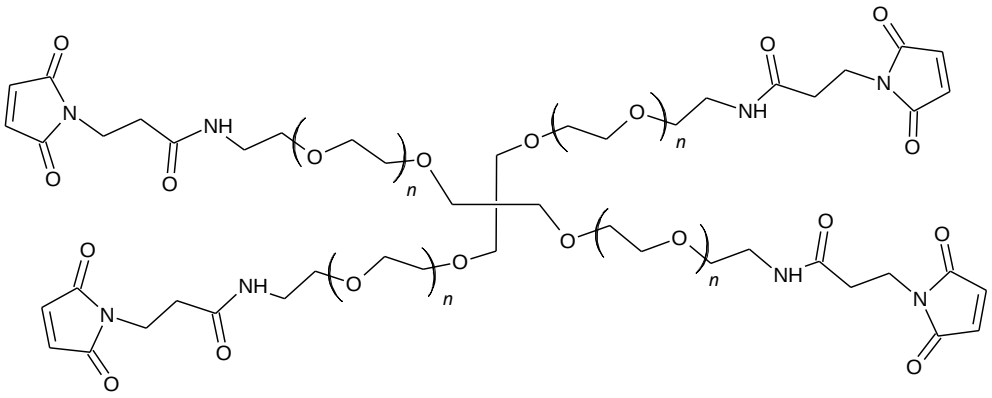

Scheme 7.2 – Chemical structure of the tetrafunctional water-soluble TTMI cross-linker.

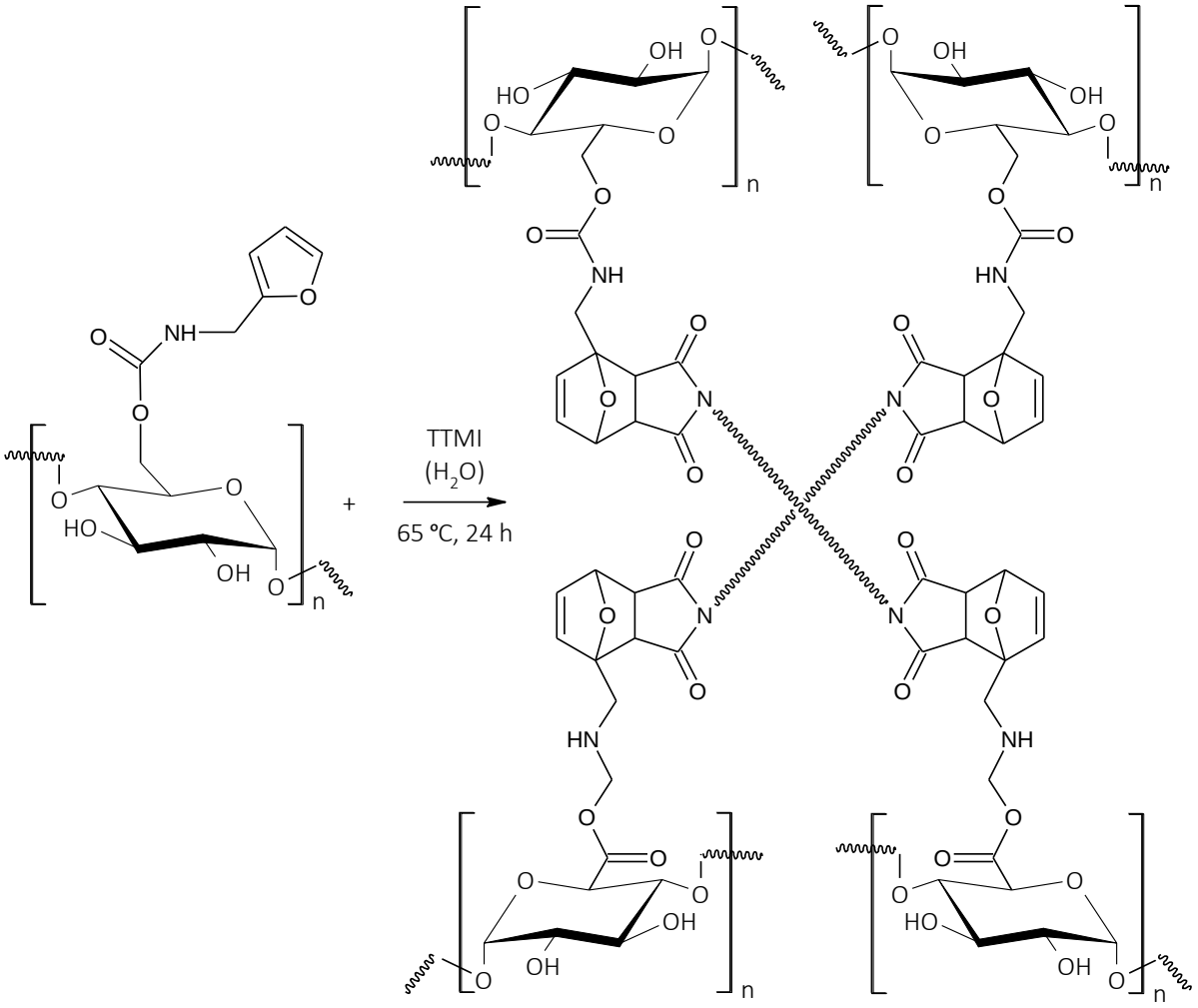

Scheme 7.3 – DA cross-linking reaction between S-FI and TTMI.

7.2.3. Preparation of nanocomposite hydrogels by Diels-Alder reaction

In order to prepare the nanocomposite hydrogels, different CNC contents (i.e. 2.5 and 5 wt.% relative to the S-FI plus TTMI total weight) were incorporated into the hydrogel matrix (Scheme 7.4). For that, as described above, 0.128 g of S-FI were dissolved in the distilled water (6 wt. %) overnight and, after that, the desired amount of CNC was incorporated to the solution, previously dispersed in distilled water by ultrasonication. Then, 0.064 g of TTMI were added and the reaction was conducted at 65 °C for 24 h in a close vial. As in case of the non-reinforced hydrogels, the 1:0.5 Fu:Mal ratio was used to prepare the hydrogel nanocomposites.

The cross-linked nanocomposite hydrogels were referred as HSFI4 plus the nanocrystal content, i.e. HSFI4 - 2.5CNC and HSFI4 - 5CNC.

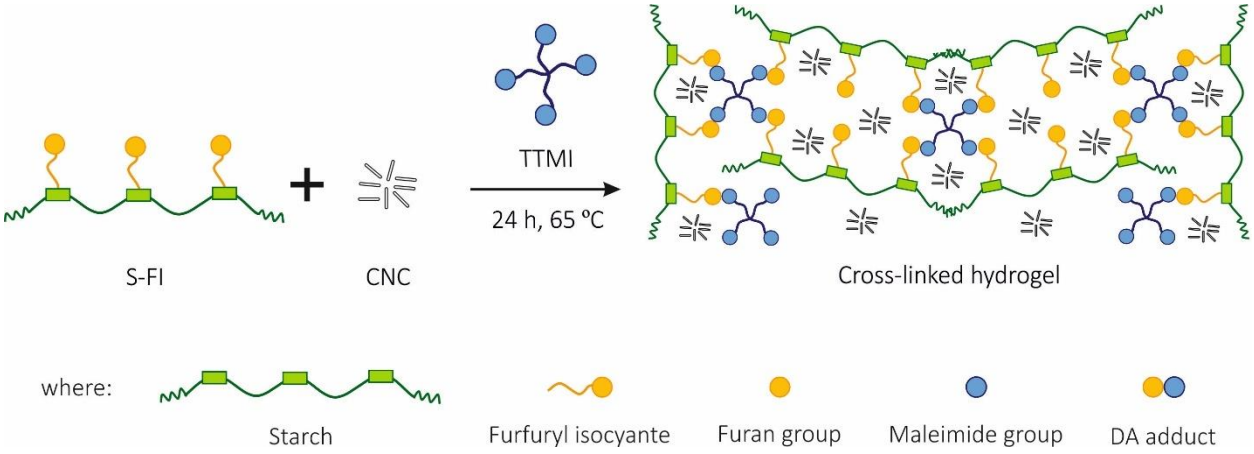

Scheme 7.4 – Model of DA cross-linking reaction to obtain CNC containing nanocomposite hydrogels.

7.3. SYNTHESIS OF FURAN-MODIFIED STARCH

The furan-modification of starch was performed by reaction of gelatinized starch and furfuryl isocyanate. ^{1}H NMR was carried out in order to verify the success of the functionalisation.

7.3.1. Nuclear magnetic resonance

^{1}H NMR analysis was performed in order to corroborate the chemical structure of the starch derivative and used for the quantification of the substitution degree (DS). ^{1}H NMR spectra of gelatinised starch and the furanic derivative are both presented in Figure 7.1a and 7.1b, respectively.

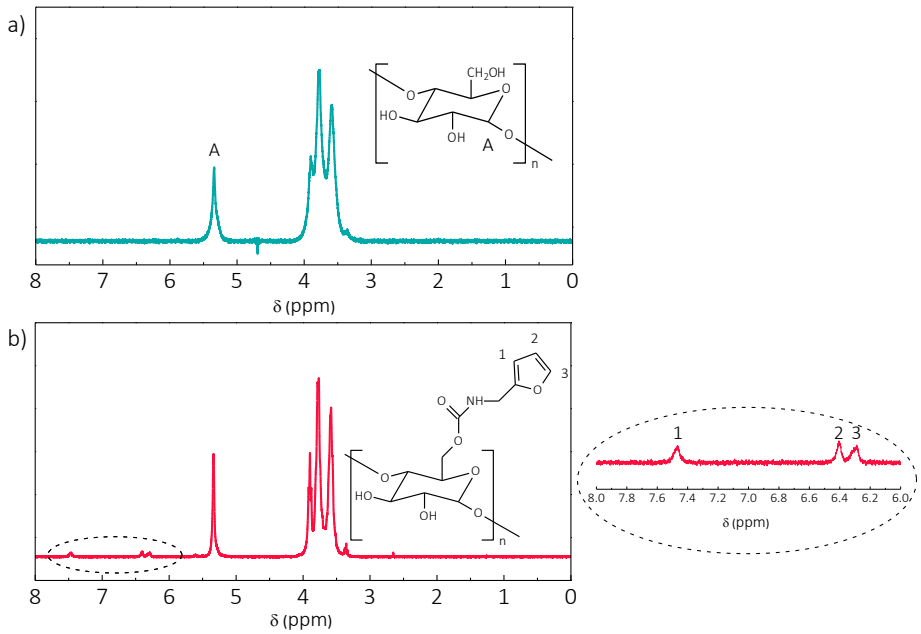

Figure 7.1 – ^{1}H NMR spectra of a) gelatinized starch and b) whole scan range (left) and magnification from 8 to 6 ppm (right) of the furanic starch derivative (Temperature = room temperature, solvent = D_2O).

The ^{1}H NMR spectrum of starch is characterised by the presence of a peak at 5.34 ppm corresponding to the α-anomeric hydrogen (peak A in the Figure 7.1a) and multiple peaks in the 3.3 - 4.0 ppm interval, associated to the other six hydrogens of the anhydroglucose unit [2]. New peaks related to the furan ring were observed at 7.46, 6.40 and 6.28 ppm for the modified starch (Figure 7.1b) [1,3,4]. According to the literature, the primary hydroxyl (OH) group at C6 is more reactive than the secondary OH at C2 and C3 [2]. Hence, the insertion of the furanic molecule was likely to occur at that position varying slightly the intensity of the signal located at 4.0 ppm. The integration value of the furanic protons relative to that of the α-anomeric hydrogen signal was used for the determination of the DS value and was found to be 0.04. Several attempts were performed in order

to increase the final DS value by increasing the starch to furfuryl isocyanate ratio. However, as the DS value did not further increase from 0.04, the 1:0.1 ratio was finally taken as optimized value. Guaresti et al. [5] and Montiel-Herrera [6] reported chemical modifications of chitosan with furan groups and they found minor proton signals at higher displacements associated to unbounded furanic moieties. In this case, the spectrum of S-FI did not present those signals related to unreacted furanic moieties indicating that the furan isocyanate reacted completely with starch or that any excess was efficiently removed after the reaction.

7.4. ANALYSIS OF THE PREPARED HYDROGELS

Hydrogels were prepared following the protocol defined previously by our research group for furan modified gelatine, with slight modifications [3]. In this case, furan modified starch was cross-linked with a commercial tetrafunctional maleimide by DA reaction. As shown in Figure 7.2 the obtained hydrogels resulted in solid like robust materials that maintained the shape in their hydrated state. The success of the click DA reaction was assessed by FTIR and UV-vis spectroscopy measurements.

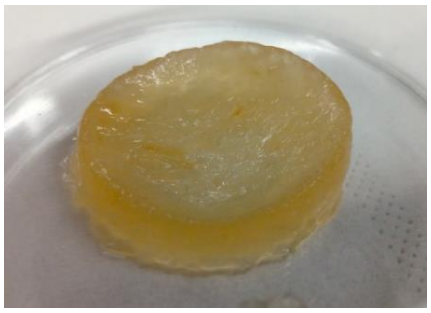

Figure 7.2 – Image of the synthesised hydrogels after the DA reaction.

7.4.1. Fourier transform infrared spectroscopy

The resulting hydrogels were analysed by infrared spectroscopy. Figure 7.3 shows the obtained FTIR spectrum in comparison with that of the S-FI.

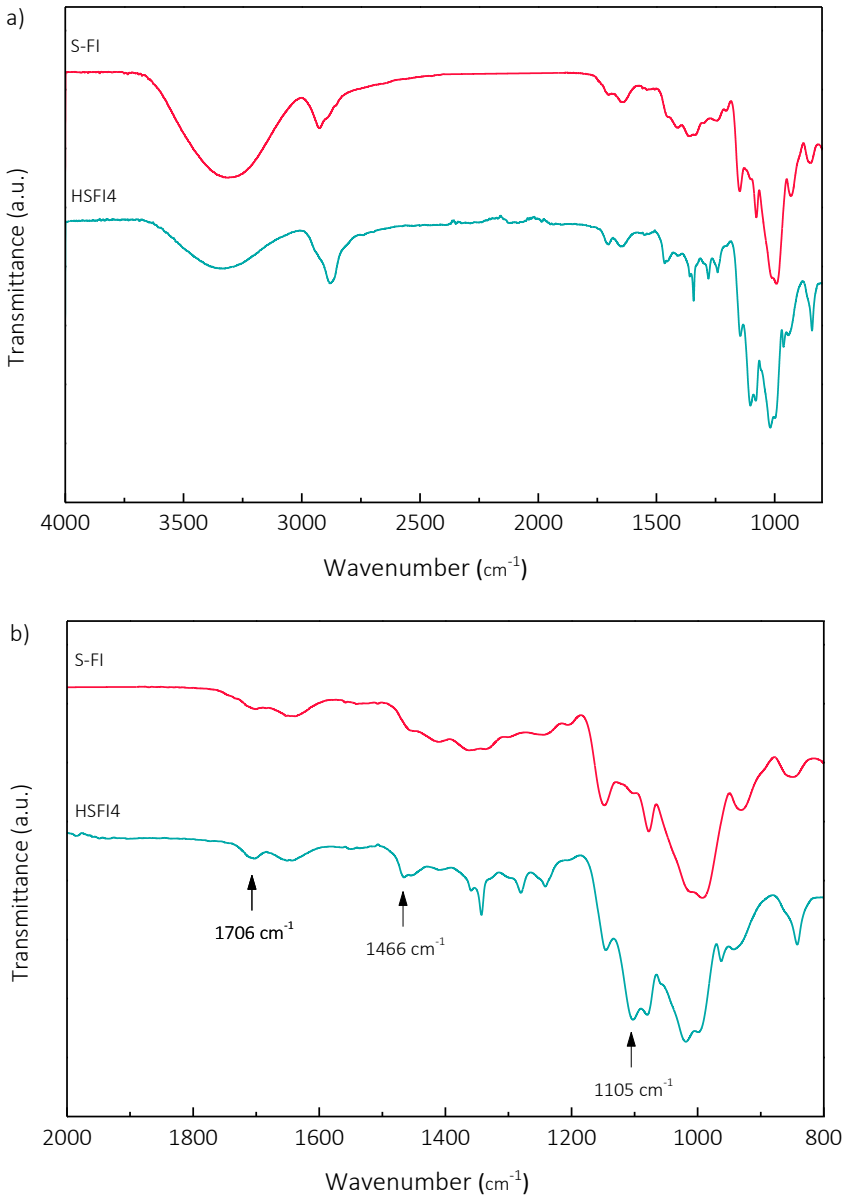

Figure 7.3 – FTIR spectra of S-FI and the cross-linked starch hydrogel a) in the range of 4000 - 600 cm^{-1} and b) a magnification of the 2000 - 600 cm^{-1} interval at room temperature.

As it could be observed, the spectrum of the obtained hydrogel showed a new peak related to the carbonyl maleimide groups (C=O) located at 1706 cm^{-1} [7]. In addition, new peaks associated to the formation of the DA adduct could also be observed. On one hand, the peak shown at 1466 cm^{-1} is usually ascribed to the stretching vibration of the double bond (C=C) in the DA adduct [5,8–10]. Besides, the peak centred at 1105 cm^{-1} is associated with the stretching vibration of the ether linkage

(C-O-C) in the DA cycle [7]. However, due to the numerous signals that appeared in the same region the verification of the DA reaction was difficult only based on the FTIR spectra.

7.4.2. Ultraviolet-visible spectroscopy

In order to study the kinetics of the DA reaction, UV-vis spectroscopy was employed. The measurements were performed at 65 °C using a temperature-controller device collecting spectra every 30 min during a total reaction time of 24 hours. The obtained results are shown in Figure 7.4.

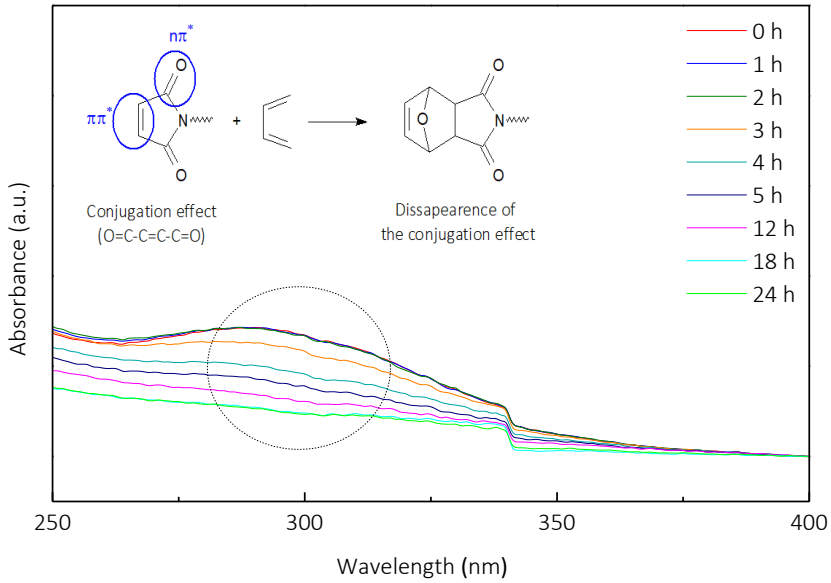

Figure 7.4 – UV-vis spectra of the evolution of the DA reaction at 65 °C.

During the DA cycloaddition, the maleimide groups of the cross-linker reacted with the pendant furan group of the starch to form the DA adduct. Therefore, as the reaction proceeded the quantity of accessible maleimide groups is expected to decrease. Maleimide compounds showed an absorbance signal with a maximum value near 300 nm [3,11] due to the conjugated effect of the double bond ππ* (C=C) and the two carbonyl groups nπ* (C=O) chromophore excitations of the maleimide ring [7,12]. Thus, the DA reaction could be corroborated by monitoring the evolution of the mentioned absorbance signal since it is expected to decrease due to the disappearance of the conjugation as a consequence of the adduct formation [11,13,14].

As observed in Figure 7.4, the absorbance peak associated with the maleimide ring decreased as the reaction proceeded and after 24 hours the signal was not detectable, indicating the consumption of the maleimide to form the DA adduct.

7.5. ANALYSIS OF CELLULOSE NANOCRYSTAL COINTAINING NANOCOMPOSITE HYDROGELS

The nanocomposite hydrogels were prepared by adding CNC as nanoreinforcement at 2.5 and 5 wt.%. Several attempts were made to increase the nanocrystal content above the 5 wt.%, however, it was not feasible since the mixture was too viscous and non-homogeneous. Due to the demonstrated affinity with the matrix (Chapters 4 and 5) and their nanoscale dimensions, it was expected that the addition of CNC would also contribute to the improvement of the mechanical properties and, at the same time, modulate the swelling and/or the capacity for sustained delivery of drugs of the developed novel hydrogels. Thus, the influence of the CNC content in the rheological behaviour, swelling capacity and microstructure was analysed. Besides, the drug delivery profiles and the cytotoxicity were also studied.

7.5.1. Rheological behaviour

The viscoelastic behaviour of unfilled and NCs containing hydrogels was analysed by rheological measurements. Firstly, preliminary strain sweep tests were performed in order to determine the linear viscoelastic region of each sample where both the storage (G') and loss modulus (G") were independent of the applied strain. Thus, a constant strain of 1% was selected to perform the frequency sweep tests. G' and G" vs frequency curves are presented in Figure 7.5.

As could be observed, all hydrogels showed the typical viscoelastic pattern of cross-linked solid gels, being G' almost constant in the studied frequency range and always higher than G" [15]. Thus, it could be concluded that the hydrogels besides to physical interaction possessed a cross-linked permanent network leading to a rigid and strong behaviour [17].

As expected, the addition of CNC led to the increase of G' value, measuring 1381 Pa for unfilled hydrogel and 2011 Pa for the HSFI4-5CNC hydrogel. Therefore, it could be concluded the effective contribution of CNC to the elasticity of the hydrogel [17] since the addition of CNC into the matrix increased the efficiency of the network. In effect, during the DA reaction the CNC were trapped in the hydrogel network leading to the formation of intermolecular H-bonds between OH groups of CNC and those of the starch macromolecule. It is worth to noting that preliminary investigations developed for gelatine based DA hydrogels reinforced with CNCs [16] found that when the CNCs were not functionalised the G' value of the hydrogel was not improved. Recently, Kumar et al. [18] developed hybrid polyacrylamide/carboxymethyl cellulose hydrogels and observed that the addition of 2.5 wt.% of CNCs to the hydrogel did not increase the G' value. In the case of our starch hydrogel the improvement was achieved using bare nanocrystals and, furthermore, the elastic solid-like behaviour was measured even at the lowest frequency values as a consequence of permanent covalent DA cross-links.

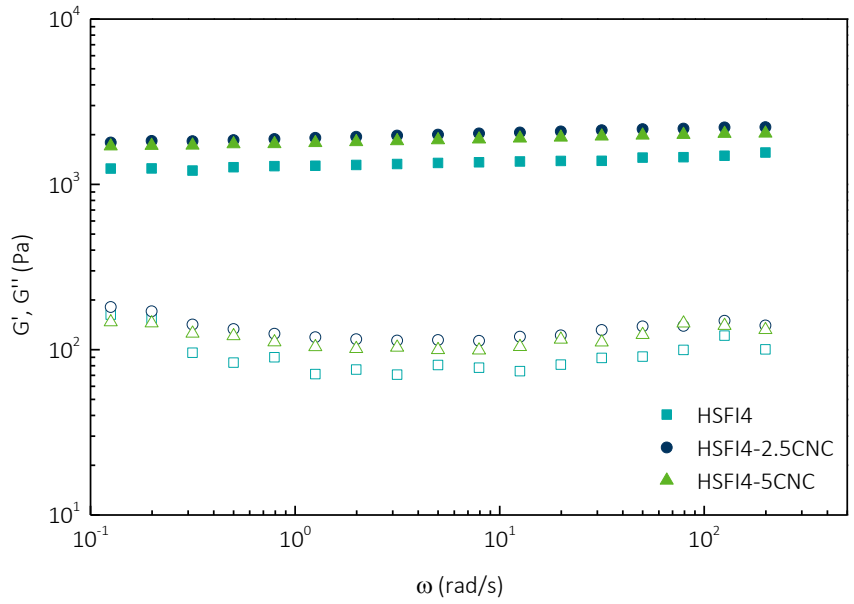

Figure 7.5 – Frequency sweep measurements of ■ HSFI4, ● HSFI4-2.5CNC and ▲ HSFI4-5CNC: G' (filled symbols) and G" (empty symbols). Tests conditions: 37 °C and 10 Hz.

7.5.2. Swelling capacity

The swelling behaviour is one of the most important property to be evaluated in hydrogels [19,20], in particular when they are used in biomedical applications [21]. The swelling capacity of the CNC containing starch-based hydrogels was evaluated gravimetrically by swelling freeze-dried samples (n=3) in phosphate buffer solution (PBS) medium at 37 °C and pH = 7.4. The swelling ratio (SR) was determined using the Equation 2.10. The obtaining SR vs time curves are presented in Figure 7.6.

It was noticed that the swelling patterns of all samples occurred in two steps. During the first period, the SR increased rapidly, while during the second step the SR increased slowly until the hydrogel acquired the maximum amount of fluid that is able to retain and thus, achieved the equilibrium. As it could be observed in the Figure 7.6, the swelling equilibrium was achieved earlier for the unfilled hydrogel that also showed the highest SR value in the first period.

On the other hand, the SR value decreased due to the incorporation of CNCs. As it is well known [3,7,16,22], the SR of hydrogels depends on numerous factors that involves the employed external stimuli (ionic strength, pH, temperature) and the nature of the polymer, i.e. the hydrophilic character of the polymer, the concentration, the cross-linking density of the network and the porosity of the hydrogel. The results were in agreement with those reported by other authors [23,24], the SR value of polysaccharide-based hydrogels decreased by the addition of CNC as nanofiller. It is assumed that the H-bonding interactions formed between the CNC and the polysaccharide, starch in our case,, reduced the mobility of the network [23] and prevented the permeation of the solution inside the hydrogel. Thus, increasing the CNC content the mobility of the cross-linked network was hindered, leading to lower amounts of permeated PBS and lower SR values.

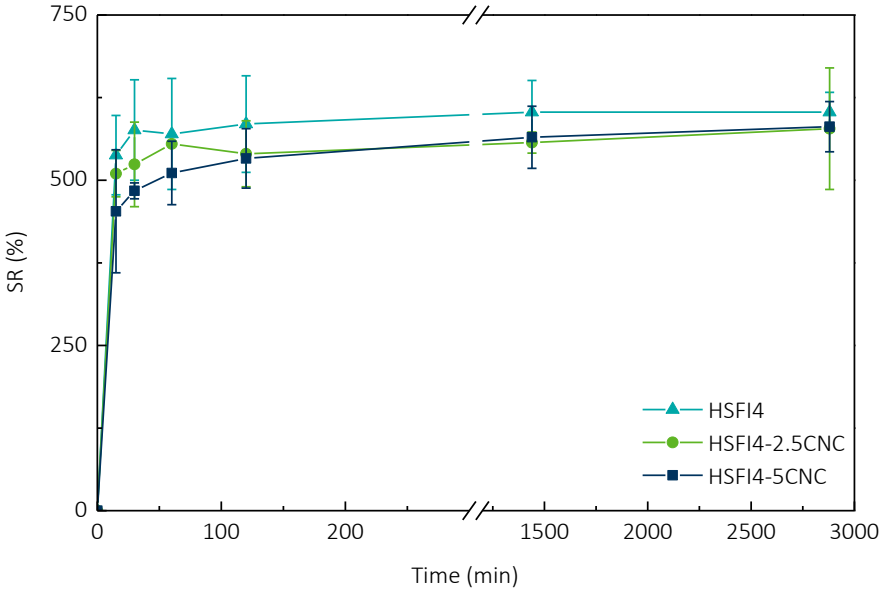

Figure 7.6 – SR versus time curves of HSFI4, HSFI4-2.5CNC and HSFI4-5CNC in PBS at 37 °C.

7.5.3. Drug delivery

The synthesised hydrogels were evaluated in terms of their ability as sustained release drug delivery systems. Hydrogels were firstly loaded with Chloramphenicol (ClPh) following the methodology described in Chapter 2. The amount of drug loaded was found to be similar in all cases, i.e. drug loaded values of 1.58, 1.57 and 1.61 mg ClPh g^{-1} hydrogel were obtained for unfilled hydrogels and hydrogels reinforced with 2.5 and 5 wt.% of CNC, respectively. Drug release studies were then performed at 37 °C during 4 h in phosphate buffer solution (PBS) that simulates intestinal pH conditions. During the test an aliquot of the released media was analysed by UV-vis spectroscopy each 30 min returning the aliquot to the beaker once analysed. The obtained Cumulative Release (CR) profiles are shown in Figure 7.7.

As it could be observed, in all cases controlled and sustained delivery of the antibiotic was achieved but significant differences were detected between the three hydrogels. Indeed, the CR profile was more sustained in case of the unfilled hydrogel, whereas higher CR values were observed for nanoreinforced hydrogels with increasing initial release slope as the CNC content increased.

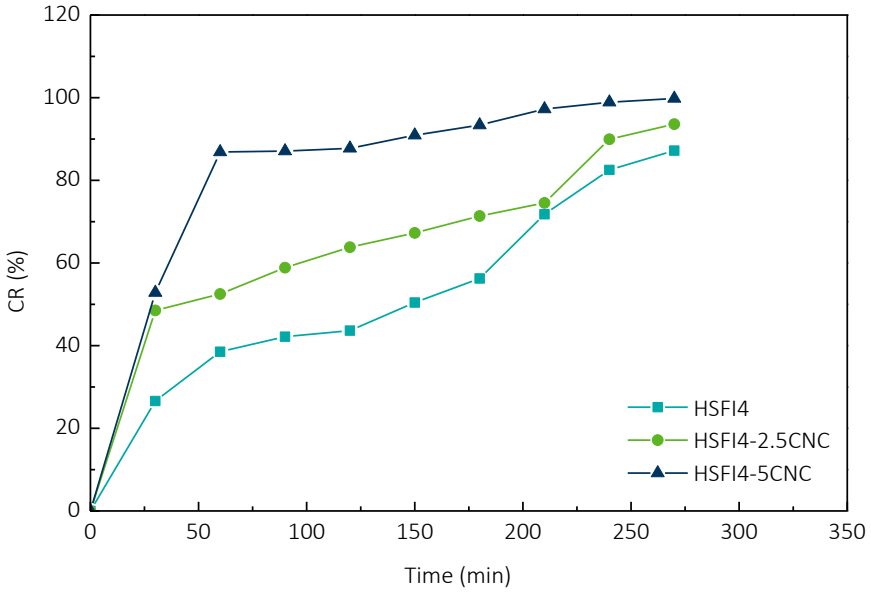

Figure 7.7 – Drug release profiles in PBS at 37 °C of HSFI4, HSFI4-2.5CNC and HSFI4-5CNC.

7.5.4. Scanning electron microscopy

The morphology, the inner pore structure and the pore size and distribution are decisive factors for drug delivery systems [23]. Indeed, an interconnected porous structure is desirable for hydrogels to be applied as drug carriers [3], as the porous network would facilitate the transport and delivery of required molecules [25]. Hence, the morphology of the unfilled matrix and the resulting nanocomposite hydrogels was analysed by SEM. Samples were freeze-dried after swollen in distilled water. It is generally accepted that, the interconnected domains occupied by water in the swollen samples, changed after the freeze-drying process to a porous structure due to the ice crystals formation [9]. Figure 7.8 shows the SEM images of each sample.

In all cases, an interconnected porous microstructure was obtained. However, the pore size was influenced by the content of the CNC, resulting in higher pore size while increasing the CNC content. Indeed, adding 5 wt.% of CNC the pore size increases from values next to 10 μm to values near 90 μm. Similar behaviour was observed by other authors with hydrogels based on cyclodextrin/triblock copolymer and reinforced with cellulose and chitin NCs [17], concluding that

both the pore size and the thickness of the wall increased with the NC content. It seemed that the H-bonds formed during the hydrogel formation in the presence of CNCs, hindered the compaction of the polymeric network and thus, the obtained pore size for nanocomposite hydrogels was larger.

The observed effect of the CNCs incorporation in the internal morphology and the pore size of the hydrogels would be related to the previously discussed swelling and drug release behaviour. Indeed, the pore distribution and size is generally assumed to be crucial for the swelling capacity as well as to affect the release of the drug [23]. As concluded by SEM images the pore size increased notably due to the addition of CNC what could be the reason for the initial "burst effect" that was observed for nanocomposite hydrogels by comparing with the more sustained profile of the unfilled one. This phenomenon is usually ascribed to the release of the drug fixed to the surface or within the upper layers of the hydrogel instead the release of the drug absorbed inside the polymeric network [26].

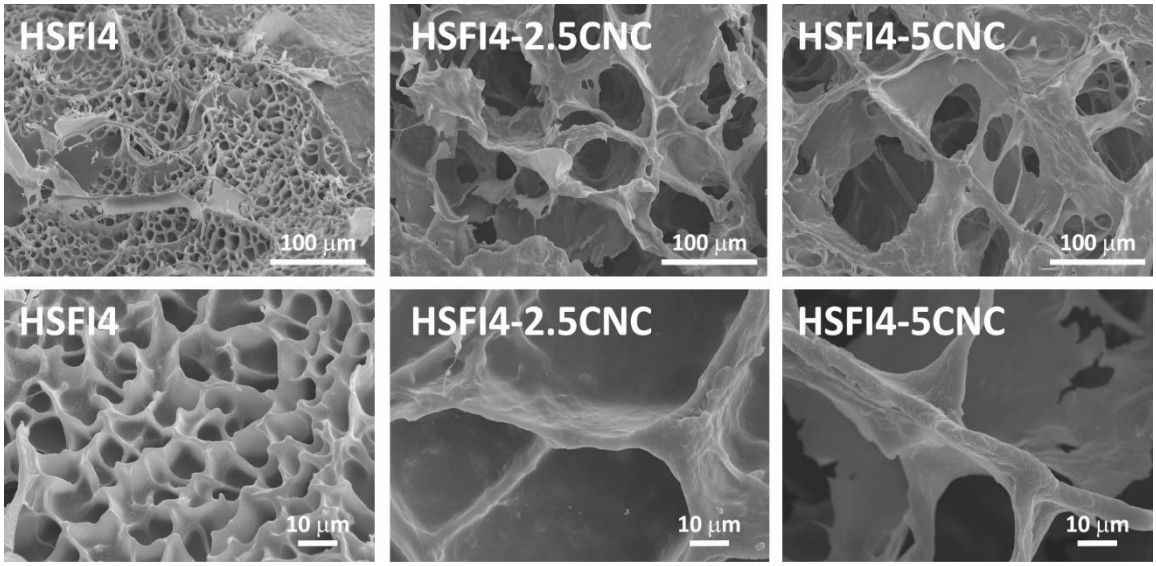

Figure 7.8 – SEM images of the porous microstructure of HSFI4, HSFI4-2.5CNC and HSFI4-5CNC hydrogels.

7.5.5. Cytotoxicity

Since these hydrogels were developed as possible candidates to be used as drug delivery systems in biomedical applications, in vitro cell viability and proliferation was studied by short-term cytotoxicity assays evaluating changes in cellular growth, incubating L 929 mouse fibroblast cells for 24 h and 48 h in the hydrogels. The obtained results are shown in Figure 7.9a and b.

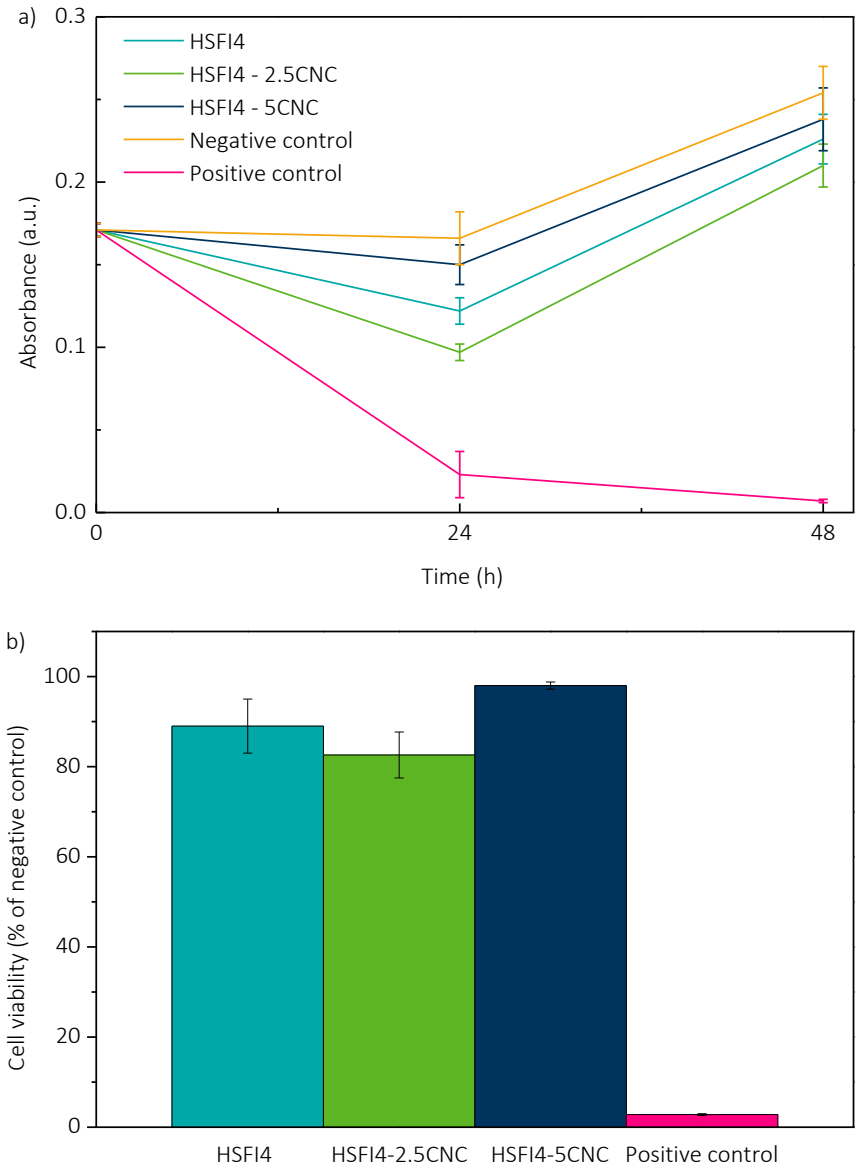

Figure 7.9 – (a) Absorbance at 540 nm versus incubation time of a positive control, negative control and HSFI4, HSFI4-2.5CNC and HSFI4-5CNC hydrogels and b) viability of L-929 murine fibroblast cells in extracted media at 48 h of positive control and HSFI4, HSFI4-2.5CNC and HSFI4-5CNC hydrogels.

Preliminary viability results showed that the hydrogels presented non-toxic behaviour and allowed the cell growth. The proliferation curve of hydrogels (Figure 7.9a) showed the same increasing pattern of the negative control, whereas the positive control presented decreasing slope for the proliferation curve. As mentioned, the cell viability was measured up to 48 hours in cells cultured in extracted medium from hydrogels, showing cell viability values higher than the acceptance limit of 70% (compared with the negative control) as established by ISO 10993-12 standard. Indeed, values of 89.0, 82.6 and 98.0%, were obtained for the unfilled hydrogel and samples reinforced with 2.5 and 5 wt.% of CNC, respectively. These results indicated that hydrogels could be initially considered as biocompatible, and thus, would be suitable for biomedical applications.

7.6. CONCLUSIONS

Starch cross-linked hydrogel nanocomposites were satisfactorily prepared by DA click reaction in aqueous media between synthesised furanic starch derivative (S-FI) and tetrafunctional maleimide cross-linker (TTMI). Firstly, the furan functionalisation of maize starch was assessed by ^{1}H NMR. Besides, the success of the DA reaction was corroborated by FTIR and UV-vis spectroscopy. In addition, hydrogel nanocomposites were prepared adding different CNC content (2.5 and 5 wt.%). The results demonstrated that the addition of CNC led to slightly higher storage modulus and lower SR values, influencing notably both the morphology of the hydrogels, with larger pores and thicker walls, and, particularly, the drug delivery performance of the materials. Finally, it was found that the prepared hydrogels showed non-toxic behaviour, concluding that they showed potential applicability as drug delivery systems in biomedical applications.

7.7. REFERENCES

[1] T.S. Nossa, N.M. Belgacem, A. Gandini, A.J.F. Carvalho, Thermoreversible crosslinked thermoplastic starch, Polym. Int. 64 (2015) 1366–1372. doi:10.1002/pi.4925.

[2] T. Jordan, S. Schmidt, T. Liebert, T. Heinze, Molten imidazole – a starch solvent, Green Chem. 16 (2014) 1967. doi:10.1039/c3gc41818a.

[3] C. García-Astrain, A. Gandini, C. Peña, I. Algar, A. Eceiza, M. Corcuera, N. Gabilondo, Diels–Alder "click" chemistry for the cross-linking of furfuryl-gelatin-polyetheramine hydrogels, RSC Adv. 4 (2014) 35578. doi:10.1039/C4RA06122E.

[4] C. García-astrain, R. Hernández, O. Guaresti, L. Fruk, C. Mijangos, A. Eceiza, N. Gabilondo, Click crosslinked chitosan/gold nanocomposite hydrogels, Macromol. JOurnals. 301 (2016) 1295–1300. doi: 10.1002/mame.201600247.

[5] O. Guaresti, C. García–Astrain, T. Palomares, A. Alonso–Varona, A. Eceiza, N. Gabilondo, Synthesis and characterization of a biocompatible chitosan–based hydrogel cross–linked via 'click' chemistry for controlled drug release, Int. J. Biol. Macromol. 102 (2017) 1–9. doi:10.1016/j.ijbiomac.2017.04.003.

[6] M. Montiel-Herrera, A. Gandini, F.M. Goycoolea, N.E. Jacobsen, J. Lizardi-Mendoza, M. Recillas-Mota, W.M. Argüelles-Monal, N-(furfural) chitosan hydrogels based on Diels-Alder cycloadditions and application as microspheres for controlled drug release, Carbohydr. Polym. 128 (2015) 220–227. doi:10.1016/j.carbpol.2015.03.052.

[7] C. García-Astrain, I. Algar, A. Gandini, A. Eceiza, M.Á. Corcuera, N. Gabilondo, Hydrogel synthesis by aqueous Diels-Alder reaction between furan modified methacrylate and polyetheramine-based bismaleimides, J. Polym. Sci. Part A Polym. Chem. 53 (2015) 699–708. doi:10.1002/pola.27495.

[8] C.M. Nimmo, S.C. Owen, M.S. Shoichet, Diels-alder click cross-linked hyaluronic acid hydrogels for tissue engineering, Biomacromolecules. 12 (2011) 824–830. doi:10.1021/bm101446k.

[9] M. Fan, Y. Ma, Z. Zhang, J. Mao, H. Tan, X. Hu, Biodegradable hyaluronic acid hydrogels to control release of dexamethasone through aqueous Diels-Alder chemistry for adipose tissue engineering, Mater. Sci. Eng. C. 56 (2015) 311–317. doi:10.1016/j.msec.2015.04.004.

[10] O. Guaresti, C. García-Astrain, R.H. Aguirresarobe, A. Eceiza, N. Gabilondo, Synthesis of stimuli–responsive chitosan–based hydrogels by Diels–Alder cross–linking `click´ reaction as potential carriers for drug administration, Carbohydr. Polym. 183 (2018) 278–286. doi:10.1016/j.carbpol.2017.12.034.

[11] T. Engel, G. Kickelbick, Thermoreversible reactions on inorganic nanoparticle surfaces: Diels-alder reactions on sterically crowded surfaces, Chem. Mater. 25 (2013) 149–157. doi:10.1021/cm303049k.

[12] A. Gandini, D. Coelho, A.J.D. Silvestre, Reversible click chemistry at the service of macromolecular materials. Part 1: Kinetics of the Diels-Alder reaction applied to furan-maleimide model compounds and linear polymerizations, Eur. Polym. J. 44 (2008) 4029–4036. doi:10.1016/j.eurpolymj.2008.09.026.

[13] A. Gandini, D. Coelho, M. Gomes, B. Reis, A. Silvestre, Materials from renewable resources based on furan monomers and furan chemistry: work in progress, J. Mater. Chem. 19 (2009) 8656. doi:10.1039/b909377j.

[14] C. Vilela, L. Cruciani, A.J.D. Silvestre, A. Gandini, Reversible polymerization of novel monomers bearing furan and plant oil moieties: a double click exploitation of renewable resources, RSC Adv. 2 (2012) 2966. doi:10.1039/c2ra20053h.

[15] B. Mandal, A.P. Rameshbabu, S.R. Soni, A. Ghosh, S. Dhara, S. Pal, In Situ Silver Nanowire Deposited Cross-Linked Carboxymethyl Cellulose: A Potential Transdermal Anticancer Drug Carrier, ACS Appl. Mater. Interfaces. 9 (2017) 36583–36595. doi:10.1021/acsami.7b10716.

[16] C. García-Astrain, K. González, T. Gurrea, O. Guaresti, I. Algar, A. Eceiza, N. Gabilondo, Maleimide-grafted cellulose nanocrystals as cross-linkers for bionanocomposite hydrogels, Carbohydr. Polym. 149 (2016) 94–101. doi:10.1016/j.carbpol.2016.04.091.

[17] X. Zhang, J. Huang, P.R. Chang, J. Li, Y. Chen, D. Wang, J. Yu, J. Chen, Structure and properties of polysaccharide nanocrystal-doped supramolecular hydrogels based on Cyclodextrin inclusion, Polymer (Guildf). 51 (2010) 4398–4407. doi:10.1016/j.polymer.2010.07.025.

[18] A. Kumar, K.M. Rao, S.S. Han, Mechanically viscoelastic nanoreinforced hybrid hydrogels composed of polyacrylamide, sodium carboxymethylcellulose, graphene oxide, and cellulose nanocrystals, Carbohydr. Polym. 193 (2018) 228–238. doi:10.1016/j.carbpol.2018.04.004.

[19] G.-F. Wang, H.-J. Chu, H.-L. Wei, X.-Q. Liu, Z.-X. Zhao, J. Zhu, Click synthesis by Diels-Alder reaction and characterisation of hydroxypropyl methylcellulose-based hydrogels, Chem. Pap. 68 (2014). doi:10.2478/s11696-014-0574-2.

[20] H.L. Wei, Z. Yang, Y. Chen, H.J. Chu, J. Zhu, Z.C. Li, Characterisation of N-vinyl-2-pyrrolidone-based hydrogels prepared by a Diels-Alder click reaction in water, Eur. Polym. J. 46 (2010) 1032–1039. doi:10.1016/j.eurpolymj.2010.01.025.

[21] F. Yu, X. Cao, Y. Li, L. Zeng, J. Zhu, G. Wang, X. Chen, Diels–Alder crosslinked HA/PEG hydrogels with high elasticity and fatigue resistance for cell encapsulation and articular cartilage tissue repair, Polym. Chem. 5 (2014) 5116–5123. doi:10.1039/C4PY00473F.

[22] F. Yu, X. Cao, L. Zeng, Q. Zhang, X. Chen, An interpenetrating HA/G/CS biomimic hydrogel via Diels-Alder click chemistry for cartilage tissue engineering, Carbohydr. Polym. 97 (2013) 188–195. doi:10.1016/j.carbpol.2013.04.046.

[23] X. Yang, E. Bakaic, T. Hoare, E.D. Cranston, Injectable polysaccharide hydrogels reinforced with cellulose nanocrystals: Morphology, rheology, degradation, and cytotoxicity, Biomacromolecules. 14 (2013) 4447–4455. doi:10.1021/bm401364z.

[24] K. Madhusudana Rao, A. Kumar, S.S. Han, Polysaccharide based bionanocomposite hydrogels reinforced with cellulose nanocrystals: Drug release and biocompatibility analyses, Int. J. Biol. Macromol. 101 (2017) 165–171. doi:10.1016/j.ijbiomac.2017.03.080.

[25] X. Bai, S. Lü, Z. Cao, B. Ni, X. Wang, P. Ning, D. Ma, H. Wei, M. Liu, Dual crosslinked chondroitin sulfate injectable hydrogel formed via continuous Diels-Alder (DA) click chemistry for bone repair, Carbohydr. Polym. 166 (2017) 123–130. doi:10.1016/j.carbpol.2017.02.062.

[26] A.I. Freeman, E. Mayhew, Targeted drug delivery, from Nanomaterials for Medical Applications. 1986. doi: 10.1016/B978-0-12-385089-8.00005-4

CHAPTER 8:

NANOCOMPOSITE HYDROGELS BASED ON CROSS-LINKED STARCH AND GRAPHENE

8. NANOCOMPOSITE HYDROGELS BASED ON CROSS-LINKED STARCH AND GRAPHENE

8.1. OBJECTIVE

In the present chapter starch-based chemically cross-linked hydrogels were obtained by reaction between furan-modified starch (S-FI) and bismaleimide (BMI) in several ratios. Besides, graphene (G) nanoflakes were added in order to provide specific properties to the hydrogel, as electrical conductivity and antimicrobial properties.

Therefore, cross-linked hydrogels were prepared by DA reaction in aqueous media between the furan-modified starch (synthesised according to the Section 7.2.1) and the properly synthesised water-soluble BMI cross-linker. Considering that the effectiveness of the cross-linked network could be affected by the furan/maleimide (Fu:Mal) ratio, different cross-linker amounts were used in order to analyse its influence in the characteristic properties of the hydrogels as rheological behaviour, swelling capacity and morphology. In addition, nanocomposite hydrogels were prepared with G as conductive nanofiller, using Salvia plant extracts as water dispersion stabiliser. The influence of adding G into the matrix was studied in terms of mechanical behaviour, morphology, antimicrobial and electrical properties.

8.2. OBTAINMENT OF CROSS-LINKED STARCH-BASED HYDROGELS

8.2.1. Synthesis of bismaleimide cross-linker (BMI)

The synthesis of the water soluble BMI cross-linker was performed following the method developed previously by our group [1]. The reaction steps are shown in Scheme 8.1. Briefly, 25.87 mmol of Jeffamine® ED 900 were added dropwise over 50 mL of maleic anhydride solution (50.97 mmol) in chloroform. The reaction was maintained at 10 °C for 3 h under nitrogen atmosphere. Then, the product was kept under magnetic stirring at room temperature for 2 h and dried under

vacuum. Then, 4.56 mmol of the dried intermediate product, i.e. bismaleamic acid, were mixed with trimethylamine (2.96 mmol) and sodium acetate trihydrate (3.47 mmol) in 10 mL of acetone under nitrogen atmosphere. Acetic anhydride (28.96 mmol) was then added and the reaction was maintained at 70 °C for 2.5 h. The BMI was obtained by solvent evaporation under vacuum.

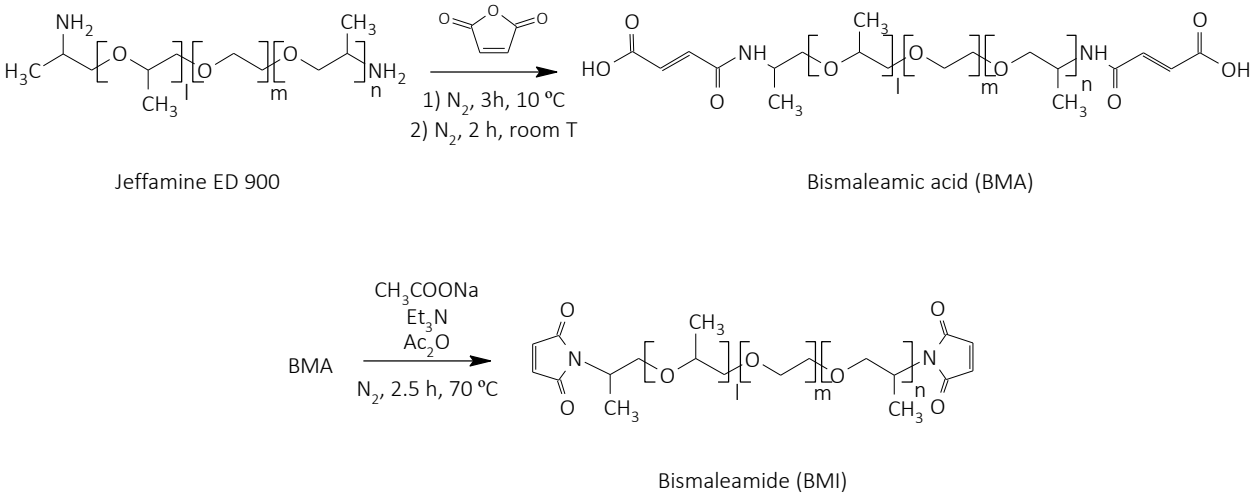

Scheme 8.1 – Synthesis of BMI.

8.2.2. Hydrogel formation by Diels-Alder reaction between S-FI and BMI

Starch-based hydrogels were obtained by the DA reaction of S-FI and the BMI cross-linker. DA reaction is illustrated in Scheme 8.2. The synthesis of S-FI was performed following the method defined in Section 7.2.2. The hydrogel was obtained by mixing the S-FI aqueous solution and the desired amount of BMI and allowing to react at 65 °C for 24 h in a closed vial.

Three different hydrogels were prepared with different S-FI:BMI weight ratios (Fu:Mal), 1:0.5; 1:1.0 and 1:1.5. The S-FI/Jeffamine® ED 900 weight ratio of 1:0.5 was also prepared at the same temperature and time cycle as the reference (control). The corresponding hydrogels were named as HSFI plus de functionality of the cross-linker (in this chapter the cross-linker is bifunctional) followed by the Fu:Mal ratio. In order to evaluate the influence of the BMI content, the hydrogels were characterised as-prepared.

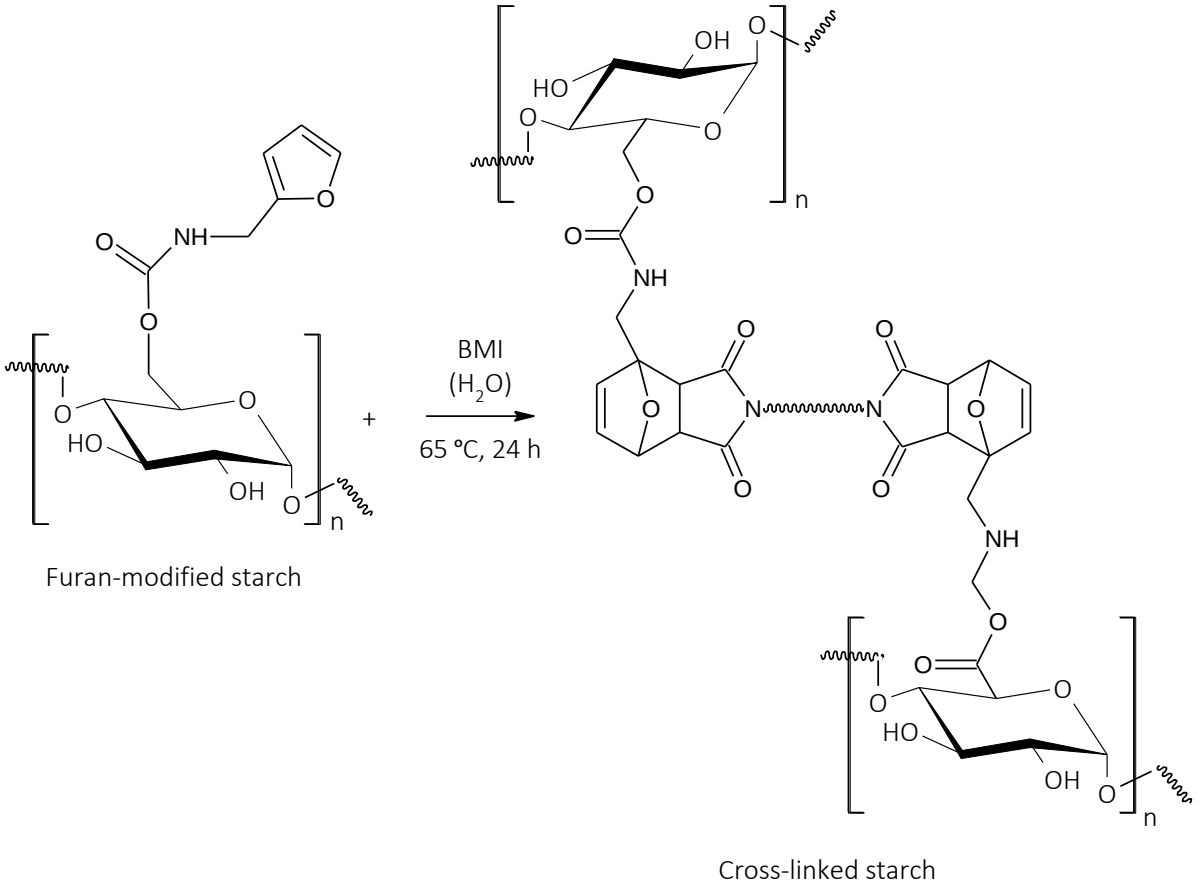

Scheme 8.2 – DA cross-linking reaction of S-FI and BMI.

8.2.3. Preparation of nanocomposite hydrogels by Diels-Alder reaction

Nanocomposite hydrogels were prepared by adding G into the reactive mixture of the hydrogel. The exfoliation of graphite to G was performed as described in Section 4.2.2.1, whereas the preparation of Salvia extracts was carried out by infusion method according to the protocol described in Section 6.2.1.

Firstly, G and Salvia extracts aqueous dispersion was prepared by ultrasonication for 6 h. 0.128 g of S-FI were then dissolved in that aqueous dispersion and 0.192 g of BMI were added in a 1:1.5 weight ratio. The reaction was performed at 65 °C for 24 h in a closed vial. G and Salvia extracts contents were 0.2 wt.%, respectively, relative to the (S-FI+BMI) total weight. The nanocomposite hydrogel will be referred as HSFI2-1:1.5GE.

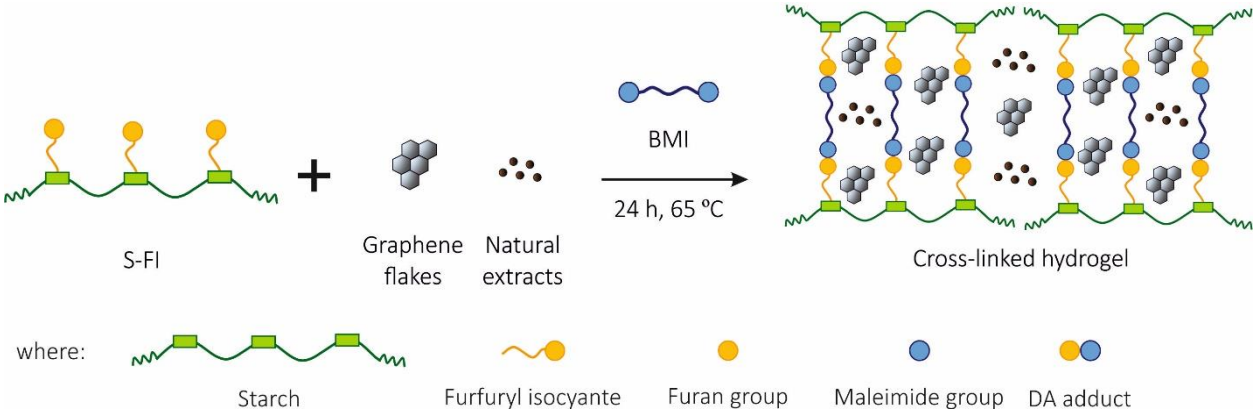

Scheme 8.3 – DA cross-linking reaction to obtain G containing nanocomposite hydrogels.

8.3. CHARACTERISATION OF BISMALEIMIDE

The water soluble bismaleimide was synthesised by the reaction of Jeffamine® ED 900 with maleic anhydride and the subsequent cyclization of the maleimide ring. The success of the synthesis of the bifunctional cross-linker was corroborated by nuclear magnetic resonance.

8.3.1. Nuclear magnetic resonance

^{1}H NMR and ^{13}C NMR spectra of the obtained water-soluble BMI are presented in Figure 8.1. As observed in the ^{1}H NMR spectrum, the typical multiple signals related to the Jeffamine® ED 900 were observed at 3.5 and 1.3 ppm [2]. Besides, a new small peak associated with the hydrogen of the (C=C) double bond of the maleimide ring appeared at 6.20 ppm. Similarly, in the case of ^{13}C NMR, new peaks related to the double bond (C=C) and the carbonyl bond (C=O) of the maleimide ring were observed at 135 and 171 ppm, respectively. The results are in agreement with previously reported literature [2] indicating that the BMI cross-linker was successfully synthesised.

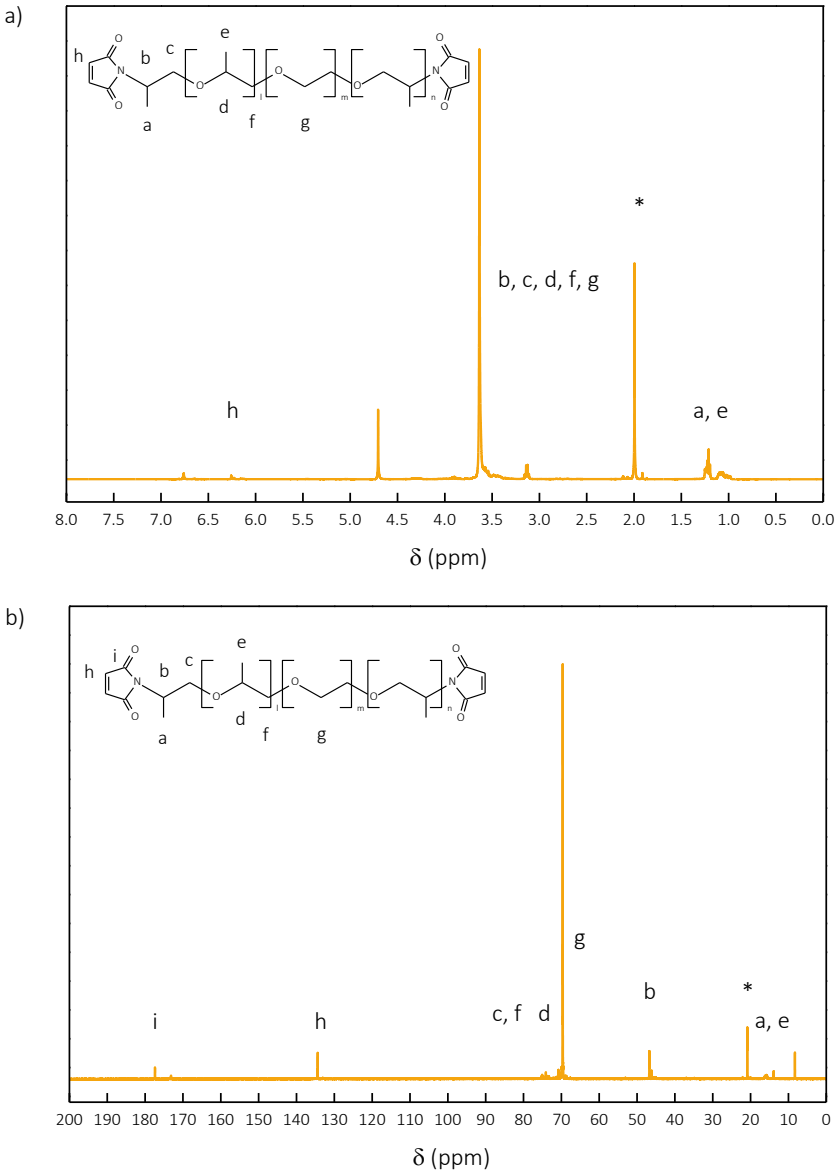

Figure 8.1 – a) ^{1}H NMR and ^{13}C NMR spectra of BMI (* refers to acetic acid impurities).

8.4. ANALYSIS OF THE PREPARED HYDROGELS

Starch based Diels-Alder cross-linked hydrogels were prepared with different Fu:Mal weight ratios similarly to the previous work reported by our group and based on furan modified gelatine, with some modifications [1]. Besides, a reference sample (control) was prepared by mixing the unmodified Jeffamine® ED 900 with S-FI using a weight ratio of 1:0.5.

As it could be deduced by the pictures showed in Figure 8.2, all the targeted hydrogels were successfully cross-linked DA reaction after the reaction time, whereas the control sample, that without maleimide groups, remained in the liquid state.

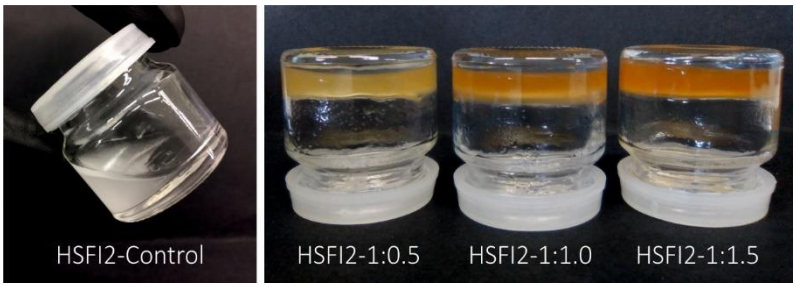

Figure 8.2 – Images of the synthesised hydrogels after the DA reaction.

8.4.1. Fourier transform infrared spectroscopy

The hydrogels were analysed by FTIR in order to observe the new absorption bands associated with the Diels Alder adduct. The resulting spectra are shown in Figure 8.3. Due to the high number of the signals in the same region, the new peaks were hardly distinguishable and, hence, a magnification of 2000-600 cm^{-1} interval is also presented.

For all cross-linked hydrogels new peaks of carbonyl maleimide group (C=O) could be observed at 1745 and 1706 cm^{-1} [2]. In addition, new peaks related to the stretching vibration of the double bond (C=C) in the DA adduct appeared at 1455 cm^{-1} [3–6], as well as another new peak associated with ether group (C-O-C) stretching vibration of the DA adduct at 1100 cm^{-1} [2]. However, as concluded in Chapter 7, the numerous peaks that appeared in the same region make difficult to discern the DA adduct formation by means of FTIR spectra.

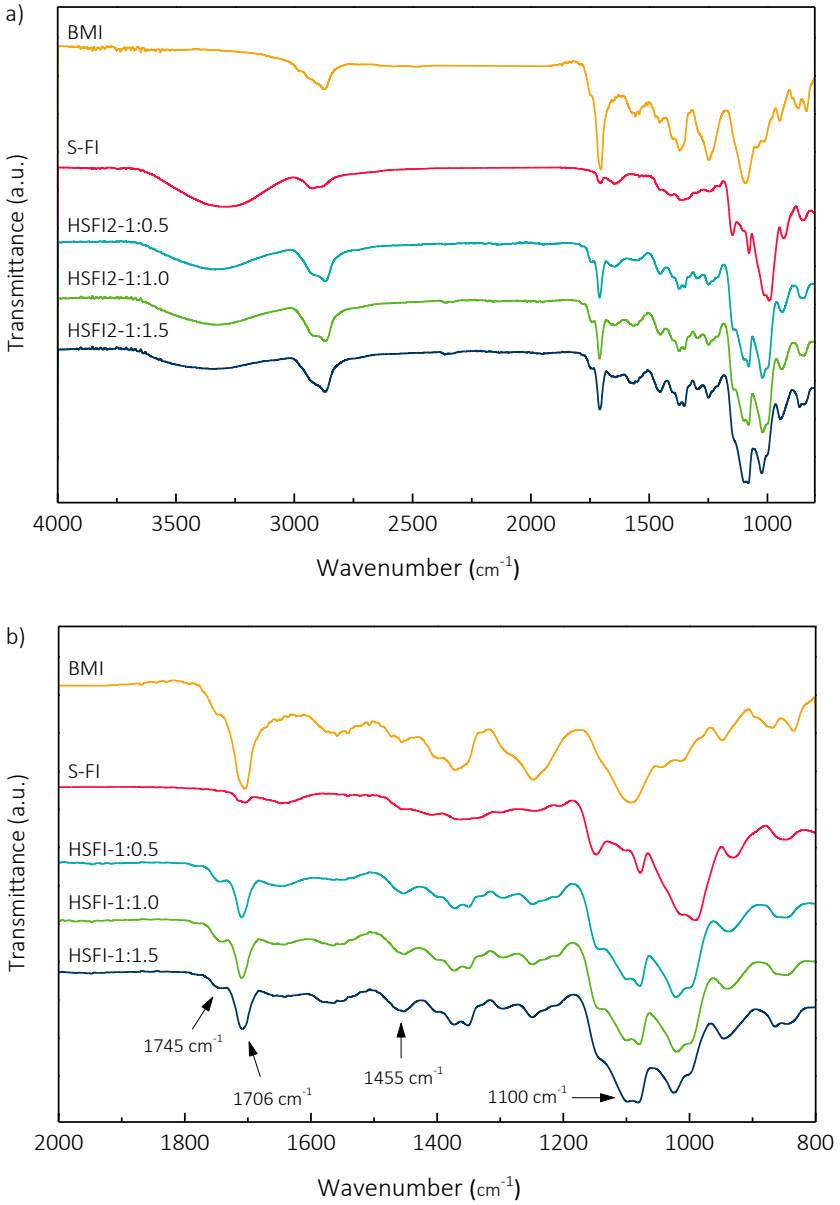

Figure 8.3 –FTIR spectra of BMI, S-FI and the three final cross-linked starch hydrogels a) in the range of 4000 - 600 cm^{-1} and b) the magnification in the 2000 - 600 cm^{-1} interval at room temperature.

8.4.2. Ultraviolet-visible spectroscopy

In order to further verify the DA reaction, the reaction between the furan-modified starch and the BMI was monitored by UV–vis spectroscopy using a temperature-controlled device. The measurements were carried out at 65 °C using the Fu:Mal weight ratio of 1:1.5 as the reference by

recording one spectrum each 30 min, during 24 h. Figure 8.4 shows the obtained UV-vis spectra collection.

As discussed in Chapter 7, as the reaction proceeds and the DA adduct is formed, the disappearance of the absorbance associated to the maleimide ring occurs [7–9].

As illustrated in Figure 8.4, the absorbance band related to the maleimide groups decreased progressively as the cross-linking reaction proceeded to form the DA adduct. The intensity of the absorbance band decreased until disappearing at the end of the reaction. The results proved that the DA reaction occurred completely, and the success of the proposed strategy was then assessed.

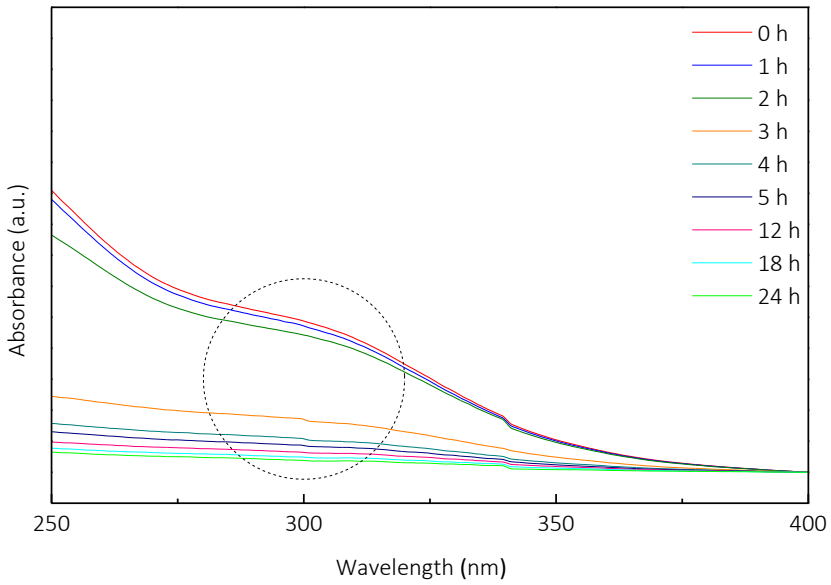

Figure 8.4 – UV-vis spectra of the evolution of the DA reaction at 65 °C.

8.5. EFFECT OF THE FURAN TO MALEIMIDE WEIGHT RATIO ON HYDROGEL PROPERTIES

The DA hydrogels were prepared by reaction between S-FI and different cross-linker amounts in order to evaluate the influence of the furan to maleimide weight ratio on the final properties of

starch-based hydrogels. Thereby, the increase of the cross-linker agent amount in viscoelastic behaviour, the porous morphology and the swelling capacity was studied.

8.5.1. Rheological behaviour

The viscoelastic behaviour of the hydrogels (n=3) was analysed in order to study the effect of the Fu:Mal weight ratio. The influence of the amount of cross-linker in the stiffness of the hydrogels was evaluated. Firstly, preliminary strain sweep tests were carried out in order to determine the linear viscoelastic region of each sample, i.e. the region in which both the storage (G') and loss modulus (G") were independent of the applied strain. Thus, a constant strain of 1% was selected to perform the frequency sweep tests. Results are shown in Figure 8.5. As observed, after a small period of stabilisation the samples showed a solid-like gel behaviour [10,11] which is characteristic of an elastic pattern. Thus, G' was maintained almost constant and always higher than G" in the whole studied frequency range (0.1–500 rad s^{-1}) [12]. Some noticeable differences were observed between the different hydrogels. When comparing HSFI2-1:0.5 and HSFI2-1:1.0 hydrogels, it was found that G' values were 1720 ± 243 Pa and 1600 ± 173 Pa, respectively. However, increasing the BMI amount up to the 1:1.5 wt.% ratio resulted in higher G' values (3750 ± 353 Pa). The value of the G' is generally assumed to be closely related to the cross-linking density of the hydrogel network. Similar results were observed in our group both increasing the cross-linker amount [2] and also when using CNC grafted with maleimide groups as additional cross-linkers [13]. Hence, the remarkable increase in the G' value for the 1:1.5 sample could be ascribed to a larger amount of cross-linking points.

The field of application of hydrogels synthesised from biodegradable polymers is mainly related to biomedical applications as scaffolds or implants. It is therefore of great relevance the stiffness of the final material as it could directly affect its final performance. The G' value, as indicator of the rigidity of the material, was found to be in the range between 1600-3750 Pa, which is comparable with those values of liver, fat, relaxed muscle and breast gland tissue (10^3–10^4 Pa) [14].

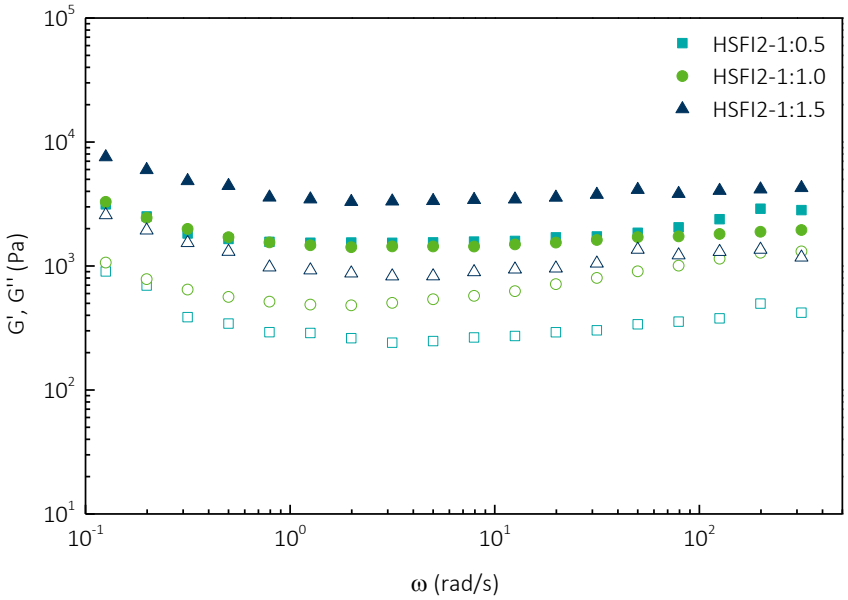

Figure 8.5 – Frequency sweep measurements of ■ HSFI2-1:0.5, ● HSFI2-1:1.0 and ▲ HSFI2-1:1.5:G' (filled symbols) and G" (empty symbols). Tests conditions: 37 ˚C and 1%.

8.5.2. Scanning electron microscopy

Achieving an interconnected porous internal structure is a key issue to consider in the formation of hydrogels for biomedical applications [1,15]. Therefore, the microstructure of hydrogels was studied by SEM over freeze dried samples after being swollen in distilled water. Figure 8.6 shows the microstructure of each sample analysed by SEM.

As noticed, the morphology of hydrogels was strongly influenced by the amount of the cross-linker. A porous structure was obtained in all cases, which was expected to retain a great amount of water [15]. However, as it could be observed, increasing the Fu:Mal weight ratio led to a more porous structure. HSFI2-1:0.5 sample showed a quite compact morphology with both smooth areas and pits, whereas for HSFI2-1:1.0 and HSFI2-1:1.5 hydrogels more homogeneous porous microstructure was observed. Moreover, the pore size was found to be much smaller for the latter (around 25 μm for HSFI2-1:1.0 and around 10 μm for HSFI2-1:1.5) being them regularly distributed along the sample. It is normally accepted that the use of higher amounts of cross-linker in the formulations led to smaller pore sizes since higher cross-linking densities are obtained [15]. Hence,

these results would be in concordance with those previously presented from the rheological data, and therefore, could indicate that the 1:1.5 Fu:Mal weight ratio achieved the highest degree of cross-linking, showing the highest elastic modulus value and the smaller pore size.

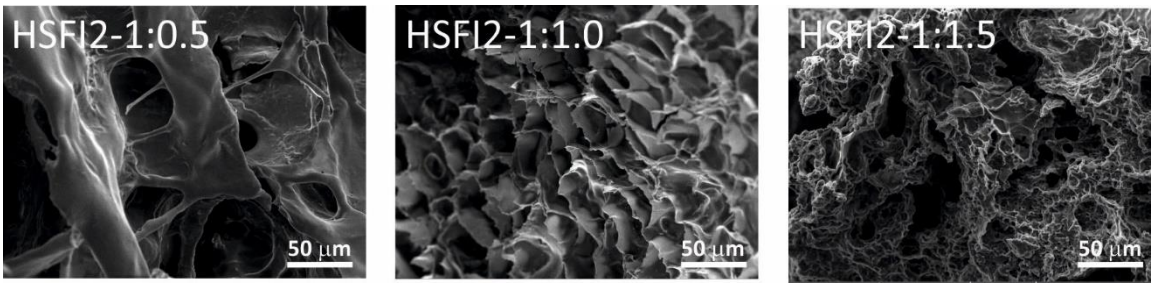

Figure 8.6 – SEM images of the porous microstructure of starch-based hydrogels HSFI2-1:0.5, HSFI2-1:1.0 and HSFI2-1:1.5 samples.

8.5.3. Swelling capacity

The swelling capacity of the hydrogels was gravimetrically measured by swelling freeze-dried samples (n=3) in simulated intestinal fluid (phosphate buffer (PBS), pH=7.4 at 37 °C. The SR was determined by the Equation 2.10. The obtained swelling curves are shown in Figure 8.7.

The swelling patterns of all samples involved two steps of different swelling rates. During the first step, the SR increased rapidly up to a value of 400% for the 1:0.5 hydrogel and 800% for the other two formulations, whereas in the second step the swelling degree grew slowly until the equilibrium was achieved. The equilibrium value was reached after similar time interval in all cases.

As discussed in Chapter 7, the swelling capacity of hydrogels would be determined by the internal porous microstructure. In addition, it depends also on the amount and the hydrophilic character of the employed polymer and cross-linker [1,2,13,16] since increasing hydrogen bonding interactions between the hydrophilic polymeric chains and water molecules bring the aqueous solution inside the network leading to higher SR [16].

Therefore, the cross-linking density and the hydrophilic nature of the BMI would be decisive variables. Commonly the SR value decreases when a highly cross-linked polymeric network is obtained, since the 3D network hinders the permeation of the solution inside the hydrogel and, at the same time, the polymeric chains mobility is reduced, preventing the separation and the subsequent swelling [13,16].

According to the rheological results and the microstructure analysed by SEM, higher cross-linker densities were attributed to the hydrogel with the largest amount of BMI. Thus, it could be expected lower SR values to be obtained for higher Fu:Mal weight ratios. However, in our case the opposite effect was observed, i.e. the SR increased when using higher BMI amounts. Consequently, the HSFI2-1:1.5 sample is the one with higher swelling degree. The strong hydrophilic character of the used cross-linker is likely to be the main reason for these swelling behaviour, in agreement with previously findings reported by our group [5]. Similar results were obtained in a preliminary study using the BMI and a furanic modified gelatine [17].

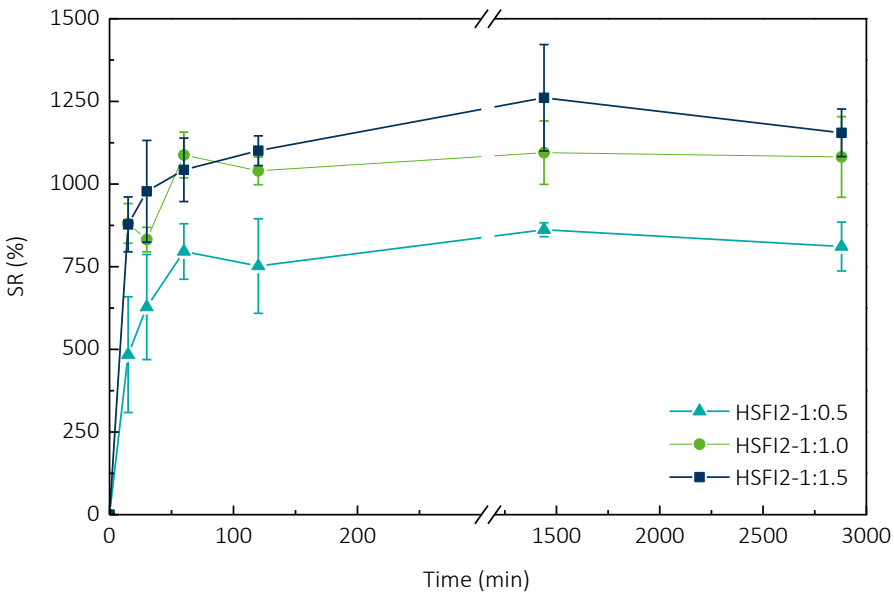

Figure 8.7 – SR (%) versus time curves of obtained starch hydrogels in PBS at 37 °C.

8.5.4. Hydrolytic degradation

In order to evaluate the long-term stability of the hydrogels, they were maintained immersed in PBS (n=3) for one week and the hydrolytic degradation was assessed by determining the final weight loss (Equation 2.11). Similar degradation values (in %) were obtained for HSFI2-1:1.0 (53 ± 2%) and HSFI2-1:1.5 (52 ± 5%) hydrogels, whereas higher values were achieved for HSFI2-1:0.5 sample (79 ± 1%). These results are in concordance with the literature [3,6], which stated that the degradation is influenced by the cross-linking degree, thus higher cross-linked network result in lower hydrolytic degradation values.

8.6. ANALYSIS OF GRAPHENE CONTAINING NANOCOMPOSITE HYDROGELS

Soft, flexible, biocompatible, and electroactive hydrogels have applications in diverse areas such as switchable drug delivery devices, tissue engineering scaffolds with built-in stimulation and sensing, and as coatings for neural electrodes and implants [18]. Therefore, we hypothesised that conductive hydrogels could be developed by the incorporation of G nanoflakes as conductive reinforcement into our starch-based hydrogels.

Thus, for the development of nanocomposite hydrogels, and according to the results obtained previously for neat hydrogels, HSFI2-1:1.5 was selected as the matrix since it presented the highest modulus and swelling ratio values whereas along with the lowest pore size. For the incorporation of G (0.2 wt.%) it was firstly homogenously dispersed in water using Salvia extracts as dispersion stabilisers. As it was discussed in Chapter 6, the use of polyphenolic compounds, such as natural extracts, contribute to the obtainment of stable dispersions of G nanoflakes in water [19]. Besides, Salvia extracts are known to present antimicrobial and anti-inflammatory activities features that could be relevant in the biomedical field [20]. The image of the obtained G containing nanocomposite hydrogel (HSFI2- 1:1.5GE) is shown in Figure 8.8.

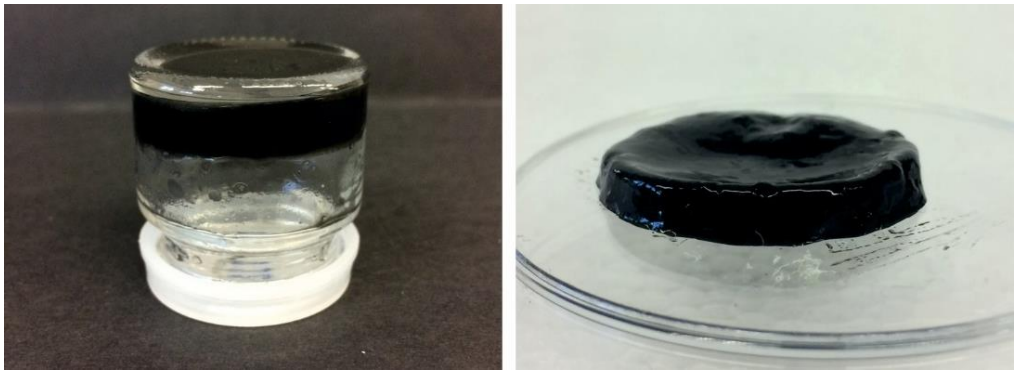

Figure 8.8 – Image of HSFI2-1:1.5GE sample.

8.6.1. Rheological behaviour

The effect of adding G nanoflakes on the viscoelastic behaviour of starch-based hydrogels was evaluated following the same methodology described for the neat hydrogels. The corresponding results are shown in Figure 8.9.

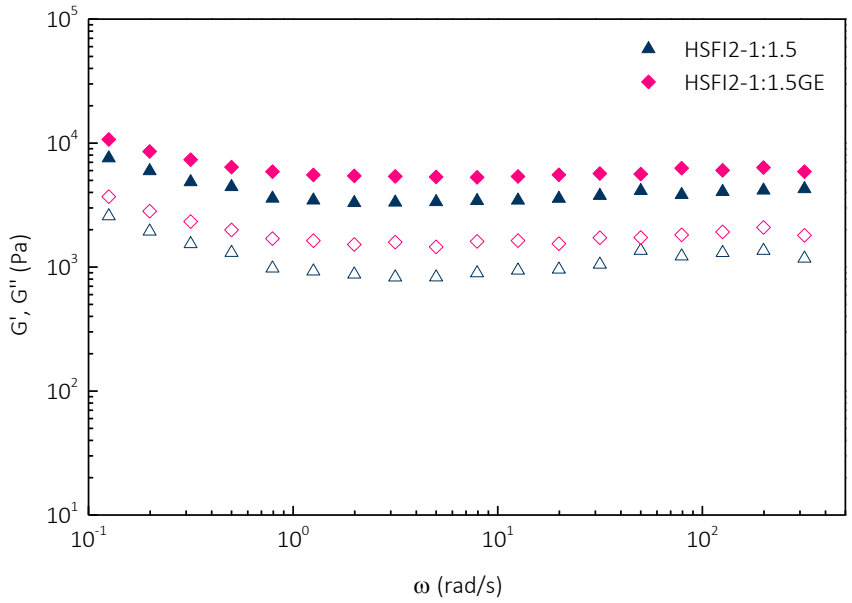

Figure 8.9 – Frequency sweep measurements of ▲ HSFI2-1:1.5 and ◆ HSFI2-1:1.5GE: G' (filled symbols) and G" (empty symbols). Tests conditions: 37 °C and 1%.

It could be noticed that HSFI2-1:1.5GE presented the same viscoelastic pattern as its counterpart without G (HSFI2-1:1.5). Indeed, G' was higher than G" and remained constant in the studied frequency range.

In addition, upon the addition of 0.2 wt.% of graphene, G' increased from 3660 ± 352 Pa for the unfilled hydrogel to 5680 ± 362 Pa for the nanocomposite. These results are in concordance with those reported by Ganguly et al. [21] with G reinforced acrylic hydrogels, where the G' was found to increase with increasing G content.

8.6.2. Electrical conductivity

Electroactive hydrogels could be developed following different strategies that include the use of insulating traditional polymers combined with intrinsically conductive constituents as carbon nanostructures (nanofibers, nanotubes or G), metallic nanoparticles or conducting polymers. The electrical response of HSFI2-1:1.5 hydrogel with and without G was analysed by electrical conductivity measurements by a two-probe technique measuring the resulting current intensity for each applied voltage in the range of 0-5 V. G was incorporated as conductive nanofiller, thus it was expected the conductivity to be increased. From the measurements the electrical conductivity was calculated to be 1.23×10^{-4} S m^{-1} for the HSFI2-1:1.5, whereas HSFI2-1:1.5GE hydrogel showed an electrical conductivity of 1.16×10^{-3} S m^{-1}. The increase of the conductivity up to a decade indicated that the G would be acting as effective conductor nanoreinforcement of the hydrogel. Ganguly et al. [21] and Alam et al. [22] reported values of around 0.40 vol% of G as that for the percolation threshold of electrical conductivity for G containing acrylic hydrogels which is higher than the G concentration studied for the prepared starch hydrogels. However, the percolation threshold is strongly dependent on the nature and chemical structure of the macromolecular network and the created conductive pathway. Therefore, further investigations would be required varying the G content into the starch hydrogel matrix in order to assess the electrical percolation threshold for the greatest conductivity improvement.

8.6.3. Antimicrobial activity

The antimicrobial activity is also a relevant issue when designing materials for being applied in biomedical applications. G is an outstanding candidate as antimicrobial agent [23,24], due to its capacity to inactivate and control various microorganisms proliferation [25]. Moreover, it is worth noting that Salvia extracts are also commonly used as effective antibacterial, antioxidant and anti-inflammatory agents [20,26,27]. The antimicrobial activity of G containing hydrogels was analysed against *Escherichia coli* CECT 405 and *Staphylococcus aureus* CECT 239 bacteria. The inoculated samples were incubated at 37 °C for 24 h and 48 h and tested using the disc-plate antibiogram technique. The bacterial growth inhibition zones were measured (Figure 8.10).

The HSFI2-1:1.5GE hydrogel presented inhibitory activity against both *E. coli* and *S. aureus* bacteria. After 24 h of incubation, an inhibitory halo of 7.0 mm was obtained in the case of *E. coli*, whereas for *S. aureus* the diameter reached up to 9.5 mm. Furthermore, it was observed that after 48 h of incubation, the size of the inhibition halo remains constant for *E. coli*. On the contrary, in the case of *S. aureus* the inhibition zone decreased from 9.5 mm to 4.5 mm. Nevertheless, the existence of the halo after 48 h denotes that the antibacterial activity against *S. aureus* bacteria keeps effective. Santamaria-Echart et al. [27] reported that when Salvia extracts were added ex situ into a waterborne polyurethane matrix in 3 and 5 wt.%, the resulting materials presented proliferation against *S. aureus* in some cases after 96 h. It should be noted that in this work an effective antibacterial activity against *S. aureus* was obtained using significantly lower extracts content. Therefore, it seemed that, in our case, the antibacterial activity was also influenced by the addition of G nanoflakes into the hydrogel matrix. Thus, it could be concluded that the incorporation of G dispersed in the Salvia extracts into the starch-based hydrogels led to efficient antibacterial materials.

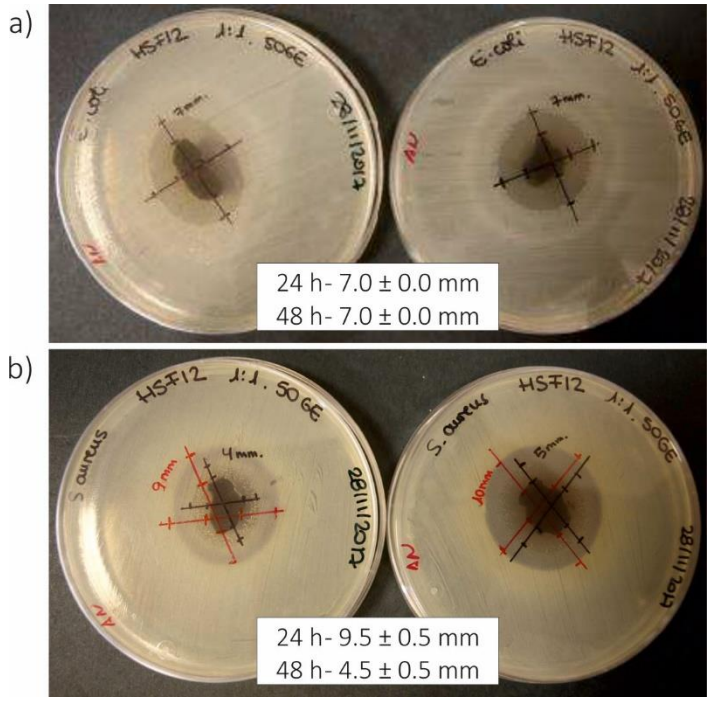

Figure 8.10 – Antibacterial tests of HSFI2-1:1.5GE for a) *E. coli* (duplicated) and b) *S. aureus* (duplicated) indicating the inhibition zones at 24 h (red line) and 48 h (black line).

8.6.4. Scanning electron microscopy

The microstructure of the nanocomposite hydrogels was also analysed by SEM. In a similar way, the G and extracts containing hydrogel was swollen in distilled water and freeze-dried. Figure 8.11 shows the microstructure of the resulting nanocomposite hydrogel analysed by SEM.

As it could be observed, the nanocomposite hydrogel showed the desired homogeneous porous structure. However, it is worth noting that the addition of the nanofiller resulted in higher pore sizes. Indeed, the pore size increased from 10 μm (for the unfilled matrix) to 100 μm (for the nanocomposite hydrogel). Similarly to that concluded for the nanocrystals containing hydrogels in Chapter 7, it seemed that the incorporation of the G nanoflakes altered the formation of an effective cross-linked network leading to higher pore sizes.

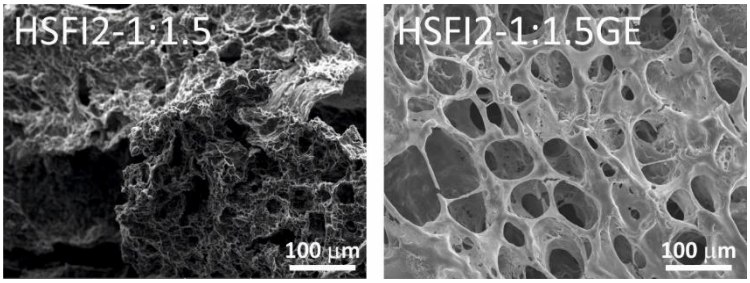

Figure 8.11 – SEM images of the porous microstructure of starch-based hydrogels HSFI2-1:1.5 and HSFI2-1:1.5GE samples.

8.7. CONCLUSIONS

Starch-based hydrogels were successfully obtained by DA reaction between furan-modified starch and the hydrophilic BMI cross-linker in aqueous media. The effectiveness of DA reaction to form starch-based hydrogels was demonstrated by FTIR and UV-vis spectroscopy. The Fu:Mal weight ratio was found to affect significantly the rheological properties and the microstructure of the final hydrogels, decreasing the pore size and increasing the storage modulus value with the 1:1.5 ratio. G nanoflakes were incorporated as conductive nanofiller to the reaction medium using Salvia extracts as dispersion stabilisers. As expected, the obtained nanocomposite hydrogel presented not only mechanical behaviour improvement but also antimicrobial activity against both gram positive and gram-negative bacteria, whereas the electrical conductivity of the material was improved in a decade. These biobased novel materials have promising properties in view of future biomedical applications, in particular those were electrical responsive hydrogels could be required.

8.8. REFERENCES

[1] C. García-Astrain, A. Gandini, C. Peña, I. Algar, A. Eceiza, M. Corcuera, N. Gabilondo, Diels–Alder "click" chemistry for the cross-linking of furfuryl-gelatin-polyetheramine hydrogels, RSC Adv. 4 (2014) 35578. doi:10.1039/C4RA06122E.

[2] C. García-Astrain, I. Algar, A. Gandini, A. Eceiza, M.Á. Corcuera, N. Gabilondo, Hydrogel synthesis by aqueous Diels-Alder reaction between furan modified methacrylate and polyetheramine-based bismaleimides, J. Polym. Sci. Part A Polym. Chem. 53 (2015) 699–708. doi:10.1002/pola.27495.

[3] M. Fan, Y. Ma, Z. Zhang, J. Mao, H. Tan, X. Hu, Biodegradable hyaluronic acid hydrogels to

control release of dexamethasone through aqueous Diels-Alder chemistry for adipose tissue engineering, Mater. Sci. Eng. C. 56 (2015) 311–317. doi:10.1016/j.msec.2015.04.004.

[4] O. Guaresti, C. García–Astrain, T. Palomares, A. Alonso–Varona, A. Eceiza, N. Gabilondo, Synthesis and characterization of a biocompatible chitosan–based hydrogel cross–linked via 'click' chemistry for controlled drug release, Int. J. Biol. Macromol. 102 (2017) 1–9. doi:10.1016/j.ijbiomac.2017.04.003.

[5] O. Guaresti, C. García-Astrain, R.H. Aguirresarobe, A. Eceiza, N. Gabilondo, Synthesis of stimuli–responsive chitosan–based hydrogels by Diels–Alder cross–linking `click´ reaction as potential carriers for drug administration, Carbohydr. Polym. 183 (2018) 278–286. doi:10.1016/j.carbpol.2017.12.034.

[6] C.M. Nimmo, S.C. Owen, M.S. Shoichet, Diels-alder click cross-linked hyaluronic acid hydrogels for tissue engineering, Biomacromolecules. 12 (2011) 824–830. doi:10.1021/bm101446k.

[7] T. Engel, G. Kickelbick, Thermoreversible reactions on inorganic nanoparticle surfaces: Diels-alder reactions on sterically crowded surfaces, Chem. Mater. 25 (2013) 149–157. doi:10.1021/cm303049k.

[8] A. Gandini, D. Coelho, M. Gomes, B. Reis, A. Silvestre, Materials from renewable resources based on furan monomers and furan chemistry: work in progress, J. Mater. Chem. 19 (2009) 8656. doi:10.1039/b909377j.

[9] C. Vilela, L. Cruciani, A.J.D. Silvestre, A. Gandini, Reversible polymerization of novel monomers bearing furan and plant oil moieties: a double click exploitation of renewable resources, RSC Adv. 2 (2012) 2966. doi:10.1039/c2ra20053h.

[10] B. Mandal, A.P. Rameshbabu, S.R. Soni, A. Ghosh, S. Dhara, S. Pal, In situ slver nanowire deposited cross-Linked carboxymethyl cellulose: A potential transdermal anticancer drug carrier, ACS Appl. Mater. Interfaces. 9 (2017) 36583–36595. doi:10.1021/acsami.7b10716.

[11] S. Wang, J. Wang, W. Zhang, J. Ji, Y. Li, G. Zhang, F. Zhang, X. Fan, Ethylenediamine modified graphene and its chemically responsive supramolecular hydrogels, Ind. Eng. Chem. Res. 53 (2014) 13205–13209. doi:10.1021/ie501448p.

[12] C. García-astrain, R. Hernández, O. Guaresti, L. Fruk, C. Mijangos, A. Eceiza, N. Gabilondo, Click crosslinked chitosan/gold nanocomposite hydrogels, Macromol. JOurnals. 301 (2016) 1295–1300. doi: 10.1002/mame.201600247

[13] C. García-Astrain, K. González, T. Gurrea, O. Guaresti, I. Algar, A. Eceiza, N. Gabilondo, Maleimide-grafted cellulose nanocrystals as cross-linkers for bionanocomposite hydrogels, Carbohydr. Polym. 149 (2016) 94–101. doi:10.1016/j.carbpol.2016.04.091.

[14] C. García-Astrain, I. Ahmed, D. Kendziora, O. Guaresti, A. Eceiza, L. Fruk, M.A. Corcuera, N. Gabilondo, P. Yang, I.K. Kwon, J.M. Greneche, Effect of maleimide-functionalized gold nanoparticles on hybrid biohydrogels properties, RSC Adv. 5 (2015) 50268–50277. doi:10.1039/C5RA06806A.

[15] X. Bai, S. Lü, Z. Cao, B. Ni, X. Wang, P. Ning, D. Ma, H. Wei, M. Liu, Dual crosslinked chondroitin sulfate injectable hydrogel formed via continuous Diels-Alder (DA) click

chemistry for bone repair, Carbohydr. Polym. 166 (2017) 123–130. doi:10.1016/j.carbpol.2017.02.062.

[16] F. Yu, X. Cao, L. Zeng, Q. Zhang, X. Chen, An interpenetrating HA/G/CS biomimic hydrogel via Diels-Alder click chemistry for cartilage tissue engineering, Carbohydr. Polym. 97 (2013) 188–195. doi:10.1016/j.carbpol.2013.04.046.

[17] C. García-Astrain, O. Guaresti, K. González, A. Santamaria-Echart, A. Eceiza, M.A. Corcuera, N. Gabilondo, Click gelatin hydrogels: Characterization and drug release behaviour, Mater. Lett. 182 (2016) 134–137. doi:10.1016/j.matlet.2016.06.115.

[18] R.K. Pal, E.E. Turner, B.H. Chalfant, V.K. Yadavalli, Mechanically robust, photopatternable conductive hydrogel composites, React. Funct. Polym. 120 (2017) 66–73. doi:10.1016/j.reactfunctpolym.2017.09.006.

[19] A. Mohamed, T. Ardyani, S. Abu Bakar, M. Sagisaka, Y. Umetsu, J.J. Hamon, B.A. Rahim, S.R. Esa, H.P.S. Abdul Khalil, M.H. Mamat, S. King, J. Eastoe, Rational design of aromatic surfactants for graphene/natural rubber latex nanocomposites with enhanced electrical conductivity, J. Colloid Interface Sci. 516 (2018) 34–47. doi:10.1016/j.jcis.2018.01.041.

[20] N. Martins, L. Barros, C. Santos-Buelga, M. Henriques, S. Silva, I.C.F.R. Ferreira, Evaluation of bioactive properties and phenolic compounds in different extracts prepared from Salvia officinalis L., Food Chem. 170 (2014) 378–385. doi:10.1016/j.foodchem.2014.08.096.

[21] S. Ganguly, D. Ray, P. Das, P.P. Maity, S. Mondal, V.K. Aswal, S. Dhara, N.C. Das, Mechanically robust dual responsive water dispersible-graphene based conductive elastomeric hydrogel for tunable pulsatile drug release, Ultrason. Sonochem. 42 (2018) 212–227. doi:10.1016/j.ultsonch.2017.11.028.

[22] A. Alam, Q. Meng, G. Shi, S. Arabi, J. Ma, N. Zhao, H.C. Kuan, Electrically conductive, mechanically robust, pH-sensitive graphene/polymer composite hydrogels, Compos. Sci. Technol. 127 (2016) 119–126. doi:10.1016/j.compscitech.2016.02.024.

[23] B. Gao, J. Mei, Y. Ma, G. Yuan, L. Ren, Environmental-fFriendly assembly of functional graphene hydrogels with excellent antibacterial properties, ChemistrySelect. 2 (2017) 7474–7482. doi:10.1002/slct.201701419.

[24] C.D. Grande, J. Mangadlao, J. Fan, A. De Leon, J. Delgado-Ospina, J.G. Rojas, D.F. Rodrigues, R. Advincula, Chitosan cross-linked graphene oxide nanocomposite films with antimicrobial activity for application in food industry, Macromol. Symp. 374 (2017) 1–8. doi:10.1002/masy.201600114.

[25] X. Zeng, G. Wang, Y. Liu, X. Zhang, Graphene-based antimicrobial nanomaterials: rational design and applications for water disinfection and microbial control, Environ. Sci. Nano. 4 (2017) 2248–2266. doi:10.1039/C7EN00583K.

[26] M. Ghorbanpour, M. Hatami, K. Kariman, P. Abbaszadeh Dahaji, Phytochemical variations and enhanced efficiency of antioxidant and antimicrobial ingredients in salvia officinalis as inoculated with different rhizobacteria, Chem. Biodivers. 13 (2016) 319–330. doi:10.1002/cbdv.201500082.

[27] A. Santamaria-Echart, I. Fernandes, F. Barreiro, A. Retegi, A. Arbelaiz, M.A. Corcuera, A. Eceiza, Development of waterborne polyurethane-ureas added with plant extracts: Study of different incorporation routes and their influence on particle size, thermal, mechanical and antibacterial properties, Prog. Org. Coatings. 117 (2018) 76–90. doi:10.1016/j.porgcoat.2018.01.006.

CHAPTER 9:

GENERAL CONCLUSIONS, FUTURE WORKS AND PUBLICATIONS

9. GENERAL CONCLUSIONS, FUTURE WORKS AND PUBLICATIONS

9.1. GENERAL CONCLUSIONS

The aim of this work was the development and the characterisation of novel maize starch-based materials in order to overcome some of their limitations as well as explore new fields of application. With this purpose different strategies were proposed that include the employment of new plasticisers, the use of different processing technologies, the development of nanocomposite films and the derivatization and cross-linking for hydrogel synthesis.

Regarding the plasticisers, PLS was obtained using glycerol, D-isosorbide and 1,3-propanediol by both solvent casting and extrusion/compression methods. The use of different plasticisers resulted in differences with respect to the transparency and contact angle values, mechanical and barrier properties as the same time that changed the principal relaxation transitions of the material. Indeed, D-isosorbide outstands between them and reveals as the most effective against the retrogradation derived changes of PLS.

WSNC and CNC were successfully isolated by acid hydrolysis. Besides, graphite was used as raw material for obtaining G and GO by sonication/centrifugation and oxidation, respectively.

Glycerol plasticised maize starch-based nanocomposites were developed by solvent casting and extrusion/compression methods adding WSNC and CNC as nanoreinforcements. On one hand, it was observed that the incorporation of WSNC affected to the two main relaxation transitions of the material and, at the same time, improved the mechanical behaviour and the OP of the neat PLS. Besides, it could be concluded that the addition of CNC enhanced significantly the mechanical properties.

Comparing the results for the films obtained by solvent casting with those obtained by extrusion/compression, it could be concluded that the latter, in addition to facilitate the large-scale production, led to higher transparency and better mechanical properties, whereas no significant differences were observed in the barrier properties.

Glycerol plasticised PLS nanocomposite films incorporating G and GO were successfully obtained by solvent casting method. Stable G aqueous dispersions were obtained by using Salvia extracts as surfactants. The resulting nanocomposites presented improved mechanical properties as well as electrical conductivity. However, it could be concluded that the use of Salvia extracts seemed to act as co-plasticiser for the PLS. The characterisation of the GO containing PLS nanocomposites showed strong starch/GO interactions and a good dispersion of the nanofiller was achieved. Moreover, the acidic treatment applied for the reduction of the GO was found to be effective, obtaining electrically conductive films.

Finally, maize starch was derivatized with pendant furanic moieties by the reaction with furfuryl isocyanate and novel starch based crosslinked hydrogels were successfully obtained by the DA reaction using water-soluble maleimides with different functionalities as cross-linkers. The addition of CNC into the hydrogels prepared with the TTMI, led to higher storage modulus values and pore sizes showing faster drug release rates. Finally, conductive and antibacterial starch-based DA nanocomposite hydrogels cross-linked with the BMI were synthesized incorporating G nanoflakes.

9.2. FUTURE WORKS

Based on the results obtained in this PhD thesis the following ideas and strategies are proposed as future works to continue in the field of the performed research and open new research lines:

- Increase the total NC content when WSNC and CNC are incorporated together in the PLS matrix, analysing deeply their synergistic effect in order to improve the mechanical and barrier properties.
- Prepare extruded PLS films reinforced with G and GO in order to evaluate the mechanical and barrier properties of PLS films obtained with a large-scale production and compare with their analogous obtained by solvent casting.
- Synthesize the maleimide functionalised derivative of starch. It would be interesting to modify starch by reaction with a maleimide ended compound such as it could be the counterpart of the S-FI for the development of totally starch based DA new hydrogels.
- Develop DA hydrogel nanocomposites adding surface functionalized polysaccharide NCs. It is suggested to modify both CNC and WSNC with maleimides with the aim of use them as co-cross-linkers.
- Increase the G content in conductive and antimicrobial DA hydrogels. The optimization of the G and extracts content is proposed in order to obtain tailor-made electrical conductivity and antimicrobial properties.
- Complete the characterisation of obtained DA hydrogels from a biomedical point of view. Taken into account the proposed biomedical applications of the hydrogels, we consider necessary to perform a more exhaustive characterisation.

9.3. PUBLICATIONS

Below are detailed the publications and the contributions to conferences resulting from this thesis research work.

9.3.1. Publications

Authors: Kizkitza González, Clara García-Astrain, Arantzazu Santamaria-Echart, Lorena Ugarte, Luc Avérous, Arantxa Eceiza, Nagore Gabilondo.

Title: Starch/graphene hydrogels via click chemistry with relevant electrical and antibacterial properties.

Journal: Carbohydrate Polymers.

Year: 2018.

Impact factor: 5.158 (JCR 2017)

Rank: Polymer Science 7/87 (JCR 2017)
Applied Chemistry 2/71 (JCR 2017)
Organic Chemistry 6/57 (JCR 2017)

Authors: Kizkitza González, Loli Martin, Alba González, Aloña Retegi, Arantxa Eceiza, Nagore Gabilondo.

Title: D-isosorbide and 1,3-propanediol as plasticizers for starch-based films: Characterization and aging study.

Journal: Journal of Applied Polymer Science.

Year: 2017.

Impact factor: 1.901 (JCR 2017)

Rank: Polymer Science 38/87 (JCR 2017)

Authors: Kizkitza González, Aloña Retegi, Alba González, Arantxa Eceiza, Nagore Gabilondo.

Title: Starch and cellulose nanocrystals together into thermoplastic starch bionanocomposites.

Journal: Carbohydrate Polymers.

Year: 2015.

Impact factor: 5.158 (JCR 2017)

Rank: Polymer Science 7/87 (JCR 2017)
Applied Chemistry 2/71 (JCR 2017)
Organic Chemistry 6/57 (JCR 2017)

Collaborations

Authors: Arantzazu Santamaria-Echart, Lorena Ugarte, Kizkitza González, Loli Martin, Lourdes Irusta, Alba González, María Ángeles Corcuera Arantxa Eceiza.

Title: The role of cellulose nanocrystals incorporation route in waterborne polyurethane for preparation of electrospun nanocomposites mats.

Journal: Carbohydrate Polymers.

Year: 2016.

Impact factor: 5.158 (JCR 2017)

Rank: Polymer Science 7/87 (JCR 2017)
Applied Chemistry 2/71 (JCR 2017)
Organic Chemistry 6/57 (JCR 2017)

Authors: Clara García-Astrain, Olatz Guaresti, Kizkitza González, Arantzazu Santamaria-Echart, Arantxa Eceiza, Maria Ángeles Corcuera, Nagore Gabilondo.

Title: Click gelatin hydrogels: Characterization and drug release behaviour.

Journal: Materials Letters.

Year: 2016.

Impact factor: 2.687 (JCR 2017)

Rank: Applied Physics 44/146 (JCR 2017)
Multidisciplinary Materials Science 97/285 (JCR 2017)

Authors: Clara García-Astrain, Kizkitza González, Tania Gurrea, Olatz Guaresti, Itxaso Algar, Arantxa Eceiza, Nagore Gabilondo.

Title: Maleimide-grafted cellulose nanocrystals as cross-linkers for bionanocomposite hydrogels.

Journal: Carbohydrate Polymers.

Year: 2016.

Impact factor: 5.158 (JCR 2017)

Rank: Polymer Science 7/87 (JCR 2017)
Applied Chemistry 2/71 (JCR 2017)
Organic Chemistry 6/57 (JCR 2017)

9.3.2. Conferences

Authors: Kizkitza González, Clara García-Astrain, Arantzazu Santamaria-Echart, Lorena Ugarte, Luc Avérous, Arantxa Eceiza, Nagore Gabilondo

Title: Tailor-made starch-based hydrogels by means of 'Click' cross-linking strategies.

Conference: 10th ECNP International Conference on Nanostructured Polymers and Nanocomposites.

Contribution: Poster.

Year: 2018.

Place: Donostia.

Authors: Kizkitza González, Clara García-Astrain, Arantzazu Santamaria-Echart, Lorena Ugarte, Luc Avérous, Arantxa Eceiza, Nagore Gabilondo

Title: Tailor-made starch-based hydrogels by means of 'Click' cross-linking strategies.

Conference: 6th Young Polymer Scientists Conference

Contribution: Oral presentation.

Year: 2018.

Place: Donostia.

Authors: Kizkitza González, Leire Iturriaga, Tamara Calvo-Correas, Alba González, Arantxa Eceiza, Nagore Gabilondo.

Title: Strategies for improving the behaviour of extruded starch based films (Best Poster Award)

Conference: 9th Conference on Green Chemistry and Nanotechnologies in Polymeric Materials

Contribution: Oral presentation.

Year: 2018.

Place: Cracow, Poland.

Authors: Kizkitza González, Clara García-Astrain, Arantzazu Santamaria-Echart, Lorena Ugarte, Luc Avérous, Arantxa Eceiza, Nagore Gabilondo.

Title: Almidoian oinarritutako saretutako 'klik' hidrogel eroaleak.

Conference: Materialen Zientzia eta Teknologia IV. kongresua.

Contribution: Oral presentation.

Year: 2018.

Place: Donostia.

Authors: Kizkitza González, Clara Carcia-Astrain, Arantzazu Santamaria-Echart, Lorena Ugarte, Luc Avérous, Arantxa Eceiza, Nagore Gabilondo

Title: Starch based 'click' cross-linked conductive nanocomposite hydrogels.

Conference: ImagineNano2018 International Conference

Contribution: Oral presentation.

Year: 2018.

Place: Bilbo.

Authors: Kizkitza González, Clara García-Astrain, Luc Avérous, Arantxa Eceiza, Nagore Gabilondo.

Title: Furan-modified starch hydrogels cross-linked through Diels-Alder reaction.

Conference: 6th International Conference on Biobased and Biodegradable Polymers, BIOPOL.

Contribution: Poster.

Year: 2017.

Place: Mons, Belgium.

Authors: Kizkitza González, Olatz Guaresti, Clara García-Astrain, Arantxa Eceiza, NagorenGabilondo.

Title: Diels-Alder reaction for the cross-linking of maize starch based materials.

Conference: 4th International Conference on Biobased Materials and Composites, ICBMC.

Contribution: Poster.

Year: 2017.

Place: Nantes, France.

Authors: Kizkitza González, Clara García-Astrain, Arantxa Eceiza, Nagore Gabilondo.

Title: Functionalization and cross-linking of maize starch through Diels-Alder reaction.

Conference: Seminario de jóvenes investigadores en polímeros.

Contribution: Oral presentation.

Year: 2016.

Place: Madrid, España.

Authors: Kizkitza González, Clara García-Astrain, Olatz Guaresti, Arantxa Eceiza, Nagore Gabilondo.

Title: Functionalized polysaccharides ready for the Diels-Alder reaction.

Conference: The 3rd International Conference on Bioinspired and Biobased Chemistry & Materials.

Contribution: Poster.

Year: 2016.

Place: Nice, France.

Authors: Kizkitza González, Clara García-Astrain, Olatz Guaresti, Arantxa Eceiza, Nagore Gabilondo.

Title: Diels-Alder "klik" erreakzio bidez elkar-gurutzatutako polisakaridoak.

Conference: UPV/EHU-ko I. Doktorego jardunaldiak.

Contribution: Poster.

Year: 2016.

Place: Bilbao

Authors: Kizkitza González, Loli Martin, Alba González, Arantxa Eceiza, Nagore Gabilondo

Title: `Green´ plasticizers for thermoplastic starch based materials.

Conference: 5th International Conference on Biobased and Biodegradable Polymers, BIOPOL.

Contribution: Poster.

Year: 2015.

Place: Donostia

Authors: Kizkitza González, Clara García-Astrain, Arantxa Eceiza, Nagore Gabilondo.

Title: Bionanocomposite hydrogel from cross-linked cellulose nanocrystals.

Conference: 6th Workshop on Green Chemistry and Nanotechnologies in Polymer Chemistry Bragança.

Contribution: Poster.

Year: 2015.

Place: Bragança, Portugal

Authors: Kizkitza González, Loli Martin, Alba González, Arantxa Eceiza, Nagore Gabilondo.

Title: Bioresoruced plasticizers for thermoplastic starch: preparation, characterization and ageing studies.

Conference: 3rd International Symposium International Meeting on Packaging Material / Bioproduct Interactions (MATBIM 2015)

Contribution: Poster.

Year: 2015.

Place: Zaragoza, España.

Authors: Kizkitza González, Itxaso Algar, Leire Urbina, Alba González, Arantxa Eceiza, Nagore Gabilondo.

Title: Thermoplastic starch based bionanocomposites reinforced with combined polysaccharide nanocrystals.

Conference: 5th Workshop Green Chemistry and Nanotechnologies in Polymer Chemistry, ECLIPSE Workshop, BIOPURFIL Workshop.

Contribution: Poster.

Year: 2014.

Place: Donostia.

Authors: Kizkitza González, Aloña Retegui, Alba González, Arantxa Eceiza, Nagore Gabilondo

Title: Polisakarido nanokristalen konbinaketa almidoi termoplastiko bionanokonpositeetan

Conference: Materialen Zientzia eta Teknologiaren II. kongresua.

Contribution: Poster.

Year: 2014.

Place: Donostia.

Authors: Kizkitza González, Aloña Retegi, Silvia Goyanes, Alba González, Arantxa Eceiza, Nagore Gabilondo.

Title: Starch and cellulose nanocrystals together into thermoplastic starch bionanocomposites.

Conference: 4th International Conference of Biodegradable and Biobased Polymers, BIOPOL.

Contribution: Poster.

Year: 2013.

Place: Roma, Italia.

Collaborations:

Authors: Olatz Guaresti, Kizkitza González, Arantxa Eceiza, Nagore Gabilondo.

Title: Thiolated chitosan based hydrogels using Michael addition and by controlling the macromolecular architecture.

Conference: 10th ECNP International Conference on Nanostructured Polymers and Nanocomposites.

Contribution: Poster.

Year: 2018.

Place: Donostia.

Authors: Leire Urbina, Itxaso Algar, Kizkitza González, Arantxa Eceiza, Nagore Gabilondo, Maria Ángeles Corcuera, Nagore Gabilondo.

Title: Biodegradable composites with improved optical and barrier properties from the impregnation of PLA to bacterial cellulose membranes.

Conference: 3rd International Symposium International Meeting on Packaging Material / Bioproduct Interactions (MATBIM 2015)

Contribution: Poster.

Year: 2015.

Place: Zaragoza, España.

Authors: Leire Urbina, Itxaso Algar, Kizkitza González, Arantza Eceiza, Aloña Retegi.

Title: Bionanocomposites obtained from renewable resources.

Conference: 5th Workshop Green Chemistry and Nanotechnologies in Polymer Chemistry, ECLIPSE Workshop, BIOPURFIL Workshop.

Contribution: Poster.

Year: 2014.

Place: Donostia.

Authors: Leire Urbina, Itxaso Algar, Kizkitza González, Arantza Eceiza, Aloña Retegi.

Title: Iturri berriztagarrietatik eratorritako bionanokonpositeak.

Conference: Materialen Zientzia eta Teknologiaren II. kongresua.

Contribution: Poster.

Year: 2014.

Place: Donostia.

ANNEXES

ANNEXES

LIST OF TABLES

Chapter 2: Materials and characterisation techniques

Chapter 3: Films based on plasticized starch

Chapter 5: Nanocomposite films based on starch and polysaccharide nanocrystals

Chapter 6: Nanocomposite films based on starch and carbonaceous nanoparticles

LIST OF FIGURES

Chapter 1: Introduction

Chapter 6: Nanocomposite films based on starch and carbonaceous nanoparticles

Chapter 8: Nanocomposite hydrogels based on cross-linked starch and graphene

LIST OF SCHEMES

Chapter 7: Nanocomposite hydrogels based on cross-linked starch and cellulose nanocrystals

LIST OF ABBREVIATION

^{1}HNMR	Proton nuclear magnetic resonance spectroscopy
AFM	Atomic force microscopy
ARES	Advanced Rheometric Expansion System
CNC	Cellulose nanocrystals
DA	Diels-Alder
DMA	Dynamic mechanical analysis
DMSO	Dimethyl sulfoxide
DS	degree of substitution
DSC	Differential scanning calorimetry
FTIR	Fourier transform infrared spectroscopy
NMP	N-methyl pyrrolidone
NMR	Nuclear magnetic resonance
OTR	Oxygen transmission rate
PBS	Phosphate buffered saline
PLS	Plasticised Starch
RH	Relative humidity
SEM	Scanning electron microscopy
SR	Swelling ratio
TGA	Thermogravimetric analysis
TPS	Thermoplastic starch
UV-vis	Ultraviolet-visible
WSNC	Waxy maize starch nanocrystals

WVTR	Water vapor transmission rate

LIST OF SYMBOLS

θ	Contact angle
2θ	Reflectance angle
λ	Incident radiation wavelength
θ_a	Advancing contact angle
θ_r	Receding contact angle
A	Area of film
a^* and b^*	Chromaticity parameters
a_{ext}	Penetrant activity outside the cell
a_{int}	Water activity
d	Shortest distance between successive identical planes in the crystal
E'	Stored modulus
E"	Loss modulus
G'	Storage modulus
G"	Loss modulus
I_d/I_g	Intensity ratio of D and G bands
I_x	Peak intensity of a crystallographic plane
l	Film thickness
L^*	Luminosity
m	Weight loss of the cell
n	Whole number (in our case 1)
R_q	Roughness
tan δ	Tangent of phase angle
Tg	Glass transition
T_{gel}	Gelatinisation temperature
$T_{\alpha 1}$	Temperature of the plasticizer-rich phase
$T_{\alpha 2}$	Temperature of the starch-rich phase
W_d	Initial weight of the freeze-dried sample

W_s	Weight of the swollen simple
W_t	Weight of the final dried simple
ΔE	Total difference parameter
ΔH_{gel}	Gelatinisation enthalpy
ω	Frequency